








# Impact of APOE3 Astrocytes on APOE4 Neuronal Phenotype

**Shuhan Li**

**Kellogg College**

**University of Oxford**

**Department of Psychiatry**

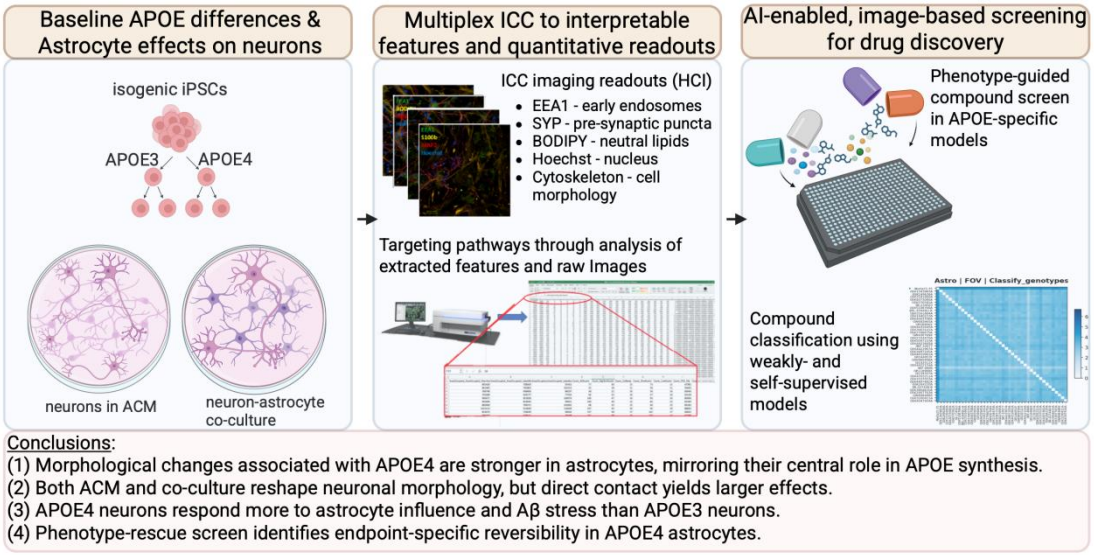
**Kavli Institute for Nanoscience Discovery**

**Hilary Term 2026**

**Thesis submitted for the degree of Doctor of Philosophy**

**Supervisors: Professor Noel J Buckley, Professor Francis G Szele, Dr Andrey Kormilitzin, Dr Helen A Rowland**

# Abstract




Background: Sporadic Alzheimer's disease (AD) is the major cause of dementia, which is driven by risk architecture rather than single-gene determinism. *APOE*4 is the most robust genetic contributor, while *APOE*3 is disease-neutral. However, the primary cellular site where APOE4 exerts its detrimental effects remains unclear. Elucidating the initial locus is crucial for understanding how the pathology subsequently progresses. This project aims to: (i) define how *APOE*4 alters neuron-astrocyte interactions, and (ii) establish a phenotype-driven platform to identify compounds that reverse *APOE*4-associated pathology.
Methods: Using isogenic human iPSC pairs (*APOE*3↔*APOE*4) from multiple donors, cortical neurons and astrocytes are differentiated to build astrocyte conditioned media and co-culture models. High-content ICC imaging (MAP2, SYP, EEA1, BODIPY, S100B, Hoechst) with automated morphological analysis (Harmony pipelines) were applied to systematically extracted ~60 cellular features spanning neurites, synapses, nuclei, lipids, early endosomes and cytoplasmic geometry. Analyses combined two-way ANOVA and ML (random forest, Kolmogorov-Smirnov test, weakly/self-supervised embeddings). In collaboration with GSK, a phenotype-rescue screen was performed in *APOE*-isogenic astrocytes to identify pathway-specific rescue compounds.
Results: (1) APOE4-dependent differences were present but were stronger in astrocytes than in neurons. Given this cell-type specificity and the investigated pathways, it is hypothesized that dysfunction in astrocytic lipid handling, endosomal function, and nuclear architecture could constitute core vulnerable pathways. The primary cellular locus of APOE4 morphology resides in astrocytes, which is consistent with astrocytes being the main APOE producers. (2) Both ACM and co-culture reshape neuronal morphology, but direct co-culture yielded broader effects than ACM, consistent with additional local/contact-associated or bidirectional mechanisms. (3) APOE4 neurons respond more to astrocyte influence and Aβ stress than APOE3 neurons. (4) Phenotype-rescue screen identifies endpoint-specific reversibility in APOE4 astrocytes. Endosome and nuclear shape are plastic and drug-responsive; lipid load and global cell geometry are more resistant.

Conclusion: This work provides evidence positioning astrocytes as a key cellular site contributing to *APOE*4 risk and dominant modulators of neuronal morphology via contact-dependent mechanisms. By translating genetic risk into quantitative image-based endpoints, it delivers a drug screen pipeline that distinguishes specific APOE4-related cellular features tractable to short-term (24hr) pharmacological intervention from those that are entrenched, enabling target prioritization, compound triage, and precision stratification. This framework not only refines the mechanistic understanding of sAD pathogenesis at the cellular level but also provides a scalable strategy for prioritizing therapeutic targets and compounds, moving the field closer to effective mechanism-based therapies.

# Acknowledgements

I would like to express my deepest and most sincere gratitude to all those who have walked alongside me during this challenging yet rewarding PhD journey. I am especially indebted to all the people who have generously invested their time, expertise and care in supporting me throughout this journey. Their guidance, encouragement and companionship have sustained me both scientifically and personally.

First and foremost, I am profoundly indebted to my primary supervisors, Professor Noel Buckley and Dr Helen Rowland. Noel, your thoughtful guidance and unwavering support, both professionally and personally, have been my anchor. Thank you for welcoming me into your group and for your steady guidance from the very beginning. Your thoughtful questions, critical feedback and broad perspective have continually pushed me to refine my thinking and to situate my work within the larger field. Helen, I am profoundly grateful for your patient supervision at the bench. Your hands-on mentorship in my daily experiments, your meticulous attention to detail, and your rigorous standards have been invaluable in shaping this work and me as a scientist.

I am also very grateful to Dr Andrey Kormilitzin for the mentorship and support throughout this work! Andrey, your guidance on data analysis, presentation skills, machine learning and statistical rigor has been invaluable. Thank you for patiently walking me through different analytical approaches, helping me understand assumptions behind tests, and offering constructive critiques of my analysis plans. The time you spent reviewing my figures, discussing alternative models and checking my code greatly improved the robustness and clarity of this thesis. Francis, thank you for your insightful comments and advice. Your perspective has helped me to see beyond individual experiments and to appreciate the bigger picture.

My appreciation extends to all my collaborators. I am particularly thankful to Professor Alejo Nevado-Holgado for his brilliant input and to the entire team for creating such a supportive environment. I wish to extend a special thanks to, Hanjun Zhao, Joshua Sammet, Ying Chen, Dr Laura Winchester and Dr Qiang Liu for their patient guidance and enlightening discussions on statistics and bioinformatics, which were crucial for navigating the complexities of my data.

My heartfelt thanks go to my wet-lab comrades. To Dr Nate Gould and Dr Diogo Dias, sharing a bench and a tissue culture room with you has been one of the most enjoyable parts of this journey. Thank you for your generosity in sharing protocols, reagents and tips. To Itzel Aguilar Gonzalez, my fellow PhD student, for your solidarity and for making the long hours in the lab feel lighter, especially during the 2023 Christmas.

I must especially thank Dr Anne Hedegaard and Dr Ishan Agrawal. Your expertise and

patience in guiding me through the lentiviral astrocyte culture protocol were instrumental to key chapters of this thesis.

I would also like to acknowledge the broader community within my department and college. I am grateful to all the staff, administrators and technical support teams who have kept the laboratories and facilities running smoothly, and who have helped with countless forms, bookings and practical matters behind the scenes. Their often unseen work has provided the stable environment in which this research could take place.

On a personal note, my deepest gratitude is reserved for my family. To my parents, thank you for your unconditional love and for believing in me even when I doubted myself, and for supporting my decision to pursue a long and sometimes uncertain academic path far from home. Your belief in me has always been my foundation. To my beloved partner, Zepeng, I cannot adequately express my appreciation for your patience, care and companionship throughout. Thank you for your immense emotional support, your boundless understanding, and for the daily life we have built together, from every shared meal you prepared to ease my burden, to every joke that lifted my spirits on a tough day. Your presence has brought warmth and balance to my life, and this thesis would not have been completed without your understanding and support.

Finally, to all who have contributed in big and small ways, please accept my sincerest thanks.

## Declaration Statement

I declare that this thesis is entirely my own work and describes my own research, except where otherwise stated. Content included in Chapter 7, Sections 7.2.6 and 7.2.7 is derived from a small component of collaborative work between my laboratory and GSK. Within that collaboration, astrocyte cell culture, plating, and immunocytochemistry staining were performed by the dissertation author; drug application and image acquisition were performed by Dr Helen Rowland; and the AIML analysis pipelines were developed by Ying Chen, Professor Alejo Nevado-Holgado, and Dr Andrey Kormilitzin. In the sections, Table 7.3 and Figures 7.7–7.10 present outcomes from these AIML analyses. All analysis, interpretation, and writing in this thesis are my own unless explicitly indicated otherwise, and all contributors are acknowledged above and in the relevant figure legends and methods.

Word count: 48,013

# Table of contents

**Abstract** ..... **2**

**Acknowledgements** ..... **4**

**Declaration Statement** ..... **6**

***Table of contents*** ..... ***7***

**List of figures** ..... **9**

**List of tables** ..... **13**

**List of Abbreviations** ..... **14**

**Chapter 1: Introduction** ..... **16**

1.1. Alzheimer's disease overview ..... 16

1.2. Current therapeutic interventions of AD ..... 19

1.3. APOE: a multifaceted player in AD ..... 24

1.4. Neuron-astrocyte interactions ..... 41

1.5. Cell-based models of AD and isogenic iPSC models ..... 44

1.6. Artificial intelligence machine learning ..... 57

1.7. Project aims and experimental design ..... 60

**Chapter 2: Materials and methods** ..... **62**

2.1. Materials ..... 62

2.2. Tissue culture ..... 68

2.3. Immunocytochemistry ..... 80

2.4. Real-time quantitative polymerase chain reaction (rt-qPCR) ..... 82

2.5. BCA protein assay ..... 85

2.6. Western blot ..... 85

2.7. Image acquisition and Harmony feature extraction ..... 87

2.8. Harmony extract features pipelines ..... 88

2.9. Statistics ..... 96

**Chapter 3: Characterization and iPSC-derived cell induction** ..... **104**

3.1. Introduction ..... 104

3.2. Results ..... 109

3.3. Discussion ..... 119

**Chapter 4: The effects of small-molecule astrocytes on neuronal phenotype** ..... **122**

4.1. Introduction ..... 122

4.2. Results ..... 126

4.3. Discussion ..... 153

**Chapter 5: The effects of lentiviral-induced astrocytes on neuronal phenotype** ..... **161**

5.1. Introduction ..... 161

5.2. Results ..... 162

5.3. Discussion ..... 181

**Chapter 6: The effects of Aβ stress on astrocytic and neuronal phenotype ..... 190**
6.1. Introduction ..... 190
6.2. Results ..... 193
6.3. Discussion ..... 210

**Chapter 7: Drug screening using lentiviral-induced astrocytes reveals feature-specific and genotype-dependent rescue of APOE4-associated phenotypes ..... 215**
7.1. Introduction ..... 215
7.2. Results ..... 219
7.3. Discussion ..... 258

**Chapter 8: Discussion ..... 268**
8.1. Strengths and unique value of isogenic human iPSC lines ..... 269
8.2. The relevance and importance of studying neuro-glial cross talk. ..... 271
8.3. APOE as a network-level perturbation of neuroglia crosstalk ..... 273
8.4. Limitations alternative research models and the functional validations ..... 275
8.5. Potential for future drug screen development ..... 280

**Concluding remarks ..... 286**

**References ..... 289**

# List of figures

*Fig.1.1. Cell-type specific roles of APOE pathways in the CNS. ..... 33*

*Figure 2.1. Lentiviral induction of human iPSC-derived astrocytes and timing of induction treatments. ..... 73*

*Figure 2.2. Schematic of a neuronal monoculture exposed to astrocyte-conditioned medium (ACM) from E3/E3 and E4/E4 astrocytes ..... 74*

*Figure 2.3. Schematic of a co-culture paradigm across APOE genotypes ..... 76*

*Fig 2.4. Representative image-analysis pipeline for feature extraction from neuronal monocultures. ..... 90*

*Fig 2.5. Representative image-analysis pipeline for feature extraction from astrocyte monocultures. ..... 93*

*Fig 3.1. RNA expression levels of OCT4 and MAP2 iPSCs and neurons. ..... 113*

*Fig 3.2. ICC images of iPSC clones stained with pluripotency and neuronal markers. 114*

*Fig 3.3. ICC staining of co-culture and monoculture confirms successful differentiation of neurons and astrocytes. ..... 117*

*Fig 3.4. BCA assay results of ACM samples collected for treatment on neurons. .... 118*

*Figure 3.5. Western blot of APOE in astrocyte conditioned media. ..... 118*

*Figure 3.6. Representative morphology of iPSC-derived astrocytes under the medium conditions used for ACM collection. ..... 119*

*Fig. 4.1. Synaptic features from monocultures of APOE3 and APOE4 neurons maintained in neuronal maintenance media (NMM). ..... 132*

*Fig. 4.2. Neurite morphological features from monocultures of APOE3 and APOE4 neurons maintained in NMM. ..... 133*

*Fig. 4.3. Nuclear features from monocultures of APOE3 and APOE4 neurons maintained in NMM. ..... 134*

*Fig. 4.4. Early endosomal features from monocultures of APOE3 and APOE4 neurons maintained in NMM. ..... 135*

*Fig. 4.5. Nuclear features changes of small molecules astrocytes co-cultured with APOE3 and APOE4 neurons. ..... 137*

*Fig. 4.6. Cellular morphology changes of from small molecules astrocytes co-cultured with APOE3 and APOE4 neurons. ..... 138*

*Fig. 4.7. Early endosomal changes of small molecules astrocytes co-cultured with APOE3 and APOE4 neurons. ..... 139*

*Fig. 4.8. Synaptic morphological changes of neurons to ACM treatment using astrocytes derived generated through small molecule stimulation. ..... 140*

*Fig. 4.9. Neurite morphology changes to ACM treatment using astrocytes generated through small molecule stimulation. ..... 141*

*Fig. 4.10. Neuronal nuclear changes after ACM treatment using astrocytes generated through small molecule stimulation. ..... 142*

*Fig. 4.11. Neuronal early endosomal changes to ACM treatment using astrocytes generated through small molecule stimulation. .....143*

*Fig. 4.12. Neuronal neurite changes after co-culture treatment using astrocytes generated through small molecule stimulation. .....145*

*Fig. 4.13. Neuronal nuclear changes after co-culture treatment using astrocytes generated through small molecule stimulation. .....146*

*Fig. 4.14. Early endosomal changes of neurons after co-culture treatment using astrocytes generated through small molecule stimulation. ..... 147*

*Fig. 5.1. Nuclear features from APOE3 and APOE4 lentiviral astrocytes co-cultured with neurons. ..... 164*

*Fig. 5.2. Cellular morphological features from APOE3 and APOE4 lentiviral astrocytes co-cultured with neurons. .....165*

*Fig. 5.3. Early endosomal features from APOE3 and APOE4 lentiviral astrocytes co-cultured with neurons. .....166*

*Fig. 5.4. Synaptic morphology changes to ACM treatment using astrocytes derived via lentiviral induction. .....169*

*Fig. 5.5. Neurites changes to ACM treatment using astrocytes derived via lentiviral induction. .....170*

*Fig. 5.6. Neuronal nucleus changes to ACM treatment using astrocytes derived via lentiviral induction. .....171*

*Fig. 5.7. Early endosomal changes to ACM treatment using astrocytes derived via lentiviral induction. .....172*

*Fig. 5.8. Synaptic morphology changes to co-culture treatment using astrocytes derived via lentiviral induction. ..... 176*

*Fig. 5.9. Neurites changes to co-culture treatment using astrocytes derived via lentiviral induction. .....177*

*Fig. 5.10. Neuronal nucleus changes to co-culture treatment using astrocytes derived via lentiviral induction. .....178*

*Fig. 5.11. Early endosomal changes to co-culture treatment using astrocytes derived via lentiviral induction. .....179*

*Fig. 6.1 Neuronal synaptic morphology changes to $A\beta_{25-35}$ exposure in APOE3 and APOE4 monoculture neurons. .....194*

*Fig. 6.2 Neurite changes to $A\beta_{25-35}$ exposure in APOE3 and APOE4 monoculture*

*neurons. ..... 195*

*Fig. 6.3 Neuronal nucleus changes after Aβ$_{25-35}$ exposure in APOE3 and APOE4 monoculture neurons. ..... 196*

*Fig. 6.4 Neuronal early endosome changes after Aβ$_{25-35}$ exposure in APOE3 and APOE4 monoculture neurons. ..... 197*

*Fig. 6.5 Neuronal synaptic changes after Aβ$_{25-35}$ exposure in APOE3 and APOE4 neurons treated with APOE3 or APOE4 ACM. ..... 201*

*Fig. 6.6 Neurite changes after Aβ$_{25-35}$ exposure in APOE3 and APOE4 neurons treated with APOE3 or APOE4 ACM. ..... 202*

*Fig. 6.7 Neuronal nucleus changes after Aβ$_{25-35}$ exposure in APOE3 and APOE4 neurons treated with APOE3 or APOE4 ACM. ..... 203*

*Fig. 6.8 Neuronal early endosomal changes after Aβ$_{25-35}$ exposure in APOE3 and APOE4 neurons treated with APOE3 or APOE4 ACM. ..... 204*

*Fig. 6.9 Cytoplasmic morphology of lentiviral-induced astrocytes in monoculture under Aβ$_{25–35}$ treatment. ..... 206*

*Fig. 6.10 Nuclear morphological features of lentiviral-induced astrocytes in monoculture under Aβ$_{25–35}$ treatment. ..... 207*

*Fig. 6.11 Astrocytic lipid droplet profiles in monoculture under Aβ$_{25–35}$ treatment. 208*

*Fig. 6.12 Astrocytic early endosomal features in monoculture under Aβ$_{25–35}$ treatment. ..... 209*

*Figure 7.1. Empirical cumulative distribution functions (ECDFs) for APOE4 + Compound #085 compared to the APOE3 + vehicle (DMSO). ..... 234*

*Figure 7.2. Empirical cumulative distribution functions (ECDFs) for APOE4 + #220 compared to the APOE3 + vehicle (DMSO). ..... 237*

*Figure 7.3. Empirical cumulative distribution functions (ECDFs) for APOE4 + #660 compared to the APOE3 + vehicle (DMSO). ..... 240*

*Figure 7.4. Empirical cumulative distribution functions (ECDFs) for APOE4 + #033 versus APOE3 + vehicle (DMSO). ..... 243*

*Figure 7.5. Empirical cumulative distribution functions (ECDFs) for APOE4 + #581 compared to APOE3 + vehicle (DMSO). ..... 246*

*Figure 7.6. Cell count per well of the neurons in five selected drug treatments and vehicle control across three donors. ..... 247*

*Fig 7.7. Genotype structure in well-level image embeddings within donors. ..... 252*

*Figure 7.8. Self-supervised FOV-level embeddings of untreated astrocyte reveal genotype-dependent structure. ..... 254*

*Figure 7.9. Embedding-based projection shows strong donor influence and modest compound responses in astrocytes. ..... 256*

*Figure 7.10. Treatment–treatment distance matrix from astrocyte FOV embeddings.257*

# List of tables

*Table 1.1. APOE4 carrier status, Alzheimer's disease (AD) frequency, and mean age at clinical onset. .....37*

*Table 1.2. APOE genotype, frequency, and association with Alzheimer's Disease. ...37*

*Table 1.3. Summary of in vitro studies on APOE modulated neuron-astrocyte interactions in multiple disease models. .....53*

*Table 1.3. Summary of in vitro studies on APOE modulated neuron-astrocyte interactions across multiple disease and developmental contexts. .....56*

*Table 2.1. Description of the three CRISPR-edited isogenic iPSC line pairs. ..... 63*

*Table 2.2. Media and reagents used for cell culture and differentiation of iPSCs. .... 64*

*Table 2. List of primary and secondary antibodies used in confocal microscopy. ..... 82*

*Table 4.1. Experimental groups in ACM culture conditions categorized by neuronal APOE genotype and culture media. .....131*

*Table 4.2. Experimental groups in neuron–astrocyte co-culture conditions categorized by neuronal and astrocyte APOE genotypes. .....131*

*Table 4.3. Overview of the Figures and Feature Categories in ACM and co-culture experiments. ..... 150*

*Table 4.4. Matrix summary of APOE- and context-dependent neuronal phenotypes affected by small-molecules induced astrocytes. .....151*

*Table 5.1. Matrix summary of APOE- and context-dependent neuronal phenotypes affected by lentiviral-induced astrocytes. .....180*

*Table 5.2. Summary of neuronal phenotypic comparisons between lentiviral- and small molecule-induced astrocytes ..... 189*

*Table 7.1. Statistical summary of drug-induced phenotypic rescue across three donors and five cellular features (with BH–FDR correction). ..... 223*

*Table 7.2. Baseline separation of APOE3 and APOE4 astrocytes across donors quantified by Kolmogorov–Smirnov (KS) tests. ..... 227*

*Table 7.3. Information content in astrocyte embeddings: SVM readouts for donor/genotype classification. .....251*

# List of Abbreviations

| | |
|---|---|
| **Aβ** | β-amyloid |
| **ACM** | Astrocyte conditioned media |
| **AD** | Alzheimer's disease |
| **AIML** | Artificial intelligence machine learning |
| **ALS** | Amyotrophic lateral sclerosis |
| **ANOVA** | Analysis of variance |
| ***APOE*** | Apolipoprotein E gene |
| **APOE** | Apolipoprotein E protein |
| **APP** | Amyloid precursor protein |
| **BSA** | Bovine serum albumin |
| **Cas9** | CRISPR-associated protein 9 |
| **cDNA** | Complementary deoxyribonucleic acid |
| **CNS** | Central nervous system |
| **CRISPR** | Clustered regularly interspaced short palindromic repeats |
| **DMSO** | Dimethyl sulfoxide |
| **DMEM** | Dulbecco's Modified Eagle's Medium |
| **DNA** | Deoxyribonucleic acid |
| **DPBS** | Dulbecco's phosphate-buffered saline |
| **EEA1** | Early endosome antigen 1 |
| **fAD** | Familial Alzheimer's disease |
| **GAPDH** | Glyceraldehyde-3-phosphate dehydrogenase |
| **GFAP** | Glial fibrillary acidic protein |
| **GWAS** | Genome-wide association studies |
| **hiPSC** | Human induced pluripotent stem cells |
| **kDa** | Kilodaltons |
| **OCT4** | Octamer-binding transcription factor 4 |
| **MAP2** | Microtubule-associated protein 2 |
| **NADH** | Hydrogenated nicotinamide adenine dinucleotide |
| **NMM** | Neural maintenance medium |
| **PD** | Parkinson's disease |
| **PBST** | Phosphate-buffered saline with 0.1% Tween-20 |
| **PBSTX** | Phosphate-buffered saline with 0.25% Triton-X |
| **PSEN1/2** | Presenilin 1/2 |
| **PVDF** | Polyvinylidene difluoride |
| **qPCR** | Quantitative polymerase chain reaction |
| **RNA** | Ribonucleic acid |
| **ROS** | Reactive oxygen species |
| **RT** | Room temperature |
| **S100B** | S100 calcium-binding protein β |
| **sAD** | Sporadic Alzheimer's disease |

| | |
|---|---|
| **SEM** | Standard error of the mean |
| **SYP** | Synaptophysin |
| **TREM-2** | Triggering receptor expressed on myeloid cells 2 |

# Chapter 1: Introduction

## 1.1. Alzheimer’s disease overview

Alzheimer’s disease (AD) is a devastating neurodegenerative disorder characterized by the progressive accumulation of extracellular amyloid-beta (Aβ) plaques and intracellular neurofibrillary tangles (NFTs) composed of hyperphosphorylated tau protein (p-Tau). These pathological hallmarks are accompanied by chronic neuroinflammation, synaptic dysfunction, gliosis, and widespread metabolic disturbances. Additionally, AD involves alterations in endocytic and cellular degradation pathways, elevated DNA damage, disruptions in the blood-brain barrier (BBB), and dysregulation of lipid metabolism as well as intra- and intercellular transportation. Over time, these cellular and molecular abnormalities lead to irreversible neuronal death, manifested as progressive brain atrophy (Long & Holtzman, 2019; Rajmohan & Reddy, 2017).

Beyond these pathological changes, AD leads to severe and progressive functional impairments at the individual level (Kumar et al., 2025). Cognitive dysfunction is one of the earliest and most prominent features, with deficits in episodic memory being particularly notable. Patients often struggle to recall recent events, names, or conversations. Executive dysfunction also emerges, impairing planning, judgment, and problem-solving abilities, making tasks such as managing finances or following complex instructions increasingly difficult. Depending on the affected brain regions, additional deficits arise. For instance, damage to Broca’s and Wernicke’s areas results in language impairments, including word-finding difficulties (anomia), reduced verbal fluency, and eventual decline in

comprehension (aphasia). Visuospatial deficits further contribute to disability, as patients may struggle to navigate familiar environments, become easily disoriented, or misjudge distances. In late-stage AD, motor impairments develop, including gait disturbances, dysphagia (swallowing difficulties), and eventual immobility.

Behavioral and psychological symptoms of dementia (BPSD) are also common, significantly impacting quality of life (Cloak et al., 2025). Apathy, characterized by a loss of motivation and interest in activities, is frequently observed. Agitation and aggression may manifest as restlessness, irritability, or verbal and physical outbursts. Mood disturbances such as depression and anxiety are prevalent, often linked to the patient's awareness of cognitive decline in early stages or directly to neurodegeneration in later phases. Some patients develop psychosis, experiencing delusions (e.g., paranoia or false beliefs about theft) or, less commonly, hallucinations. Sleep disturbances, including insomnia, fragmented sleep, or excessive daytime drowsiness, further exacerbate cognitive and behavioral decline.

As the disease progresses, patients exhibit a marked decline in daily functioning. Instrumental activities of daily living (IADLs), such as managing medications, driving, shopping, or using technology, have become increasingly challenging. Eventually, even basic activities of daily living (BADLs), including dressing, bathing, eating, and toileting, are compromised, leading to complete dependence on caregivers. Social and occupational dysfunction further isolates patients, as communication difficulties and cognitive decline result in withdrawal from social interactions and an inability to self-maintain (Kwon & Lee, 2021).

These functional abnormalities stem directly from the underlying neurodegenerative processes, including Aβ plaque accumulation, tau pathology, synaptic loss, and widespread neuronal death. The cumulative effect of these changes leads to profound disability, ultimately stripping patients of their autonomy in the advanced stages of AD. The relentless progression of both pathological and functional decline underscores the devastating nature of this disease, highlighting the urgent need for effective therapeutic interventions.

AD is the most common form of dementia, accounting for 60-80% of all dementia cases worldwide. It represents a major public health challenge, with significant implications for patients, caregivers, and healthcare systems. Epidemiological studies estimate approximately 50 million people worldwide currently live with dementia, a figure projected to triple by 2050 due to aging populations and increasing life expectancy (WHO). The economic burden is substantial, with annual global costs exceeding $1.3 trillion, driven by medical care, long-term support, and lost productivity (Lastuka et al., 2024).

Age remains the strongest non-modifiable risk factor for AD, with prevalence doubling approximately every five years after the age of 65 (‘2025 Alzheimer’s Disease Facts and Figures’, 2025). While early-onset AD accounts for less than 10% of cases, the vast majority of patients develop late-onset sporadic AD. Geographically, high-income countries report the highest prevalence due to longer life expectancies, yet low- and middle-income countries are experiencing the fastest growth in dementia cases, driven by rapid demographic transitions and limited healthcare infrastructure.

## 1.2. Current therapeutic interventions of AD

Despite over a hundred years of extensive research since 1907, therapeutic interventions for AD have historically faced substantial limitations with the majority of conventional treatments offering only symptomatic relief rather than disease modification, such as cholinesterase inhibitors and memantine targeting specific neurotransmitters. The development of disease-modifying therapies has been particularly contentious, as many drugs targeting Aβ pathways have failed to demonstrate consistent clinical benefits despite showing promise in preclinical models. Anti-amyloid monoclonal antibodies have changed the therapeutic landscape for early symptomatic AD. Lecanemab and donanemab have demonstrated statistically significant slowing of cognitive and functional decline in phase 3 trials in patients with biomarker-confirmed early AD, although the absolute clinical benefit at the group level remains modest and must be balanced against treatment burden and safety considerations, particularly amyloid-related imaging abnormalities (ARIA) (van Dyck et al., 2023; Sims et al., 2023). These antibodies target distinct aggregated Aβ species and promote amyloid clearance, supporting Aβ as a therapeutically tractable component of AD pathology while also emphasising the importance of early intervention and careful patient selection.

APOE4 genotype is particularly relevant to this benefit-risk assessment. Although, an APOE4 gene-dose relationship remains evident, with the highest ARIA incidence generally observed in homozygotes comparing to heterozygotes or non-carriers. (van Dyck et al., 2023; Paczynski et al., 2025; Zimmer et al., 2025), they can receive anti-amyloid therapy in some clinical settings under careful MRI surveillance. An emerging alternative strategy particularly relevant to APOE4 homozygotes is valiltramiprosate (ALZ-801), an orally administered

small-molecule inhibitor of Aβ oligomer formation. In the 78-week phase 3 APOLLOE4 trial conducted specifically in APOE4 homozygotes with early AD, the overall study population did not achieve a significant benefit on the primary clinical endpoint, although significant slowing of hippocampal atrophy was observed. In the prespecified mild cognitive impairment subgroup, nominally significant benefits were reported for cognitive and functional outcomes together with reduced brain atrophy, while ARIA incidence was not increased relative to placebo (Abushakra et al., 2025, 2026). These findings highlight the rapidly evolving and increasingly genotype-informed therapeutic landscape of AD.

Simultaneously, research into tau-targeting therapies has advanced, with anti-tau antibodies (e.g., semorinemab) and tau aggregation inhibitors (e.g., HMTM) undergoing clinical trials. Diranersen (BIIB080; formerly MAPTRx), an intrathecally administered antisense oligonucleotide targeting MAPT mRNA, demonstrated dose-dependent CSF tau lowering in a phase 1b trial (Mummery et al., 2023). In 2026, the phase 2 CELIA study reported robust reductions in CSF tau and tau-PET pathology together with prespecified signals of slower clinical decline across treatment groups. Importantly, CELIA did not meet its primary endpoint testing a dose – response relationship for change in CDR-SB at week 76; nevertheless, the combined biomarker and clinical signals were considered sufficient by the sponsor to support progression to registrational development (Biogen, 2026). Thus, the phase 2 findings are encouraging proof-of-concept for tau lowering and have supported progression of diranersen towards confirmatory phase 3 development. Small-molecule approaches, including kinase inhibitors to reduce tau hyperphosphorylation, have also shown promise in preclinical studies (Congdon et al., 2023). Beyond Aβ and tau, emerging

strategies focus on neuroinflammation (e.g., TREM2 agonists), metabolic dysfunction (e.g., insulin sensitizers), and synaptic repair (e.g., BDNF mimetics) (Weaver et al., 2023).

However, their limitations stem from several factors, including poor BBB penetration, restricted target specificity, and an inability to address downstream tau pathology and neuroinflammation that drive neurodegeneration. Critically, the clinical translation of anti-Aβ therapies has been complicated by the disconnect between amyloid reduction and meaningful cognitive improvement (Zhang et al., 2024). This discrepancy suggests that amyloid accumulation, while central to AD pathogenesis, may represent an early trigger rather than the sole driver of late-stage disease progression.

Safety remains an important consideration for anti-Aβ monoclonal antibodies, particularly amyloid-related imaging abnormalities (ARIA-E and ARIA-H). ARIA is frequently asymptomatic and manageable with MRI surveillance, and its incidence is not only influenced by APOE genotype, but also baseline cerebrovascular pathology and other clinical risk factors (Dyck et al., 2023; Paczynski et al., 2025; Zimmer et al., 2025). Importantly, safety considerations differ according to therapeutic modality. ARIA is principally associated with amyloid-clearing monoclonal antibodies and should not be generalised to all tau-directed therapies. Tau-targeting monoclonal antibodies and tau-lowering ASOs also differ mechanistically: antibodies predominantly target accessible extracellular tau species, whereas diranersen reduces MAPT transcript and consequently lowers tau production. Consistent with this mechanism, the characteristic ARIA profile associated with anti-Aβ monoclonal antibodies has not been observed with diranersen to date. Instead, reported

adverse events in the CELIA study were predominantly related to intrathecal administration or other treatment-associated effects, including procedural pain, post-lumbar puncture syndrome and transient confusional states (Mummery et al., 2023; Biogen, 2026). Thus, tau-directed antibodies and ASOs should be considered separately with respect to mechanism, route of administration and safety profile.

Importantly, substantial Aβ pathology does not invariably translate into cognitive impairment, indicating that the clinical expression of AD is modified by factors beyond amyloid burden alone. This remains relevant even in the context of strong genetic risk. APOE4 homozygote is associated with highly penetrant AD biology and earlier biomarker abnormalities, but genetic risk should not be interpreted as complete determinism of clinical phenotype (Fortea et al., 2024). Studies of cognitively healthy centenarians further demonstrate that resilience to AD is associated with a favourable polygenic background. In the 100-plus Study, cognitively healthy centenarians carried substantially lower polygenic AD risk than AD cases and age-matched controls, with protective genetic effects particularly enriched in immune and endolysosomal pathways (Tesi et al., 2024). More recent spatial transcriptomic analyses of cognitively resilient centenarians have shown that substantial Aβ deposition can coexist with relatively limited tau pathology and preserved cognition, with differences in microglial state transitions potentially contributing to divergent trajectories towards dementia or resilience (Lu et al., 2026). Together, these findings suggest that APOE operates within a broader genetic and cellular context, in which polygenic background and downstream resilience mechanisms may modify the phenotypic consequences of a major risk allele.

The persistent gap between pathological findings and clinical outcomes, combined with the limited success of Aβ-targeting therapies, underscores the urgent need to reconceptualize AD from a more comprehensive, systems-level perspective. This requires a paradigm shift that prioritizes upstream genetic risk factors as the primary drivers of pathogenesis, followed by the downstream molecular and cellular disruptions they initiate, including metabolic disturbances, mitochondrial dysfunction, impaired protein clearance mechanisms, chronic neuroinflammation, and vascular contributions, all of which may interact synergistically to drive disease progression and eventually, the cascade of neurodegeneration (Hajjo et al., 2022; Kok et al., 2022).

To unravel this complex interplay, modern multi-omics approaches, including genomics, transcriptomics, proteomics, and metabolomics, are proving indispensable. Artificial intelligence Machine learning (AIML) further enhances the possibility to integrate these high-dimensional datasets, uncovering disease subtypes, biomarkers, and therapeutic targets (Nam et al., 2024). These advanced methods enable researchers to validate findings across analyses and explore the intricate interactions among genetic, molecular, and cellular factors in the disease. By combining genetic insights with high-throughput technologies, it becomes possible to gain a more nuanced understanding of how genetic risk factors set off complex pathological cascades in AD, paving the way for more targeted and effective therapies.

AD is broadly classified into two main forms: fAD with early-onset and sporadic AD (sAD) with late-onset. fAD, a rare form accounting for less than 5% of cases with age of onset

around 40 to 50, is directly caused by autosomal dominantly inherited mutations in genes involved in amyloid precursor protein (APP) metabolism, comprising APP, PSEN1 and PSEN2 (Ryan & Rossor, 2010; Shea et al., 2016). The latter two alter γ-secretase processivity of APP cleavage, generating Aβ peptides of varying lengths, predominantly 40 or 42 amino acids (Aβ40 and Aβ42) with longer forms such as Aβ42 being more aggregation prone. These mutations could lead to increased total Aβ42 production (e.g., PSEN1 M146V), Aβ42/Aβ40 ratio (e.g., PSEN2 N141I), aggregation propensity (e.g., APP E693G) or β-secretase cleavage (e.g., APP KM670/671NL) (Hampel et al., 2021).

In contrast, sAD, the most prevalent form, typically manifests after the age of 65 and is considered a multifactorial disease arising from a complex interplay of genetic, environmental, and lifestyle factors, without a clear Mendelian inheritance pattern. While no sAD-causative mutations have been found, large-scale GWAS have identified 90 independent risk loci as of the most recent meta-analysis (Bellenguez et al., 2022).

## 1.3. APOE: a multifaceted player in AD

APOE is a 34 kDa polymorphic protein that serves as a major component of lipoprotein particles, playing an essential role in cholesterol and triglyceride transport throughout the body. In the central nervous system, APOE is primarily synthesized and secreted by astrocytes, where it facilitates lipid distribution to neurons and other glial cells, maintaining neuronal homeostasis and synaptic integrity. *APOE*, located on chromosome 19 (19q13.32), encodes three major protein isoforms distinguished by single amino acid substitutions at residues 112 and 158. These isoforms—APOE2 (Cys112, Cys158), APOE3 (Cys112, Arg158),

and APOE4 (Arg112, Arg158)—arise from two common missense mutations (rs429358 and rs7412) and exhibit distinct structural and functional properties due to their differing cysteine-arginine configurations (Liu et al., 2013).

### *1.3.1. APOE as a risk factor for sporadic AD*

Genome-wide association studies (GWAS) confirm *APOE4* as the strongest genetic risk factor for sAD, though its effect size varies by population (Altshuler et al., 2005). The risk conferred by *APOE4* is highest in East Asian individuals, followed by White individuals, Black individuals, and Hispanic individuals. In populations of African ancestry, *ABCA7* is the most significant risk gene, and *APOE G145D* is uniquely associated with AD in African American individuals. Similarly, the protective effect of *APOE2* displays population-dependent patterns with the most protective in White individuals, with weaker effects in Black individuals and Hispanic individuals, and no significant association in East Asian individuals (Belloy et al., 2023).

Emerging evidence suggests that APOE3 and APOE4 can indirectly and directly modulate gene expression by binding to nuclear proteins and transport to the nucleus, altering critical pathways in lipid metabolism, neuroinflammation, and synaptic function (Theendakara et al., 2018). These early transcriptional changes set the stage for protein-level dysfunction and disrupted proteostasis, ultimately leading to the hallmark pathologies of Aβ and NFT.

The clinical impact of *APOE* allelic variation follows a clear dose-dependent hierarchy. Heterozygous *APOE4* carriers face a 2- to 3-fold increased AD risk compared to *APOE3* homozygotes, while homozygous *APOE4* carriers experience an 8- to 12-fold elevation in risk. In contrast, while *APOE2* reduces AD risk, it increases susceptibility to type III

hyperlipoproteinemia (familial dysbetalipoproteinemia), especially in *APOE2* homozygotes showing elevated cholesterol/triglycerides.

*APOE* allele frequencies exhibit significant population variation while maintaining the overall hierarchy of *APOE3* > *APOE4* > *APOE2 (Yamazaki et al., 2019),* such that *APOE4* frequency ranges from 10-15% in East Asian individuals to 25-30% in Northern European individuals and *APOE2* is rarest in East Asian individuals (<5%) but reaches around 10% in some European and African groups (Corder et al., 1993).

### *1.3.2. APOE isoforms: E2, E3, E4*

The genetic variations underlying these allele frequencies translate directly into functional differences at the protein level. The cysteine/arginine substitutions at residues 112 and 158 – determined by APOE SNPs rs429358 and rs7412 – generate structurally distinct isoforms with divergent biochemical properties. These structural differences influence lipid binding affinity, receptor interactions, and aggregation propensity. Critically, the presence of cysteine residues in APOE2 (Cys112/Cys158) and APOE3 (Cys112) enables intramolecular disulfide bond formation, conferring greater structural stability compared to the arginine-rich APOE4 isoform, especially in the N-terminal domain (Riddell et al., 2008; Serrano-Pozo et al., 2021). This fundamental difference in protein folding underlies the isoforms' divergent biochemical behaviors, including lipid binding and receptor interactions. Moreover, APOE levels are highest in APOE2 carriers, followed by APOE3 carriers, and lowest in APOE4 carriers, due to the preferred degradation and therefore reduced APOE4 secretion by astrocytes.

### *1.3.3. Global expression and general function of APOE*

In the central nervous system (CNS), APOE is primarily synthesized, lipidated, and secreted by astrocytes, with microglia contributing to a lesser extent. Notably, neurons can also express APOE under specific stress conditions, suggesting context-dependent regulation (Blumenfeld et al., 2024; Mahley & Huang, 2012). As previously discussed, secreted APOE binds lipids to form lipoprotein particles that mediate cholesterol transport to neurons through interactions with LDLR family members, particularly LRP1. This lipid transport system is vital for maintaining neuronal membrane integrity, synaptic plasticity, and overall neuronal homeostasis.

The brain is the body's organ richest in cholesterol, bearing approximately 20% of total body cholesterol, and APOE is the primary lipoprotein responsible for lipid transport and maintenance of cholesterol homeostasis in the brain. All isoforms bind low-density lipoprotein receptor (LDLR) family members, while APOE4 shows higher affinity for low-density (LDL) and very low-density lipoproteins (VLDL) (Kim et al., 2009). Poorly lipidated APOE4 fails to properly export lipids from astrocytes, causing lipid droplet accumulation in glia and bloodstream (Garcia et al., 2021). The accumulated cholesterol in astrocytes stabilizes Aβ-producing lipid rafts as membrane domains that facilitate APP processing, while deficient Aβ removal accelerates plaque formation (Hicks et al., 2012; Lee et al., 2021). This disrupts normal lipid homeostasis and promotes pro-inflammatory glial activation.

Besides astrocytes, neurons expressing APOE4 are highly prone to lipid peroxidation and struggle to efflux toxic lipids, including peroxidized fatty acids, to astrocytes for

detoxification and incorporation into lipid droplets. This impaired lipid handling leads to oxidative stress and mitochondrial dysfunction. Additionally, APOE4 is associated with reduced levels of APOE-bound cholesterol, which is crucial for neurite outgrowth and synaptic function and therefore disrupts plasticity and repair mechanisms (Lane-Donovan & Herz, 2017; Wang et al., 2021). In addition to lipid dysfunction, APOE4 impairs synaptic plasticity by reducing reelin-dependent NMDA receptor phosphorylation and sequestering APOER2, NMDA, and AMPA receptors in intracellular compartments (Chen et al., 2010). The compromised receptor trafficking and localization of APOE4 excitatory neurons diminish surface expression of excitatory receptors and cause excessive accumulation in degradative pathways.

The disruptions also show neuron subtype specificity. When comparing isogenic *APOE4* with *APOE3* hiPSC-derived GABAergic neuron progenitors, APOE4 inhibitory cells exhibit decreased p-tau levels, axonal degeneration, and overall neuron loss (Wang et al., 2018). This finding aligns with clinical observations of network hyperexcitability in APOE4 carriers (Tabuena et al., 2024).

Additionally, APOE4 is linked to enlarged and increased endosomes, possibly due to endolysosomal trafficking dysfunction. This is further exacerbated by APOE4-driven upregulation of ADP-ribosylation factor 6 (ARF6), which disrupts ATP-binding cassette transporter A1 (ABCA1) recycling by trapping it in late endosomes (Fernández-Calle et al., 2022). As a result, deficient ABCA1 function impairs receptor-mediated endocytosis of Aβ, leading to reduced clearance and increased aggregation of Aβ plaques. This deficiency

compromises clearance of plaques through receptor-mediated endocytosis, allowing aggregates to accumulate.

APOE4 disrupts multiple receptor systems through shared endosomal pathology (Cataldo et al., 1997; Lin et al., 2018). In addition to sequestering APOER2 and glutamate receptors, APOE4 aggregates and retains insulin receptors in early endosomes, suppressing cell surface IR expression and impairing insulin signaling (Zhao et al., 2017). Pharmacological reduction of the pH in endosomes by inhibiting NHE6 reverses the APOE4-mediated endosomal dysfunction and restores synaptic function (Xian et al., 2018). In a follow-up study by the same group, deletion of NHE6 reduces APOE-mediated amyloid plaque buildup in an AD animal model (Pohlkamp et al., 2021).

Intriguingly, selective ablation of astrocytic APOE4 has been shown to mitigate tau-mediated synaptic degeneration, normalize disease-associated gene expression patterns, and attenuate excessive microglial phagocytosis of synapses (Tai et al., 2015; Vitek et al., 2009). APOE influences brain inflammatory responses by interacting with microglia and modulating cytokine production (Cash et al., 2012; Lynch et al., 2003). APOE4 carriers exhibit elevated levels of proinflammatory cytokines like IL-8 and TNFα, along with increased production of damage-inducing nitric oxide. Additionally, APOE4 has been linked to inflammation-related metabolic disorders.

Mitochondrial dysfunction is another key APOE4-specific pathology, occurring early in AD, even before the development of Aβ plaques and tau tangles, though the precise role of APOE4 in mitochondrial pathogenesis remains unclear (Simonovitch et al., 2019). APOE4 can

be cleaved at Met272, producing the APOE4 (Δ272-299) fragment, which is released under neuronal stress (Liang et al., 2021). Notably, the expression of APOE4 and the APOE4 (Δ272-299) fragment in mice leads to AD-like pathological changes and damages mitochondrial respiratory chain complexes in neurons, with the fragment having a stronger effect than full-length APOE4 (Pires et al., 2023). The neuron-specific expression impairs mitochondrial function by triggering ER stress, up-regulating GRP75 expression, and increasing the formation of mitochondria-associated ER membranes (MAMs) (Nakayama et al., 2009). This leads to mitochondrial calcium overload, fragmentation, and disrupted mitochondrial morphology and function. Recent studies also demonstrate APOE4-associated reductions in Complex IV activity, increased ROS production, and impaired mitochondrial motility in neurons (Cai & Tammineni, 2017; Orr et al., 2019). The disruptions further contribute to bioenergetic failure, reflected in decreased ATP levels and synaptic dysfunction in APOE4-expressing cells.

APOE coordinates lipid trafficking and receptor-mediated signaling across multiple players in the CNS (Fig.1.1), thereby shaping neuronal membrane composition, synaptic stability, innate immune tone, and proteostasis. As the predominant CNS source of APOE, astrocytes assemble HDL-like lipoproteins by ABCA1/ABCG1-dependent lipidation and LCAT activity to deliver cholesterol and phospholipids (Mahley & Huang, 2012). APOE-lipoproteins and extracellular ligands are internalized via LDLR/LRP1/APOER2 and HSPGs into EEA1 positive early endosomes, where recycling versus degradation is modulated by endosomal pH regulators such as NHE6 (Kanekiyo et al., 2014; Prasad & Rao, 2018b). Astrocytes clear Aβ

through LRP1/HSPG-mediated uptake and endolysosomal processing (Nixon, 2017). Through the tripartite synapse, astrocytes support synaptogenesis and transmission via lipid supply, ECM interactions, and glia-transmission (Allen & Eroglu, 2017). Under stress, astrocytes accumulate lipid droplets, engage lipophagy/β-oxidation, and adopt context-specific reactive states that reshape immune tone (Escartin et al., 2021).

Neurons acquire APOE-lipids via APOER2/LRP1/VLDLR to tune membrane composition, receptor trafficking, and synaptic stability, including crosstalk with the Reelin pathway (Herz & Chen, 2006; Kanekiyo et al., 2014). APOE isoforms modulate Aβ uptake and endosomal flux (Cataldo et al., 2000). APOE4 cells show increased susceptibility to oxidative and metabolic stress and lower homeostatic reserve, reflected as neurite fragility and reduced synaptic puncta (Butterfield & Mattson, 2020; He et al., 2024). Microglia integrate lipid and damage signals through the TREM2–APOE axis, driving transitions toward disease-associated microglia (DAM) when challenged with lipidated debris (Keren-Shaul et al., 2017; Nugent et al., 2020). Complement-tagged synapses are engulfed via CR3-dependent phagocytosis (Raiders et al., 2021; Werneburg et al., 2020). Oligodendrocytes depend on APOE-lipids for myelin synthesis and repair, and recycle lipids from myelin debris after injury (Berghoff et al., 2021; Camargo et al., 2017). LDLR-family signaling shapes OPC proliferation and maturation (Philips & Rothstein, 2017). Lipid stress impairs remyelination programs (Camargo et al., 2017). At the blood–brain barrier (BBB), APOE–LRP1 signaling in endothelium and pericytes regulates transcytosis and clearance of Aβ and lipoproteins (Pflanzner et al., 2011; Storck et al., 2015). APOE4 is associated with increased BBB permeability (Reas et al., 2024).

Together, these cell-type specific roles position APOE as a network-level organizer of neuroglial crosstalk.

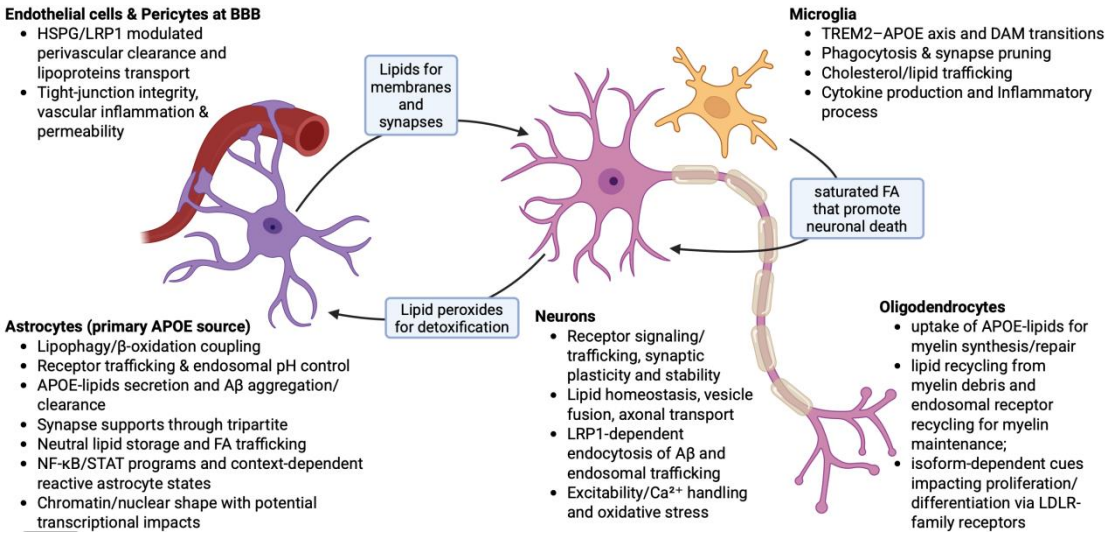



***Fig.1.1. Cell-type specific roles of APOE pathways in the CNS.***

*Schematic overview of pathways through which APOE influences endothelial/pericyte, astrocyte, neuron, microglial, and oligodendrocyte biology. At the BBB (left), endothelial cells and pericytes regulate perivascular clearance and lipoprotein transport through HSPG/LRP1-mediated mechanisms, in concert with tight-junction integrity and vascular inflammation/permeability control. Astrocytes (primary CNS source of APOE) coordinate lipophagy β-oxidation coupling; receptor trafficking and endosomal pH control; APOE lipoprotein secretion and Aβ aggregation/clearance; tripartite synapse support; neutral lipid storage and fatty-acid trafficking; NF-κB/STAT programs underlying context-dependent reactive states; and nuclear/chromatin architecture with potential transcriptional impacts. Neurons depend on astrocyte-supplied lipids for membranes and synapses and exhibit receptor signaling/trafficking that supports plasticity and stability; lipid homeostasis, vesicle fusion, and axonal transport; LRP1-dependent endocytosis of Aβ and endosomal trafficking; and excitability/$Ca^{2+}$ handling with oxidative-stress responses. Microglia engage the TREM2-APOE axis during disease-associated microglia (DAM) transitions, coupling phagocytosis/synapse pruning with cholesterol/lipid trafficking and cytokine-driven inflammatory programs; saturated fatty acids can promote neuronal toxicity (right). Oligodendrocytes take up APOE-lipids for myelin synthesis/repair, recycle lipids from myelin debris, and depend on endosomal receptor recycling for myelin maintenance; isoform-dependent APOE cues can influence proliferation/differentiation via LDLR-family receptors. Arrows indicate paracrine exchange, including lipids for membranes/synapses (from astrocyte to neuron) and lipid peroxides routed for detoxification, as well as potentially neurotoxic saturated FA exposure. Schematic created with BioRender.com*

*Abbreviations: Aβ, amyloid-β; APOE, apolipoprotein E; BBB, blood–brain barrier; $Ca^{2+}$, calcium; DAM, disease-associated microglia; FA, fatty acid; HSPG, heparan sulfate proteoglycan; LDLR, low-density lipoprotein receptor; LRP1, LDLR-related protein 1; NF-κB, nuclear factor kappa-B; STAT, signal transducer and activator of transcription; TREM2, triggering receptor expressed on myeloid cells 2.*

### *1.3.4. APOE-Aβ metabolism*

APOE plays a central role in Aβ metabolism, regulating both its production and clearance through isoform-dependent mechanisms . APOE co-deposits with Aβ in amyloid plaques and upregulates APP transcription and Aβ production in human iPSC-derived neurons, with APOE4 showing the strongest effect (E4>E3>E2) (Huang et al., 2017; Namba et al., 1991). APOE4 facilitates Aβ fibrillization by accelerating the nucleation of Aβ deposition, while lipidated APOE (via ABCA1) binds Aβ monomers to promote their clearance through multiple pathways (Cole & Vassar, 2007; Hampel et al., 2021; Loch et al., 2023). Receptor-mediated clearance occurs through LRP1 uptake of Aβ/APOE complexes, though this process is impaired with APOE4. Additionally, APOE promotes extracellular Aβ degradation through neprilysin (NEP) and insulin-degrading enzyme (IDE) in an isoform-dependent manner, with APOE4's reduced lipidation capacity compromising this proteolytic pathway (Kanekiyo et al., 2014).

While the mechanisms remain incompletely understood, perivascular drainage appears altered in APOE4 carriers, with mouse models showing associated changes in extracellular matrix proteins (elevated laminin/collagen IV, reduced fibronectin) (Hawkes et al., 2012). Aβ binding to APOE4 redirected the rapid clearance of free Aβ40/42 from the LDL receptor-related protein 1 (LRP1) to the VLDLR, which internalized APOE4 and Aβ-APOE4 complexes at the BBB more slowly than LRP1 (Deane et al., 2008). In contrast, APOE2 and APOE3, as well as Aβ-APOE2 and Aβ-APOE3 complexes, were cleared at the BBB via both VLDLR and LRP1 at a substantially faster rate than Aβ-APOE4 complexes. When examining conditioned media from human iPSC-derived neurons, APOE4 cells were found to secrete

significantly higher levels of Aβ40 and Aβ42 compared to APOE3 neurons. However, this effect was not observed in either *in vitro* or *in vivo* AD mouse models, highlighting critical interspecies differences in APOE function and its regulation of Aβ metabolism (Castellano et al., 2011; Wang et al., 2018). These findings underscore the importance of human iPSC-based systems for modeling APOE-related mechanisms.

*APOE* genotype also determines the response of astrocytes to Aβ. Although APOE4 primary neurons treated with conditioned media from resting APOE4 astrocytes had similar metabolism to APOE3 neurons treated with APOE3 CM, when challenged astrocytes with Aβ42, APOE4 neurons showed increased basal mitochondrial and glycolytic metabolic rates than their APOE3 counterparts (Fleeman et al., 2023). APOE4 astrocytes lack an Aβ-stimulus cytokine signaling response but upregulate glycolytic ATP production. These findings indicate that APOE4 creates subtle shifts in reactive astrocytic responses to Aβ, which stresses neuronal metabolism, resulting in potential susceptibility to disease insults.

Microglial phagocytosis is similarly modulated. Although binding between TREM2 and APOE occurs to a similar extent among the three different APOE isoforms, but enhanced by APOE lipidation. TREM2 deficiency impairs microglial uptake of Aβ, especially when complexed with APOE4 lipoproteins (Yeh et al., 2016). Another study showed higher TREM2 expression in patient-derived mononuclear blood cells from APOE4-carriers with mild cognitive impairment and AD compared to non-carriers (Casati et al., 2018). Moreover, a decrease of TREM2 in microglia has been reported in mice expressing APOE4 (Heneka, 2023). This

differential capacity represents a key pathway through which APOE genotypes influence AD risk.

| APOE4 carrier status | APOE4 | | |
|---|---|---|---|
| | Non-carrier | Heterozygous | Homozygous |
| AD frequency | 20% | 47% | 91% |
| Mean age of clinical onset | 84 | 76 | 68 |

***Table 1.1. APOE4 carrier status, Alzheimer's disease (AD) frequency, and mean age at clinical onset.*** *Summary of AD occurrence and onset age stratified by APOE4 status: Non-carrier (no E4 allele; e.g., E2/E2, E2/E3, E3/E3), Heterozygous (one E4 allele; e.g., E2/E4 or E3/E4), and Homozygous (two E4 alleles; E4/E4). AD frequency denotes the percentage of individuals in the referenced cohort who received a clinical diagnosis of late-onset AD; the Mean age of clinical onset indicates the average age at diagnosis within each genotype group. Estimates are as reported by (Lin et al., 2018)*

| ***APOE*** **Genotype** | **Approximate Distribution Frequency** | **AD Risk (Odds Ratio vs. E3/E3)** | **Mean Age of Clinical Onset** | **Key References** |
|---|---|---|---|---|
| E2/E2 | ~0.7% | ~0.6 (Protective) | Later than E3 | (Farrer et al., 1997) |
| E2/E3 | ~11.0% | ~0.6 (Protective) | ~84 years | Farrer et al. (1997) |
| E3/E3 | ~59.0% | 1.0 (Reference) | ~84 years | Farrer et al. (1997) |
| E2/E4 | ~2.2% | ~2.6 | Unknown | Farrer et al. (1997) |
| E3/E4 | ~23.0% | ~3.7 | ~76 years | (Liu et al., 2013) |
| E4/E4 | ~1.9% | ~14.9 | ~68 years | Liu et al. (2013) |

***Table 1.2. APOE genotype, frequency, and association with Alzheimer's Disease.*** *Frequencies indicate rough distribution in outbred populations (predominantly of European ancestry) and vary by cohort and ancestry. AD risk is expressed as an odds ratio (OR) relative to the E3/E3 reference genotype; values <1.0 denote a protective association and values >1.0 denote increased risk. Reported ages reflect the approximate mean age of clinical onset for late-onset AD in meta-analyses and may differ across studies; Unknown indicates insufficient data for a stable estimate. Figures are drawn from seminal meta-analyses (Farrer et al., 1997; Liu et al., 2013). Minor discrepancies can arise due to rounding. The distribution frequencies are global averages and can vary significantly between different ethnic and geographical populations. The Odds Ratios and onset ages are primarily derived from large-scale meta-analyses for general illustration.*

### *1.3.5. APOE targeted therapy*

Understanding the role of APOE in these AD pathways is crucial for developing effective therapeutic strategies. Many of these APOE-related pathways are interconnected, contributing to the complex pathogenesis of AD. For example, impaired Aβ clearance can lead to neuroinflammation, synaptic dysfunction, and mitochondrial impairment. Similarly, disrupted lipid metabolism can contribute to neuroinflammation and synaptic dysfunction. Recognizing that effective intervention in AD may require addressing the root causes of the disease, rather than solely targeting downstream consequences, researchers are increasingly focusing on APOE-targeted therapies. These strategies aim to intervene at the source of APOE-related pathologies, preventing the cascade of events that lead to AD. Targeting APOE or its downstream pathways could potentially modify disease progression and improve cognitive outcomes (Table 1.3).

As the most upstream therapeutic strategy, genetic correction aims to modify disease predisposition by altering *APOE* expression profiles. Preclinical studies demonstrate that targeted *APOE*2 gene delivery can effectively elevate levels of this protective isoform in the brain (Lexeo Therapeutics, 2024). This approach seeks to shift the APOE isoform equilibrium toward a neuroprotective state, potentially intervening before irreversible neurodegeneration occurs. The beneficial effects of APOE2 operate through both Aβ-related pathways (enhanced Aβ clearance) and Aβ-independent mechanisms (improved lipid metabolism and synaptic maintenance). Notably, epidemiological studies reveal APOE2's dual role as both an AD protective factor and a longevity gene, suggesting systemic

anti-aging properties (Z. Li et al., 2020). However, APOE2 carriers show increased susceptibility to cerebral amyloid angiopathy (CAA) and certain cerebrovascular disorders, highlighting the importance of balanced APOE modulation in therapeutic development.

In addition to gene-based strategies, direct APOE modulation employs small molecules to alter APOE structure or function. Compounds such as PH0022 (Wang et al., 2018) and bumetanide (Taubes et al., 2021) have been investigated as APOE structure converters, while LRP1 agonists may enhance Aβ clearance by promoting APOE-LRP1 interactions. Drugs that enhance LRP1 activity could promote Aβ removal from the brain, addressing a critical downstream effect of APOE dysfunction, while still acting relatively early in the disease process (Salomon-Zimri et al., 2016). Another approach involves immunotherapy, where anti-APOE antibodies, like 'HAE-4', could prevent APOE4 from interacting with Aβ or facilitate its clearance, thereby reducing plaque accumulation and associated neurotoxicity (Liao et al., 2018; Williams et al., 2020).

Given the broader influence of APOE on multiple cellular pathways, additional therapeutic efforts focus on modulating APOE-related mechanisms. β-secretase inhibitors (βSi-II and OM99-2) but not γ-secretase inhibitors (CPD-E and DAPT) target APP processing, preventing excessive Aβ production (Israel et al., 2012). APOE4 is also known to impair endocytic trafficking, which is essential for synaptic maintenance and intracellular signaling. This defect can be rescued by enhancing PICALM function, an endocytic adaptor protein that restores trafficking efficiency in APOE4-expressing astrocytes (Narayan et al., 2020). Mitochondrial function, another key aspect of APOE pathology, may be improved through interventions

like methyl-β-cyclodextrin (MbCD) and simvastatin, which mitigate cholesterol burden and restore mitochondrial respiration (Lee et al., 2023). Moreover, research on the BBB dysfunction associated with APOE4 suggests that compounds such as FK506, cyclosporine A, and INCA6 may help restore BBB integrity, validated in APOE4 pericytes, which play a crucial role in maintaining vascular health (Blanchard et al., 2020).

Several classes of lipid metabolism regulators have demonstrated potential in restoring lipid homeostasis in APOE4-associated AD. Cyclodextrins reduce intracellular cholesterol accumulation, while Triacsin C, an ACSL1 inhibitor, blocks the de novo synthesis of glycerol-lipids and cholesterol esters (Blanchard et al., 2022). Statins, such as simvastatin and atorvastatin, also play a role in modulating lipid balance.

These compounds exhibit cell-type-specific effects that highlight the complexity of lipid metabolism in AD. For instance, LXR agonists (GW3965, T901317) rescued decoupled lipid and cholesterol metabolism in APOE4-expressing astrocytes, but showed limited efficacy in microglia (Tcw et al., 2022). The application of MbCD or simvastatin not only mitigated cholesterol burden but also restored mitochondrial respiration in APOE4 astrocytes, underscoring the intimate connection between lipid homeostasis and bioenergetics in disease progression (Lee et al., 2023).

Beyond pharmacological interventions, lifestyle modifications remain an essential component of AD risk reduction and management. While diet, exercise, and cognitive stimulation do not directly target APOE, they may bolster cerebral resilience by reducing

systemic inflammation and improving vascular health—factors known to interact with APOE4's pathogenic effects.

These preventative measures, in combination with APOE-targeted therapies, offer a comprehensive approach to reducing AD risk and slowing disease progression. By intervening at different nodes of the APOE pathway cascade, from genetic correction to functional restoration, this multipronged approach offers hope for disrupting AD's pathogenic sequence before clinical symptoms emerge. Future success will depend on optimizing combination therapies that address both APOE's upstream origins and its downstream consequences.

## 1.4. Neuron-astrocyte interactions

For much of neuroscience history, glial cells were regarded merely as passive support cells, maintaining neuronal function but playing no direct role in cognition or disease. Early research focused almost exclusively on neurons, as the most important player in brain activity and cognition. However, over the past few decades, a paradigm shift has taken place, recognizing glia, including astrocytes, microglia, oligodendrocytes, etc., as dynamic and essential regulators of brain function rather than just neuronal 'assistants' (Dossi et al., 2018).

Astrocytes are now shown to be crucial for synapse formation, maintenance, and elimination, as well as for neurotransmitter regulation, ion homeostasis, metabolic support, and BBB integrity through their role in tripartite synapses between neurons and capillary.

The discovery of glia-transmission, in which astrocytes actively release signaling molecules to influence environmental cellular activity, further highlighted their independent contributions (de Ceglia et al., 2023). Moreover, the ability of astrocytes to respond to injury, inflammation, and neurodegeneration has positioned them as key players in neurological diseases, including AD (Lee et al., 2022). In addition to gap junction intercellular communication, one of the ways astrocytes exert this influence is through the secretion of neurotransmitters, growth factors, and inflammatory molecules, which can regulate neuronal activity, synaptic plasticity, and neuroinflammation. Astrocytes release various neurotransmitters such as glutamate, ATP, and D-serine, the latter being a key co-agonist of NMDA receptors and essential for synaptic plasticity (Kim et al., 2019). They also secrete growth factors, including brain-derived neurotrophic factor (BDNF), nerve growth factor (NGF), and glial cell-derived neurotrophic factor (GDNF), all of which support neuronal survival and synaptic function (Feng et al., 2012). In addition, astrocytes contribute to the brain's inflammatory environment by releasing cytokines such as TNF-α, IL-1β, and IL-6, which are pro-inflammatory, as well as TGF-β and IL-10, which exert anti-inflammatory effects (Al-Qahtani et al., 2024). As research advanced, the interplay between astrocytes and neurons emerged as a fundamental aspect of brain homeostasis and dysfunction. Astrocytes form extensive networks that communicate with neurons, delivering metabolic substrates via the astrocyte-neuron lactate shuttle, regulating glutamate uptake and recycling, and contributing to synaptic functions (Andersen et al., 2021). They also play a key role in vascular regulation, ensuring adequate blood flow to active brain regions (MacVicar & Newman, 2015).

However, in AD, these interactions become disrupted, leading to synaptic dysfunction, metabolic stress, and neurotoxicity. APOE4-bearing astrocytes, in particular, exhibit impairments in lipid metabolism, Aβ clearance, and glutamate regulation, which exacerbate neuronal vulnerability and cognitive decline (Qi et al., 2021a). Reactive astrogliosis, a hallmark of AD, leads to excessive glutamate uptake, neuroinflammatory responses, and synapse loss (Preman et al., 2021). Notably, the pattern of astrocyte dysfunction and its impact on neurons in AD shares similarities with epilepsy, where aberrant astrocyte activity contributes to neuronal hyperexcitability and seizure susceptibility (Wu et al., 2025). Additionally, astrocyte-driven pathological features have also been reported in other neurodegenerative and neuropsychiatric disorders, including amyotrophic lateral sclerosis (ALS) (Madill et al., 2017), Huntington's disease (Garcia et al., 2019), schizophrenia (Fritschi et al., 2021), and so on, where astrocytes modulate disease progression through dysregulated neurotransmitter clearance, oxidative stress, and inflammatory signaling. These parallels across disease contexts reinforce the critical and active role of astrocytes as key participants in the tripartite synapse in the CNS and highlight the therapeutic potential of targeting astrocyte-neuron interactions in a broad spectrum of neurological disorders (Wu et al., 2025).

Given the critical role of APOE in regulating neuron-astrocyte interactions, a deeper understanding of astrocyte dysfunction in AD may open new avenues for intervention. Targeting these pathways holds promise for mitigating neuronal damage and slowing disease progression. As research continues to redefine the role of astrocytes in

neurodegenerative diseases, their interactions with neurons remain a central focus for understanding *APOE*-mediated AD pathogenesis.

## 1.5. Cell-based models of AD and isogenic iPSC models

Mouse models that successfully mimic age-dependent neurodegeneration rely mostly on neuronal overexpression of human proteins carrying FAD-causing mutations. These models have significantly advanced our understanding of the molecular underpinnings of FAD, as genes such as APP, PSEN1, and PSEN2 exhibit clear genetic penetrance and strong linkage to AD, particularly in relation to amyloid plaque formation. However, they do not adequately represent sAD, which comprises the majority of cases and does not typically result from highly penetrant mutations, including previously mentioned APOE, TREM2, and CLU. Yet, unlike FAD mutations, these risk variants are not directly causal, and their pathogenic mechanisms are often more subtle, context-dependent, and influenced by gene–environment interactions. This discrepancy highlights the urgent need for sAD models that do not rely on mutations of FAD genes but instead reflect the more complex and multifactorial nature of sporadic disease (Lambert et al., 2013).

Even the effort to generate sAD transgenic mouse models by deleting or introducing the expression of *APOE* (Balu et al., 2019), however, these models face fundamental limitations due to species differences. For example, the mouse *APOE* gene, located on chromosome 7, does not naturally encode the APOE4 isoform found in humans. Therefore, to study APOE isoform-specific effects in sAD, human alleles must be inserted into mice. Even so, the relevance of these models remains limited, as mice often fail to recapitulate key aspects of

human disease pathology (Masopust et al., 2017). Notably, the manifestation of neurodegenerative phenotypes in mice typically requires overexpression of mutated human proteins at levels far exceeding physiological norms, further distancing these models from the endogenous conditions seen in patients (Penney et al., 2020a).

The advent of induced pluripotent stem cell (iPSC) technology in 2007 has significantly transformed the landscape of AD research by enabling the generation of patient-specific human brain cells (Takahashi et al., 2007). iPSC lines have been generated from both early and late-onset AD patients, as well as healthy age- and sex-matched individuals, and numerous repositories have been established around the world to make such lines available to researchers (Huang et al., 2019; Penney et al., 2020). Moreover, the major brain cell types can now be differentiated from iPSCs, while increasingly complex co-culture systems and protocols are being published (Shi et al., 2017). Notably, iPSC-derived neurons and astrocytes retain aspects of the clinical phenotype of the individuals from whom they are derived, providing a valuable model for studying patient-specific features of AD (Heinzelmann et al., 2024; Ng et al., 2022; Rowland et al., 2025). This opens the door to personalized medicine approaches, where disease-relevant phenotypes and drug responses can be studied within a human cellular context that retains the patient's unique genetic background.

However, this patient-specificity also has a downside. Donor variability introduces a major confounding factor, as differences in genetic background can mask or amplify disease-relevant phenotypes (Volpato & Webber, 2020). This variability, combined with the

technical demands of iPSC culture and the difficulty of scaling to large sample sizes, complicates experimental analysis. This poses challenges when attempting to isolate the effects of individual genetic variants. To overcome this, gene-editing tools such as CRISPR/Cas9 have been instrumental (Jinek et al., 2012). By enabling precise editing of specific genetic loci while maintaining an otherwise isogenic background, researchers can directly assess the impact of particular mutations or risk variants. Careful validation is still required to rule out batch effects, but this approach has become central to dissecting gene-specific contributions to disease mechanisms. Moreover, incorporating multiple isogenic pairs from the different donors could further ensure that the findings are not driven by background genetic variability.

While iPSC-based models do not fully replace *in vivo* systems, they do represent a step forward, offering a platform for mechanistic studies, especially when combined with genome editing and multi-omics technologies to model sAD in a more nuanced and human-relevant context.

As mentioned, growing evidence suggests that astrocytes play an active and influential role not only in shaping neuronal phenotypes but also in regulating brain function and cognition, particularly in the context of neurological diseases such as AD. In addition, astrocytes derived from patient-specific iPSCs with sAD backgrounds have exhibited pathological features, including altered metabolism, impaired neuronal support, and elevated secretion of inflammatory molecules (Brezovakova et al., 2022; Supakul et al., 2024). Notably, these astrocytic dysfunctions are not simply secondary responses to neuronal degeneration, but

rather, the diseased astrocytes could potentially actively contribute to the neuronal dysfunctions, underscoring the existence of a bidirectional interplay between neurons and astrocytes. In such cases, isogenic iPSC-derived models are particularly beneficial, where the APOE genotype is the sole variable, enabling precise dissection of isoform-specific effects on neuronal function mediated by astrocytes. Given that astrocytes are the principal source of APOE in the central nervous system, these models are also powerful for elucidating the roles of APOE in each neuron or astrocyte as well as their interaction in AD pathogenesis.

### *1.5.1. Co-culture and conditioned media approaches*

To interrogate the interactions, two main experimental paradigms have proven especially informative: co-culture systems and conditioned media (CM) approaches. Co-culture systems, where neurons and astrocytes are grown together on the same surface, enable the study of direct cell-cell interactions, including physical contact, gap junction, and signaling via membrane-bound molecules. On the other hand, CM or Transwell experiments offer a complementary strategy and enable researchers to assess the non-cell-autonomous effects of astrocytes on neurons by isolating astrocyte-secreted factors from direct cell contact (Stöberl et al., 2023). In this approach, neurons are exposed to media conditioned by astrocytes (astrocyte conditioned media, or ACM), which contains >180 defined soluble secreted factors, cytokines and extracellular matrix proteins that are critical for neuronal differentiation and maturation (Greco et al., 2010; L. Li, 2009)

Experimental parameters across studies vary but follow certain common practices as summarized in Table 1.3. ACM is typically collected after 24-72 hours of incubation. The

media are often used as ratios of dilutions with fresh neuronal medium ranging from 30%, 50% or 100%, though some studies employ lower concentrations (e.g., 1%) during neuronal differentiation or maturation phases for extended incubation time over a few weeks. Some studies employ chronic exposure paradigms for several days of incubation with neurons, while others use acute treatments (1 hour) to examine fast-acting signaling mechanisms. The temporal dynamics of exposure can yield divergent results. For instance, in primary mice model, neuronal activity measured via live-cell calcium imaging increased after acute administration of APOE4 astrocyte medium, but this enhancement was not sustained with long-term treatment (Konings et al., 2021).

Besides, there are wide range of astrocytes used from primary rodent sources to human iPSC-derived lines, including disease-relevant genotypes such as APOE4, SOD1-G93A, or C9ORF72 with or without exogenously added stressors to induce a diseased condition (particularly the A1 subtype), such as Aβ or reactive astrocytes-associated cytokines. Neuronal targets likewise include primary cells, human iPSC-derived motor neurons, dopaminergic precursors, retinal ganglion cells, or cortical neurons.

Functional outcomes are assessed via cell viability assays, electrophysiology (e.g., sEPSC, spike patterns), autophagy markers, synaptic protein levels, calcium imaging, and various metabolic and lipidation assays. These systematic setups provide robust platforms to dissect astrocyte-to-neuron signaling under both physiological and pathological conditions.

Under normal control conditions, wild-type astrocytes promote neural stem/progenitor cell proliferation and neuronal maturation. ACM from resting astrocytes can enhance neuronal

maturation, increasing NeuN+ cells in differentiation protocols and promoting dopaminergic neuron fiber outgrowth mediated through secreted proteins like BDNF and extracellular matrix components that support neurite outgrowth (P. Jiang et al., 2016). During disease models of ACM or astrocytes, neurotoxic responses are frequently elicited, including reduced neuronal viability, increased apoptosis, impaired autophagic flux, suppressed synaptic activity, and disrupted spine morphology. A1-type reactive astrocytes consistently reduce neuronal activity, decreasing spike frequency and amplitude adaptation while increasing apoptosis (Barbar et al., 2020). These effects are partially mediated by inflammatory cytokines (TNFα/IL1α) as demonstrated by IL-6 antibody blockade experiments, and by the reactive oxygen species present in the CM of activated astrocytes.

The models are used in various neurodegenerative diseases. In sAD models, APOE4 astrocytes promote neuronal amyloidogenic processing through excessive cholesterol delivery, leading to lipid raft expansion and increased Aβ production (S.-I. Lee et al., 2021). These effects correlate with impaired synaptic support, as APOE4 astrocytes show reduced ability to upregulate PSD-95 in co-cultured neurons compared to their APOE3 counterparts. Cerebral organoid studies further reveal APOE4-associated dysregulation of cholesterol metabolism, with neurons exhibiting elevated cholesterol biosynthesis gene expression and filipin staining intensity (J. Zhao et al., 2023). Patient-derived astrocytes produce robust neurotoxicity (Welby & Ebert, 2023). This manifests electrophysiologically as reduced spike frequency and amplitude adaptation in patch-clamp recordings, and morphologically as decreased spine density and simplified dendritic arbors.

Amyotrophic lateral sclerosis (ALS) models also demonstrate striking ACM-mediated toxicity (Birger et al., 2019; Rojas et al., 2023), such that CM from TDP43- or C9ORF72-mutant astrocytes induces oxidative stress in motor neurons, reduces MHC class I expression, and triggers ER stress responses. SOD1-G93A ACM fails to support progenitor development, unlike wild-type ACM which enhances motor neuron generation. However, the neurotoxic effects appear selective for motor neurons, with interneurons remaining unaffected by ALS astrocyte secretions.

Besides astrocyte genotypes and disease-associated mutations, their developmental stage and activation state critically determine astrocyte influences. Neonatal rat astrocytes outperform adult astrocytes in promoting neural stem cell proliferation (Jiang et al., 2016). The interaction also matters. While direct contact with healthy astrocytes rescues spinal muscular atrophy (SMA) motor neuron activity, CM alone proves ineffective, suggesting contact-dependent mechanisms (Welby & Ebert, 2023). Similarly, long-term potentiation requires physical astrocyte-neuron contact rather than secreted factors alone (Shen et al., 2023).

The interaction effect is also cellular context-dependent. While baseline metabolic profiles appear similar in neurons treated with conditioned media from resting APOE3 or APOE4 astrocytes, a divergence occurs upon exposure to Aβ-challenged APOE4 astrocyte media. This pathological condition triggers a selective metabolic hyperactivation in APOE4 neurons, characterized by elevated mitochondrial respiration and glycolytic flux, which was not observed in APOE3 neurons under identical conditions (Fleeman et al., 2023). This

APOE4-specific metabolic vulnerability to astrocyte-mediated inflammatory signaling may represent an early pathological mechanism preceding overt neurodegeneration.

Importantly, the emerging picture of APOE-mediated effects reveals a complex, cell type-dependent paradigm with critical implications for experimental design. Measured by live cell $Ca^{2+}$ imaging, it has revealed that APOE can target synapses and differentially affects neuronal activity in a cell-type-dependent manner (Wang et al., 2018). For example, neuronal APOE3 induces the most active and efficient neuronal activity, whereas astrocyte-derived APOE4 elicits the strongest initial neuronal firing. In other words, whether APOE is produced by astrocytes or neurons matters.

These findings necessitate careful consideration when choosing between organoid models and co-culture systems, particularly for studies investigating how APOE isoforms affect astrocyte-neuron interactions. The neuronal responses are jointly determined by both the astrocytic *APOE* genotype (through secreted factors) and the endogenous neuronal *APOE* genotype (through cell-autonomous mechanisms). In iPSC-derived organoids, astrocytes and neurons typically originate from the same differentiation trajectory and thus share an identical genetic background (Jusop et al., 2023). While this preserves developmental consistency, it limits the ability to dissect genotype-specific interactions. To investigate cross-genotype effects—such as whether APOE4 astrocytes exert toxic effects on APOE3 neurons, or whether APOE3 astrocytes can mitigate APOE4-associated neuronal phenotypes, co-culture systems offer a more suitable platform. By enabling the combination of cell types

with distinct *APOE* genotypes, co-culture models provide a more flexible and controlled approach for studying non-cell-autonomous mechanisms and genotype-specific crosstalk.

Together, these observations underscore the multifaceted interplay between genetic background (*APOE* genotype), cell types (astrocyte vs neuron-derived), and disease context (resting vs activated) in shaping neuronal function and survival. Crossing different research models from 2D monocultures to cerebral organoids, co-cultures, these studies paint a comprehensive picture of how astrocyte secretions shape disease-specific neuronal phenotypes through diverse mechanisms, including metabolic regulation, synaptic support, and inflammatory signaling.

These cell-based approaches, particularly when deployed using isogenic lines that differ only in specific risk genes, have proven invaluable for uncovering the downstream mechanisms by which astrocytes bearing different APOE isoforms contribute to neurodegenerative pathology. They allow researchers to tease apart the relative contributions of contact-mediated versus soluble signaling mechanisms and to examine how APOE isoforms influence neuron-astrocyte communication. By leveraging both co-culture and ACM systems, studies can more fully elucidate the role of astrocytes in mediating neuronal dysfunctions. Ultimately, these insights will help reveal the effects of APOE isoforms on neuronal function and identify new therapeutic targets and guide the development of interventions that address the cellular and molecular complexity of AD at an earlier and more causal stage of pathogenesis.

***Table 1.3. Summary of in vitro studies on APOE modulated neuron-astrocyte interactions in multiple disease models.***

| Ref. | Astrocyte origin | Neuron etc. origin | Means of contact | Contact duration | Observations | Diseases |
|---|---|---|---|---|---|---|
| (Konings et al., 2021) | mice | mice | conditioned for 48hr used as 50% | 1 or 24hr | Neuronal $Ca^{2+}$ activity increases after acute but not long-term administration of APOE4 ACM | AD |
| (Qi et al., 2021a) | mice | mice | co-culture using Transwell or ACM used as 30% | 48hr | APOE4 astrocytes exhibit diminished metabolic and synaptic support to neurons | AD |
| (Watanabe et al., 2023) | isogenic hiPSC | isogenic hiPSC | co-culture | 5d | APOE4 astrocytes impair neuronal dendritic spine dynamics by increased matrix protein EDIL3 | AD |
| (Fleeman et al., 2023) | mice | mice | used as 50% | 72hr | ACM challenged with Aβ increases the basal mitochondrial and glycolytic metabolic rates of APOE4 | AD |
| (Wang et al., 2018) | hiPSC | hiPSC | | 1wk | Neuron-derived, but not astrocyte-derived APOE4 affect tau phosphorylation, GABAergic neuron degeneration, and Aβ production in neurons | AD |
| (Blanchard et al., 2020) | hiPSC | hiPSC (iBBB) | conditioned for 48hr and used as 50% | 96hr | More amyloid accumulation shows in APOE4 compared to APOE3 iBBB | AD |
| (Zhao et al., 2017) | hiPSC | hiPSC | co-culture using Transwell | 7d | Astrocytes co-culture promotes neuronal survival and synaptogenesis with APOE4 astrocytes less effective than APOE3 | AD |
| (Zhao et al., 2023) | hiPSC | hiPSC | cerebral organoids | | APOE4 organoids show enhanced eIF2α phosphorylation levels, and higher cellular cholesterol levels | AD |
| (Lee et al., 2021) | hiPSC | hiPSC | | | APOE4 astrocytes contribute to neuronal amyloidosis by expanding lipid rafts and facilitating Aβ production through an oversupply of cholesterol | AD |
| (Song et al., | rodent | rodent | 2d | 42hr | ACM promote differentiation into TH+ DA neurons with increased fiber | PD |

| | | | | | | |
|---|---|---|---|---|---|---|
| n.d.) | | | | | outgrowth and branching | |
| (Rojas et al., 2023) | Primary/ human | mice | 7d | 5d | ALS/FTD astrocytes reduce healthy motoneurons numbers | ALS/FTD |
| (Christou et al., 2013) | mice | mice | | | SOD1-G93A ACM does not promote motor neuron differentiation specifically as WT ACM, but interneurons are unaffected. | ALS/motor neuron diseases |
| (Marton et al., 2023) | rat | rat | | 24-48hr | SOD1G93A ACM decreases motor neurons survival or neurite length (mediated by miR-155-5p) | ALS/motor neuron diseases |
| (Madill et al., 2017) | hiPSC | hiPSC | conditioned for 5d | 5d | ALS astrocytes decrease motor neuron viability, impair autophagic flux and protein clearance | ALS |
| (Birger et al., 2019) | hiPSC | hiPSC | conditioned for 2d | 2d | C9orf-astrocyte CM increases motor neurons oxidative stress | ALS |
| (Song et al., 2016) | mice | mice | co-culture | 1-5d | SOD1 G93A astrocytes decrease MHC class I level in motor neurons by inducing ER stress | ALS |
| (Welby & Ebert, 2023) | hiPSC | hiPSC | conditioned for 48h and used as 50% | 2d | Healthy ACM improves SMA motor neuron activity but to a less degree than astrocyte co-culture | Spinal muscular atrophy |
| (Kerkering et al., 2023) | hiPSC | hiPSC | co-culture | | Benign MS (but not HC, PMC) astrocytes protect neurons from TNF-α/IL-17-induced neurite damage, via JAK/STAT signaling | MS |
| (Sourial & Doering, 2016) | rat | rat | concentrated 10X and used as 10% | | Fmr1-KO ACM restricted NP proliferation | Fragile X Syndrome |
| (Sharma et al., 2023) | hiPSC | hiPSC | conditioned for 48h and used as 50% | 5wk | Astrocyte co-culture determines neuronal phenotype; ACM determines neuronal firing patterns | Fragile X Syndrome |

| | | | | | | |
|---|---|---|---|---|---|---|
| (Kushwaha et al., 2021) | mice | mice | co-culture; ACM conditioned for 3d | 10-12d | Prion astrocytes co-culture impairs neuronal growth, dendritic spine development and synapse maturation; reactive ACM damages neuronal viability and synaptogenesis functions | Prion |
| (Vadodaria et al., 2021) | hiPSC | hiPSC | conditioned for 24hr | 1wk | Stimulated BD astrocyte CM reduces neuronal activity (mediated by IL-6) | Bipolar disorder |
| (Zhu et al., 2006) | rat | rat | 4-6d | 4d | ACM protects neurons against corticosterone-induced damage | Corticosterone-induced damages |
| (LI et al., 2014) | rat | rat | | 4d | Reactive astrocytes CM promote NS/PC proliferation by HMGB1 | Brain Injury/reactive astrocytes |
| (Dai et al., 2019) | rat | rat | | | Neonatal astrocytes promote NS proliferation | Brain Injury/reactive astrocytes |
| (Smith et al., 2022) | hiPSC | hiPSC | stimulated for 48hr | 5-8d | Reactive astrocytes are not cytotoxic but can inhibit OPC differentiation thereby limiting their remyelination capacity and inducing inflammatory | Reactive astrocytes |
| (Jiang et al., 2016) | hiPSC | mice (mixed glia/neuron culture) | conditioned for 3d, concentrated 50X and used at 100ug/ml | 14d | Immature astroglia promote OPCs proliferation and differentiation | Development |
| (Barbar et al., 2020) | hiPSC | hiPSC | conditioned for 2d and used as 67% | every 6hr for 72hr | A1 ACM increase neuronal apoptosis and immature firing pattern | no |
| (Sharlow et al., 2023) | ACM from ScienCell | hiPSC | used as 1% | 4wk | ACM increases the percentage of mature neurons | no |
| (Fan et al., | Primary/ | hiPSC | 24hr | 24hr | C2-ceramide-treated ACM reduces RGC numbers (mediated by TNF-α) | no |

| | | | | | | |
|---|---|---|---|---|---|---|
| 2021) | human | | | | | |
| (Yang et al., 2003) | rat | rat | | | Neurons co-cultured with astrocytes can undergo LTP, but not in ACM | no |
| (Song et al., 2019) | rat | rat | 48hr | | ACM protects neurons from glutamate-induced death | no |
| (Nägler et al., 2001) | rat | rat | 3 times/wk, half collected | | ACM Increases neuronal autopsies' number | no |

***Table 1.3. Summary of in vitro studies on APOE modulated neuron-astrocyte interactions across multiple disease and developmental contexts.*** *Studies listed evaluate how APOE isoform influences astrocyte-neuron functions across mouse and human iPSC models in vitro. The details provided for each reference include the biological origin of the astrocytes and neurons/other cell types, the method of co-culture (e.g., direct contact, transwell, astrocyte-conditioned medium (ACM)), the duration of the co-culture or ACM exposure, primary observations related to APOE genotype (primarily APOE4 vs. APOE3), and the disease context. Key observations highlight APOE4-specific detrimental effects on neuronal function, including calcium signaling, synaptic support, and response to Aβ (amyloid-β), as well as intrinsic astrocytic deficits in metabolism and lipid handling. CM, conditioned medium; wk, week; h, hour; iBBB, induced blood-brain barrier; AD, Alzheimer's Disease; PD, Parkinson's disease; ALS, amyotrophic lateral sclerosis; FTD, frontotemporal dementia; MS, multiple sclerosis; and no, non-disease-specific studies.*

## 1.6. Artificial intelligence machine learning

With the rapid advancement of artificial intelligence machine learning (ML) technologies, their application in biomedical research has opened new avenues for uncovering findings that are subtle, complex, and otherwise difficult to detect using conventional approaches (Athanasopoulou et al., 2022). For instance, natural language processing techniques are widely used to interpret clinical documentation and extract meaningful insights from unstructured health records (Hossain et al., 2023; Scharp et al., 2024). Convolutional neural networks, such as DeepMind AlphaGo, have been employed to predict molecular, particularly protein structures and identify biomarkers or potential pharmacological candidates for specific diseases (Aborode et al., 2025; Visan & Negut, 2024; You et al., 2022). In image-based biological research, deep learning models have shown great promise in analyzing diverse imaging data, ranging from X-rays, MRI and CT scans aiding clinical diagnostics to microscopy images from basic research, by automatically learning features for cell classification, segmentation, and phenotype discovery (Hosny et al., 2018; Y. Kumar et al., 2023).

Without relying on predefined human-selected features, ML enables direct extraction of patterns from raw data, thus minimizing subjective biases. Particularly, recent advances in deep learning have further enabled end-to-end modeling approaches, where raw images are input into a model that directly outputs predictions (Fulton, 2010). This allows for the

discovery of complex, non-linear relationships and latent phenotypic patterns that are difficult to interpret.

ML approaches can generally be categorized into two major types: supervised and unsupervised learning (Sarker, 2021). In supervised learning, the model was trained on a portion of the data set as the input, which was labeled with a known outcome or category (Black et al., 2023). The goal is to learn the mapping from inputs to outputs through the hidden layers, enabling the model to make predictions or classifications on the rest of the data set which is new and unseen to the model. This approach is well-suited for tasks like cell classification, where images are annotated according to known phenotypes or treatment groups, allowing the model to distinguish between morphological changes associated with different genotypes or experimental treatments.

In contrast, unsupervised learning deals with unlabeled data. The objective is to discover patterns, structures, or groupings in the data without explicit instruction. In biological imaging, this can be used to detect subtle phenotypic shifts or rare cell subtypes. A representative example is cosine-similarity learning, where models are trained to measure how similar two images are based on their features, without requiring specific class labels (Canessa et al., 2020). This approach can be useful for grouping cells by morphological similarity or identifying outliers that deviate from typical cellular states.

In this study, both classification and similarity tasks were employed. The classification model was trained to classify neuronal cell phenotypes based on morphological changes in response

to astrocyte treatments and *APOE* genotype across different experimental conditions. It assigned each image to a predefined category (e.g., APOE3 neurons co-cultured with APOE3 astrocytes vs. APOE4 co-cultured with APOE3 astrocytes), while similarity analysis embedded cell images into a high-dimensional space to assess how closely related different samples are in an unsupervised or semi-supervised manner. Together, these complementary strategies enabled the identification of both known and novel cellular phenotypes with high sensitivity.

However, one key limitation of these end-to-end models is their 'black box' nature. While they excel at predictive accuracy, they often lack interpretability in tracing exactly which cellular features the model was relying on to drive its decisions with a biologically meaningful explanation (Górriz et al., 2023). Therefore, they serve as a powerful complement to conventional, feature-based image analysis. The former is better suited for comprehensive discovery of differences and holds broader application potential. In contrast, the latter is crucial for deciphering results in fine detail and providing an interpretable, feature-specific understanding of phenotypic differences. Our conventional analysis pipeline was built using Harmony software (PerkinElmer, Waltham, MA, USA) to design pipelines and extract specific cellular and molecular features. These extracted features were then statistically compared across groups and regression was modeled using generalized linear models (GLM) to evaluate the individual contribution of each extracted feature in relation to experimental variables (*APOE* genotypes, astrocytes, cell lines, etc.), providing a more interpretable, feature-specific understanding of the observed phenotypic differences.

## 1.7. Project aims and experimental design

The overarching hypothesis of this thesis was that APOE genotype would be associated with cellular phenotype at both cell-autonomous and neuron – astrocyte interaction levels, and that the mode of interaction (soluble astrocyte-derived factors versus direct co-culture) would influence the magnitude and direction of the observed neuronal phenotypes. A secondary translational hypothesis was that reproducible APOE-dependent cellular features could be identified prospectively and used as quantitative endpoints in a phenotypic drug screen. These hypotheses were tested sequentially using donor-matched isogenic APOE3 or APOE4 iPSC-derived neurons and astrocytes, conditioned-medium and direct co-culture models, acute $A\beta_{25\text{-}35}$ stress, and high-content image-based phenotyping.

Specificially, human iPSC-derived neurons homozygous for APOE3 or APOE4 were co-cultured with astrocytes homozygous for APOE3 or APOE4 in a two-by-two design. This layout tests the effects of neuronal genotype, astrocyte genotype, and their interaction on neuronal morphology under identical culture conditions. iPSC-derived neurons homozygous for APOE3 or APOE4 were incubated in (i) APOE3-astrocyte CM, (ii) APOE4-astrocyte CM, or (iii) unconditioned neuronal maintenance medium as a blank control, yielding a two-by-three design. This paradigm isolates effects of diffusible astrocytic factors. To model early AD-relevant stress and amplify isoform-dependent vulnerabilities in developmental-stage iPSC cultures, an acute Aβ challenge ($A\beta_{25–35}$) was applied on top of the paradigms. Post-stress neuronal responses were assessed in the same assay framework, enabling direct comparison to unstressed baselines.

Across all conditions, high-content immunocytochemistry imaging was performed. Pre-specified morphological features extracted using standardized Harmony pipelines were used for hypothesis testing; additional AIML image analyses were used to quantify whole-image shifts. Statistical comparisons were performed within each donor, and effects were highlighted as significant only when they were consistent across multiple donors. Based on these results, a phenotype-guided compound screen in lentiviral-induced astrocytes was conducted to determine whether APOE4-associated astrocytic phenotypes can be reversed by potential compounds.

# Chapter 2: Materials and methods

## 2.1. Materials

### *2.1.1. Cell lines*

Three pairs of homozygous CRISPR-edited isogenic *APOE*3 and *APOE*4 human iPSCs were available through EBiSC and Coriell. To simplify the nomenclature, the cell lines are referred to as in Table 2.1:

(1) AG09173 (homozygous for *APOE*3) and AG09173-1336 (homozygous for *APOE*4) originated from a healthy control donor.

(2) AG10788 (homozygous for *APOE*4) and AG10788-1207 (homozygous for *APOE*3) originated from a sAD donor.

(3) UKBi011-A (homozygous for *APOE4*) and UKBi011-A-3 (homozygous for *APOE*3) originated from a sAD donor.

| Cell Lines | Pair Name | Background | *APOE* | Origin | Donor inf. |
|---|---|---|---|---|---|
| AG09173 | control donor 1 | Control-Parental Line | E3 | fibroblast | white, Germany, female, 75y |
| AG09173-1336 | control donor 1 | Control | E4 | fibroblast | |
| AG10788-1207 | sAD donor 1 | Sporadic AD | E3 | fibroblast | white, female, 87y |
| AG10788 | sAD donor 1 | Sporadic AD-Parental Line | E4 | fibroblast | |
| UKBi011-A-3 | sAD donor 2 | Sporadic AD | E3 | blood | Caucasian, Germany, male, 80-84y |
| UKBi011-A | sAD donor 1 | Sporadic AD-Parental Line | E4 | blood | |

***Table 2.1. Description of the three CRISPR-edited isogenic iPSC line pairs.*** *All three pairs were engineered using CRISPR-Cas9 to differ exclusively at the APOE locus, resulting in homozygous APOE3 or APOE4 genotypes. The table details the original commercial cell line identifier, the abbreviated pair name used herein, the pathological context of the donor, the confirmed APOE genotype, the biological origin of the iPSCs, and the sex and age of the donor at the time of cell collection. All listed cell lines are homozygous for the specified APOE allele.*

***Table 2.2. Media and reagents used for cell culture and differentiation of iPSCs.***

| Media | Cell type | Purpose | Product | Concentration | Catalog number | Company |
|---|---|---|---|---|---|---|
| mTeSR™1 media | hiPSCs | Maintenance | mTeSR™1 kit | mTeSR™1 basal media | 05850 | STEMCELL Tech. |
| | | | | mTeSR™1 5X supplement | | |
| Neural Induction Media (NIM) | hiPSCs to neural progenitor cells (NPC) | Neural induction | Neurobasal | 50% | 21103-049 | ThermoFisher |
| | | | DMEM/F12 | 50% | 21331020 | |
| | | | B27 supplement | 50X | 17504.044 | |
| | | | N2 supplement | 100X | 17502-048 | |
| | | | GlutaMAX | 1% | 35050-038 | |
| | | | Penicillin-Streptomycin (10,000 U/mL) | 100X | 15140122 | |
| | | | SB-431542 | 10µM | ZRD-SB-50 | Cambridge Bioscience |
| | | | LDN-193189 | 1µM | SML0559 | Sigma |
| Neural Maintenance Media (NMM) | NPC to neurons | Maintenance | Neurobasal | 50% | 21103-049 | ThermoFisher |
| | | | DMEM/F12 | 50% | 21331020 | |
| | | | B27 supplement | 50X | 17504.044 | |
| | | | N2 supplement | 100X | 17502-048 | |
| | | | GlutaMAX | 1% | 35050-038 | |
| | | | Penicillin-Streptomycin (10,000 U/mL) | 100X | 15140122 | |
| Expansion | Lentiviral transduced hiPSCs | Astrocytes | ADMEM/F12 | 88% | 12634028 | ThermoFisher |

| | | | | | | |
|---|---|---|---|---|---|---|
| media | to astrocytes | induction | Glutamax | 1% | 35050-038 | |
| | | | N2 supplement | 1% | 17502-048 | |
| | | | FBS | 10% | F4135-500ML | Merck |
| | | | Doxycycline (Dox) | 2 µg/mL | D9891-1G | Sigma |
| FGF media | Lentiviral induced astrocytes | Astrocytes induction | Neurobasal | 95% | 21103-049 | ThermoFisher |
| | | | Glutamax | 1% | 35050-038 | |
| | | | B27 supplement | 2% | 17504.044 | |
| | | | Non Essential Amino Acids (NEAA) | 1% | 11140035 | |
| | | | FBS | 1% | F4135-500ML | Merck |
| | | | FGF-2 | 8 ng/mL | 4114-TC | R&D |
| | | | CNTF | 5 ng/mL | 450-13-20 | Peprotech |
| | | | BMP4 | 10 ng/mL | PHC9534 | Invitrogen |
| | | | Dox | 2 µg/mL | D9891-1G | Sigma |
| Lentiviral selection | Lentiviral induced astrocytes | Antibiotic selection | Hygromycin | 200 µg/mL | 10843555001 | Sigma |
| Maturation media | Lentiviral induced astrocytes | Maintenance | Neurobasal | 49% | 21103-049 | ThermoFisher |
| | | | ADMEM/F12 | 9% | 12634028 | |
| | | | Glutamax | 1% | 35050-038 | |
| | | | N2 supplement | 1% | 17502-048 | |
| | | | N-acetyl cysteine | 5 µg/mL | A8199-10G | Sigma |
| | | | HBEGF | 5 ng/mL | E4643-50UG | Sigma |
| | | | CNTF | 10 ng/mL | 450-13-20 | Peprotech |
| | | | BMP4 | 10 ng/mL | PHC9534 | Invitrogen |
| | | | dbcAMP | 500 µg/mL | D0627-250MG | Merck |

| | | | | | | |
|---|---|---|---|---|---|---|
| | | | Dox | 2 µg/mL | D9891-1G | Sigma |
| Glial Expansion Medium | Small molecules induced astrocytes | Astrocytes induction | DMEM/F12 | 100% | 21331020 | ThermoFisher |
| | | | Glutamax | 50X | 35050-038 | |
| | | | N2 supplement | 100X | 17502-048 | |
| | | | B27 supplement | 50X | 17504.044 | |
| | | | FGF-2 | 10ng/ml | 4114-TC | R&D |
| | | | Human EGF | 10ng/ml | 130-093-825 | Miltenyi |
| Astrocyte Induction Medium | Small molecules induced astrocytes | Astrocytes induction | DMEM/F12 | 100% | 21331020 | ThermoFisher |
| | | | Glutamax | 50X | 35050-038 | |
| | | | N2 supplement | 100X | 17502-048 | |
| | | | B27 supplement | 50X | 17504.044 | |
| | | | Human EGF | 10ng/ml | 130-093-825 | Miltenyi |
| | | | Human LIF | 10ng/ml | 300-05-50 | PeproTech |
| Astrocyte Maturation Medium | Small molecules induced astrocytes | Astrocytes induction | DMEM/F12 | 100% | 21331020 | ThermoFisher |
| | | | Glutamax | 50X | 35050-038 | |
| | | | N2 supplement | 100X | 17502-048 | |
| | | | B27 supplement | 50X | 17504.044 | |

| | | | | | | |
|---|---|---|---|---|---|---|
| | | | CNTF | 20ng/ml | 450-13-20 | Peprotech |

***Table 2.2. Media and reagents used for cell culture and differentiation of iPSCs. This table summarizes the culture media, supplements, and small molecules used at each stage of the differentiation workflows described in this chapter. Media are grouped by cell type and experimental purpose, including hiPSC maintenance, neural induction, neuronal maintenance, and astrocyte induction and maturation using either lentiviral (NfiB-driven) or small-molecule–based protocols. For each formulation, the base medium, key additives, working concentrations, catalog numbers, and manufacturers are provided to ensure reproducibility. All media were prepared using sterile technique and pre-warmed to 37 °C prior to use. Abbreviations: hiPSC, human induced pluripotent stem cell; NPC, neural progenitor cell; NIM, neural induction medium; NMM, neuronal maintenance medium; Dox, doxycycline; FBS, fetal bovine serum; FGF, fibroblast growth factor; CNTF, ciliary neurotrophic factor; BMP4, bone morphogenetic protein 4; EGF, epidermal growth factor; NEAA, non-essential amino acids.***

### *2.1.2. Coating procedures*

All the cells in the project, iPSCs, NPCs, neurons, lentiviral-induced and small-molecule-induced astrocytes, including co-culture of neurons and astrocytes were cultured on plates coated with Cultrex Stem Cell Qualified extracellular matrix protein (R&D, 3434-005-02) on the surface. Cultrex, 8-10mg/mL,was first thawed and diluted to 1:100 with DMEM/F12 solution on ice, then plated on culture plates as a volume of 300 µL per $cm^2$, and incubated at 37°C for at least half an hour or at room temperature (RT) for at least one hour. Immediately before seeding cells on top, Cultrex solution was aspirated in order to prevent drying out.

## 2.2. Tissue culture

### *2.2.1. Human iPSC culture*

iPSCs were maintained on coated Cultrex plates and cultured in enzyme- and serum-free mTeSR™1 medium with daily full media change. Cells were passaged using Versene (Gibco, 15040066) dissociation reagent as cells reach 80% confluence with the procedure as follows: mTeSR™1 was aspirated, and Versene was applied to cells, followed by a couple of minutes of incubation. After checking under the microscope, there was space showing up between cells within the clones. Versene was removed. An appropriate amount of mTeSR™1 with 10µM ROCKi was added to detach the cells, which was subsequently transferred to the coated wells at a 1:6 ratio. Minimal pipetting was carried out to avoid breaking the cell clones too much

and causing single cells. All cells were maintained in incubators at 37°C, 5% CO2.

### *2.2.2. iPSC-neurons induction*

Cortical neurons were generated from human iPSCs by dual inhibition of the SMAD pathway, using the standard operation protocol (SOP) from King's College London, adapted from the Shi et al. protocol (Shi et al., 2012). Specifically, cell media was switched from mTeSR™1 to NIM immediately when the confluency of iPSCs culture reaches 100%. Full media changes of NIM were conducted daily for 7 days. On Day 7, the NPCs were passaged for the 1st time as follows. For cell dissociation, 1mL Accutase (Life Technologies, A11105-01) was applied to each well of 6-well plates (6wps; Corning) right after aspirating NIM and incubated at 37 °C for a couple of minutes. Then suspend the dissociation reaction by adding an extra 4mL DMEM/F12 per well, collect the solution and centrifuge at 300G for 4 minutes. Finally, remove the supernatant, resuspend the cell pellets in NIM supplemented with 10µM Y-27632, ROCK inhibitor (ROCKi; Stratech, A3008-APE-10mg), and replate on 6wps as a ratio of 1:1.

Starting Day 8, NIM was replaced by NMM to perform a daily full media change. On Day 12, NPCs were replated again using the above procedure at a ratio of 1:1 with 10µM ROCKi supplemented NMM. On Day 15 and D18, cells were passaged for the 3rd and fourth time as a ratio of 1:2. Until Day 21, neurons were ready for terminal plating or cell banking in liquid nitrogen. Eventually, neurons can be seeded or thawed on coated plates as 10k per well of half-area 96-well plates (ha-96wps; Greiner, 655090) for ICC and 1 x $10^6$ per well of 6-well plates (6wps; Costar, 3506) for western blot and RNA extraction. Neurons were cultured in

NMM with media changes twice a week.

### *2.2.3. iPSC-astrocytes induction by small molecules*

Astrocyte induction protocol was adapted from Perriot et al. (2018). Following the above neural induction procedure till Day 7, NPCs were split into two portions before replating, such that the majority of NPCs were seeded in 6wps toward neuronal differentiation trajectory and 1/10 were seeded on coated 10cm dishes for astrocyte differentiation. On Day8, medium was switched to Glial Expansion medium and changed twice a week until cells reach confluency for passage and expansion as a ratio of 1:10. From Day7-Day21, massive cells were frozen up in media containing 10% DMSO (Sigma, D2650) supplemented with 10µM ROCKi and banked in liquid nitrogen. In the next stage, glial progenitor cells were plated on coated dishes at 50,000 cells/$cm^2$ in Astrocyte Induction medium with media change twice a week for 2 weeks. Finally, for maturation, cells were maintained for 4 weeks in Astrocyte Maturation medium.

After 4 weeks, mature astrocytes were cultured in NMM until over Day 100 and ready for further experiments.

### *2.2.4. iPSC-astrocytes induction by lentivirus*

The other method used for generating homogeneous mature astrocytes was by overexpressing the NfiB gene. The SOP was kindly provided by Dr Anne Hedegaard and adapted from Canals et al. (2018). Specifically, 2 plasmids containing NfiB

(LV-TetO-NfiB-IRES-Hygro, Addgene plasmid # 117271) and rtTA (LV-Ubiq-rtTA, Addgene plasmid #19780) were transduced into the genome of iPSC lines using lentivirus.

To start lentiviral transduction, prepare lentiviral media by supplementing mTeSR™1 media with 10µM ROCKi, 5 µg/mL polybrene (Merck, TR-1003-G) and 2 lentiviruses purchased from Edinburgh containing the two constructs at a multiplicity of infection (MOI) of 5 and stored temperately on ice. For iPSCs dissociation, mTeSR™1 media was replaced by TrypLE Express (ThermoFisher, 12604-013) and incubated for a few minutes until the edge of the iPSC clones was slightly lifted. The cells were diluted with 10X v/v DMEM/F12 and collected in a centrifuge tube. After evenly mixing the cells in the solution with a serological pipette, an aliquot was taken for cell count to determine the appreciate number of cells for lentiviral transduction which were then centrifuged at 300 x g for 3 minutes. The cell number was measured using Trypan Blue (Gibco, 15250061), placed onto Countess Cell Counting Chamber Slides (Invitrogen, C10228), and measured using the Countess 3 FL Automated Cell Counter (Invitrogen).

After removing the supernatant, cell pellets were resuspended with the prepared lentiviral media. Cultrex coating was aspirated from the wells, and the cell suspension was distributed evenly across the wells. The cells were incubated at 37°C for approximately 6 hours (or overnight if the virus was not causing excessive cell death) before retrieving the virus replacing the media with fresh mTeSR™1 supplemented with 10 µM ROCKi.

The transduced iPSCs were fed with mTeSR™1 daily until the next passage. All virus-containing media and contaminated consumables were decontaminated with Virkon.

Once the transduced iPSCs reach confluency and were split twice, they were frozen down as a master stock for future use.

On Day 0 of astrocyte induction, frozen vials of the transduced iPSCs were thawed in a 37°C warm bath, diluted in 10X v/v DMEM/F12 and centrifuged at 300 x g for 3 minutes. The cell pellets were resuspended with Expansion Media containing 2 µg/mL Dox and 10 µM ROCKi. The cells were plated in a density of 0.5 x $10^6$ cells per well of 6-well plates. On Day 1, a 100% media change was performed using expansion media. From Day 2 to Day 6, hygromycin selection was initiated at 200 µg/mL. Concurrently, a gradual transition from expansion media to FGF media occurs over the 4 days, with the proportion of FGF media increasing 25% daily while maintaining the hygromycin concentration.

On Day 7, the neural epithelial-like cells were passaged again using Accutase at a ratio of 1:4-6, seeding at a density of 0.5 x$10^6$ cells per well of a 6-well. Following centrifugation at 500xg for 5 minutes, the cell pellets were resuspended in FGF media containing Dox. From Day 8, after a full media change with FGF media, the media was changed twice weekly with a gradual transition to Maturation medium, increasing by 50% with each media change. On Day 14, the astrocytes were ready for terminal plating. They were plated as 7k per well of a

half-area 96-well plate and 0.5 x $10^6$ per well of a 6-well plate . Cells were maintained for maturation and used for experiments on Day 18.

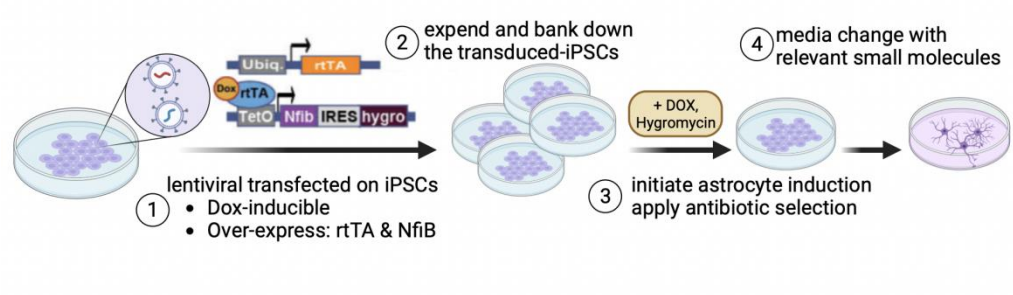



***Figure 2.1. Lentiviral induction of human iPSC-derived astrocytes and timing of induction treatments.*** *(1) iPSCs were transduced with two lentiviral constructs—LV-TetO-NfiB-IRES-Hygro (Addgene #117271) and LV-Ubiq-rtTA (Addgene #19780)—to enable doxycycline (Dox)–inducible over-expression of NfiB via the rtTA/TetO system.*
*(2) Transduced iPSCs were expanded and cryobanked as master stocks.*
*(3) Astrocyte induction was initiated by adding Dox and applying hygromycin selection (typically 200 µg/mL, Days 2–18), followed by passage on Day 7. Culture media were transitioned from Expansion to FGF to Maturation according to the schedule in Methods (Section 2.2.4).*
*(4) During scheduled media changes, the small molecules listed in 'Media formation and cell culture reagents' above were added for induction. By Day 14–18, cells displayed mature, star-shaped astrocytic morphology and were used for downstream assays (plating densities as specified in Methods).*
*Abbreviations: Dox, doxycycline; rtTA, reverse tetracycline-controlled transactivator; TetO, tetracycline-responsive promoter; Hygro, hygromycin resistance cassette. Schematic created with BioRender. The two plasmids of the lentivirus constructs were adapted from Canals et al. (2018).*

### *2.2.5. Astrocyte conditioned media*

Fresh NMM was applied to mature astrocytes (defined as lentiviral-induced astrocytes beyond Day 18 and small-molecule-induced astrocytes beyond Day 100 in culture) and applied for 3 days. The media was then collected for astrocyte-conditioned media (ACM). For sterilization and removal of the cell debris, the ACM was filtered through a hydrophilic polyethersulfone membrane with 0.22-µm pores (Merck Millipore, SLGP033RS) in a

syringe-driven filter unit (Medicina, IVS20). After performing the BCA assay to measure total protein levels, the ACM was aliquoted and stored at -80°C.

During ACM experiments, the media of neurons was changed to pre-warmed ACM for 2 weeks with a media change in the on Day 7. Fresh NMM, instead of ACM was applied on Day 7 as control.

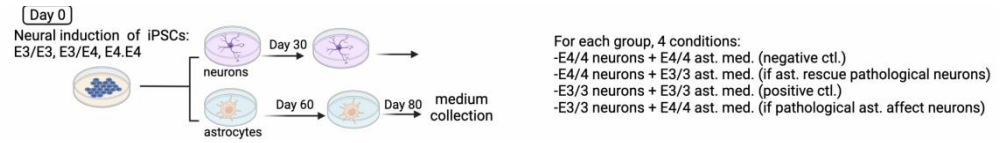



***Figure 2.2. Schematic of a neuronal monoculture exposed to astrocyte-conditioned medium (ACM) from E3/E3 and E4/E4 astrocytes*** *(e.g., with small molecule-induced astrocytes). The schematic figure illustrates the paracrine/secreted-factor paradigm used to test whether astrocytes reshape neuronal morphology without direct contact. Human iPSC-derived neurons were matured in monoculture till Day 21. In parallel, small molecule-induced astrocytes were matured to over Day 60 and maintained until Day 80 for conditioned-medium (ACM) collection under standardized treatment schedules (see Methods 2.2.5 for ACM preparation).*
*For each neuronal genotype group, four ACM conditions were applied:*
*(1) E4/E4 neurons + E4/E4 ACM (genotype-matched negative control for rescue),*
*(2) E4/E4 neurons + E3/E3 ACM (tests rescue by healthy astrocyte secretome),*
*(3) E3/E3 neurons + E3/E3 ACM (genotype-matched positive control for healthy baseline),*
*(4) E3/E3 neurons + E4/E4 ACM (tests whether a pathological astrocyte secretome imposes vulnerability).*
*Media exchanges followed a fixed schedule of full media changes twice a week. Schematic created with BioRender.*

### *2.2.6. Co-culture*

Day21 neurons were resuspended in NMM with ROCKi and were seeded directly on top of mature astrocytes (over Day100 for small molecules-induced astrocytes; Day16 for lentiviral-induced astrocytes) and co-cultured for 2 weeks with media changed twice weekly. Direct neuron–astrocyte co-culture conditions were optimised before the experimental

workflow was fixed, with the aim of maintaining both neuronal morphology and astrocyte survival while remaining compatible with automated high-content imaging. NMM was selected as the common co-culture medium because it supported neuronal maintenance and was compatible with astrocyte culture without the additional astrocyte-specific growth factors used during astrocyte maturation. Astrocytes were plated first at $2 \times 10^4$ cells per well in Cultrex-coated 96-well plates and allowed to attach and settle for one day. Day 21 neurons were then resuspended in NMM with ROCK inhibitor and seeded directly onto the astrocyte monolayer at $3 \times 10^4$ cells per well, corresponding to an astrocyte:neuron ratio of 1:1.5.

The final co-culture condition used mature small-molecule-induced astrocytes (>Day 100) or lentiviral-induced astrocytes (Day 16), followed by the addition of Day 21 neurons. Co-cultures were maintained in NMM for 2 weeks, with medium changed twice weekly. The final plating densities and cell ratio were selected empirically to provide sufficient astrocyte coverage while maintaining a predominantly monolayer culture without excessive astrocyte overgrowth, and simultaneously to support neuronal viability and the development of extensive neurite networks suitable for automated morphological analysis. Conditions that were too sparse provided insufficient astrocyte coverage, whereas excessive astrocyte density reduced the available surface area for neuronal network formation and complicated image-based separation of neuronal and astrocytic features. The selected condition therefore represented a practical balance between astrocyte coverage, neuronal network development and compatibility with the downstream imaging workflow. phenotypic validation was

conducted during cell culture and by ICC.

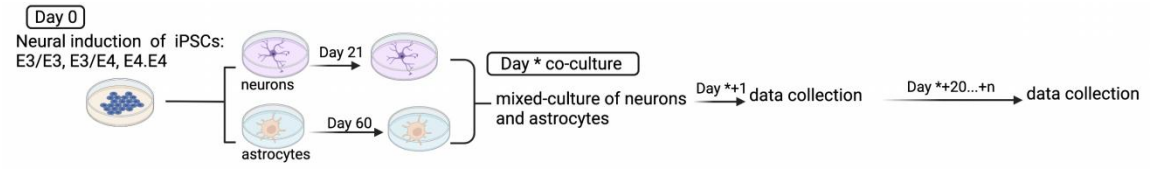



***Figure 2.3. Schematic of a co-culture paradigm across APOE genotypes*** *(e.g., with small molecule-induced astrocytes). Shown was the experimental setup for direct neuron–astrocyte co-culture used to test contact-dependent effects across APOE genotypes. Human iPSCs (genotypes illustrated: E3/E3, E3/E4, E4/E4) underwent neural induction (Day 0). Neurons were matured to Day 21, whereas astrocytes generated by a small-molecule induction protocol matured to over Day 100 were seeded on top of neurons.The final conditions were selected following optimisation of cell density and ratio to maintain astrocyte coverage and neuronal network morphology while remaining compatible with automated high-content imaging. Schematic created with BioRender.*

### *2.2.7. . Aβ$_{25-35}$ preparation and treatment*

Aβ$_{25–35}$ trifluoroacetate salt (BACHEM AG, Bubendorf, Switzerland; #4030205) was supplied as 5 mg peptide at 97% purity, corresponding to 4.85 mg Aβ$_{25–35}$ (molecular weight 1060.28 g/mol). The peptide was dissolved in 2.43 mL nuclease-free water to prepare a 2 mg/mL stock solution (1.88 mM), which was stored at −20°C until use. Nuclease-free water at the corresponding volume was used as the vehicle control. Aβ$_{25–35}$ was used as a controlled acute amyloid-related stressor to assess APOE genotype-associated cellular responses within a time window compatible with the high-content imaging workflow. The purpose of using Aβ$_{25–35}$ was not to reproduce the complete sequence, aggregation behaviour or chronic pathology associated with full-length Aβ$_{1–42}$, but rather to generate a reproducible acute perturbation that could be applied consistently across APOE3 and APOE4 neuronal and astrocytic cultures.

The working concentration was determined empirically during optimisation. An initial concentration of 1 µM $A\beta_{25–35}$ was evaluated but produced only a delayed morphological response within the experimental time window. A concentration of 10 µM was therefore selected for subsequent experiments because it produced a reproducible and readily detectable morphological response while retaining sufficient cell numbers and cellular structure for automated high-content image analysis. Cultures treated with 10 µM $A\beta_{25–35}$ were compared with genotype- and donor-matched cultures receiving the corresponding volume of nuclease-free water.

The aggregation state of the $A\beta_{25–35}$ preparation was not independently characterised using biophysical methods. Therefore, no specific claim is made regarding the presence of defined oligomeric or fibrillar Aβ species, and the treatment is referred to throughout this thesis as an acute $A\beta_{25–35}$ stress paradigm.

### *2.2.8. Compound screen in lentiviral-induced astrocytes*

Lentiviral-induced human astrocytes were used to assess the pharmacological reversibility of APOE4-associated cellular phenotypes under high-content imaging conditions. Astrocytes were generated from isogenic homozygous *APOE* iPSC lines from three donors using NfiB–driven lentiviral conversion according to established protocols (as described in Section 2.2.4). On Day 18 of differentiation, astrocytes displayed a stable, predominantly astrocytic morphology and marker profile and were selected as the screening time point.

For the compound screen, astrocytes at Day 14 were dissociated to a single-cell suspension

and plated into 384-well plates with black walls and optically clear bottoms (Greiner, 781077), which had been pre-treated for tissue culture–treated plates compatible with automated high-content imaging. *APOE3* and *APOE4* isogenic pairs for each donor were distributed across plates in matched layouts to allow direct within-donor genotype comparisons. Additionally, APOE2 astrocytes and a 1:1 mixture of APOE3 and APOE4 astrocytes were included as reference controls. Based on scaling from standard culture formats, the seeding density was $5 \times 10^4$ cells/cm². Specifically, this corresponded to $12 \times 10^3$ cells per well in 96-well plates. After plating, cells were allowed to recover and mature in astrocyte maintenance medium before subsequent experimental procedures.

A focused library of small molecules (40 test compounds) plus DMSO vehicle control and $A\beta_{25\text{-}35}$ was prepared. Compounds were selected by GSK to cover pathways relevant to sporadic AD and APOE4 biology and put onto the plates using an Echo 550 acoustic liquid handler (Labcyte) into the 384-well plates. On the Day 18, the drugs were transferred onto the 384-well plates pre-seeded with astrocytes using a CyBio FeliX pipetting robot for liquid handling system (Analytik Jena) to minimize pipetting variability. For each treatment well, a final concentration of 1 μM per compound was administered. Each compound condition was measured in 3 replicate wells per donor, whereas the DMSO vehicle control was represented by 18 wells to provide a stable reference distribution for statistical comparisons. Final DMSO concentration was kept constant across all wells, including controls. APOE3 and APOE4 astrocytes from each donor were exposed in parallel to the full compound panel and vehicle.

Compounds were applied for 24h at a single concentration.

In parallel, total cell counts per well were monitored to exclude overt toxicity-induced cell death. In subsequent analyses (Section 2.11), embedding-based AIML models were applied to the same image sets to assess whole-image morphological impact without manually extracted features, including weakly supervised encoders and a self-supervised DINO model trained without labels. Each image was mapped to a high-dimensional embedding using UMAP visualization. Drug effects were then quantified as the cosine distance between each treatment well and its donor-matched vehicle (larger distance = stronger whole-image morphological shift).

In this experiment, astrocyte culture, plating, immunocytochemistry (ICC) staining of screening plates, Harmony-based feature extraction, and conventional statistical analyses on the extracted features were performed by the dissertation author. Compound dispensing and image acquisition were conducted by Dr Helen A. Rowland. AIML pipelines for raw-image analysis were developed by Ying Chen, Prof. Alejo Nevado-Holgado, and Dr Andrey Kormilitzin.

## 2.3. Immunocytochemistry

Cell cultures were fixed in Dulbecco's phosphate-buffered saline (DPBS; Gibco, 14190094) with 4% paraformaldehyde (PFA; Thermo Scientific, 28908) and incubated at RT for 15 minutes. Blocking and permeabilization were performed simultaneously by incubating the cells in DPBS with 0.25% Triton X-100 (Sigma, P9284) and 10% donkey serum (Sigma, D9663-10ML) for 1 hour at RT to prevent non-specific binding. Primary antibodies were diluted in PBSTX with 5% donkey serum at a concentration of 1:500, except for the MAP2 antibody, which was used at 1:5000. The cells were then incubated with primary antibody overnight at 4°C.

The following day, the cells were gently washed three times for 5 minutes each in DPBS at RT and then incubated in secondary antibody solutions diluted 1:500 in DPBS at RT for 2 hours, protected from light with tinfoil. Followed by one DPBS wash, cell nuclei were stained with Hoechst (Thermo Scientific, 62249) diluted 1:5,000 in DPBS and neutral lipids were stained with BODIPY$^{TM}$ 493/503 (Thermo Scientific, D3922) diluted 1:2,000 in DPBS for 5 minutes each. Minimal washing was carried out to prevent cell detachment. Finally, cells were washed again and stored in DPBS at 4°C until imaging.

Different primary antibody combinations were applied depending on the culture condition. In mono-cultures of neurons, the primary antibody panel comprised MAP2 (chicken), EEA1

(rabbit), and SYP (mouse). In neuron and astrocyte co-cultures with lentiviral-induced astrocytes, two complementary antibody panels were used: MAP2 (chicken), EEA1 (rabbit), and S100B (mouse) to assess astrocyes and neurons and their endosomal features, and MAP2 (chicken), GFAP (rabbit), and SYP (mouse) to visualize astrocytes and neurons and neuronal synaptic markers. In mono-cultures of astrocytes, the primary antibody combination consisted of S100B (mouse), EEA1 (rabbit), and BODIPY to enable quantification of endosomal and lipid-associated features. Antibody host species were selected to ensure compatibility with multiplex fluorescent detection.

### *2.3.1. Immunocytochemistry of the compound screen in astrocytes*

At the end of the treatment period, cells were fixed and processed for ICC with panels including Hoechst, BODIPY$^{TM}$ 493/503, EEA1 (Cellsignaling, 3288) and S100B (Abcam, Ab222956). All plates were processed, washed at the same time and stored under identical conditions. High-content imaging was performed on an automated confocal platform (Opera Phenix) using matched exposure settings, objectives and acquisition parameters across plates and experiments. For each well, 17 fields-of-view (FOVs) were acquired across all channels to capture sufficient cell numbers and reduce sampling bias. Image analysis was conducted using the Harmony software. Feature extraction and segmentation pipelines were outlined in the following section (Section 2.8).

***Table 2. List of primary and secondary antibodies used in confocal microscopy.***

| Antigen/Antibody | Antigen raised in | Source | Dilution |
|---|---|---|---|
| MAP2 | Chicken | Sigma-Aldrich Ab5392 | 1:5000 |
| EEA1 | Rabbit | Cellsignaling 3288 | 1:500 |
| SYP | Mouse | Abcam Ab52636 | 1:500 |
| S100B | Mouse | Abcam Ab222956 | 1:500 |
| GFAP | Rabbit | ThermoFisher 14-9892-82 | 1:500 |
| Alexa Fluor™ 568 | Goat, Anti-Mouse | Invitrogen A-11004 | 1:500 |
| Alexa Fluor™ 488 | Goat, Anti-Rabbit | Invitrogen A-11008 | 1:500 |
| Alexa Fluor™ 647 | Goat, Anti-Chicken | Invitrogen A-21449 | 1:500 |

## 2.4. Real-time quantitative polymerase chain reaction (rt-qPCR)

RNA extraction was performed following the protocol of RNeasy Mini Kit (Qiagen, 74106), a silica-membrane-based system. Briefly, cell pellets were lysed in Buffer RLT, a highly denaturing guanidine-thiocyanate-containing buffer that disrupts cells and inactivates RNases to prevent RNA degradation. 70% ethanol was then added to the lysate to provide appropriate binding conditions for RNA to the silica membrane. The mixture was transferred to an RNeasy Mini spin column, and RNA was selectively bound to the membrane during 10,000G centrifugation. Contaminants and extra proteins were removed by washing the column membrane with Buffer RW1, followed by Buffer RPE to eliminate residual salts and ethanol. An on-column DNase digestion was performed using RNase-Free DNase Set (Qiagen,

79254) to remove DNA. Finally, purified RNA was eluted with RNase-free water. RNA concentration and purity (A260/A280 and A260/A230 ratios) were assessed using NanoDrop spectrophotometer (ThermoFisher).

cDNA was synthesised with the TaqMan Reverse Transcription kit (Invitrogen, N8080234). For a 10 µL reverse transcription reaction, the following reagents were used: 500 ng of RNA, brought up to a volume of 3.85 µL with nuclease-free water; 1 µL of 10X reverse transcription buffer; 2.2 µL of magnesium chloride solution; 2 µL of a 10 mM deoxynucleoside triphosphate (dNTP) mixture; 0.5 µL of 50µM random hexamers; 0.25 µL of MultiScribe reverse transcriptase; and 0.2 µL of RNase inhibitor. The reagents were then run in the Veriti 96 Well Thermal Cycler (Applied Biosystems, 4375305) following the programme: first, primer annealing was performed at 25°C for 10 minutes; then, DNA polymerization occurs at 37°C for 30 minutes; subsequently, enzyme deactivation was carried out at 95°C for 5 minutes; finally, the reaction product was stored at 4°C. No RNA was contained as a negative control. After RT, cDNA concentration and purity (A260/280, A260/230) were assessed on a NanoDrop One/One$^{c}$ microvolume UV-Vis spectrophotometer (ThermoFisher) using 1 µL per measurement. For downstream qPCR, cDNA was diluted in nuclease-free water and added at up to 100 ng per 20 µL reaction, the maximum recommended by TaqMan Assays.

Primer sequences were obtained from published literature and synthesised by Sigma. The primer sequences (5'-3') were as follows: OCT4, forward GCCCGAAAGAGAAAGCGAAC and

reverse ACACTCGGACCACATCCTTC (Seo et al., 2021); MAP2, forward AGGCTGTAGCAGTCCTGAAAGG and reverse CTTCCTCCACTGTGACAGTCTG (Melková et al., 2018); and GAPDH, forward GTGGAGGGACTCATGACCAC and reverse GTGAGCTTCCCATTCAGCTC (Seo et al., 2021). GAPDH was used as the internal housekeeping control. Primer specificity was confirmed by melt-curve analysis. Reagents of rt-qPCR was prepared following the protocol of FastStart SYBR Green Master (Roche, 04673484001), which contains 25 µL of FastStart SYBR Green Master, 0.5 µL of forward primer (10 µM stock, resulting in a 100 nM final concentration), 0.5 µL of reverse primer, and 19 µL of PCR-grade water, 5 µL of diluted cDNA products for a total volume of 50 µL. Rt-qPCR reactions were run in triplicate by loading the reagents in 96-well reaction plates (Applied Biosystems, 4346906) which were sealed with adhesive film (Applied Biosystems Cat#4311971), centrifuged at 2,000 RCF for 2 minutes, then loaded in the StepOnePlus Real-Time PCR System (Applied Biosystems Cat#4376600). The PCR program begins with an initial denaturation step at 95°C for 10 minutes to activate the DNA Polymerase. The amplification phase consists of 40 cycles. Each cycle includes a denaturation step at 95°C for 15 seconds, a primer annealing step at 59 °C for 60 seconds, and an extension step at 72°C for 30 to 60 seconds. Relative quantification of gene expression was calculated using the Pfaffl method (Pfaffl, 2001) based on the average Ct values of the housekeeper gene (HKG) from the control group.

## 2.5. BCA protein assay

The BCA assay was carried out on the collected ACM using the Pierce BCA Protein Assay Kit (Thermo Scientific, 23227) to determine the total protein concentration. Several dilutions of the provided bovine serum albumin (BSA) were used as a reference to determine the protein concentrations of each sample, including 2 mg/mL, 1 mg/mL, 0.5 mg/mL, 0.25 mg/mL and 0mg/mL. Subsequently, 1 µL of each ACM sample and 9 µL of MilliQ water were loaded in triplicate in a transparent 96wp (Fisher Scientific Cat#3596). BCA Reagent B, Copper sulphate, was diluted 1:50 in BCA Reagent A. Then the mixture was quickly added to all the sample-loaded wells 100 µL per well using multi-channel pipettes. The plate was incubated at 37°C for 30 minutes or longer depending on the color change. And finally, the plate was read using the PHERAstar FSX Microplate Reader (BMG Labtech), which measures the absorbance near 562 nm. The standard curve was plotted by the average blank–corrected 562 nm measurement for each BSA standard vs. its concentration in 1 µg/mL. The protein concentration of each unknown sample was calculated accordingly.

## 2.6. Western blot

Western blot was used to detect the concentration of APOE protein in the ACM samples secreted by astrocytes. At first, prior to mixing with the samples, reducing agent 2-mercaptoethanol (Bio-Rad, 1610710) was added to 4X Laemmli Sample Buffer (Bio-Rad, 1610747) as working buffer which can be stored at 4°C. 12µL ACM sample was mixed with

4µL working buffer and heated at 95°C for 10 minutes for protein denaturation. Each heated sample was then transferred to the corresponding well of a 15µL 8-16% Mini-PROTEAN TGX precast gel (Bio-Rad, 4561106) which was run in the 1: 10 diluted tris-glycine SDS buffer (Thermo Scientific, 28362) at 45 mA for 90 minutes using the Bio-Rad Mini-PROTEAN Tetra System. 5 µL of Spectra Multicolor Broad Range Protein Ladder (Thermo Scientific, 26634) was loaded on both sides of the gel, along with the samples, to report protein sizes from 10 to 260 kDa.

Proteins were separated into bands according to size in the gel, which were then transferred onto a 0.45-µm polyvinylidene difluoride (PVDF) membrane (Merck, IPFL00010) activated in methanol (Sigma, 34860-2.5L-R). The transfer cassette was prepared in ice-cold diluted 10X tris-glycine transfer buffer (Bio-Rad, 1610734) with 20% methanol using the same Bio-Rad system at 120 V for 90 minutes on ice.

After the transfer, the membrane was retrieved from the 'sandwich' and submerged in DPBS with 0.1% Tween-20 (PBST; Promega, H5152) and 5% w/v BSA (Sigma, A7906-100G) on a rocker at RT for 1 hour. After blocking, the membrane was incubated in goat anti-APOE primary antibody (Calbiochem, 178479-500UL) diluted 1:1,000 in 5% BSA in PBST stored overnight on a rocker in the cold room at 4°C. The following day, the membrane was washed three times 10 minutes per wash in PBST on a rocker at RT, then incubated in IRDye 680RD donkey anti-goat secondary antibody (LI-COR, 926-68074) diluted 1:1,000 in 5% BSA in PBST

on a rocker for 2 hours at RT. The membrane was washed twice in PBST, followed by a 10-minute wash in DPBS, before being imaged using the LI-COR Odyssey CLx Imaging System. Membrane densitometry was analyzed with the Li-COR Image Studio™ Lite Quantification Software.

## 2.7. Image acquisition and Harmony feature extraction

ICC images of cultures in 96-well plates were imaged using the PerkinElmer Opera Phenix High-Content Screening System at 40X magnification in a water objective and confocal operational mode. Three z-stacks and five light channels were selected to create a maximum projection. The images were analyzed with customized pipelines in the PerkinElmer Harmony PhenoLOGIC High-Content Imaging and Analysis Software (version 4.9). In brief, the Hoechst signal was analyzed to locate the cells. A selection criterion of the nuclei, including size, intensity, and roundness, was applied to the found cells in order to identify cortical neurons. Subsequently, MAP2 signal was analyzed on neurons to capture the morphology of neurites, for example, the length, branch level, and intensity. EEA1, BODIPY and SYP spots overlapped with MAP2 were analyzed representing the neuronal early endosomes, neutral lipids and synaptophysin proteins. Features including the number, size and intensity were reported. In total, more than 60 features were extracted from SYP, EEA1, MAP2, BODIPY, S100B, GFAP and Hoechst. For cell viabilityassessment, the number of cells per well was quantified from high-content images using a nucleus marker-based segmentation pipeline.

## 2.8. Harmony extract features pipelines

Images were taken at 40x magnification using an Opera Phenix High Content Screening System (Perkin Elmer), in a water objective and confocal operational mode.

### *2.8.1. Pipeline for neuronal features in monoculture*

Images were taken with the following properties for each channel:

- Alexa 488: time 160ms, power 100% and height 2.0µm
- Alexa 647: time 260ms, power 100% and height 2.0µm
- Alexa 568: time 260ms, power 100% and height 2.0µm
- DAPI: time 80ms, power 80% and height 2.0µm
- Brightfield: time 80ms, power 80% and height 2.0µm

For experiments, 60 wells per half-area 96-well plate were imaged including three independent neuronal differentiations, with 109 fields captured per well and 0% overlap at a single time point. For stack, 3 planes were taken per image at a height of -1µm, 0µm and +1µm.

Analysis began with 'Input Image' building block. The three planes were stacked into one image with 'Maximum Projection'. Flatfield correction was set to 'Basic' with Brightfield Correction applied to all images. In the next building block, 'Find nuclei' was added to identify the population of nuclei using DAPI channel, which were termed 'Nuclei all'. The 'Calculate morphology properties' and 'Calculate intensity properties' blocks were applied to the 'Nuclei

all' population using a standard method. The area, intensity and roundness were reported. Filtering of nuclei was achieved by using the 'Select Population' block. Nuclei were selected with an area > 40μm$^2$ and < 75μm$^2$, intensity < 5000FU generating a population of 'Nuclei neurons'. Within the 'Nuclei neurons' population, neurites were identified using the 'Find neurites' block. Neurites were identified in the Alexa 647 channel and 'CSIRO neurite analysis 2' method was used for calculating neurite segment properties. Neurites with segment length > 5 were selected using 'Select Population' block. Their length, intensity and area per neuron were measured by 'Calculate morphology properties', and 'Calculate intensity properties' blocks.

To locate neuronal EEA1 and SYP spots, 'Find cytoplasm' was built using the Alexa 647 channel within the population of 'Nuclei neurons'. Subsequently, 'Find spots' was added for identifying early endosomes and synaptic puncta using the Alexa 488 channel and the Alexa 568 channel, respectively. Their 'Correct spot intensity' and 'Spot area' were defined to exclude overexposure or random noise in the background. Within the selected spots, 'Calculate morphology properties', 'Calculate texture properties', 'Calculate location properties' and 'Calculate intensity properties' blocks were applied to measure the corresponding features in the output. In total, 50 features were defined in the results. A representative example of the neuronal image-analysis workflow is shown in Figure 2.4, illustrating the progression from the raw ICC image through nuclear identification and filtering to MAP2-based neuronal and neurite segmentation.

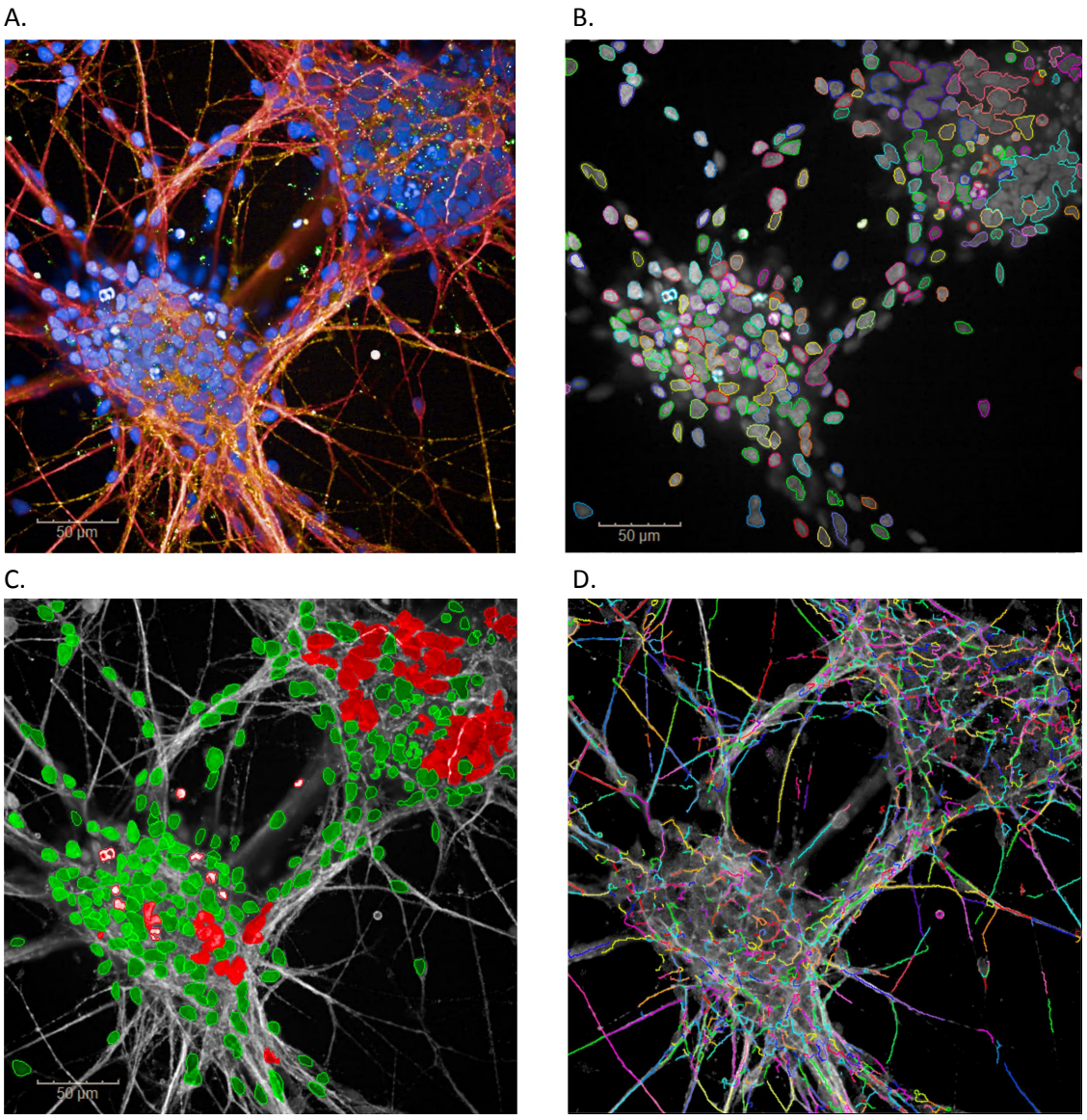



***Fig 2.4. Representative image-analysis pipeline for feature extraction from neuronal monocultures.*** *Representative images illustrate the sequential steps used for automated neuronal feature extraction in Harmony. (A) Raw multi-channel ICC image of a neuronal monoculture. (B) Initial nuclear identification based on Hoechst staining. (C) Selected nuclei after application of the predefined nuclear filtering criteria. (D) Neuronal processes identified using MAP2 staining, with the selected nuclei used as reference objects for neuronal segmentation and subsequent neurite detection. The resulting segmented neuronal compartment was used to quantify neurite-associated morphological features. These images provide representative examples of how raw neuronal ICC images were processed to generate the quantitative features analysed in the subsequent Results chapters.*

### *2.8.2. Pipeline for astrocyte features in monoculture*

Images were taken with the following properties for each channel:

- Alexa 488: time 40ms, power 100% and height 2.0µm
- Alexa 647: time 180ms, power 100% and height 2.0µm
- Alexa 568: time 160ms, power 100% and height 2.0µm
- DAPI: time 60ms, power 80% and height 2.0µm
- Brightfield: time 80ms, power 80% and height -0.5µm

For experiments, 308 wells per 384-well plate were imaged including three independent neuronal differentiations, with 17 fields captured per well and 0% overlap at a single time point. For the stack, 3 planes were taken per image at a height of -1 µm, 0 µm and +1 µm.

Analysis began with 'Input Image' building block. The three planes were stacked into one image with 'Maximum Projection'. Flatfield correction was set to 'Basic' with Brightfield Correction applied to all images. In the next building block, 'Find nuclei' was added to identify the population of nuclei using DAPI channel, which were termed 'Nuclei'. The 'Calculate morphology properties', 'Calculate intensity properties' and 'Calculate position properties' blocks were applied to the 'Nuclei' population using a standard method. The area, intensity, roundness and the position with respect to other nuclei and the edge were reported. Filtering of nuclei was achieved by using the 'Select Population' block. Nuclei were selected with an area > 65µm$^2$ and < 150µm$^2$, roundness >0.818, intensity < 7000FU, Nucleus contact area with neighbors <23% and image sides < 7% generating a population of 'Selected nuclei'.

Under the ‘Selected nuclei’ population, ‘Find cytoplasm’ was built using the Alexa 568 channel. Their nearest neighbor distance and contact area with the image border were defined to exclude half-cut or overlapped cells. Subsequently, ‘Find spots’ was added for identifying BODIPY and EEA1 using the Alexa 488 channel and the Alexa 647 channel, respectively. Their ‘Correct spot intensity’ and ‘Spot area’ were defined to exclude overexposure or random noise in the background. Within the selected spots, ‘Calculate morphology properties’, ‘Calculate texture properties’, ‘Calculate location properties’ and ‘Calculate intensity properties’ blocks were applied to measure the corresponding features in the output. In total, 45 features were defined in the results. A representative example of the astrocyte image-analysis workflow is shown in Figure 2.5, illustrating the progression from the raw ICC image through nuclear identification and filtering to S100B-based cellular segmentation and intracellular BODIPY object detection.

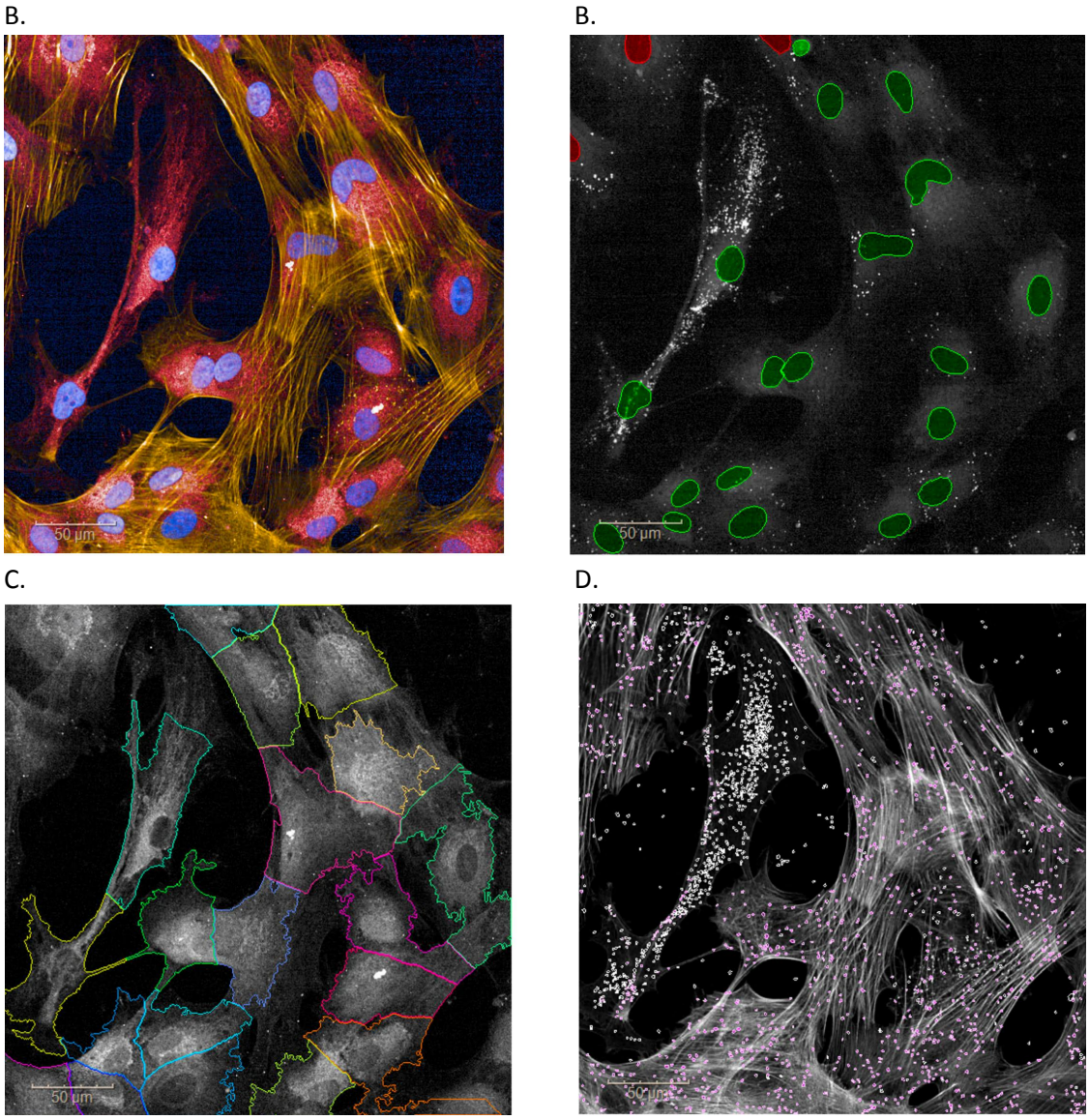



***Fig 2.5. Representative image-analysis pipeline for feature extraction from astrocyte monocultures.*** *Representative images illustrate the sequential steps used for automated feature extraction in Harmony. (A) Raw multi-channel ICC image of an astrocyte monoculture. (B) Initial nuclear identification based on Hoechst staining. (C) Selected nuclei after application of the predefined nuclear filtering criteria. (D) Astrocyte cellular boundaries defined using the selected nuclei together with S100B staining, generating the cytoplasmic region used for subsequent analysis. (E) BODIPY-positive objects detected within the image and spatially filtered to retain lipid-positive objects located within the defined astrocytic cytoplasm. These steps illustrate how raw fluorescence images were converted into segmented cellular objects for quantitative morphological and intensity measurements.*

### *2.8.3. Pipeline for feature extraction in the co-culture experiment*

Images were taken with the following properties for each channel:

- Alexa 488: time 160ms, power 100% and height 2.0µm
- Alexa 647: time 260ms, power 100% and height 2.0µm
- Alexa 568: time 260ms, power 100% and height 2.0µm
- DAPI: time 80ms, power 80% and height 2.0µm
- Brightfield: time 80ms, power 80% and height 2.0µm

For experiments, 60 wells per half-area 96-well plate were imaged including three independent neuronal differentiations, with 109 fields captured per well and 0% overlap at a single time point. For the stack, 3 planes were taken per image at a height of -1 µm, 0 µm and +1 µm.

Analysis began with 'Input Image' building block. The three planes were stacked into one image with 'Maximum Projection'. Flatfield correction was set to 'Basic' with Brightfield Correction applied to all images. In the next building block, 'Find nuclei' was added to identify the population of nuclei using DAPI channel, which were termed 'Nuclei all'. The 'Calculate morphology properties', and 'Calculate intensity properties' blocks were applied to the 'Nuclei all' population using a standard method. The area, intensity and roundness were reported. Filtering of nuclei was achieved by using the 'Select Population' block. Nuclei were selected with an area > 40µm$^2$ and < 75µm$^2$, intensity < 5000FU generating a population of 'Nuclei neurons'. 'Find nuclei' was added again to identify astrocyte nuclei using DAPI channel

with their area, intensity, roundness and the position regarding to other nuclei and the edge reported. Filtering of nuclei was achieved by using the 'Select Population' block. Nuclei were selected with an area > 65µm$^2$ and < 150µm$^2$, roundness >0.818, intensity < 7000FU, Nucleus contact area with neighbors <23% and image sides < 7% generating a population of 'Astrocyte nuclei'.

Within the 'Nuclei neurons' population, 'Find neurites' and 'Find cytoplasm' blocks were built as above using the Alexa 647 channel. Within the 'Astrocyte nuclei' population, 'Find cytoplasm' block was built using the Alexa 488 channel (GFAP). And SYP puncta were selected using the Alexa 568 channel within neuronal cytoplasmic region.

In the parallel experimental plates with the same cells and conditions, but different antibody sets, within the 'Astrocyte nuclei' population, 'Find cytoplasm' block was built using the Alexa 568 channel (S100B). And early endosomes were selected using the Alexa 488 channel within neuronal cytoplasmic region and astrocyte cytoplasmic region separately.

Their 'Correct spot intensity' and 'Spot area' were defined to exclude overexposure or random noise in the background. Within the selected spots, 'Calculate morphology properties', 'Calculate texture properties', 'Calculate location properties' and 'Calculate intensity properties' blocks were applied to measure the corresponding features in the output. In total, 69 features were defined in the results.

## 2.9. Statistics

Statistical significance was set as $p<0.05$. Statistical tests were performed with Prism GraphPad Software Version 9 (Graph Pad Software Inc., San Diego, CA, USA) and R (version 4.3.2; R Foundation for Statistical Computing, Vienna, Austria) within RStudio (version 2023.12.1). A normal distribution in cell populations was assumed and two-tailed parametric tests were used. Comparisons between two groups were made using an unpaired t-test. For comparisons of more than two groups, One-way ANOVA with Tukey's multiple comparisons post hoc test was used. For comparisons between populations with two independent variables (i.e., genotype and treatment condition), two-way ANOVA with Tukey's multiple comparisons post hoc test was used. For unbalanced group sizes, a two-way ANOVA with Type III sums of squares was used. Data was reported as bar graphs with mean $\pm$ standard deviation (SD) unless otherwise indicated.

### *2.9.1. Analysis of extracted features*

Each experiment included ≥3 technical replicates, with one well counted as one technical replicate in imaging-based assays. Experiments were reproduced across 3 biological replicates, defined as independent neuron inductions initiated from iPSC cultures at three passages (i.e., three separate inductions from iPSCs maintained through three continuous passages). Each dot represents a single well in a 96-well plate. Quantile–quantile plot (QQ plot) was performed to check for the normal distribution of each feature. Then independent-sample t-tests with Welch's correction were used for pairwise comparisons. One- and two-way

analysis of variance (ANOVA) followed by multiple comparisons post-hoc correction were used for comparisons between treatment conditions and groups with 2 independent variables. There were comparable numbers of samples in the ACM and co-culture experiments. To address the imbalanced sample sizes in the drug screen experiment due to plate design, Welch's ANOVA were applied to ensure the robustness and validity of the comparisons. This test does not assume equal variances and was more reliable for unbalanced designs. Significant overall effects were followed by post-hoc comparisons. designed for situations with unequal sample sizes and variances.

### *2.9.2. Kolmogorov-Smirnov (KS) test and phenotypic rescue quantification*

To statistically evaluate the phenotypic rescue of APOE4-associated morphologies by drug treatment, a non-parametric analytical framework was established, anchored to the isogenic *APOE3* in the control condition as the healthy reference. This approach was designed to determine whether a compound could normalize the entire distribution of a cellular feature in APOE4 astrocytes, rendering it statistically indistinguishable from the untreated APOE3 population. The analysis was therefore based on the quantification of baseline phenotypic differences. For each donor, genotype and feature, baseline separation between APOE3+DMSO and APOE4+DMSO was first quantified to define the direction and magnitude of the APOE4-associated shift. Compound effects were then evaluated by comparing APOE4+compound wells to the donor-matched APOE3+DMSO reference distribution. Two-sample tests (Welch’s correction when variances were unequal) were applied at the well level to assess whether a given compound significantly reduced the APOE4–APOE3 gap

toward an APOE3-like state. Subsequently, to validate the shortlisted candidate compounds hits without distributional assumptions and to quantify effect direction/magnitude, more advanced two-sample Kolmogorov–Smirnov (KS) tests were run on the well-level feature distributions for each donor–feature pair, reporting D, p, and the median shift from APOE4+compound to APOE3+DMSO. This distributional step reduced the risk that t-test positives reflected mean shifts driven by tails or unequal variances.

For every donor *d* and feature *f,* we first computed a baseline difference as $D_{base}(d,f)$ = KS(APOE4+Vehicle$_{d,f}$, APOE3+Vehicle$_{d,f}$), that is, the two-sample KS distance between the APOE4 and APOE3 DMSO vehicle distributions. The baseline median difference was also recorded as $\Delta_{base}(d,f)$ = median(APOE4+Vehicle$_{d,f}$) − median(APOE3+Vehicle$_{d,f}$) to show directionality (APOE4 > APOE3 or APOE4 < APOE3). $D_{base}$, the corresponding KS p-values, group medians, and Δbase were reported for every donor–feature pair.

For treatment comparisons, the APOE3 plus vehicle remained the fixed reference. For each donor per feature per compound, KS tests were computed to compare with drug-treated APOE4, $D_{treat}$(d,f,drug)=KS( APOE4+drugd,f, APOE3+Vehicled,f), and a distribution-level rescue index was reported as $\mathrm{R_{KS}(d,f,drug)} = 1 - \frac{\mathrm{D_{treat}(d,f,drug)}}{\mathrm{D_{base}(d,f)}}$. Positive RKS indicates that the treatment pulled the entire APOE4 distribution toward APOE3; negative values indicate movement away. In parallel, a location-level rescue index was reported as $\mathrm{R_{median}(d,f,drug)} = 1 - \frac{|\Delta_{\mathrm{treat}}(\mathrm{d,f,drug})|}{|\Delta_{\mathrm{base}}(\mathrm{d,f})|}$, where Δtreat=median(APOE4+drug)−median(E3+DMSO). Instead of general distribution, this index

was only interested in the changes in the central median. Both indices equal zero when a treatment has no effect and equal one if the treatment completely reverses APOE4 to APOE3.

Because it involves non-parametric distances and the research question was inherently one-sided (whether treatment moves APOE4 closer to APOE3 than baseline), inference proceeded in two stages. At the donor level, the null hypothesis was tested: $H_0$ ($D_{treat} \geq D_{base}$) versus $H_1$ ($D_{treat} < D_{base}$) using a one-sided permutation procedure in which wells were randomly re-labelled between APOE4+drug and APOE4+vehicle within donor and feature. Tail probabilities were estimated from the permutation distribution of $D_{treat}$. In parallel, 95% bootstrap confidence intervals were constructed for $R_{KS}$ and $R_{median}$ by resampling wells with replacement within groups. Additionally, a trimming sensitivity analysis was performed to remove one extreme observation per group to verify that the results were not influenced by distributional tails.

At the overall study level, p-values for a given drug-feature pair across all three donors were combined using Fisher's method. The resulting combined p-values were then adjusted for multiple testing across all drug-feature hypotheses using the Benjamini-Hochberg (BH) procedure to control the false discovery rate (FDR). Compounds were considered to show robust rescue only when associated with a consistent directional shift and an FDR-adjusted $p < 0.05$.

To visualize the data, empirical cumulative distribution functions (ECDFs) were plotted for key compound-feature pairs. In each panel, the APOE4+drug ECDF was overlaid against the

APOE3+vehicle ECDF, with vertical dotted lines marking group medians. Successful phenotypic rescue was visually evidenced by the APOE4 curve shifting towards and eventually overlapping with the APOE3 curve, accompanied by a convergence of the medians and a reduction in the area between the two distributions.

#### *2.9.3. Random forest*

A Random Forest classifier, an ensemble learning method that constructs multiple decision trees and outputs the class (classification), was used to identify variables and features that were crucial for the model to distinguish image groups. Feature importance was assessed using the mean decrease in impurity (MDI), also known as the Gini importance score.

#### *2.9.4. AIML analysis of raw high-content images*

(Credit: the following AIML pipelines for raw-image analysis were developed by Ying Chen, Prof. Alejo Nevado-Holgado, and Dr Andrey Kormilitzin.)

AIML analyses were implemented to learn morphology directly from raw immunocytochemistry images, in parallel with the predefined feature-based pipeline. Models were applied to the same high-content imaging datasets described above, enabling direct comparison of feature-and image-based readouts.

Using Opera Phenix system, astrocytes were imaged with multiple fields-of-view (FOVs) under identical exposure settings across plates. Raw multi-channel TIFF images were used as input for all AIML workflows. Images were pre-processed by per-channel intensity

normalization: for each channel, a fixed background threshold (held constant across the experiment) was applied to suppress background, and the remaining signal was linearly rescaled to [0,1]. No manual feature engineering was applied at this stage. Three spatial granularities were generated to probe complementary biological scales: (i) FOV-level tiles, containing multiple cells and their microenvironment; (ii) nucleocentric region tiles, centered on the nucleus with minimal surrounding cytoplasm.

To test whether donor and *APOE* genotype information could be recovered directly from morphology, a weakly supervised classification framework was used. An image encoder was trained on DMSO-treated astrocyte images with minimal label (only with donor identity or *APOE* genotype), without any manual annotation of individual cells or subcellular structures.

Images were randomly split into training (80%) and validation (20%) sets. The encoder was optimized using a standard cross-entropy loss to predict either donor identity or *APOE* genotype from each image. After training, well-level embeddings were obtained by averaging the encoder outputs across all tiles from the same well. These embeddings were then used for: (i) calculation of genotype and donor classification accuracy on the validation wells; and (ii) downstream analyses including UMAP visualization and treatment–vehicle distance metrics. This weakly supervised setting was defined as 'weak' because labels were assigned at the image level, and the model was required to discover discriminative morphological patterns without explicit supervision on which structures were relevant.

Additionally, a self-supervised representation learning approach was implemented using DINO (self-distillation with no labels). All available astrocyte images (across donors, genotypes, and treatments) were used without annotation. Two networks (teacher and student) received different augmented views of the same image tile, and the student was trained to match the teacher's output distribution. Standard multi-crop and colour/spatial augmentations were applied, while preserving basic biological content. The trained DINO encoder produced label-free embeddings for each image. Two-dimensional UMAP projections of embeddings (FOV and well-level) were generated for qualitative inspection of structure by donor and genotype. Clustering patterns were interpreted alongside quantitative metrics to identify dominant sources of variance. This procedure allowed assessment of whether genotype- and donor-linked morphology is an intrinsic property of the images, independent of supervised task design.

For drug-screen analyses, both weakly supervised and self-supervised embeddings were used to quantify treatment-induced shifts relative to donor-matched vehicle controls. For each donor and representation variant, a centroid was computed from the embeddings of DMSO wells. Treatment effects were then expressed as the cosine distance between each treatment group and its corresponding vehicle centroid. These distances provided an image-native estimate of how strongly a given compound perturbed astrocyte morphology as a whole. Aggregated treatment–vehicle distance profiles were compared for each donor to assess the

stability of compound effects and across compounds to determine whether any drug produced a consistent, large-scale morphological signature. $A\beta_{25–35}$ treatment served as a positive control, expected to induce robust morphological divergence from baseline.

# Chapter 3: Characterization and iPSC-derived cell induction

## 3.1. Introduction

### *3.1.1. Results overview*

Human iPSC systems now enable mechanistic studies of APOE, the leading common risk allele for sAD, under controlled genetic backgrounds (Yamazaki et al., 2019). For neurons, dual-SMAD inhibition is the prevailing non–transcription-factor approach, while astrocytes are efficiently produced either by forced expression of lineage factors(e.g., NfiB) or by stepwise small-molecule protocols (e.g., LDN, SB, EGF, FGF, LIF, CNTF). These iPSC-derived models preserve the individual genetic background of the patients and allow the examination of endogenous interactions of neurons and astrocytes. Using both ACM and co-culture systems, this study investigates how the APOE genotype of both neurons and astrocytes influences the neuronal phenotype. To better mimic the pathological environment of sAD in these fetal-age iPSC-derived models, soluble Aβ25-35 oligomers were added to neuronal cultures as a pathophysiologically relevant stressor to the iPSC-derived models. This combined approach enables dissection of the main effects and interactions influencing neuronal phenotype, which may be driven by the neurons' own APOE genotype, the APOE3 or APOE4 genotype of isogenic astrocyte treatments, and the mode of contact (ACM vs. co-culture), or by Aβ stress, without confounding effects from donor genetic backgrounds.

The effects were assessed by analyzing cellular morphology and organelle features through high-content imaging. The results begin by confirming and characterizing the cellular models used. iPSCs were validated through brightfield imaging, showing compact clones with smooth edges,

and by assessing the expression of pluripotency markers, OCT4, SOX2, SSEA, using RT-qPCR and immunocytochemistry (ICC). Differentiated iPSC-derived neurons and astrocytes were characterized by ICC staining for lineage-specific markers, including MAP2 and SYP. The quality of ACM was evaluated by total protein quantification (BCA assay) and western blot analysis of secreted APOE isoforms. Following model validation, the effects of astrocyte treatment on APOE3 and APOE4 neurons were systematically evaluated. Building upon this, the impact of Aβ25-35 was assessed in the next chapter. This approach allowed assessment of how neuronal and astrocyte APOE genotype modulates stress responses and how astrocyte-derived factors via ACM influence neuronal responses under pathological conditions.

To extend the study's relevance to therapeutic exploration, a small-molecule drug screen was conducted in collaboration with GSK. Forty-two compounds were tested in astrocyte monocultures to identify agents capable of modulating APOE-related phenotype.

The subsequent sections present the results in parts: (1) characterization of iPSCs and iPSC-derived cell models, (2) the effects of astrocytes on neuronal phenotypes across APOE genotypes, including small molecule-induced and lentiviral-induced astrocytes in ACM and co-culture models, (3) modeling early AD pathology - response to Aβ25-35 stress, including neuronal and astrocytes responses, and neurons treated with ACM, (4) therapeutic intervention using phenotype-guided drug screen in astrocytes.

### *3.1.2. Neuronal induction and characterization*

Hippocampal and cortical neurons are particularly vulnerable to Aβ accumulation, while APOE is primarily expressed by astrocytes. The differentiation protocols used in the study successfully generated cortical neurons and astrocytes, confirming their identity through marker expression and functional assays.

In 2D culture systems, iPSCs can be differentiated into neurons using strategies including mimicking developmental signaling through dual SMAD inhibition or direct conversion via overexpression of transcription factors such as NGN2. While both approaches produce functionally mature neurons expressing appropriate markers, these approaches differ in speed and developmental fidelity.

Dual SMAD inhibition using small molecules like LDN193189 and SB431542 in the culture media blocks BMP and TGF-β pathways, guiding iPSCs through a neuroectodermal lineage via neural progenitor cells. Although this *in vitro* protocol does not fully recapitulate embryonic development involving sequential formation of the three germ layers, ectoderm, mesoderm, and endoderm, it bypasses those stages and directs cells from pluripotency to neuroectoderm. Nonetheless, it preserves key developmental logic by maintaining intermediate identities such as neuroepithelial stem cells and endogenous transcriptional programs. It enables the generation of diverse neuronal subtypes and is especially valuable for modeling complex neurodevelopmental processes and genotype-specific phenotypes. In contrast, transcription factor overexpression allows rapid, direct differentiation, bypassing

progenitor stages. While efficient, it may limit cell diversity and developmental context, which could be less ideal for studying cell–cell interactions or disease mechanisms involving multiple cell types (Carter et al., 2020; Gascón et al., 2017).

Therefore, this study adopted the dual SMAD inhibition-based approach to generate iPSC-derived cortical neurons and astrocytes. As detailed in the Methods section, this strategy supports a developmentally relevant differentiation trajectory, preserves genotype-specific traits, and is essential for modeling APOE-related mechanisms in AD.

#### *3.1.3. Astrocyte induction and optimization of cell culture*

Similar to neurons, astrocytes can be derived from iPSCs using either small molecule-based signaling pathway stimulation or overexpression of transcription factors such as NfiB/SOX9, with or without serum. Although these approaches can generate astrocytes that resemble primary human cells at molecular, phenotypic, and functional levels, they typically require over 100 days of differentiation. This extended timeline posed a major limitation for timely experimentation.

Due to the extended time required for astrocyte maturation with the small molecule approach, the study adopted a lentiviral (LV) induction approach, overexpressing DOX-inducible NfiB in iPSCs to induce astrocytes. This approach resulted in a more consistent and reproducible astrocyte population across different *APOE* genotypes and donor lines. Unlike the small molecule protocol, which required over 100 days of culture to ensure maturation and still exhibited ongoing proliferation, lentiviral-induced astrocytes reached a

stable, post-mitotic state much earlier, typically between Day 18 and 25 of differentiation. This early growth arrest not only indicated accelerated maturation but also enabled experiments to be conducted within a more controlled and predictable time window.

The lentiviral induction approach substantially shortened the astrocyte differentiation timeline and provided a more practical and predictable experimental workflow. During routine culture, lentiviral-induced astrocytes appeared morphologically more consistent than the small-molecule-induced cultures and were therefore convenient for high-content imaging. However, this apparent difference in population homogeneity was not assessed using a matched quantitative comparison between the two induction methods. It is therefore described as a qualitative observation rather than a validated difference between the astrocyte populations.

Taken together, although the study initially used small molecule-induced astrocytes, the lentiviral overexpression strategy provided a practical and robust platform for generating astrocytes suitable for downstream ACM, especially co-culture, experiments. The comparison between small-molecule- and lentiviral-induced astrocytes, including marker expression and morphological characteristics, is further detailed in the characterization section.

## 3.2. Results

### *3.2.1. Characterization of iPSCs and iPSC-derived neurons and astrocytes models*

A total of six iPSC lines were used in this study, consisting of three pairs of isogenic lines derived from three individual donors. These included two donors (sAD donor 1 and sAD donor 2) who were homozygous for *APOE*4 and clinically diagnosed with sAD, and one age-matched healthy control donor who was homozygous for *APOE*3 (control donor 1).

The original iPSC lines from these donors were genetically edited using CRISPR-Cas9 technology to generate isogenic counterparts with either homozygous *APOE*3 or *APOE*4 genotypes (Table 2.1). For instance, AG09173 was derived from a healthy control donor with the *APOE*3 genotype and was edited to produce AG09173-1336, which carries the *APOE*4 genotype, enabling direct genotype comparison within the same genetic background.

iPSC cultures were maintained, expanded, and cryopreserved in mTeSR1 medium following the manufacturer's protocol. Neural differentiation was initiated using the dual SMAD inhibition method, adapted from previously established protocols (Shi et al., 2012), as summarized in Section 2.1.1. Specifically, daily media change was performed until Day 21, with the addition of LDN193189 and SB431542 during the first 7 days to inhibit BMP and TGF-β signaling.

During the early stage of differentiation, from iPSCs to the neural stem cells (NSCs) stage, cell cultures were kept at high density to promote the formation of a neuroepithelial sheet, which facilitates the emergence of neural rosettes in the subsequent stage. On Day 21, a decision point was reached to either terminally differentiate the cells for downstream experiments or cryopreserve them for future use.

Compared to undifferentiated iPSCs, the induced neural progenitor cells showed significantly reduced expression of the pluripotency marker OCT4. However, expression of the mature neuronal marker MAP2 remained minimal at this stage, particularly when compared to later-stage neurons (Fig. 3.1A, B). ICC confirmed that iPSC colonies were positive for pluripotent markers SSEA4 and SOX2, and negative for the deep-layer neuronal marker CTIP2 (Fig. 3.2), consistent with a stem cell stage before neural induction.

As detailed in the figures in Methods (Fig. 2.2. and 2.3), both monoculture and co-culture models were established using separately differentiated cells derived from isogenic iPSC pairs of the same donor. Specifically, cultures were assembled with either identical APOE genotypes in both cell types (e.g., APOE3 neurons with APOE3 astrocytes; APOE4 neurons with APOE4 astrocytes) as well as with cross-genotype pairings in which the neuronal genotype differed from the astrocytic genotype (e.g., APOE4 neurons with APOE3 astrocytes, and APOE3 neurons with APOE4 astrocytes). These models were confirmed to express

appropriate lineage-specific markers and deemed suitable for downstream phenotypic analysis.

In the neuronal monoculture, cells were stained with Hoechst (nuclear), EEA1 (early endosomes), SYP (synaptophysin), and MAP2 (neuronal cytoskeleton) antibodies (Fig. 3.3A). For neuron–astrocyte co-cultures, the staining panel included Hoechst, EEA1, S100B (astrocyte marker), and MAP2 (Fig. 3.3B, C).

Following the successful generation of human cortical astrocytes, ACM was collected for use in neuronal treatment assays. Specifically, small molecule-induced astrocytes were cultured until Day 100, while lentiviral-induced astrocytes reached maturity at Day 18. At these time points, the culture medium was switched to NMM for 2 days. The resulting supernatant was collected, passed through a 0.22 μm filter to remove cellular debris, and stored at −80 °C until use. Prior to treatment, ACM samples were analyzed for total protein concentration to ensure comparability across donor lines and kept as reference (Fig. 3.4). Additionally, the presence of APOE protein was confirmed and the expression level in ACM was quantified via Western blot (Fig. 3.5).

Two complementary astrocyte induction paradigms were employed, including small-molecule induction for long-term, developmentally-relevant modeling and lentiviral overexpression of

NfiB for rapid, high-efficiency generation of mature astrocytes focused on specific phenotypes, This choice was made to obtain a more homogeneous and stable astrocytes for baseline morphological profiling especially in image-based studies. Their morphological phenotypes were assessed in terms of the intensity and expression patterns of S100B, EEA1, and Hoechst (Fig. 3.3D).

As NMM was used during the collection of ACM, the effect of NMM exposure on astrocyte morphology was also considered. For small-molecule-induced astrocytes, NMM did not represent a major change in culture condition at the stage used for ACM collection, as these cells were >Day 100 and were already maintained in NMM. Consistent with this, no obvious change in their overall morphology was observed following the medium condition used for ACM collection. In contrast, lentiviral-induced astrocytes showed an apparent morphological change following exposure to NMM. Representative images showed a shift from the more typical stellate morphology observed under the astrocyte culture condition towards a flatter and more spread morphology in NMM (Figure 3.6). This observation was qualitative and was not quantified using morphological feature analysis. Therefore, it cannot be concluded from the present data that NMM induced a defined phenotypic state in lentiviral-induced astrocytes. Nevertheless, this visible difference indicates that the medium environment may influence the morphology of lentiviral-induced astrocytes and should be considered when interpreting ACM experiments using this model.

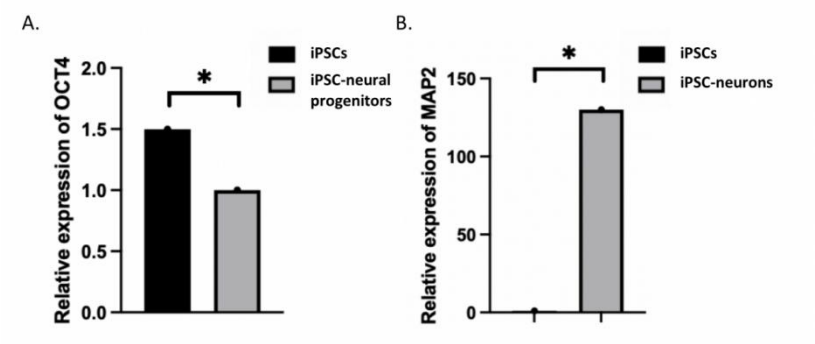



***Fig 3.1. RNA expression levels of OCT4 and MAP2 iPSCs and neurons.*** *Cells were collected from 6-well plates, and total RNA was extracted for quantitative RT-qPCR analysis. (A) Relative mRNA expression of OCT4 (a pluripotency marker) in undifferentiated iPSCs (as Day 0) and iPSC-derived neural progenitors collected on Day 15 during neuronal induction. (B) Relative mRNA expression of MAP2 (a neuronal maturation marker) in iPSCs (Day 0) and iPSC-derived mature neurons. Expression was normalized to GAPDH as the housekeeping gene. OCT4 was highly expressed in iPSCs but significantly reduced in neurons. In contrast, MAP2 expression was undetectable in iPSCs but robustly expressed in differentiated neurons, confirming successful neural induction. Asterisks indicate significant difference from the compared groups (*p < .05).*

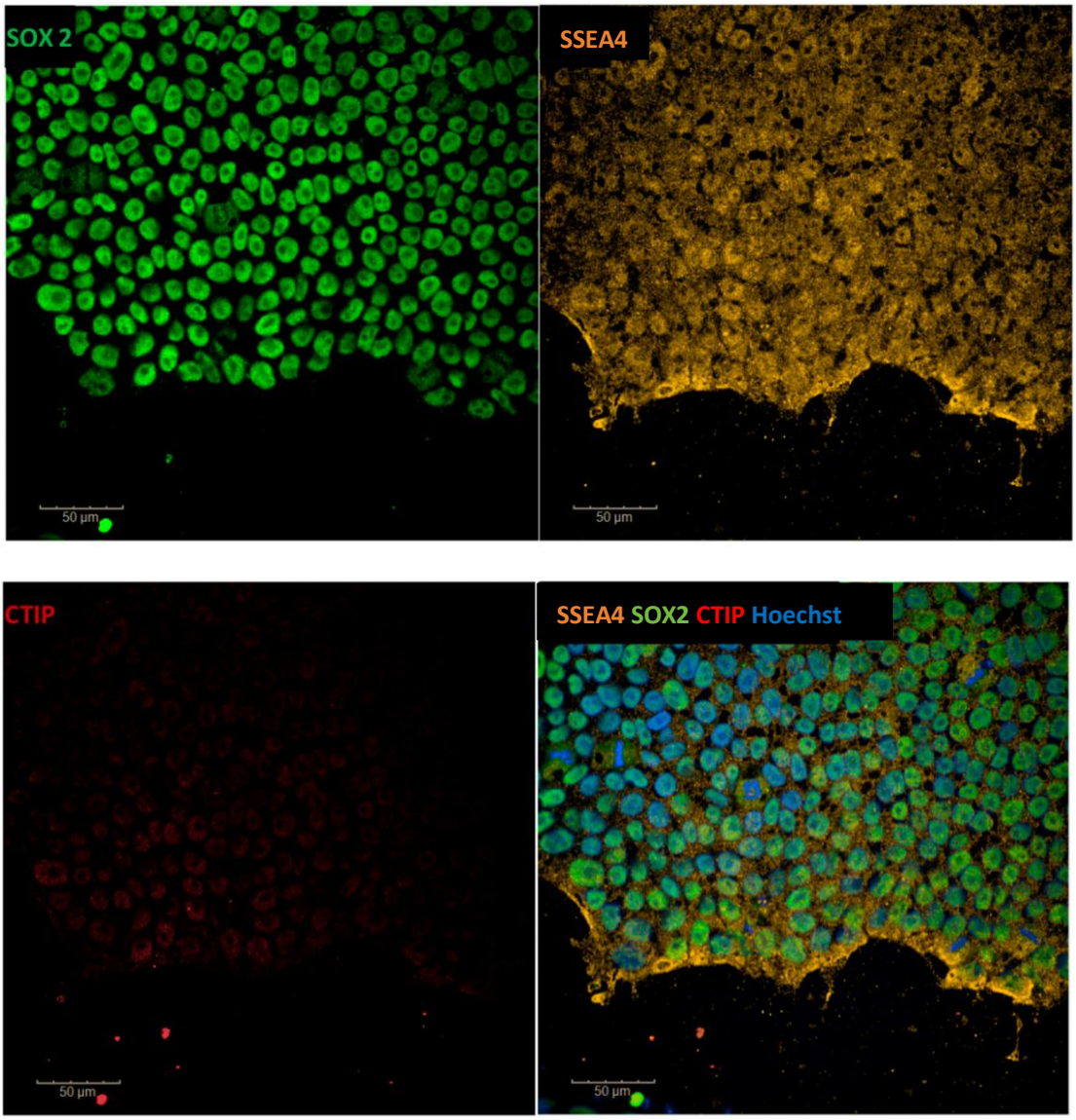
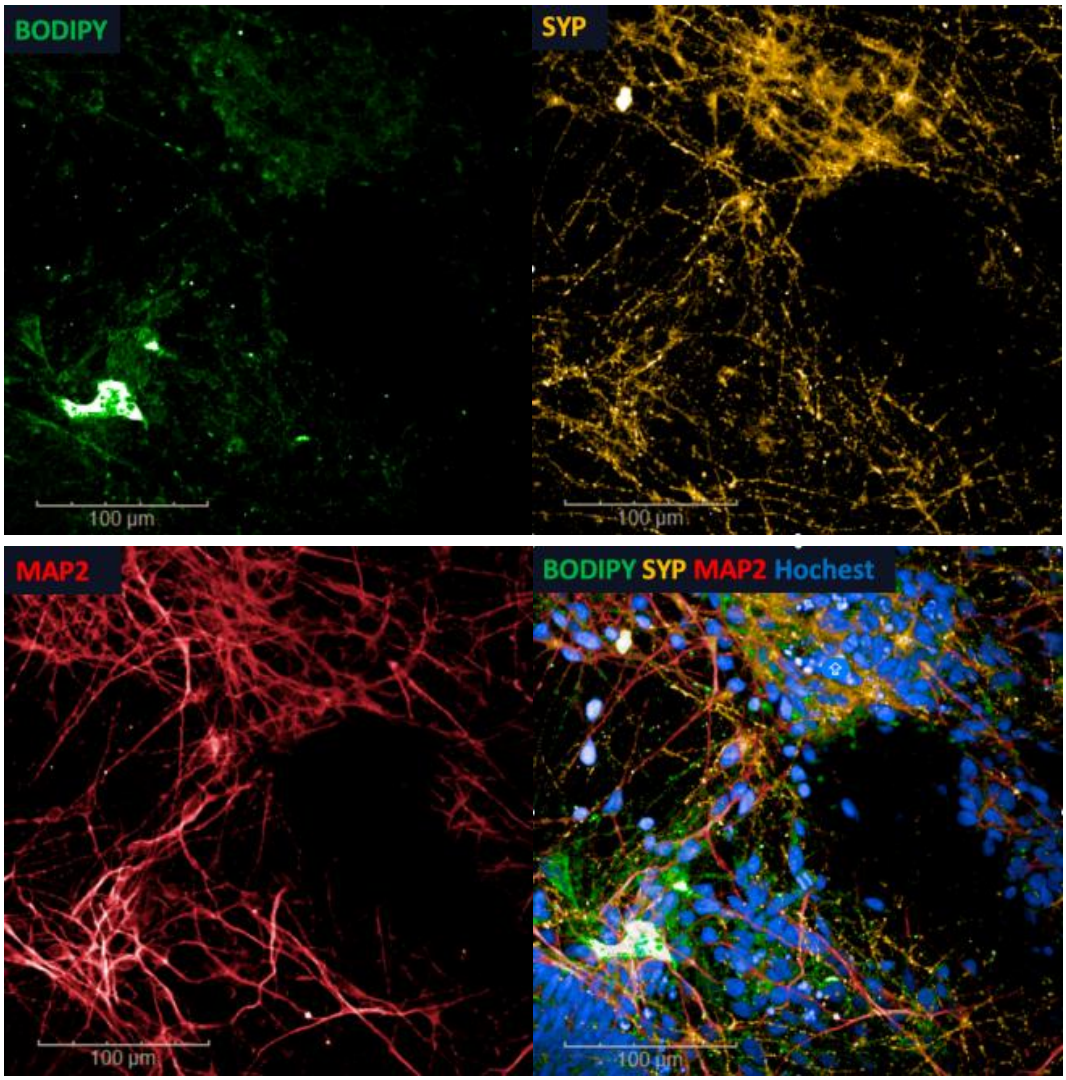


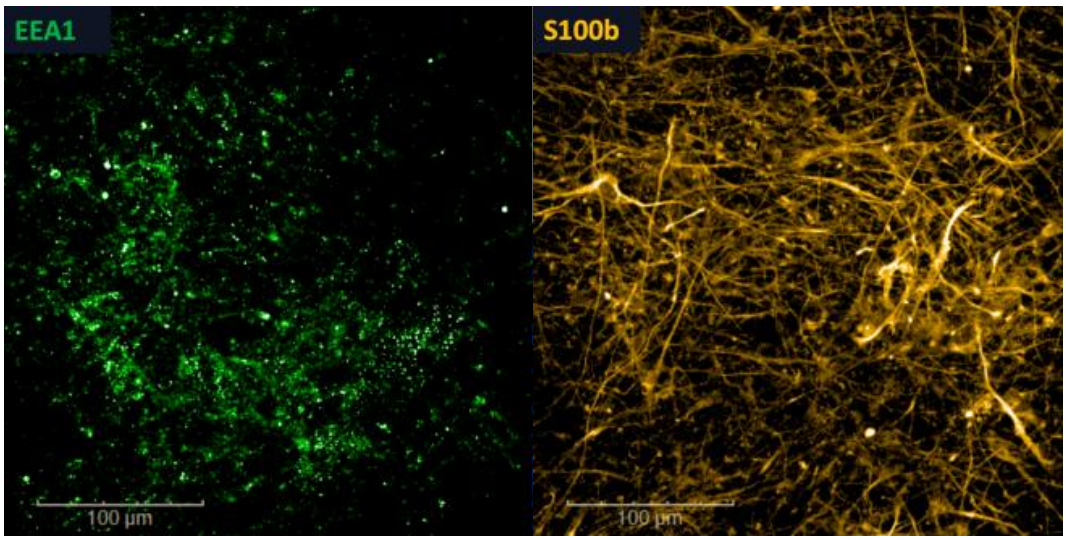

***Fig 3.2. ICC images of iPSC clones stained with pluripotency and neuronal markers.***

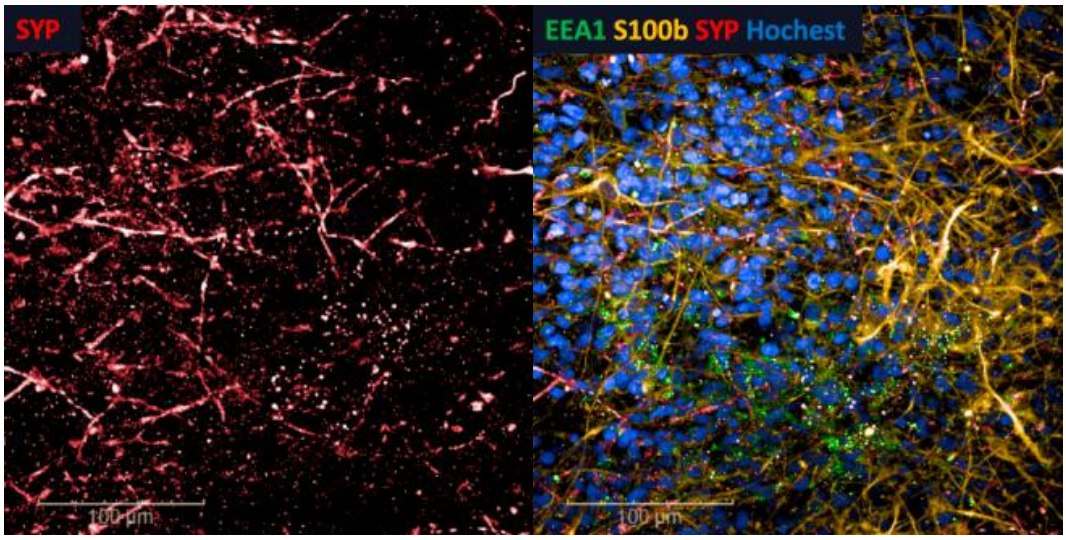
*Shown are representative fields from sAD donor 1 iPSC cultures stained to assess pluripotency and the absence of neuronal differentiation before induction. Top left: nuclear SOX2 (green), a pluripotency-associated transcription factor. Top right: cell-surface SSEA4 (orange), a pluripotency marker. Bottom left: CTIP2 (red), a deep-layer cortical neuronal marker, showing no detectable expression. Bottom right: merged image of SSEA4 (orange), SOX2 (green), CTIP2 (red) and Hoechst nuclear counterstain (blue). The presence of SOX2 and SSEA4 together with the absence of CTIP2 indicates that the cultures remained pluripotent at this stage. Images are representative of multiple iPSC lines examined prior to neural induction. Scale bar represents 50µm.*

A.

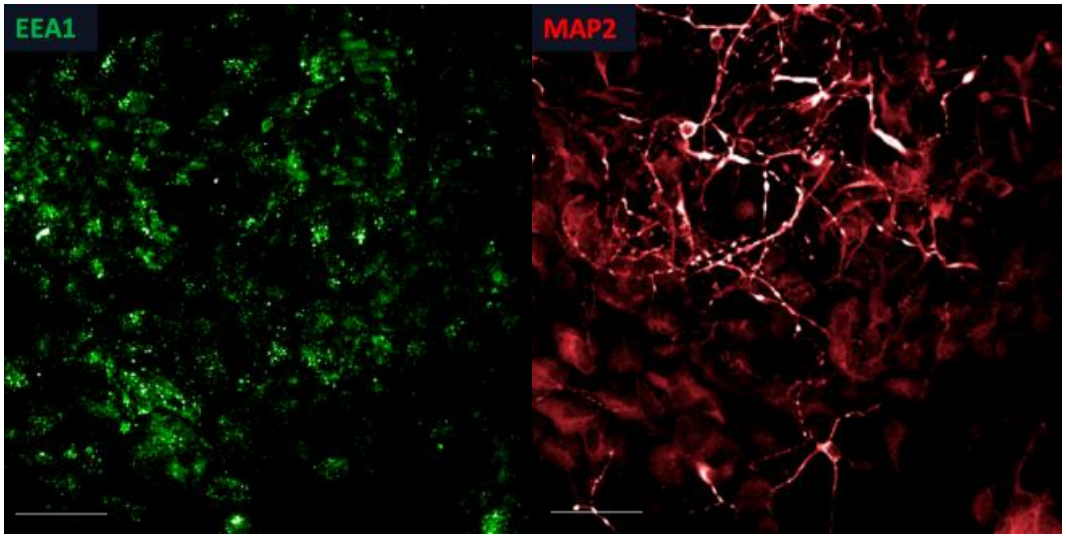

BODIPY
100 µm
SYP
100 µm
MAP2
100 µm
BODIPY SYP MAP2 Hochest
100 µm

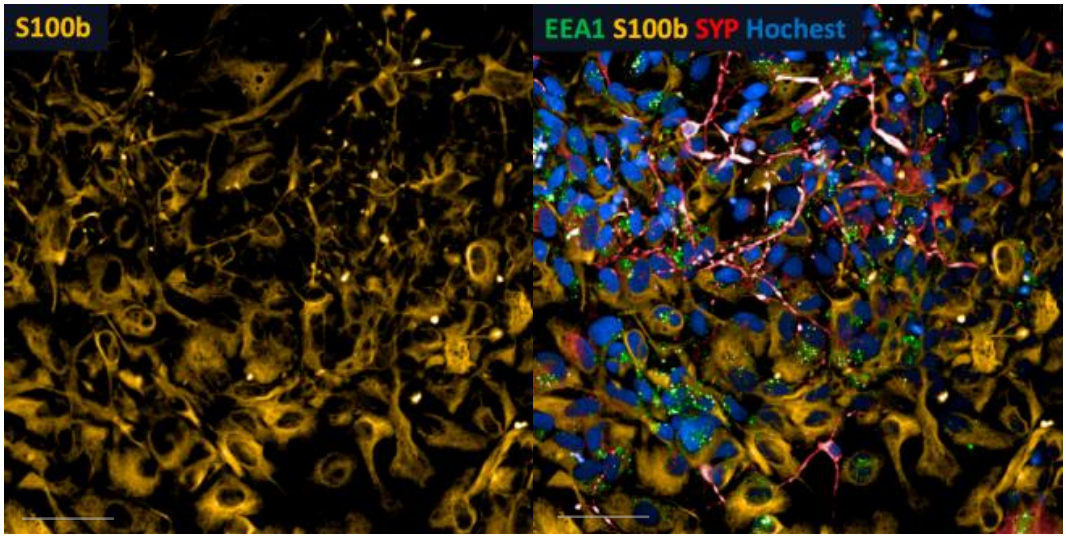
B.


EEA1
100 µm
S100b
100 µm


SYP
EEA1 S100b SYP Hochest
100 µm
100 µm

C.


EEA1
MAP2


S100b
EEA1 S100b SYP Hochest

D.

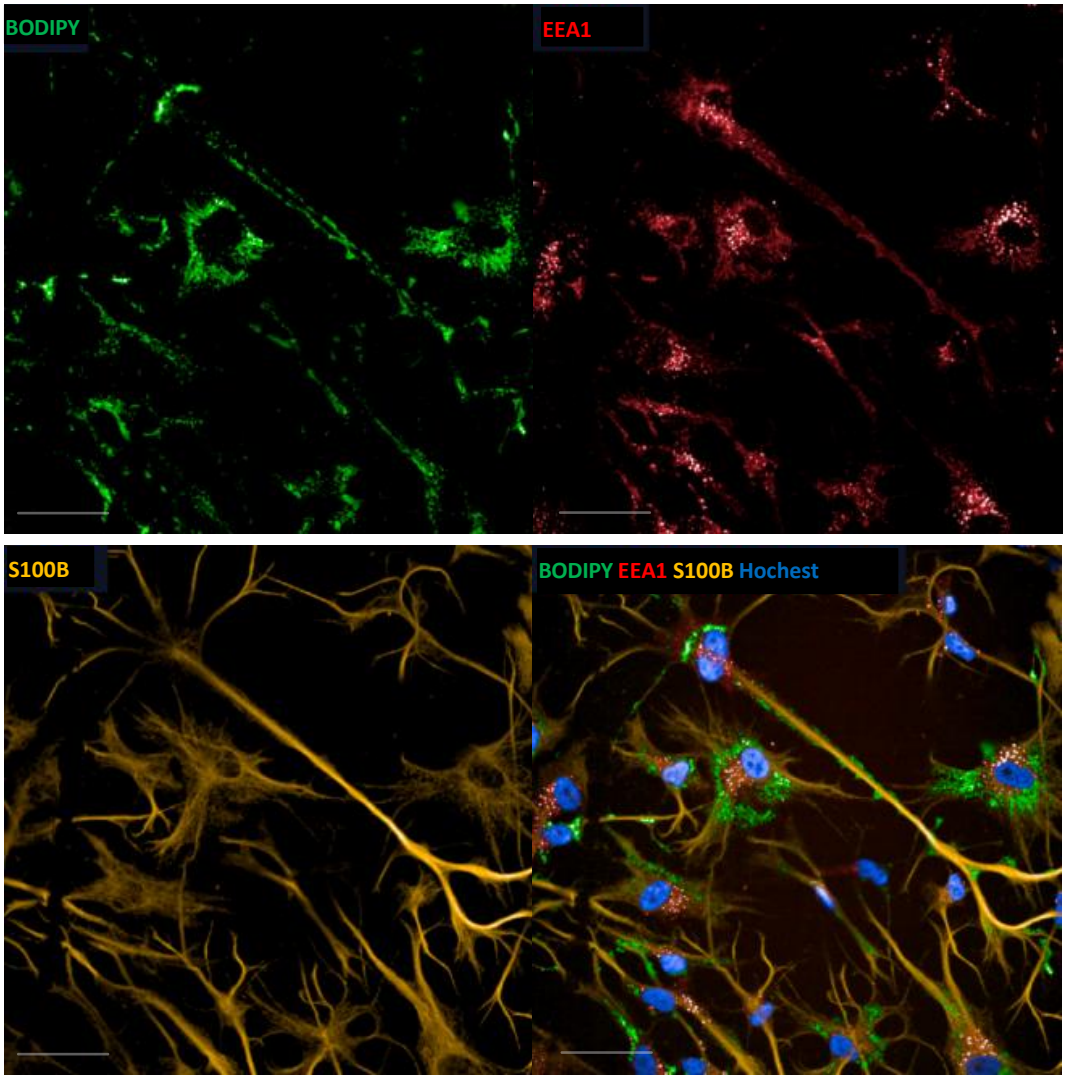



***Fig 3.3. ICC staining of co-culture and monoculture confirms successful differentiation of neurons and astrocytes.***

*(A) Representative ICC images of sAD donor 1 neuronal monocultures, stained for MAP2 (red, microtubule-associated protein 2; neuronal dendrites), BODIPY (green, neutral lipid droplets), SYP (yellow, synaptophysin; presynaptic puncta) and Hochest (nuclear counterstain) demonstrating successful neural induction and early synaptic protein expression.*

*(B) Representative images of control donor 1 neurons co-cultured with small-molecule derived astrocytes, stained for SYP (red, neuronal presynaptic puncta), EEA1 (green, early endosomes), S100B (yellow, astrocytic cytoplasmic marker) and Hochest (nuclear counterstain), confirming the presence of both neuronal and astrocytic lineages within the same culture.*

*(C) Representative images of neurons sAD donor 2 co-cultured with lentiviral-induced astrocytes, stained for EEA1, SYP, S100B and Hochest.*

*(D) Representative images of control donor 1 astrocyte monocultures generated by lentiviral overexpression of the transcription factor NfiB, stained for EEA1, BODIPY, S100B and Hochest, confirming astrocytic identity.In all panels, individual channels are shown separately for each*

*marker, with merged views used where indicated to illustrate co-localization. Images are representative of multiple independent differentiations. Scale bar represents 100µm.*

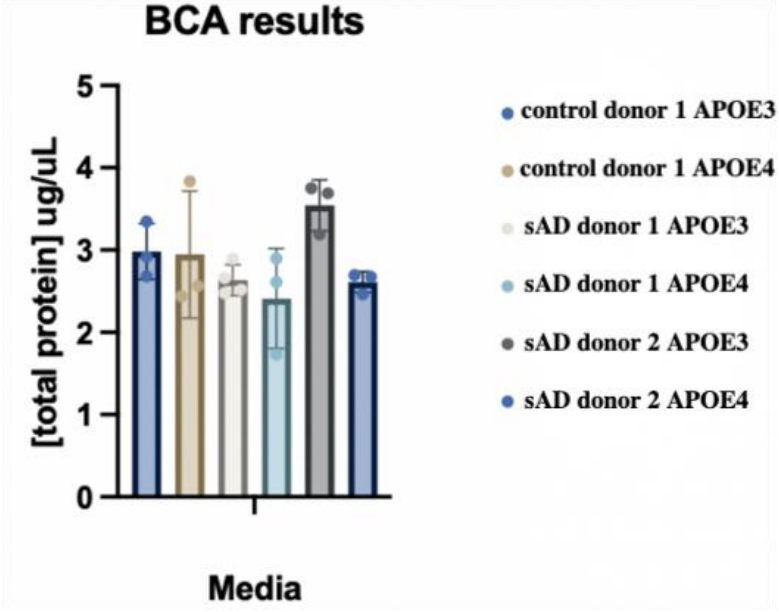



***Fig 3.4. BCA assay results of ACM samples collected for treatment on neurons.***

*Total protein concentrations of ACM collected were measured by BCA assay. ACM was collected from astrocyte cultures derived from control donor 1 and two sAD donors, across APOE3 and APOE4 genotypes, as indicated. Each point represents an independent ACM preparation. Group comparisons were performed using one-way ANOVA with no significant differences detected among groups ($p > 0.05$), indicating comparable protein levels suitable for downstream neuronal treatment experiments.*

A. B.

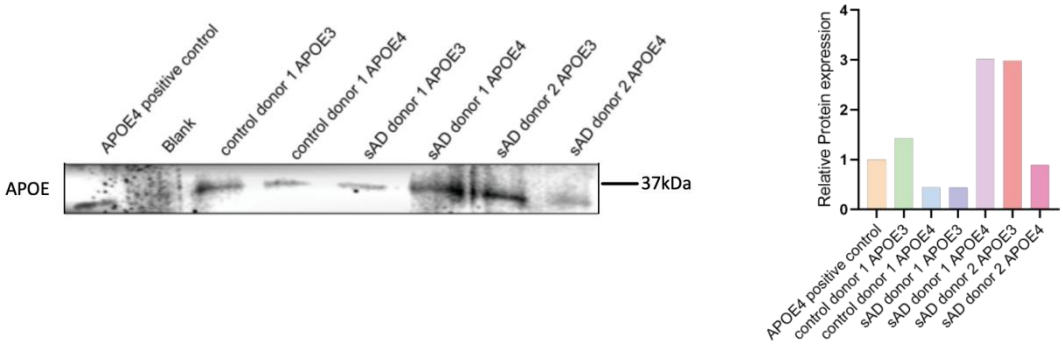



***Figure 3.5. Western blot of APOE in astrocyte conditioned media.***

*ACM samples were resolved by SDS-PAGE. APOE has an expected molecular weight of ~34 kDa.*

*(A) Western blot of APOE expression in ACM, including a positive control of 1ng APOE4 human recombinant protein.*

*(B) Quantification of relative APOE expression per medium. Densitometry was normalised to the membrane background.*

A. B.

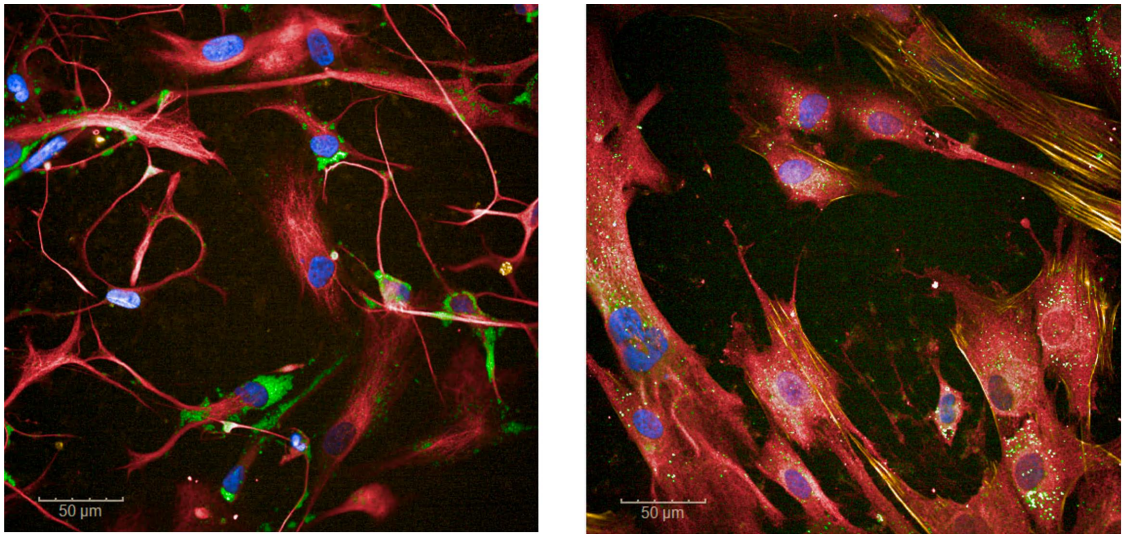



***Figure 3.6. Representative morphology of iPSC-derived astrocytes under the medium conditions used for ACM collection.***

*(A) Representative lentiviral-induced astrocytes before exposure to NMM.*

*(B) Representative lentiviral-induced astrocytes following exposure to NMM. Lentiviral-induced astrocytes appeared more stellate under the astrocyte culture condition and flatter and more spread following NMM exposure. These observations are based on representative images and were not quantitatively assessed; therefore, they are presented as qualitative morphological observations rather than evidence of a defined NMM-induced phenotypic change.*

## 3.3. Discussion

The results presented in this section confirm the successful derivation of cortical neurons and astrocytes from human iPSCs, providing a reproducible platform for dissecting *APOE* genotype–dependent mechanisms in AD. Multiple validation approaches established the fidelity of the differentiation protocols. The transition from pluripotency to lineage commitment was confirmed by the downregulation of OCT4 and concomitant upregulation of MAP2, supported by both transcriptomic (Fig. 3.1.2) and immunocytochemical (Fig. 3.1.3) analyses. ICC further demonstrated the expected expression of pluripotency markers (SSEA4,

SOX2) in iPSC clones and neuronal (MAP2) and astrocytic (S100B) markers in differentiated cultures (Fig. 3.1.4), thereby confirming the identity of each lineage. Importantly, these results were independent of donor background and *APOE* genotype, underscoring the robustness of the induction strategies.

The comparative evaluation of induction methods provided key insights into experimental optimization. For neurons, the dual SMAD inhibition approach ensured a developmentally relevant trajectory via neural progenitor stages, thereby preserving developmental trajectory that includes transient gene-expression states characteristic of early neurogenesis. This was particularly advantageous for modeling APOE-dependent neuronal phenotypes, which may be sensitive to subtle developmental contexts. For astrocytes, however, the practical limitations of the small molecule–approach including the extended timeline (>100 days) and variability in morphology, necessitated the adoption of an NfiB-driven lentiviral protocol. Lentiviral induction provided a substantially shorter differentiation timeline and a more predictable experimental workflow, which was particularly practical for high-content imaging and quantitative morphological analyses. This methodological distinction is important, as it frames lentiviral- and small molecule–derived astrocytes as complementary models: the former providing reproducibility and throughput, the latter reflecting developmental progression with greater fidelity but at the cost of time and variability.

The collected ACM was assessed with additional quality control. Protein concentrations across donor lines were compared (Fig. 3.1.5), and APOE protein expression was confirmed (Fig. 3.1.6), ensuring that downstream neuronal assays could be interpreted relative to the astrocytic secretion.

The integration of monoculture, ACM, and co-culture paradigms further strengthened the modeling strategy. While monoculture neurons provided a baseline to define intrinsic *APOE* genotype effects, ACM experiments enabled the dissection of astrocyte-derived secreted factors, and co-culture assays captured direct cell–cell interactions. Together, these complementary models established a versatile framework to interrogate how *APOE* genotype influences neuronal morphology, synaptic function, nuclear properties, and endosomal biology under both physiological and stress conditions, such as $A\beta_{25\text{-}35}$ exposure.

In summary, this section establishes that the iPSC-derived neuronal and astrocytic models are appropriately specified, genetically defined, and experimentally optimized to address *APOE* genotype–dependent mechanisms in AD. The comparisons between small molecule- and lentiviral-induced astrocytes on cortical neuronal morphology balanced between developmental fidelity and experimental practicality. These models (Figures 3.1.1–3.1.7) lay the foundation for the subsequent analyses in this thesis, where systematic comparisons of *APOE*3 and *APOE*4 backgrounds under ACM and co-culture conditions are employed to dissect the cellular and molecular phenotypes that underlie differential disease vulnerability.

# Chapter 4: The effects of small-molecule astrocytes on neuronal phenotype

## 4.1. Introduction

Astrocytes are no longer considered passive support cells in the central nervous system. Historically believed to outnumber neurons by a ratio of 10:1, but this was only based on limited datasets and has since been largely overturned; whole-brain counts in adult humans indicate approximately equal numbers of neuronal and non-neuronal cells (~1:1), and the figures referred to glia overall rather than astrocytes specifically (Azevedo et al., 2009; von Bartheld et al., 2016). Cell proportions are region specific; consequently, any single ratio must be interpreted in anatomical context. For example, within the human cerebral cortex, the astrocyte-to-neuron ratio has been estimated at ~1:1.4, whereas the mouse cortex shows ~1:3 (Degl'Innocenti & Dell'Anno, 2023).

This shift in understanding reflects the growing recognition that astrocytes actively regulate neuronal development, synaptic activity, and homeostasis (Khakh & Sofroniew, 2015; Nagai et al., 2021). Neuroenergetic support has been attributed to astrocyte-neuron metabolic coupling, including lactate shuttling and glycogenolysis (Magistretti & Allaman, 2018). Extracellular neurotransmitter and ion homeostasis critically depend on high-affinity astrocytic glutamate transporters, which tightly regulate synaptic glutamate clearance (Danbolt, 2001; Djukic et al., 2007). Clearance of interstitial solutes and cellular debris has been attributed to AQP4-dependent glymphatic flow and astrocytic phagocytosis (Iliff et al.,

2012; Jiang-Xie et al., 2024). Disruption of these astrocytic pathways has been reported to precipitate or exacerbate neuronal dysfunction across conditions such as epilepsy, ALS, and neurodegeneration (Phatnani & Maniatis, 2015).

A key advancement in the field was the proposal of the 'tripartite synapse', which introduced astrocytes as integral components of synaptic physiology alongside pre- and post-synaptic neurons. Within this framework, astrocytes release gliotransmitters such as glutamate, ATP, D-serine, and nitric oxide, modulating neuronal excitability in a calcium-dependent manner. This dynamic, bidirectional communication highlights astrocytes as crucial regulators of synaptic plasticity, circuit formation, and injury response (Araque et al., 1999; Perea et al., 2009).

To investigate the influence of astrocytes on neuronal phenotype derived from *APOE*3 and *APOE*4 backgrounds, protein expression patterns were analyzed using ICC collected from high-content imaging. This approach was taken to test the hypothesis that, in addition to neuronal genotype, astrocytes can influence neuronal morphology, thereby providing a mechanistic link between astrocytic APOE status and neuronal vulnerability. Specifically, following the establishment of ACM and co-culture models, ICC was performed to examine cellular morphology and subcellular structures using feature-extraction based quantification. Key markers include Microtubule-associated protein 2 (MAP2) MAP2, Early Endosome Antigen 1 (EEA1), S100B (astrocyte marker), BODIPY (neutral lipids), synaptophysin (SYP), and

Hoechst (nuclei). Markers were selected to capture processes relevant to APOE-linked mechanisms. MAP2 was used to quantify dendritic architecture and neuronal cytoskeleton, consistent with its dendrite-enriched localization (DeGiosio et al., 2022). SYP was used as a presynaptic vesicle marker to estimate synaptic puncta density (Wiedenmann & Franke, 1985). EEA1 was used to index early endosomal trafficking, given its role as a Rab5-dependent endosomal tether, and because endocytic/endolysosomal alterations have been reported in APOE4 contexts (Lin et al., 2018). S100B was used operationally to annotate astrocytes in co-cultures, but it also reveals neuropathology in brain regions in AD (Van Eldik & Griffin, 1994). Neutral lipid content was quantified with BODIPY to measure lipid droplets, which are modulated in APOE4 astrocytes and relevant to lipid-handling phenotypes (Qi et al., 2021b). Nuclei were stained with Hoechst to enable segmentation for cell feature extraction.

As a first step, an overview of neuronal morphology across all experimental groups, including different astrocytes and neuronal *APOE* genotype was generated.

Then to break the comparison groups down, APOE3 versus APOE4 cultures were compared under untreated control conditions, where the only variable was *APOE* genotype, to define baseline differences. Comparisons were performed in two interaction modes: neuronal monocultures exposed to ACM and neuron-astrocyte co-cultures. Building upon this and the baseline differences between APOE3 and APOE4 cultures reported earlier, the study addressed the following key questions: (1) Are phenotypic changes in neurons driven by

astrocytes?

(2) Are these effects dependent on astrocyte genotype, neuronal genotype, or the mode of interaction (ACM versus co-culture)? (3) Which neuronal features are affected by astrocyte or neuronal genotype?

As mentioned in the methods section, from high-content imaging, approximately 60 cellular features were extracted. A random forest classifier was used to identify the most informative features distinguishing APOE3 from APOE4 conditions and different astrocyte treatments. Ten features were selected for in-depth analysis across four critical cellular and molecular pathways, using ANOVAs. These include: two features related to the synaptophysin pathway (SYP number and size); two describing neuronal morphology (neurite number and length); two representing nuclear features (nucleus intensity and size); and four associated with early endosomal function (EEA1 number, intensity, area, and width-to-length ratio).

The subsequent sections present the results in the following parts: (1) the effects of small molecule-induced astrocytes on neuronal phenotype across *APOE* genotypes; (2) the effects of lentiviral-induced astrocytes on neuronal phenotype across *APOE* genotypes.

Each part aims to answer specific questions:

(1) What are the baseline morphological and molecular differences between APOE3 and APOE4 neurons and astrocytes, and how do these differences manifest in monoculture and

co-culture conditions?

(2) Do astrocytes influence the differences between APOE3 and APOE4 neurons?

(3) Is this impact determined by the genotype of the astrocytes?

(4) Is this impact determined by the genotype of the neurons?

## 4.2. Results

### *4.2.1. Overview of all groups in ACM and co-culture experiments (both astrocyte treatment and APOE genotypes influence neuronal phenotype)*

To investigate the influence of factors such as neuronal *APOE* genotype and ACM derived from astrocytes with either *APOE*3 or *APOE*4 genotype on neuronal morphology, a series of ACM experiments was performed. Six experimental groups were established: homozygous *APOE*3 or *APOE*4 neurons cultured under three different conditions—ACM from APOE3 astrocytes, ACM from APOE4 astrocytes, or neuronal maintenance media (NMM) as a control (Table 4.1). This design enables two complementary comparisons: (i) neurons of the same APOE genotype exposed to different ACM, to assess astrocyte APOE effects on neurons; and (ii) neurons of different APOE genotypes cultured under the same condition, to isolate the contribution of neuronal APOE genotype itself.

In parallel, co-culture experiments comprised four groups: homozygous *APOE*3 or *APOE*4 neurons directly co-cultured with either APOE3 or APOE4 astrocytes (Table 4.2). This setup not only allows examination of how astrocyte *APOE* genotype affects neurons of different *APOE* backgrounds, but also permits investigation into whether direct physical contact

between astrocytes and neurons is necessary to elicit these effects, or if soluble factors secreted into the ACM alone are sufficient.

#### *4.2.2. What are the baseline morphological and molecular differences between APOE3 and APOE4 neurons and astrocytes, and how do these differences manifest in monoculture and co-culture conditions?*

In monoculture of neurons bearing either the *APOE*3 or *APOE*4 genotype maintained in standard neuronal maintenance media (NMM), APOE4 neurons exhibited significantly more and longer neurites (Fig. 4.2C - C1, C3; Fig. 4.2D - D1, D3), brighter nucleus intensity (Fig. 4.3E - E2, E3), larger and brighter EEA1 spots area (Fig. 4.4I - I1, I3; Fig. 4.4H - H1, H3) but smaller SYP spots area (Fig. 4.1B - B1, B2) compared to APOE3 neurons. These differences were consistently observed across two out of three donors, suggesting that APOE isoforms influence neurite outgrowth and early endosomal protein expression patterns in neurons.

In co-cultures where neurons and astrocytes shared the same *APOE* genotype, neurons from 2 out of 3 or all 3 donors in APOE4 co-cultures exhibited brighter but smaller nucleus (Fig. 4.13C - C1, C2, C3 and Fig. 4.13D - D1, D2) compared to APOE3 neurons co-cultured with APOE3 small-molecule induced astrocytes.

In co-cultures, astrocytes from 2 out of 3 or all 3 donors in APOE4 co-cultures showed more round nuclei (Fig. 4.5B - B2, B3), larger cell area (Fig. 4.6D - D1, D2, D3), and smaller width-to-length ratio (Fig. 4.6E - E1, E2) compared to APOE3 astrocytes in APOE3 co-cultures.

### *4.2.3. Do astrocytes influence the differences between APOE3 and APOE4 neurons?*

The presence of astrocytes appears to modulate, and in some cases normalize, the baseline differences observed between APOE3 (E3) and APOE4 (E4) neurons. When neurons were treated with ACM from APOE4 small-molecule induced astrocytes, genotype-specific differences in neurite length were no longer statistically significant, but only APOE3 neurons tend to have rounder early endosomes as indicated by a larger width to length ratio than APOE4 neurons treated with APOE4 ACM (Fig. 4.11J - J1, J2, J3). However, no features showed significant differences between APOE3 and APOE4 neurons among three or more donors when treated with APOE3 ACM or co-cultured with APOE4 astrocytes.

### *4.2.4. Is this impact determined by the genotype of the astrocytes?*

When comparing the effect of different astrocytes on neurons of the same *APOE* genotype, clear genotype- and interaction-dependent differences emerged. Under the effect of secreted factors, ACM collected from APOE3 astrocytes makes APOE4 neurons have higher number of SYP, EEA1 spots and neurites (Fig. 4.8A - A2, A3; Fig. 4.11G – G2, G3; Fig. 4.9C - C2, C3), longer neurite length (Fig. 4.9D - D2, D3) and brighter nucleus intensity (Fig. 4.10E - E2, E3) than APOE4 neurons cultured in ACM collected from APOE4 astrocytes.

In contrast, when directly co-cultured with APOE3 astrocytes, APOE4 neurons exhibited the opposite pattern compared to co-culture with APOE4 astrocytes. APOE4 neurons express lower number of EEA1 and neurite (Fig. 4.14E - E2, E3; Fig. 4.12A - A2, A3), smaller EEA1 spots area (Fig. 4.14G - G2, G3), decreased nucleus intensity (Fig. 4.13C - C1, C3) and shorter

neurite length (Fig. 4.12B - B2, B3) compared to APOE4 neurons co-cultured with APOE4 astrocytes.

Whereas the above five features were altered in APOE4 neurons as a function of astrocyte genotype, astrocyte-dependent effects in APOE3 neurons were far less pronounced. The only reproducible change that was observed was an increase in nuclear area when neurons were co-cultured with APOE4 astrocytes compared with APOE3 astrocytes, and this effect was shared by both APOE3 and APOE4 neurons (Fig. 4.13D–D2, D3).

Taken together, the findings suggest that neuronal phenotypes were influenced by the astrocyte *APOE* genotype in a neuronal genotype-dependent manner. Greater sensitivity to astrocyte-derived signals was exhibited by APOE4 neurons. This highlights a genotype–genotype interaction between the two cell types, whereby neuronal APOE4 amplifies the impact of astrocytic APOE4. Such genotype differences in synaptic maintenance, endosomal trafficking, and lipid homeostasis may underlie the heightened vulnerability of APOE4-bearing neuronal networks. Moreover, the fact that APOE4 astrocytes exert opposite influences on APOE4 neurons under ACM versus co-culture conditions on features including the number of EEA1 spots and neurites, nucleus intensity, and the length of neurites, further indicates that the mode of astrocyte–neuron interaction critically determines the direction of the phenotypic outcome.

### *4.2.5. Is this impact determined by the genotype of the neurons?*

To further dissect the interaction, the influence of astrocytic APOE isoforms on neurons of a given genotype was evaluated independently.

Treatment of APOE4 neurons with ACM from APOE3 astrocytes results in higher number and larger area of SYP spots (Fig. 4.8A - A1, A3; Fig. 4.8B - B2, B3), longer neurite length (Fig. 4.9D - D2, D3), brighter nucleus intensity (Fig. 4.10E - E2, E3), but also reduced EEA1 spots fluorescence intensity and smaller EEA1 spots width/length ratio (Fig. 4.11H - H2, H3; Fig. 4.11J - J2, J3) than the APOE3 neurons treated with the same APOE3 ACM.

Similarly, fewer features were altered in APOE4 neurons upon exposure to APOE4 ACM treatment, including larger SYP spot area (Fig. 4.8B - B2, B3), brighter nucleus intensity (Fig. 4.10E - E2, E3), and smaller EEA1 spots width/length ratio (Fig. 4.11J - J1, J2, J3). In addition, APOE4 ACM was associated with a smaller nuclear area in APOE4 neurons compared with APOE3 neurons exposed to the same APOE4 ACM treatment (Fig. 4.10F–F2, F3).

Taken together, under ACM treatments from both APOE3 and APOE4 astrocytes, APOE4 neurons express brighter nucleus intensity and smaller EEA1 spot width/length ratio than APOE3 neurons under the same treatment. Importantly, APOE3 ACM affected a broader range of neuronal phenotypes than APOE4 ACM, suggesting that APOE3 astrocytes secrete more diverse or potent factors, whereas APOE4 astrocytes provide a narrower scope of phenotypic changes.

| Neuronal *APOE* genotypes / Cultured media | APOE3 neurons | APOE4 neurons |
|---|---|---|
| ACM from APOE3 astrocytes | neE3 + cmE3 | neE4 + cmE3 |
| ACM from APOE4 astrocytes | neE3 + cmE4 | neE4 + cmE4 |
| NMM | neE3 + nmm | neE3 + nmm |

***Table 4.1. Experimental groups in ACM culture conditions categorized by neuronal APOE genotype and culture media.*** *The table displays six experimental groups in the ACM experiments. Columns indicate the neuronal APOE genotype—either APOE3 or APOE4 homozygous neurons. Rows represent the three culture conditions: neurons cultured in ACM derived from APOE3 astrocytes, ACM from APOE4 astrocytes, or NMM as a control. This design allows comparison of neuronal morphology influenced by both neuronal genotype and astrocyte-derived ACM.*

| Neuronal *APOE* genotypes / Co-cultured with astrocytes (*APOE* genotypes) | APOE3 neurons | APOE4 neurons |
|---|---|---|
| APOE3 astrocytes | neE3 + astE3 | neE4 + astE3 |
| APOE4 astrocytes | neE3 + astE4 | neE4 + astE4 |

***Table 4.2. Experimental groups in neuron–astrocyte co-culture conditions categorized by neuronal and astrocyte APOE genotypes.*** *The table presents four experimental groups in the co-culture experiments. Columns represent the neuronal APOE genotypes—either APOE3 or APOE4 homozygous neurons. Rows represent the APOE genotype of astrocytes (APOE3 or APOE4) with which the neurons were directly co-cultured. This setup enables analysis of the combined effects of neuronal and astrocyte APOE genotypes on neuronal morphology under direct cell–cell contact conditions.*

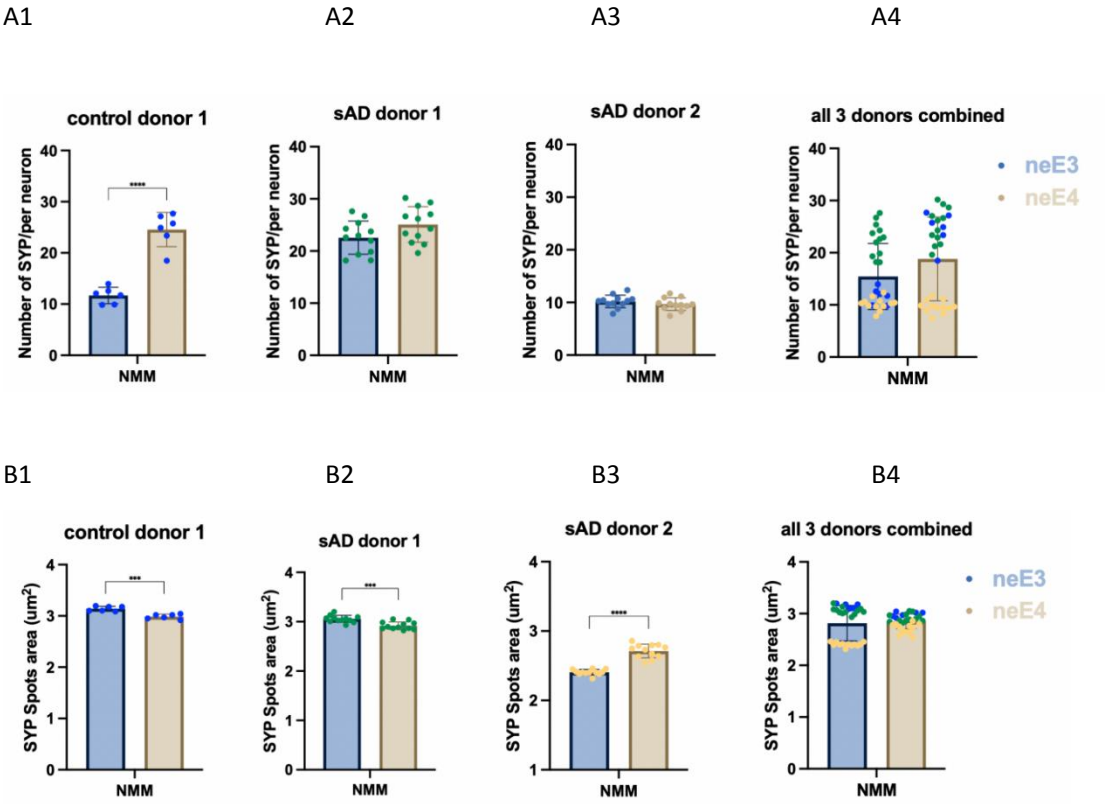



***Fig. 4.1. Synaptic features from monocultures of APOE3 and APOE4 neurons maintained in neuronal maintenance media (NMM).*** *T-test results are presented on selected features extracted by Harmony software. Row A and B represent synaptophysin number and size, respectively. The 1st panel in each row corresponds to control donor 1; the 2nd, sAD donor 1; the 3rd, sAD donor 2; and the 4th panel presents pooled data from all three donors. Dot colors indicate donor identity: blue = control donor 1, green = sAD donor 1, yellow = sAD donor 2. In each panel, bar colour denotes neuronal APOE genotype (blue bars = APOE3 neurons [neE3]; beige bars = APOE4 neurons [neE4]). Error bars represent ±1 SD. Asterisks indicate significant difference from the control group (*p < .05,** p < .01, ***p < .001).*

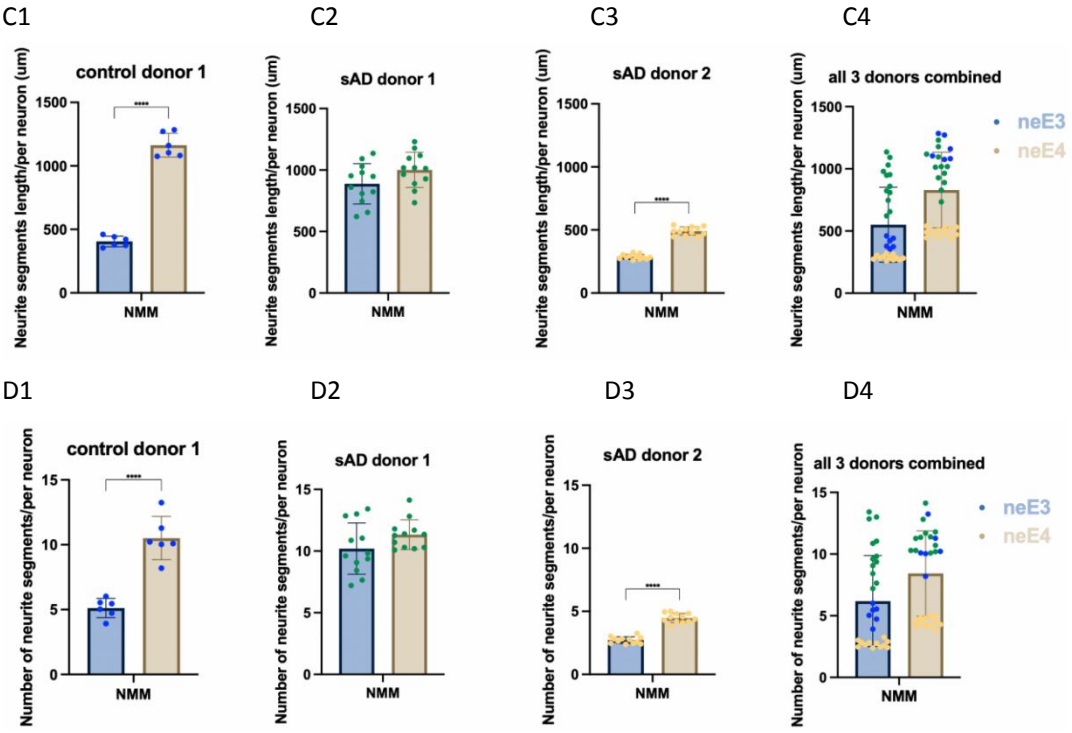



***Fig. 4.2. Neurite morphological features from monocultures of APOE3 and APOE4 neurons maintained in NMM.*** *T-test results are presented on selected features extracted by Harmony software. Row C and D represent neurite number and length, respectively. The 1st panel in each row corresponds to control donor 1; the 2nd, sAD donor 1; the 3rd, sAD donor 2; and the 4th panel presents pooled data from all three donors. Dot colors indicate donor identity: blue = control donor 1, green = sAD donor 1, yellow = sAD donor 2. In each panel, bar colour denotes neuronal APOE genotype (blue bars = APOE3 neurons [neE3]; beige bars = APOE4 neurons [neE4]). Error bars represent ±1 SD. Asterisks indicate significant difference from the control group (*p < .05,** p < .01, ***p < .001).*

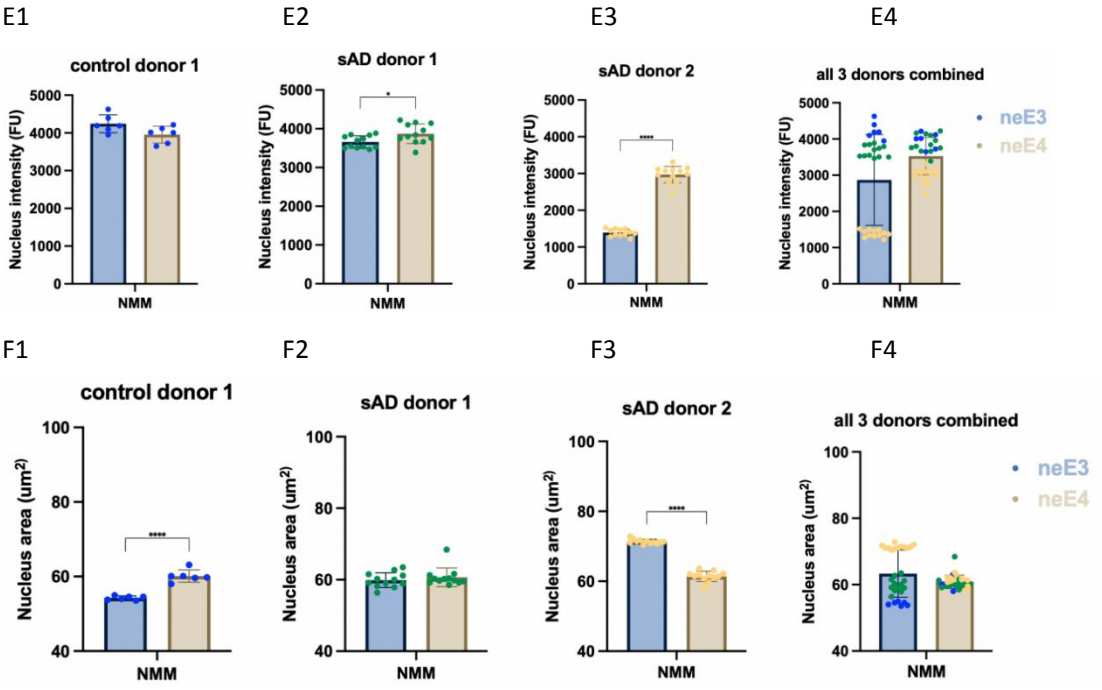



***Fig. 4.3. Nuclear features from monocultures of APOE3 and APOE4 neurons maintained in NMM.*** *T-test results are presented on selected features extracted by Harmony software. Row E and F represent nucleus intensity and size, respectively. The 1st panel in each row corresponds to control donor 1; the 2nd, sAD donor 1; the 3rd, sAD donor 2; and the 4th panel presents pooled data from all three donors. Dot colors indicate donor identity: blue = control donor 1, green = sAD donor 1, yellow = sAD donor 2. In each panel, bar colour denotes neuronal APOE genotype (blue bars = APOE3 neurons [neE3]; beige bars = APOE4 neurons [neE4]). Error bars represent ±1 SD. Asterisks indicate significant difference from the control group (*p < .05,** p < .01, ***p < .001).*

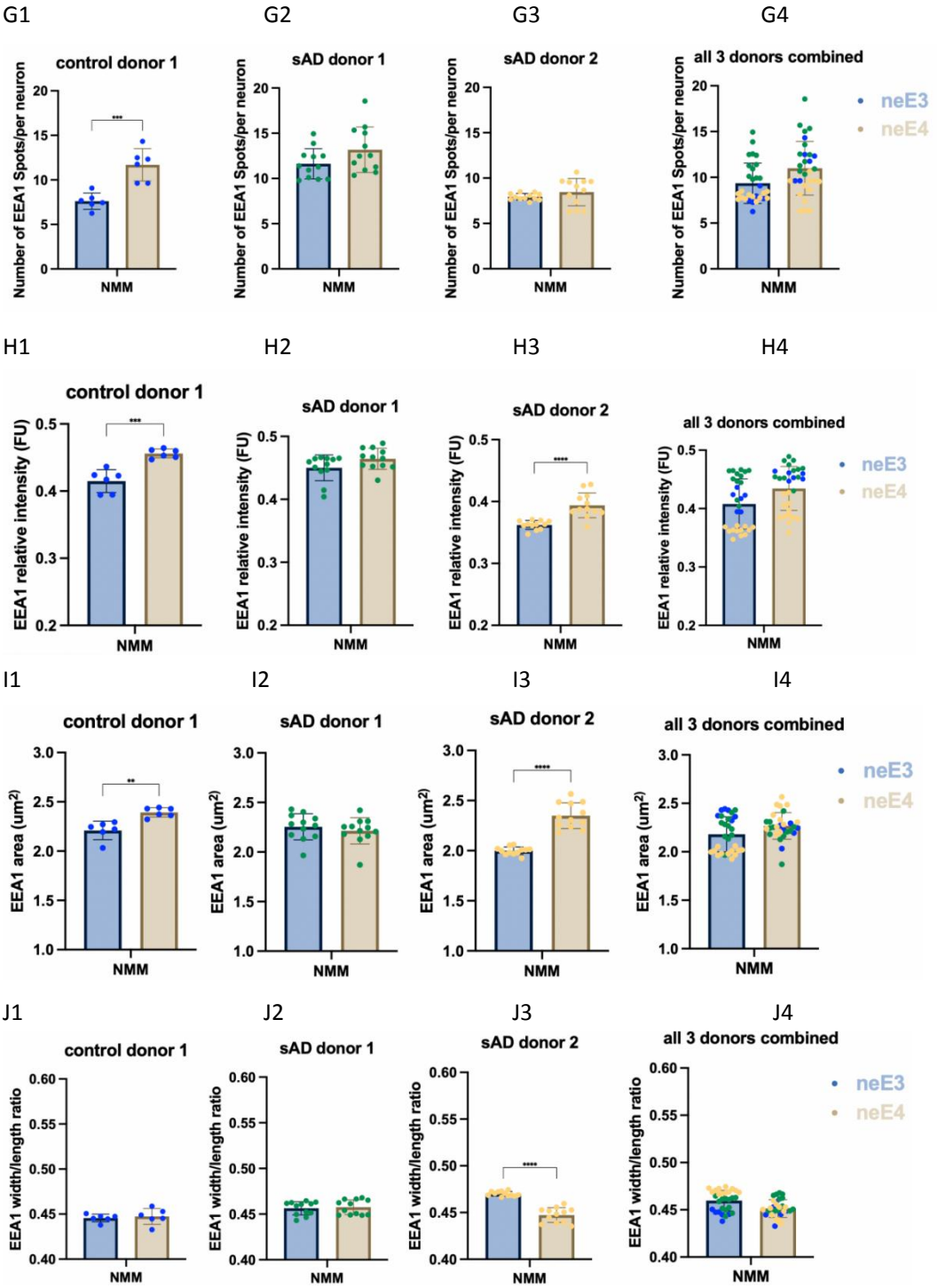



***Fig. 4.4. Early endosomal features from monocultures of APOE3 and APOE4 neurons maintained in NMM.*** *T-test results are presented on selected features extracted by Harmony software. Row G, H, I and J represent early endosomal (EEA1) number, intensity, area, and width-to-length ratio, respectively. The 1st panel in each row corresponds to control donor 1; the 2nd, sAD donor 1; the 3rd, sAD donor 2; and the 4th panel presents pooled data from all three donors. Dot colors indicate donor identity: blue = control donor 1, green = sAD donor 1, yellow = sAD donor 2. In each panel, bar colour denotes neuronal APOE genotype (blue bars = APOE3 neurons*

*[neE3]; beige bars = APOE4 neurons [neE4]). Error bars represent ±1 SD. Asterisks indicate significant difference from the control group (*p < .05,** p < .01, ***p < .001).*

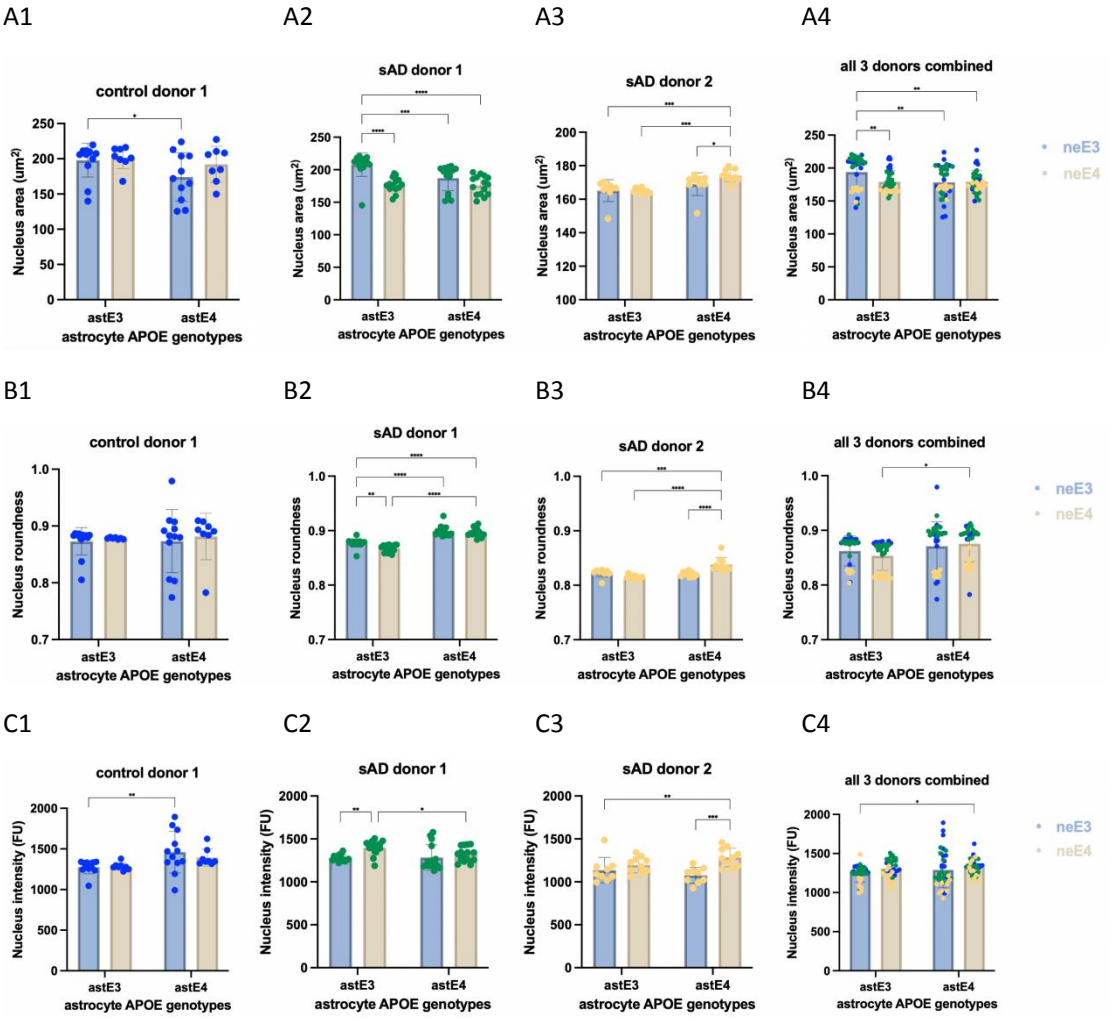



***Fig. 4.5. Nuclear features changes of small molecules astrocytes co-cultured with APOE3 and APOE4 neurons.*** *ANOVA results are presented on selected features extracted by Harmony software. Row A, B and C represent nucleus size, roundness and intensity respectively. The 1st panel in each row corresponds to control donor 1; the 2nd, sAD donor 1; the 3rd, sAD donor 2; and the 4th panel presents pooled data from all three donors. Dot colors indicate donor identity: blue = control donor 1, green = sAD donor 1, yellow = sAD donor 2. In each panel, bar colour denotes astrocytes APOE genotype (blue bars = APOE3 astrocytes [astE3]; beige bars = APOE4 astrocytes [astE4]). Error bars represent ±1 SD. Asterisks indicate significant difference from the control group (*p < .05,** p < .01, ***p < .001).*

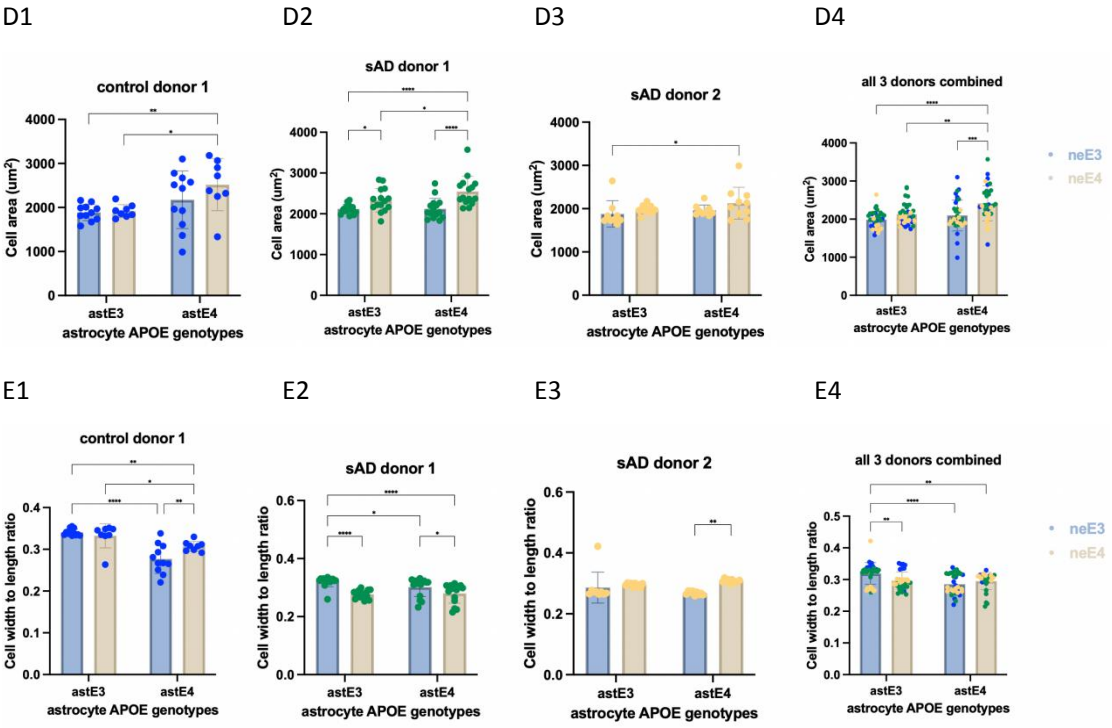



***Fig. 4.6. Cellular morphology changes of from small molecules astrocytes co-cultured with APOE3 and APOE4 neurons.*** *ANOVA results are presented on selected features extracted by Harmony software. Row D and E represent cellular size and width to length ratio respectively. The 1st panel in each row corresponds to control donor 1; the 2nd, sAD donor 1; the 3rd, sAD donor 2; and the 4th panel presents pooled data from all three donors. Dot colors indicate donor identity: blue = control donor 1, green = sAD donor 1, yellow = sAD donor 2. In each panel, bar colour denotes astrocytes APOE genotype (blue bars = APOE3 astrocytes [astE3]; beige bars = APOE4 astrocytes [astE4]). Error bars represent ±1 SD. Asterisks indicate significant difference from the control group (*p < .05,** p < .01, ***p < .001).*

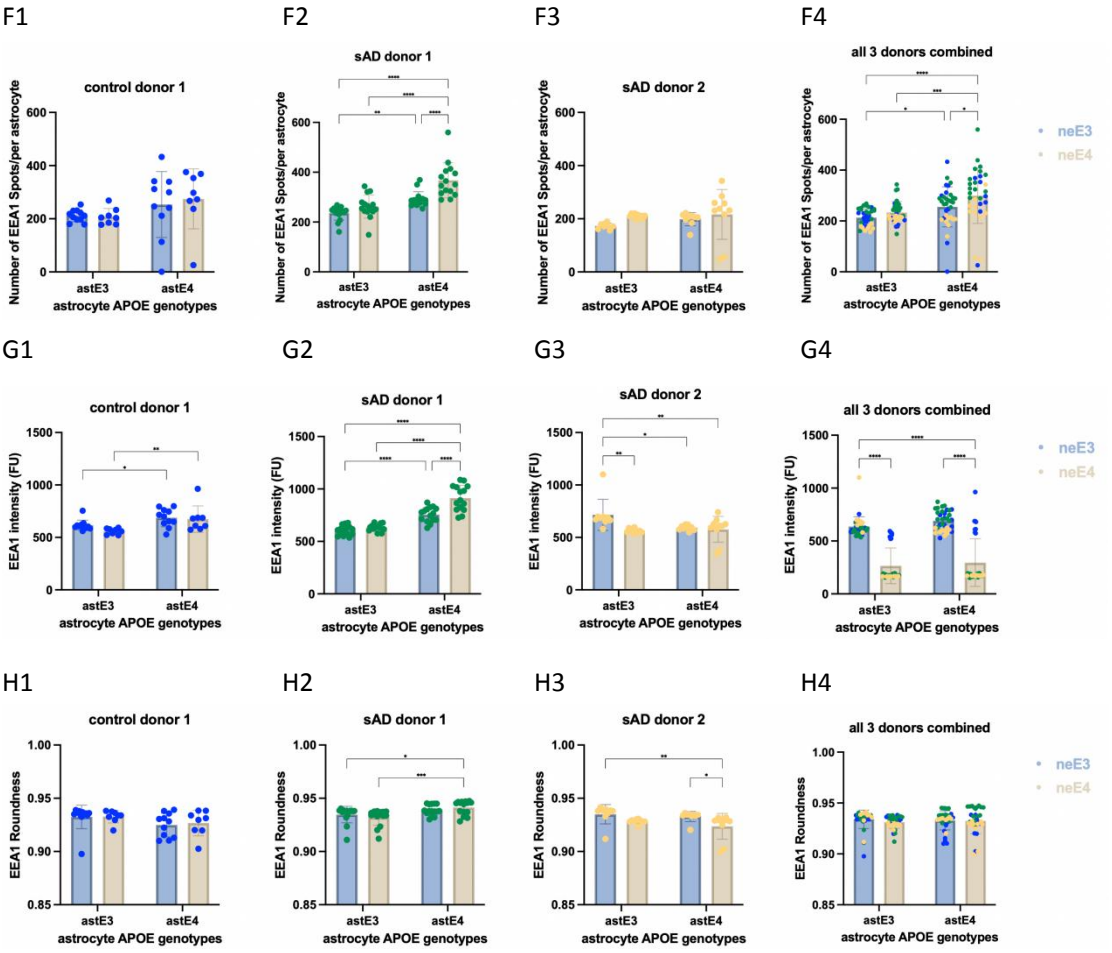



***Fig. 4.7. Early endosomal changes of small molecules astrocytes co-cultured with APOE3 and APOE4 neurons.*** *ANOVA results are presented on selected features extracted by Harmony software. Row F, G and H represent represent early endosomal (EEA1) number, intensity and roundness, respectively. The 1st panel in each row corresponds to control donor 1; the 2nd, sAD donor 1; the 3rd, sAD donor 2; and the 4th panel presents pooled data from all three donors. Dot colors indicate donor identity: blue = control donor 1, green = sAD donor 1, yellow = sAD donor 2. In each panel, bar colour denotes astrocytes APOE genotype (blue bars = APOE3 astrocytes [astE3]; beige bars = APOE4 astrocytes [astE4]). Error bars represent ±1 SD. Asterisks indicate significant difference from the control group (*p < .05,** p < .01, ***p < .001).*

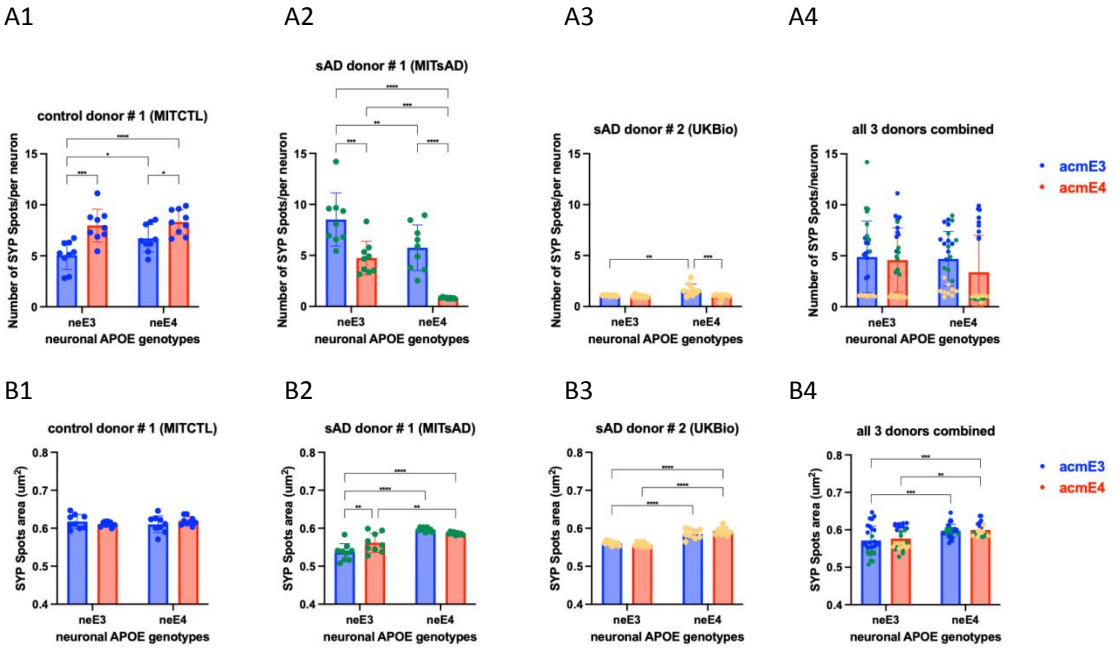



***Fig. 4.8. Synaptic morphological changes of neurons to ACM treatment using astrocytes derived generated through small molecule stimulation.*** *Two-way ANOVA results are presented on selected features extracted by Harmony software from ACM experiments with lentiviral astrocytes. Row A and B represent synaptic features - synaptophysin number and size, respectively. The 1st panel in each row corresponds to control donor 1; the 2nd, sAD donor 1; the 3rd, sAD donor 2; and the 4th panel presents pooled data from all three donors. Dot colors indicate donor identity: blue = control donor 1, green = sAD donor 1, yellow = sAD donor 2. In each panel, bar colour denotes neuronal APOE genotype (blue bars = APOE3 neurons [neE3]; red bars = APOE4 neurons [neE4]). Error bars represent ±1 SD. Asterisks indicate significant difference from the control group (*p < .05,** p < .01, ***p < .001).*

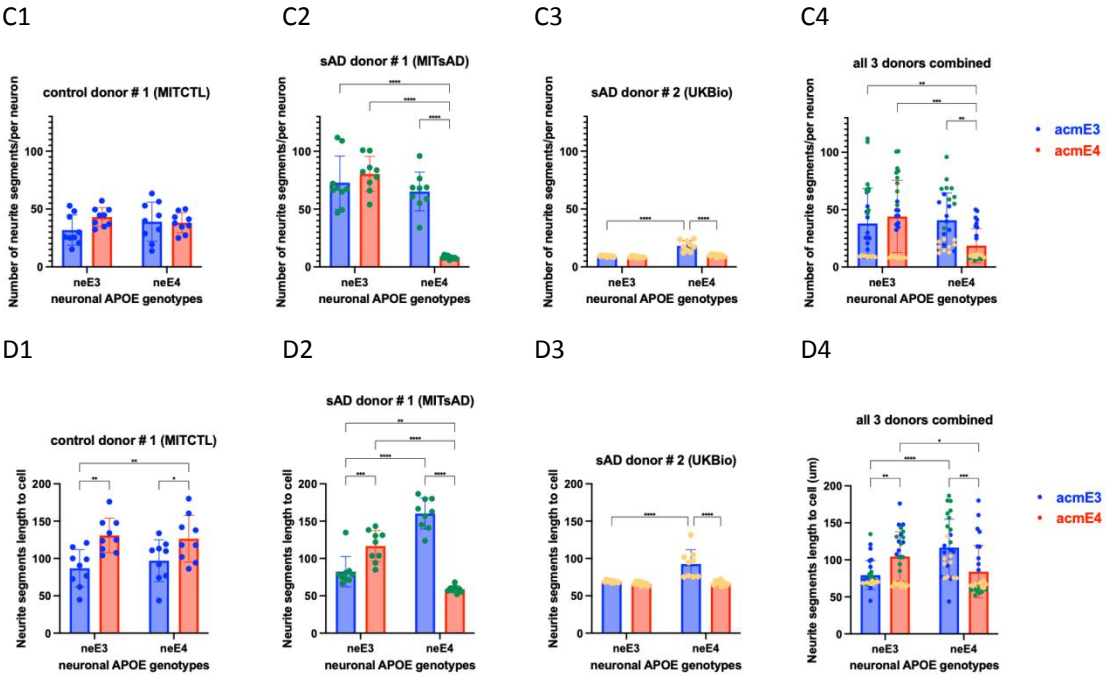



***Fig. 4.9. Neurite morphology changes to ACM treatment using astrocytes generated through small molecule stimulation.*** *Two-way ANOVA results are presented on selected features extracted by Harmony software from ACM experiments with lentiviral astrocytes. Row C and D represent neuronal morphology - neurite number and length, respectively. The 1st panel in each row corresponds to control donor 1; the 2nd, sAD donor 1; the 3rd, sAD donor 2; and the 4th panel presents pooled data from all three donors. Dot colors indicate donor identity: blue = control donor 1, green = sAD donor 1, yellow = sAD donor 2. In each panel, bar colour denotes neuronal APOE genotype (blue bars = APOE3 neurons [neE3]; red bars = APOE4 neurons [neE4]). Error bars represent ±1 SD. Asterisks indicate significant difference from the control group (*p < .05,** p < .01, ***p < .001).*

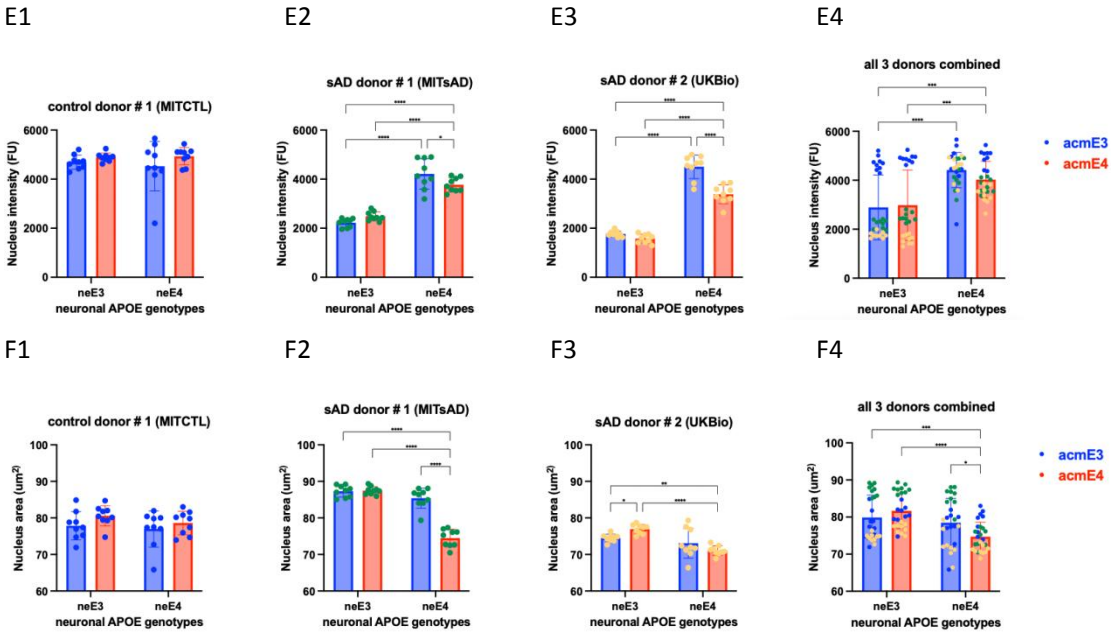



***Fig. 4.10. Neuronal nuclear changes after ACM treatment using astrocytes generated through small molecule stimulation.*** *Two-way ANOVA results are presented on selected features extracted by Harmony software from ACM experiments with lentiviral astrocytes. Row E and F represent nuclear properties - nucleus intensity and size, respectively. The 1st panel in each row corresponds to control donor 1; the 2nd, sAD donor 1; the 3rd, sAD donor 2; and the 4th panel presents pooled data from all three donors. Dot colors indicate donor identity: blue = control donor 1, green = sAD donor 1, yellow = sAD donor 2. In each panel, bar colour denotes neuronal APOE genotype (blue bars = APOE3 neurons [neE3]; red bars = APOE4 neurons [neE4]). Error bars represent ±1 SD. Asterisks indicate significant difference from the control group (*p < .05,** p < .01, ***p < .001).*

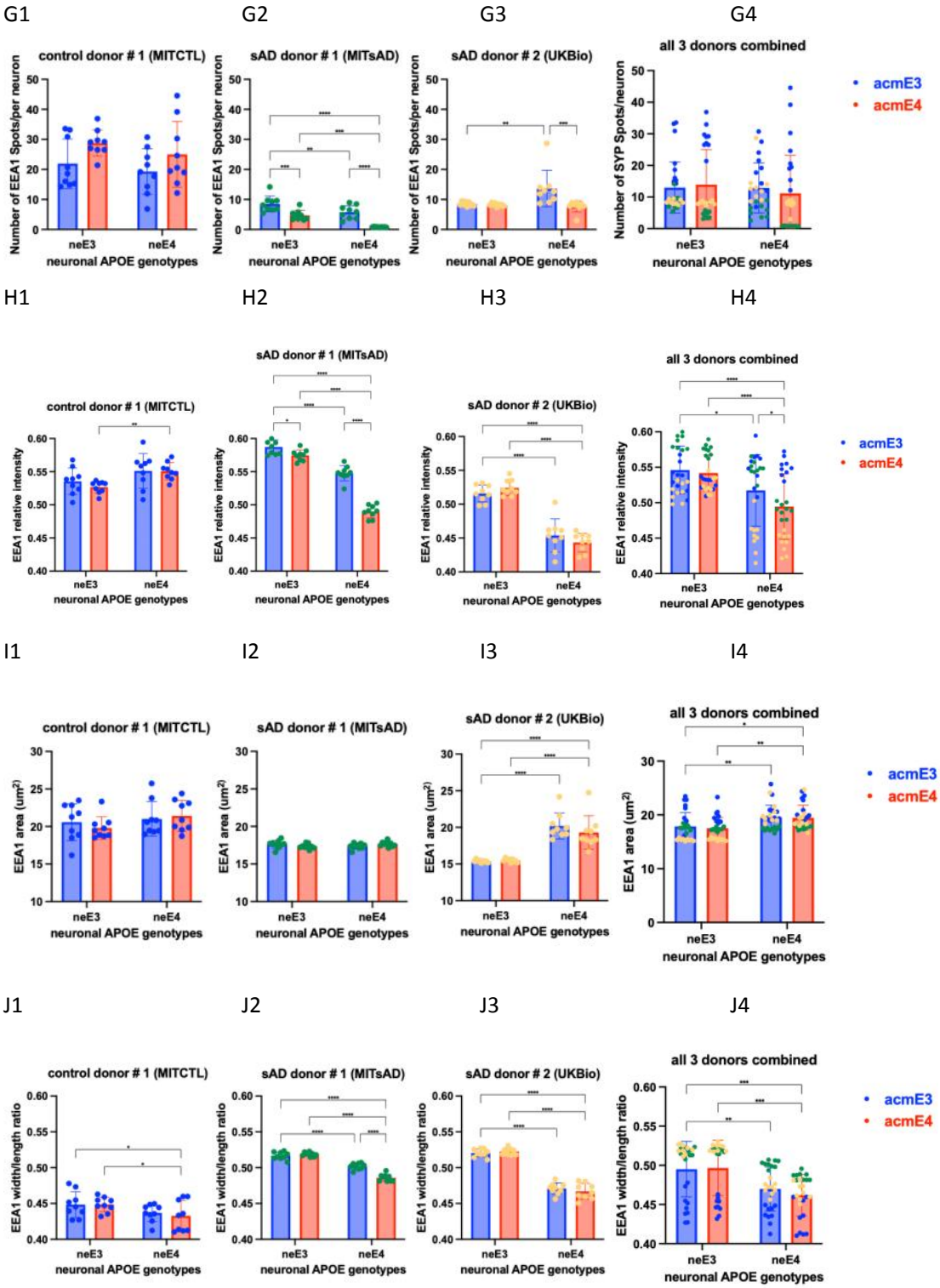



***Fig. 4.11. Neuronal early endosomal changes to ACM treatment using astrocytes generated through small molecule stimulation.*** *Two-way ANOVA results are presented on selected features extracted by Harmony software from ACM experiments with lentiviral astrocytes. Row G, H, I and J represent early endosomal proprieties - EEA1 number, intensity, area, and width-to-length ratio, respectively. The 1st panel in each row corresponds to control donor 1; the 2nd, sAD donor 1;*

*the 3rd, sAD donor 2; and the 4th panel presents pooled data from all three donors. Dot colors indicate donor identity: blue = control donor 1, green = sAD donor 1, yellow = sAD donor 2. In each panel, bar colour denotes neuronal APOE genotype (blue bars = APOE3 neurons [neE3]; red bars = APOE4 neurons [neE4]). Error bars represent ±1 SD. Asterisks indicate significant difference from the control group (*p < .05,** p < .01, ***p < .001).*

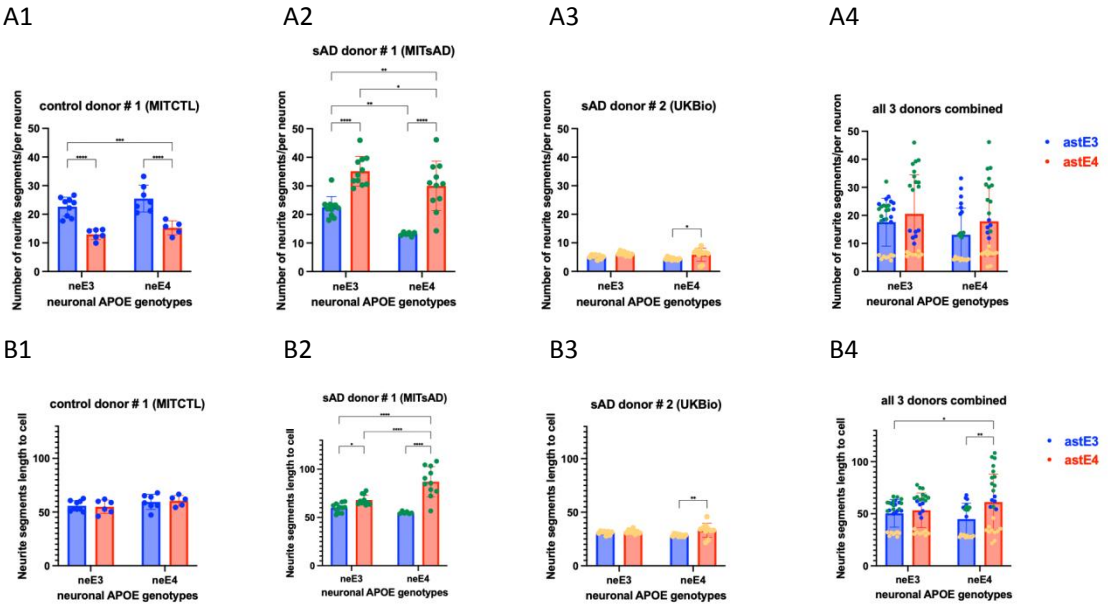



***Fig. 4.12. Neuronal neurite changes after co-culture treatment using astrocytes generated through small molecule stimulation.*** *Two-way ANOVA results are presented on selected features extracted by Harmony software from co-culture experiments with small molecule astrocytes. Row A and B represent neuronal morphology - neurite number and length, respectively. The 1st panel in each row corresponds to control donor 1; the 2nd, sAD donor 1; the 3rd, sAD donor 2; and the 4th panel presents pooled data from all three donors. Dot colors indicate donor identity: blue = control donor 1, green = sAD donor 1, yellow = sAD donor 2. In each panel, bar colour denotes neuronal APOE genotype (blue bars = APOE3 neurons [neE3]; red bars = APOE4 neurons [neE4]). Error bars represent ±1 SD. Asterisks indicate significant difference from the control group (*p < .05,** p < .01, ***p < .001).*

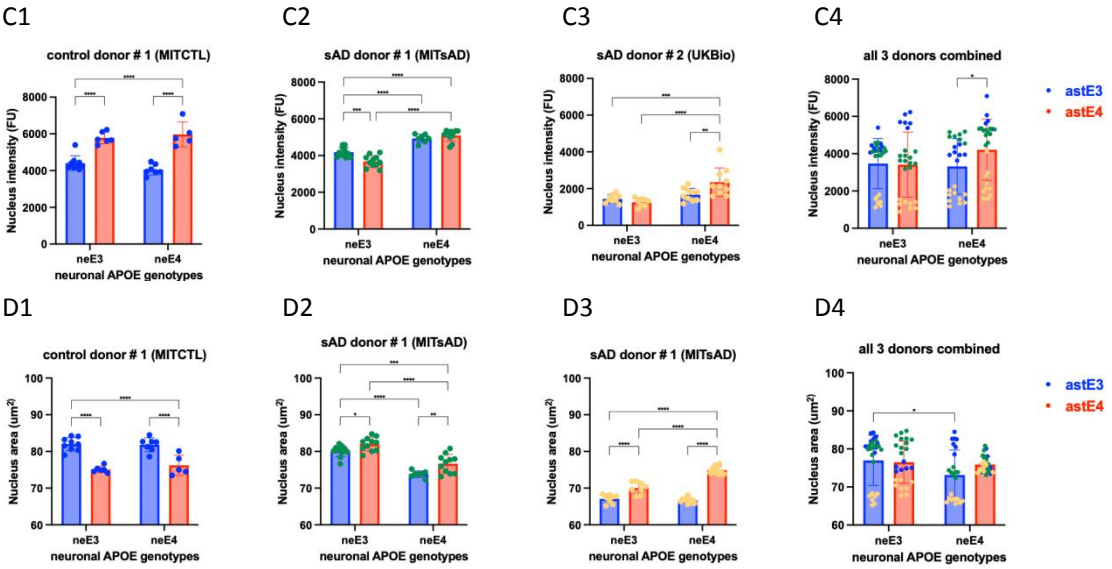



***Fig. 4.13. Neuronal nuclear changes after co-culture treatment using astrocytes generated through small molecule stimulation.*** *Two-way ANOVA results are presented on selected features extracted by Harmony software from co-culture experiments with small molecule astrocytes. Row C and D represent nuclear properties - nucleus intensity and size, respectively. The 1st panel in each row corresponds to control donor 1; the 2nd, sAD donor 1; the 3rd, sAD donor 2; and the 4th panel presents pooled data from all three donors. Dot colors indicate donor identity: blue = control donor 1, green = sAD donor 1, yellow = sAD donor 2. In each panel, bar colour denotes neuronal APOE genotype (blue bars = APOE3 neurons [neE3]; red bars = APOE4 neurons [neE4]). Error bars represent ±1 SD. Asterisks indicate significant difference from the control group (*p < .05,** p < .01, ***p < .001).*

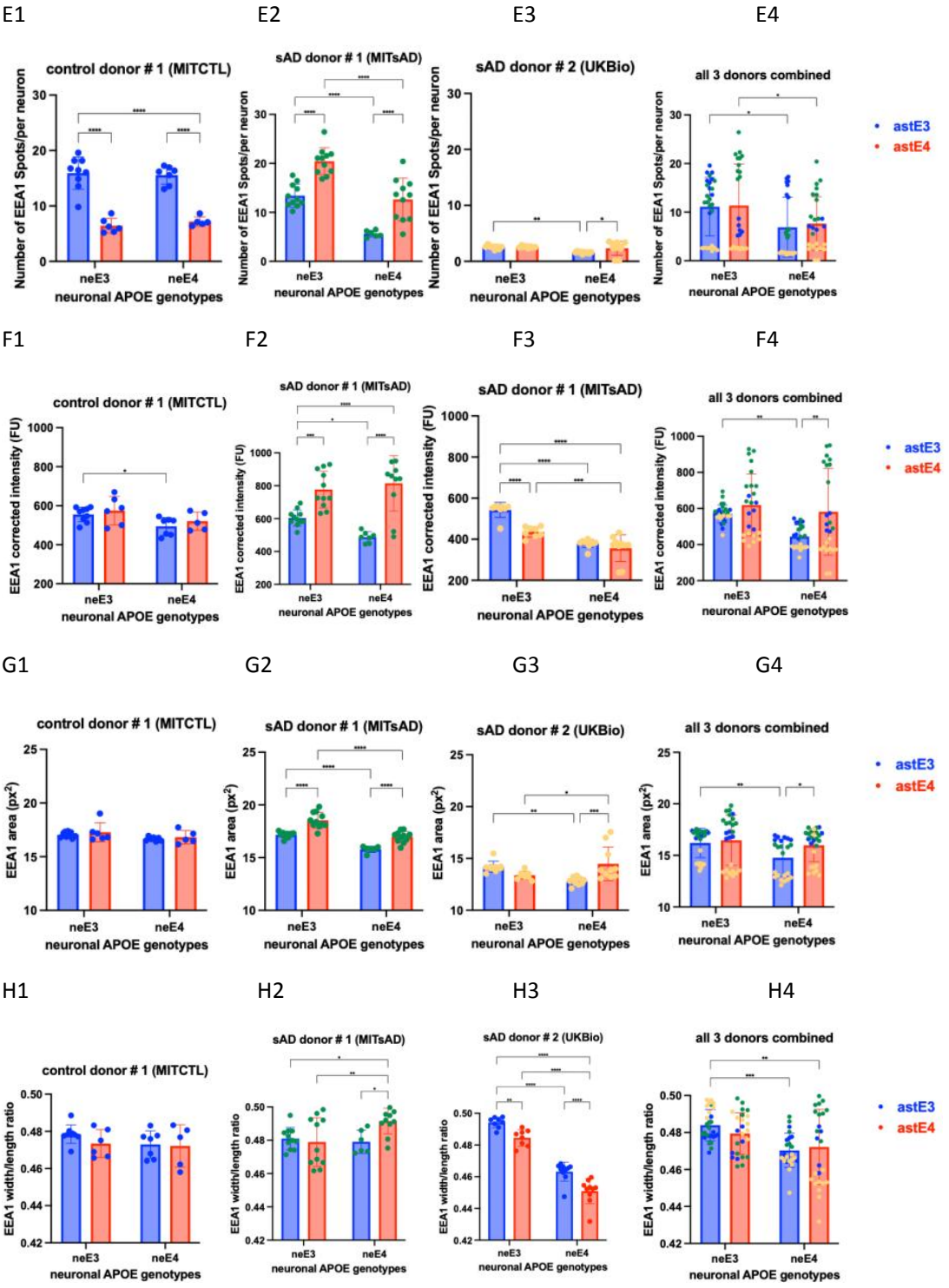



***Fig. 4.14. Early endosomal changes of neurons after co-culture treatment using astrocytes generated through small molecule stimulation.*** *Two-way ANOVA results are presented on selected features extracted by Harmony software from co-culture experiments with small molecule astrocytes. Row E, F, G and H represent early endosomal proprieties - EEA1 number, intensity, area, and width-to-length ratio, respectively. The 1st panel in each row corresponds to control donor 1; the 2nd, sAD donor 1; the 3rd, sAD donor 2; and the 4th panel presents pooled*

*data from all three donors. Dot colors indicate donor identity: blue = control donor 1, green = sAD donor 1, yellow = sAD donor 2. In each panel, bar colour denotes neuronal APOE genotype (blue bars = APOE3 neurons [neE3]; red bars = APOE4 neurons [neE4]). Error bars represent ±1 SD. Asterisks indicate significant difference from the control group (*p < .05,** p < .01, ***p < .001).*

| Results Section | Experiment | Graph Content | Graph ID |
|---|---|---|---|
| Chapter 3. Small-molecule astrocytes | Neuronal baseline in NMM | synaptophysin pathway (SYP number and size) | Fig. 4.1 - rows A & B |
| | | neuronal morphology (neurite number and length) | Fig. 4.2 - rows C & D |
| | | nuclear features (nucleus intensity and size) | Fig. 4.3 - rows E & F |
| | | early endosomal features (EEA1 number, intensity, area, and width-to-length ratio) | Fig. 4.4 - rows G, H, I & J |
| | Astrocytes in co-culture | nuclear features (nucleus area, roundness and intensity) | Fig. 4.5 - rows A, B & C |
| | | cell morphology features (cell area and width to length ratio) | Fig. 4.6 - graph rows D & E |
| | | early endosomal features (EEA1 number, intensity, area, and width-to-length ratio) | Fig. 4.7 - graph rows F, G, & H |
| | Neurons treated with ACM | synaptophysin pathway (SYP number and size) | Fig. 4.8 - rows A & B |
| | | neuronal morphology (neurite number and length) | Fig. 4.9 - rows C & D |
| | | nuclear features (nucleus intensity and size) | Fig. 4.10 - rows E & F |
| | | early endosomal features (EEA1 number, intensity, area, and width-to-length ratio) | Fig. 4.11 - rows G, H, I & J |
| | Neurons in co-culture | neuronal morphology (neurite number and length) | Fig. 4.12 - rows A & B |
| | | nuclear features (nucleus intensity and size) | Fig. 4.13 - graph rows C & D |
| | | early endosomal features (EEA1 number, intensity, and roundness) | Fig. 4.14 - graph rows E, F, G & H |
| Chapter 4. Lentiviral-astrocytes | Astrocytes in co-culture | nuclear features (nucleus area, roundness and intensity) | Fig. 5.1 - rows A, B & C |
| | | cell morphology features (cell area and width to length ratio) | Fig. 5.2 - graph rows D & E |
| | | early endosomal features (EEA1 number, intensity, area, and width-to-length ratio) | Fig. 5.3 - graph rows F, G, & H |
| | Neurons treated with ACM | synaptophysin pathway (SYP number and size) | Fig. 5.4 - graph rows A & B |
| | | neuronal morphology (neurite number and length) | Fig. 5.5 - graph rows C & D |
| | | nuclear features (nucleus intensity and | Fig. 5.6 - graph |

| | | | |
|---|---|---|---|
| | | size) | rows E & F |
| | | early endosomal features (EEA1 number, intensity, area, and width-to-length ratio) | Fig. 5.7 - graph rows G, H, I & J |
| | Neurons in co-culture | synaptophysin pathway (SYP number and size) | Fig. 5.8 - graph rows A & B |
| | | neuronal morphology (neurite number and length) | Fig. 5.9 - graph rows C & D |
| | | nuclear features (nucleus intensity and size) | Fig. 5.10 - graph rows E & F |
| | | early endosomal features (EEA1 number, intensity, area, and width-to-length ratio) | Fig. 5.11 - graph rows G, H, I & J |

***Table 4.3. Overview of the Figures and Feature Categories in ACM and co-culture experiments.*** *This table summarizes the experimental conditions analyzed in Chapter 3 and 4, which combine two astrocyte differentiation protocols, small molecule-based induction and lentiviral-induced overexpression of NfiB transcription factor. The conditions include neurons and astrocytes features as baseline and neurons treated astrocyte-conditioned media (ACM) exposure or direct astrocyte-neuron co-culture.*

*Each figure contains three to four categories of quantitative readouts, representing major morphological features analyzed through high-content imaging. These quantitative features enable comprehensive phenotypic comparisons across neurons with different APOE genotypes and astrocyte treatments, elucidating genotype- and treatment-specific impacts on neuronal and cellular function.*

| 10 neuronal features treated with astrocytes/Ab | | E3 vs. E4 co-cultures | E3 neu vs. E4 neu @NMM | E3 neu vs. E4 neu @ACM E3 | E3 neu vs. E4 neu @ACM E4 | E3 neu @ACM E3 vs. ACM E4 | E4 neu @ACM E3 vs. ACM E4 | E3 neu vs. E4 neu co-cultured with E3 ast | E3 neu vs. E4 neu co-cultured with E4 ast | E3 neu co-cultured with E3 ast vs E4 ast | E4 neu co-cultured with E3 ast vs E4 ast | E3 neu vs. E4 neu @NMM + Ab | E3 neu @ NMM vs. @NMM+ Ab | E4 neu @ NMM vs. @NMM+ Ab | E3 neu vs. E4 neu @ACM+Ab |
|---|---|---|---|---|---|---|---|---|---|---|---|---|---|---|---|
| | | small molecules-astrocytes | | | | | | | | | | | | | |
| 0 | **Variables** | **baseline** | | **same astrocyte APOE** | | **same neuronal APOE** | | **same astrocyte APOE** | | **same neuronal APOE** | | **baseline** | **same astrocyte APOE** | | **same neuronal APOE** |
| 1 | SYP # | ns. | ns. | E4>E3 (1,3) | ns. | ns. | E4<E3 (2,3) | ns. | ns. | ns. | ns. | ns. | ns. | ns. | ns. |
| 2 | SYP area | ns. | E4<E3 (1,2) | E4>E3 (2,3) | E4>E3 (2,3) | ns. | ns. | ns. | ns. | ns. | ns. | ns. | ns. | NMM < NMM+Ab | ns. |
| 3 | Neurite # | ns. | E4>E3 (1,3) | ns. | ns. | ns. | E4<E3 (2,3) | ns. | ns. | ns. | E4>E3 (2,3) | ns. | NMM < NMM+Ab | NMM < NMM+Ab | E4<E3 |
| 4 | Neurite length | ns. | E4>E3 (1,3) | E4>E3 (2,3) | ns. | ns. | E4<E3 (2,3) | ns. | ns. | ns. | E4>E3 (2,3) | E4>E3 | ns. | ns. | E4>E3 |
| 5 | Nucleus intensity | E4>E3 (3/3) | E4>E3 (2,3) | E4>E3 (2,3) | E4>E3 (2,3) | ns. | E4<E3 (2,3) | ns. | E4>E3 (2,3) | ns. | E4>E3 (1,3) | ns. | ns. | ns. | ns. |
| 6 | Nucleus area | E4<E3 (1,2) | ns. | ns. | E4<E3 (2,3) | ns. | ns. | ns. | ns. | E4>E3 (2,3) | E4>E3 (2,3) | ns. | ns. | ns. | ns. |
| 7 | EEA1 # | ns. | ns. | | ns. | ns. | E4<E3 (2,3) | E4<E3 (2,3) | | ns. | E4>E3 (2,3) | ns. | ns. | ns. | ns. |
| 8 | EEA1 intensity | ns. | E4>E3 (1,3) | E4<E3 (2,3) | ns. | ns. | ns. | E4<E3 (1,2,3) | ns. | ns. | ns. | ns. | ns. | NMM < NMM+Ab | ns. |
| 9 | EEA1 area | ns. | E4>E3 (1,3) | ns. | ns. | ns. | ns. | E4<E3 (2,3) | ns. | ns. | E4>E3 (2,3) | ns. | ns. | ns. | ns. |
| 10 | EEA1 (W/L) morphology | ns. | ns. | E4<E3 (2,3) | E4<E3 (1,2,3) | ns. | ns. | ns | ns. | ns. | ns. | ns. | ns. | NMM < NMM+Ab | ns. |

***Table 4.4. Matrix summary of APOE- and context-dependent neuronal phenotypes affected by small-molecules induced astrocytes.***

*Direction and significance of pairwise differences for 10 neuronal readouts across conditions including neuronal APOE genotype (E3 vs E4) and astrocyte context (ACM from E3 or E4 astrocytes or co-culture with E3 or E4 astrocytes). Each cell reports the direction of the effect for the row feature under the column comparison.*

*Notation: Baseline - E3 vs E4 neurons in monocultures or co-cultures. ACM - neurons exposed to astrocyte-conditioned medium from E3 or E4 astrocytes (noted as @ACM E3/E4). Co-culture - neurons directly co-cultured with E3 or E4 astrocytes (co-cultured with E3/E4 astrocytes). NMM - neuronal maturation medium. NMM+Ab - indicates $A\beta_{25-35}$ stress added to NMM (see Methods). E4 > E3 or E4 < E3 - direction of a significant difference (E4 relative to E3). ns - not significant. Numbers in parentheses (e.g.,(1,2,3)) - in which donor the effect was significant (see figures for mapping). EEA1 W/L morphology - early endosome width-to-length ratio.*

## 4.3. Discussion

In this study, neurons derived from *APOE3* and *APOE4* backgrounds showed consistent phenotypic differences, and their morphological features were further shaped by astrocytic genotype and by the mode of interaction (ACM or co-culture), as summarized in Table 4.4. In monoculture, APOE4 neurons exhibited higher number but smaller SYP puncta, more and longer neurites, brighter and larger nuclei, higher number but less bright and larger early endosomes compared to APOE3 neurons. Taken together, these features may indicate that APOE4 neurons undergo altered structural remodeling characterized by increased neurite outgrowth, formation of smaller presynaptic sites, nuclear stress, and changes in endosomal trafficking. The greater number and length of neurites might reflect enhanced sprouting or growth tendencies. First, greater neurite number and length may reflect enhanced sprouting and accelerated growth, consistent with reports that APOE4 influences neuron maturation by causing accelerated but also dysregulated development (Meyer-Acosta et al., 2025). Second, the same morphology may represent compensatory or unstable outgrowth. Concordantly, more numerous but smaller SYP puncta are consistent with a higher incidence of nascent presynaptic sites that have formed but remain immature. However, glia-derived cholesterol carried on APOE lipoproteins has been shown to promote synapse formation and maturation, providing a complementary mechanism likely to be present in ACM (Mauch et al., 2001; Wuerch & Yong, 2025). Specifically, higher numbers and enlarged early endosomes

have been directly implicated as one of the earliest pathological alterations in AD (Cataldo et al., 2000; Lin et al., 2018), providing a point of connection between APOE4-related cellular phenotypes and disease-relevant mechanisms.

Astrocytic treatment further modulated these neuronal features, with effects depending on both astrocyte and neuronal genotype. The baseline differences between APOE3 and APOE4 neurons were directionally conserved under both APOE3- and APOE4-derived ACM (e.g., SYP area and nucleus intensity), although astrocyte genotype was selectively altered in multiple features. For example, SYP number, EEA1 intensity, and neurite length differences appeared only in ACM from APOE3 astrocytes, while nucleus area differences appeared only in ACM from APOE4 astrocytes. In addition, some features not evident at baseline emerged under ACM treatment, such as increased SYP number in ACM E3 or changes in endosomal morphology (width-to-length ratio) in both ACM E3 and ACM E4. These findings suggest that soluble astrocytic factors add new layers of modulation on top of intrinsic neuronal genotype differences, potentially by selectively engaging synaptic and endosomal pathways.

The baseline differences between APOE3 and APOE4 neurons in NMM align with previous findings that endosomal enlargement (Cataldo et al., 2000) and synaptic impairments (Busche & Konnerth, 2016) represent two of the earliest detected changes in AD. Endosomes are crucial hubs where many important players intersect, either in AD pathology or normal neuronal functions, including lipids, APOE, and Aβ (Konings et al., 2023), and their

interaction can subsequently influence the intracellular accumulation of Aβ (Kuszczyk et al., 2013). APOE4 neurons are also shown to have a predisposition to accumulate cholesterol in the endolysosomal system and reduced degradative ability (Nyberg et al., 2025). Notably, neocortical biopsies showed AD pathological brains exhibit dystrophic neurites, including synaptic terminals are accumulated with endosomal compartments (Nixon et al., 2005). Together, alterations in EEA1 intensity and spot geometry implicate early endosomal trafficking steps, pointing to changes in receptor/cargo sorting with downstream consequences for synaptic receptor turnover, lipid transportation, and neurite outgrowth. Although there was no baseline difference, selective decreases in nuclear area after ACM E4 treatment and the increase of intensity in APOE4 neurons were found to be consistent with the view that nuclear architecture is plastic and governed by intracellular mechanics and chromatin state (Calero-Cuenca et al., 2018). In particular, actin–myosin–dependent rearrangements of the perinuclear cytoskeleton and shifts in chromatin compaction associated with stress-responsive transcription could provide a plausible route by which APOE4-associated soluble factors in ACM influence APOE4 neuronal nuclear morphology.

However, although APOE4 is associated with enlarged early endosomes in AD contexts (EEA1/Rab5+) (Cataldo et al., 2000), enlargement alone does not specify functional state (fast recycling to membrane vs. degradative sorting to lysosome). To test the function directly, future work should label early-endosomal pH and determine whether these cargos are retained in APOE4 conditions. If so, the subsequent step would be to see whether

depleting the endosomal pH regulator sodium-hydrogen exchanger 6 (NHE6) corrects early endosomal pH, restores recycling and synaptic functions (Pohlkamp et al., 2021). Moreover, since nucleus intensity and roundness are not specific to any single cellular functions, as changes in these features can arise from diverse states including apoptosis, differentiation, cell-cycle progression, or chromatin remodeling. To enable more precise biological interpretation, future analyses would benefit from coupling nuclear morphology with apoptosis markers or chromatin assays, such that they can reflect apoptosis, differentiation, or cell-cycle stage for more advanced interpretation.

In co-culture with APOE4 astrocytes, the baseline differences between APOE3 and APOE4 neurons were no longer detected except for nucleus intensity, which remained with APOE4 neurons brighter than APOE3 neurons. By contrast, co-culture with APOE3 astrocytes not only removes the baseline differences, but also sometimes produces opposite effects, particularly in endosomal features (number, size, and intensity) in APOE3 neurons. In these cases, differences that were present at baseline (APOE4 > APOE3) reversed direction (APOE3 > APOE4) in the presence of APOE3 astrocytes. These co-culture–specific reversals are most parsimoniously explained by contact-dependent astrocyte–neuron signaling that stabilizes synaptic compartments, such as ephrin–Eph and adhesion pathways (Nishida & Okabe, 2007). These results also imply that direct astrocyte-neuron contact exerts stronger influence than ACM alone, and that APOE3 astrocytes are more capable of reshaping baseline APOE3 vs. APOE4 neuronal differences than APOE4 astrocytes. It is in line with the

finding that direct co-culture with astrocytes was shown to drive markedly greater neurite outgrowth and arbor complexity in purified human retinal ganglion cells than by themselves alone or supplemented with ACM (VanderWall et al., 2019). Particularly, Chiareli et al. (2021) also reported that during embryonic development, direct physical contact with astrocytes serves as a critical 'priming' event for neurons, licensing them to subsequently respond to soluble synaptogenesis factors, which involve key signaling transducers like neurexins, gamma-protocadherins, and neuroligins .

The analysis of the same neuronal genotype exposed to either APOE3 or APOE4 astrocytes highlighted the effect of the APOE genotype as well. In ACM treatment, APOE3 or APOE4 astrocytes had little impact on APOE3 neurons, but APOE4 neurons were more sensitive to astrocytic treatment. For example, APOE4 neurons treated with APOE3 ACM showed reduced SYP number, EEA1 number, neurite number, and nuclear intensity, whereas APOE3 neurons were unaffected by the same treatment. This suggests that APOE4 neurons are more responsive to astrocytic signals, independent of the baseline differences when comparing APOE3 vs. APOE4 neurons.

In co-culture, APOE3 astrocytes were again less affected than APOE4 astrocytes, and for APOE4 neurons, the effects of co-culture were often opposite to those seen with ACM. APOE4 neurons in APOE4 co-culture showed more and longer neurites, brighter and larger nuclei, and more and larger EEA1-positive endosomes compared to the ACM condition.

These outcomes were consistent with the baseline pattern of APOE4 vs. APOE3 neurons, suggesting that direct contact with APOE4 astrocytes does not mask those intrinsic APOE4-associated phenotypes. A key observation is that the direction of astrocytic influence often differed between ACM and co-culture. Soluble factors in ACM treatment in some cases maintained the baseline differences, whereas direct co-culture, particularly with APOE3 astrocytes, tended to reverse them. These results suggest that the mode of astrocyte-neuron communication influences neuronal outcomes. One possible explanation is that ACM primarily reflects secreted factors, while co-culture additionally includes membrane-tethered, contact-dependent cues. Although astrocyte-secreted soluble proteins, such as SPARC-antagonized Hevin (Kucukdereli et al., 2011) and thrombospondins (Christopherson et al., 2005), are found to be crucial in CNS synaptogenesis, ACM lacks juxtacrine signaling, for example ephrin-A3–EphA4 signaling for synapse maturation and stabilization, integrin–PKC signaling triggered by astrocyte contact (Hama et al., 2004), neurexin relocalization that gates synaptogenic responsiveness (Barker et al., 2008; Liao et al., 2024) and astrocytic neuroligins that regulate astrocyte morphogenesis and synaptogenesis (Stogsdill et al., 2017). Consequently, there are chances that signals induced by soluble cues alone tend to remain presynaptically active but postsynaptically silent, unless contact-driven programs including AMPAR responsiveness are engaged (Christopherson et al., 2005).

Multiple limitations should be considered. The morphological features analyzed in the

chapter, including neurite length and branching, synaptic puncta, nuclear morphology, and endosomal parameters, serve as indirect readouts and may not directly correspond to functional outcomes. For example, increased neurite length might represent healthy outgrowth or a compensatory response of immature neurons to pathological stress, and smaller SYP puncta might reflect immature synapses rather than synaptic failure. Without additional functional assays, such as electrophysiology, live-cell trafficking studies, or apoptosis markers, these interpretations remain tentative. Moreover, the molecular mediators underlying the differences between ACM and co-culture remain unknown. Proteomic analysis of astrocyte secretomes, single-cell transcriptomics of astrocytes in co-culture, or targeted perturbation of signaling pathways could help identify the mechanisms. Candidate cues can be defined by comparative proteomics that contrasts the ACM secretome with the astrocyte surface proteins engaged specifically in co-culture, using mass spectrometry following cell-surface restricted proximity labeling. In parallel, single-cell multi-omics (e.g., CITE-seq) can be used to map contact-induced astrocyte proteins. Afterward, targeted perturbations can be applied to confirm the necessity of certain pathways that are absent under ACM.

Finally, while both small molecule- and lentiviral-induced astrocytes were examined, these protocols may not capture the full spectrum of astrocyte diversity *in vivo*, and extending differentiation timelines or incorporating region-specific astrocyte subtypes would provide further insight. A meaningful extension would specify regionally patterned astrocyte

identities (based on their functional markers, regional specificity or reactivity) by validating subtype fidelity using single-cell atlases to map region-specific astrocytes. Function would be benchmarked using measurements including EAAT2/GLT-1-mediated glutamate uptake, calcium imaging, Kir4.1-dependent $K^+$ buffering and lactate assay. Together, these steps would yield region-appropriate, better-matured astrocyte cohorts whose contact-dependent versus soluble influences on neuronal phenotypes can be tested in matched ACM and co-culture formats.

This chapter first defines how APOE genotype and astrocyte-derived signals shape neuronal phenotypes, highlighting APOE4-linked sensitivity and showing that direct contact- versus secretome-dependent cues remodel lipid handling, endosomal trafficking, and synaptic structure in the neurons. Building on this, it has the potential to translate these insights into a high-content drug screening platform, delivering a structured, scalable readout panel with stratification rules and rescue predictions for high-content imaging; while pathway-specific functional assays remain essential to confirm physiological impact, the framework sets the primary bases for pharmacodynamic assessment and donor/genotype-informed trial design and directs a clear roadmap for the next functional studies. This integrative approach would strengthen the interpretation of iPSC-based models and enhance their utility for uncovering APOE-related mechanisms in AD.

# Chapter 5: The effects of lentiviral-induced astrocytes on neuronal phenotype

## 5.1. Introduction

As mentioned above, to overcome the extended time required for astrocyte generation using small-molecule-induced astrocytes, the lentiviral induction strategy was adopted to accelerate astrocyte specification and maturation. The lentiviral induction strategy provided a shorter and more practical workflow for generating astrocytes for high-content imaging and quantitative morphological analysis. Previous studies using transcription factor-based astrocyte induction have reported rapid and reproducible generation of astrocyte populations (Sloan et al., 2017; Tchieu et al., 2019). In the present study, although the lentiviral-induced cultures appeared visually more consistent during routine culture, population homogeneity was not directly or quantitatively compared with the small-molecule-induced astrocytes in this study; therefore, this observation is not interpreted as evidence of greater biological homogeneity. The lentiviral induction strategy provided a shorter and more practical workflow for generating astrocytes for high-content imaging and quantitative morphological analysis. Taken together, although initially small-molecule–induced astrocytes were established, the lentiviral overexpression approach provided a practical, reproducible platform for downstream ACM, co-culture, and potential drug-screening experiments (Krencik & Zhang, 2011).

## 5.2. Results

### *5.2.1. What are the baseline morphological and molecular differences between APOE3 and APOE4 neurons and astrocytes, and how do these differences manifest in monoculture and co-culture conditions?*

As described in the Methods, high-content imaging was employed to extract cellular and molecular features using Harmony software (Fig 2.4 & 2.5). A total of 45 features were extracted from four fluorescence channels, which labeled nuclei, cytoskeleton, early endosomes, and synaptophysin. Among these, representative features were identified by a random forest algorithm as the most informative for the ML classification decisions. These selected features are visualized for both ACM and co-culture experiments, using astrocytes derived via either small molecule induction or lentiviral methods (Table 4.3). Within each section, the features are grouped based on the fluorescence channels, representing key cellular pathways. For each feature, 4 graphs are presented: two-way ANOVA results performed individually for each donor (3 donors total), plus a combined analysis including all donors.

To begin, it is of particular interest to characterize the baseline morphological and molecular differences between APOE3 and APOE4 neurons and astrocytes, and to determine how these differences are manifested under monoculture versus co-culture conditions.

In monocultures of astrocytes bearing either the *APOE*3 or *APOE*4 genotype cultured in control medium, APOE4 astrocytes demonstrated lower nuclear (Fig. 6.10E - E2, E3, *in the*

*next chapter*) and EEA1 roundness (Fig. 6.12J - J1, J2, J3, *in the next chapter*), along with increased cytoplasmic width-to-length ratio (Fig. 6.9B - B1, B3, *in the next chapter*), BODIPY intensity (Fig. 6.11F - F1, F2, F3 *in the next chapter*), and EEA1 intensity (Fig. 6.12I - I1, I3 *in the next chapter*) relative to APOE3 astrocytes. These results indicate that APOE isoforms modulate nuclear morphology, cytoplasmic structure, neutral lipid accumulation, and early endosomal morphology in astrocytes.

In co-cultures where neurons and astrocytes shared the same *APOE* genotype, neurons from 2 out of 3 (2/3) donors or all 3 donors in APOE4 co-cultures exhibited longer neurite length (Fig. 5.9D - D1, D2, D3), higher number of SYP spots, early endosomes and neurites (Fig. 5.8A - A2, A3; Fig. 5.11G - G2, G3; Fig. 5.9C - C2, C3), brighter nucleus intensity (Fig. 5.10E - E2, E3), and larger area of nucleus and EEA1 spots (Fig. 5.10F - F1, F2; Fig. 5.11J -J1, J3), but smaller synaptophysin size (Fig. 5.8B - B1, B2) and reduced EEA1 spots intensity (Fig. 5.11H - H1, H3) compared to APOE3 co-cultures. In co-cultures, astrocytes from 2/3 donors in APOE4 co-cultures showed more rounded nucleus (Fig. 5.1B - B1, B3) then in APOE3 co-cultures. These findings suggest that *APOE* genotype influences neuron-astrocyte interactions, particularly in pathways related to neurite development, endosomal processing, and synaptophysin expression.

In summary, genotype-dependent differences were more pronounced in astrocytes than in neurons.

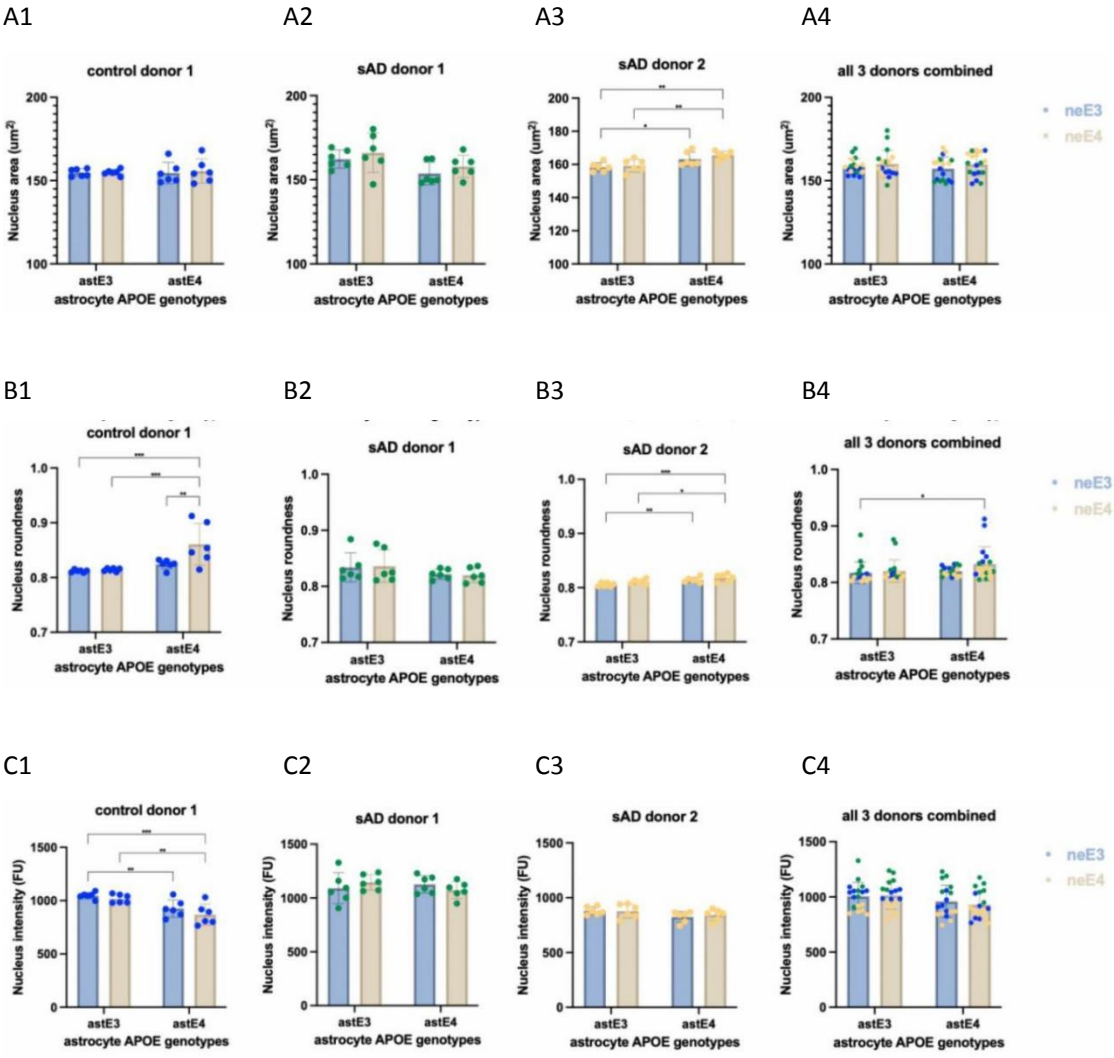



***Fig. 5.1. Nuclear features from APOE3 and APOE4 lentiviral astrocytes co-cultured with neurons.*** *ANOVA results are presented on selected features extracted by Harmony software. Rows A, B and C represent nucleus size, roundness and intensity respectively. The 1st panel in each row corresponds to control donor 1; the 2nd, sAD donor 1; the 3rd, sAD donor 2; and the 4th panel presents pooled data from all three donors. Dot colors indicate donor identity: blue = control donor 1, green = sAD donor 1, yellow = sAD donor 2. In each panel, bar colour denotes neuronal APOE genotype (blue bars = APOE3 neurons [neE3]; beige bars = APOE4 neurons [neE4]). Error bars represent ±1 SD. Asterisks indicate significant difference from the control group (*p < .05,** p < .01, ***p < .001).*

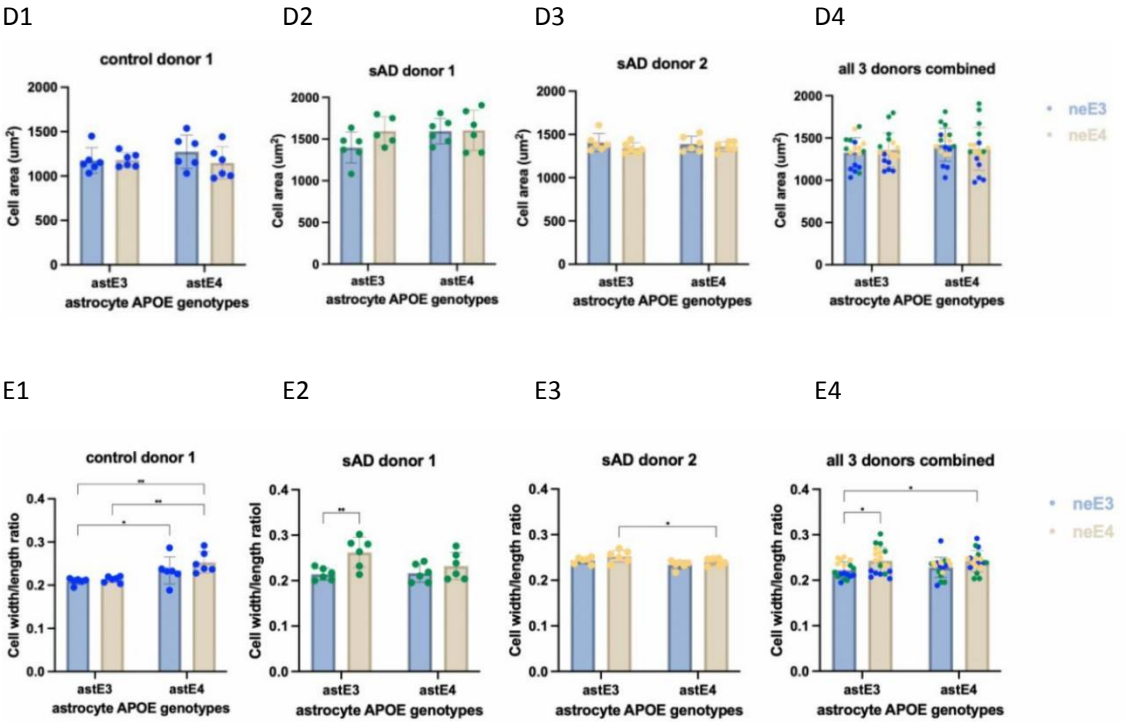



***Fig. 5.2. Cellular morphological features from APOE3 and APOE4 lentiviral astrocytes co-cultured with neurons.*** *ANOVA results are presented on selected features extracted by Harmony software. Rows D and E represent cellular size and width to length ratio respectively. The 1st panel in each row corresponds to control donor 1; the 2nd, sAD donor 1; the 3rd, sAD donor 2; and the 4th panel presents pooled data from all three donors. Dot colors indicate donor identity: blue = control donor 1, green = sAD donor 1, yellow = sAD donor 2. In each panel, bar colour denotes neuronal APOE genotype (blue bars = APOE3 neurons [neE3]; beige bars = APOE4 neurons [neE4]). Error bars represent ±1 SD. Asterisks indicate significant difference from the control group (*p < .05,** p < .01, ***p < .001).*

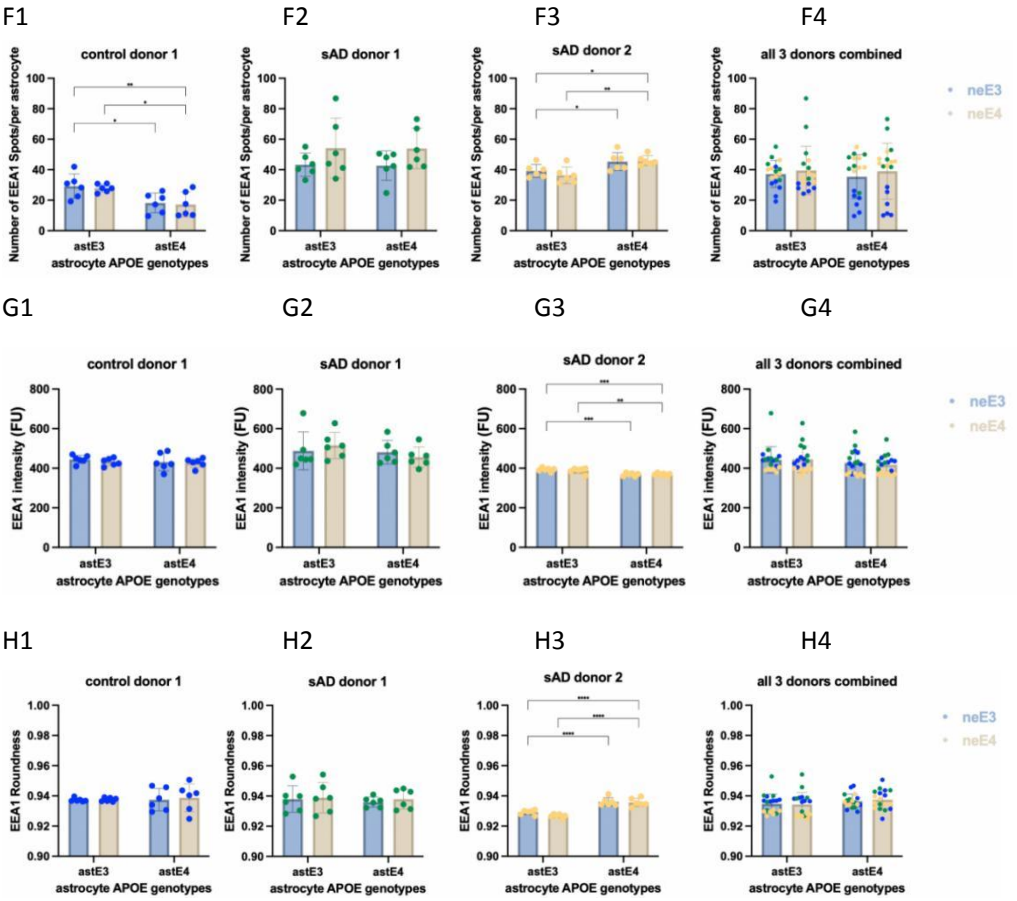



***Fig. 5.3. Early endosomal features from APOE3 and APOE4 lentiviral astrocytes co-cultured with neurons.*** *ANOVA results are presented on selected features extracted by Harmony software. Rows F, G and H represent represent early endosomal (EEA1) number, intensity and roundness, respectively. The 1st panel in each row corresponds to control donor 1; the 2nd, sAD donor 1; the 3rd, sAD donor 2; and the 4th panel presents pooled data from all three donors. Dot colors indicate donor identity: blue = control donor 1, green = sAD donor 1, yellow = sAD donor 2. In each panel, bar colour denotes neuronal APOE genotype (blue bars = APOE3 neurons [neE3]; beige bars = APOE4 neurons [neE4]). Error bars represent ±1 SD. Asterisks indicate significant difference from the control group (*p < .05,** p < .01, ***p < .001).*

### *5.2.2. Do astrocytes influence the differences between APOE3 and APOE4 neurons?*

The presence of astrocytes does not affect the baseline differences observed between APOE3 and APOE4 neurons. For instance, when neurons were treated with either APOE3 or APOE4 astrocytes by ACM or co-culture, genotype-specific differences in neurite length (previously observed under monoculture conditions) remained statistically significant, including APOE4 displaying longer neurites (Fig. 5.5D- D1, D3; Fig. 5.9D - D1, D3). When neurons were treated with either APOE3 or APOE4 ACM, APOE4 neurons express higher number of neurites (Fig. 5.5C- C1, C2, C3). Moreover, in both APOE3 and APOE4 ACM treatments, APOE4 neurons consistently exhibited brighter nuclear intensity (Fig. 5.6E - E2, E3). In co-culture conditions, APOE4 neurons were further associated with larger EEA1 spots and higher number of neurites (Fig. 5.11I - I1, I3; Fig. 5.9C -C1, C3).

Besides the impact on the neuronal baseline differences mentioned above, when treated with APOE3 ACM or co-cultured with APOE4 astrocytes, APOE4 neurons are associated with higher number of early endosomes (Fig. 5.7G - G1, G3; Fig. 5.11G - G1, G3). When co-cultured with APOE4 astrocytes, APOE4 neurons express higher number of SYP spots (Fig. 5.8A - A2, A3) than APOE3 neurons co-cultured with APOE4 astrocytes.

However, it is worth noting that in either APOE3 or APOE4 ACM treatments, APOE4 neurons showed smaller early endosomes compared with APOE3 neurons under the same treatment

(Fig.5.7I - I1, I2); when co-cultured with APOE3 astrocytes, APOE4 neurons express reduced fluorescence intensity of early endosomes (Fig.5.11H - H1, H3); when co-cultured with APOE3 astrocytes, APOE4 neurons show larger SYP spots area (Fig. 5.8B - B2, B3;) thereby reversing the original genotype-specific differences observed in monoculture.

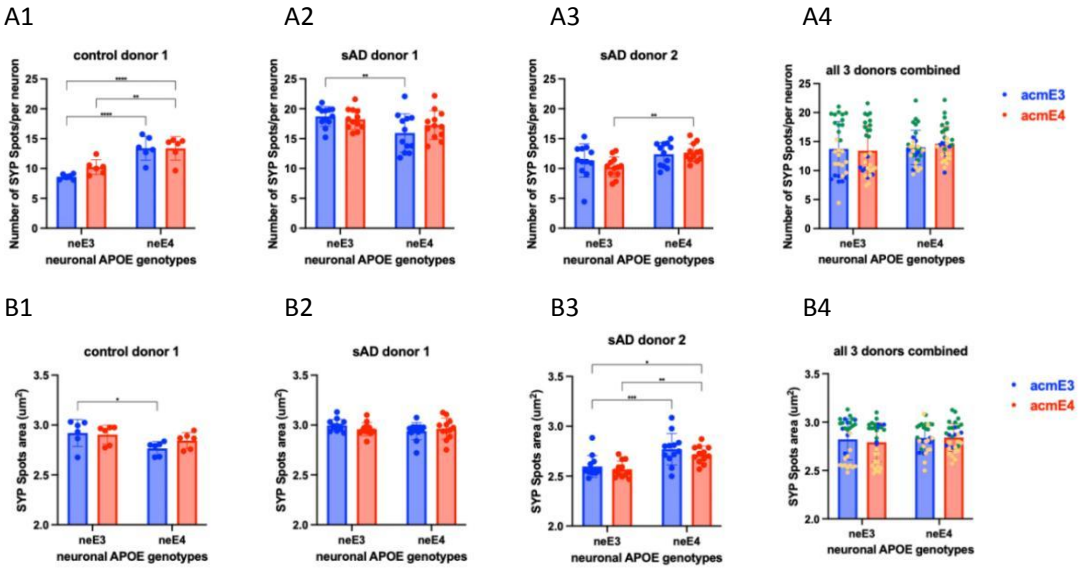



***Fig. 5.4. Synaptic morphology changes to ACM treatment using astrocytes derived via lentiviral induction.*** *Two-way ANOVA results are presented on selected features extracted by Harmony software from ACM experiments with lentiviral astrocytes. Rows A and B represent synaptic features - synaptophysin number and size, respectively. The 1st panel in each row corresponds to control donor 1; the 2nd, sAD donor 1; the 3rd, sAD donor 2; and the 4th panel presents pooled data from all three donors. Dot colors indicate donor identity: blue = control donor 1, green = sAD donor 1, yellow = sAD donor 2. In each panel, bar colour denotes neuronal APOE genotype (blue bars = APOE3 neurons [neE3]; red bars = APOE4 neurons [neE4]). Error bars represent ±1 SD. Asterisks indicate significant difference from the control group (*p < .05,** p < .01, ***p < .001).*

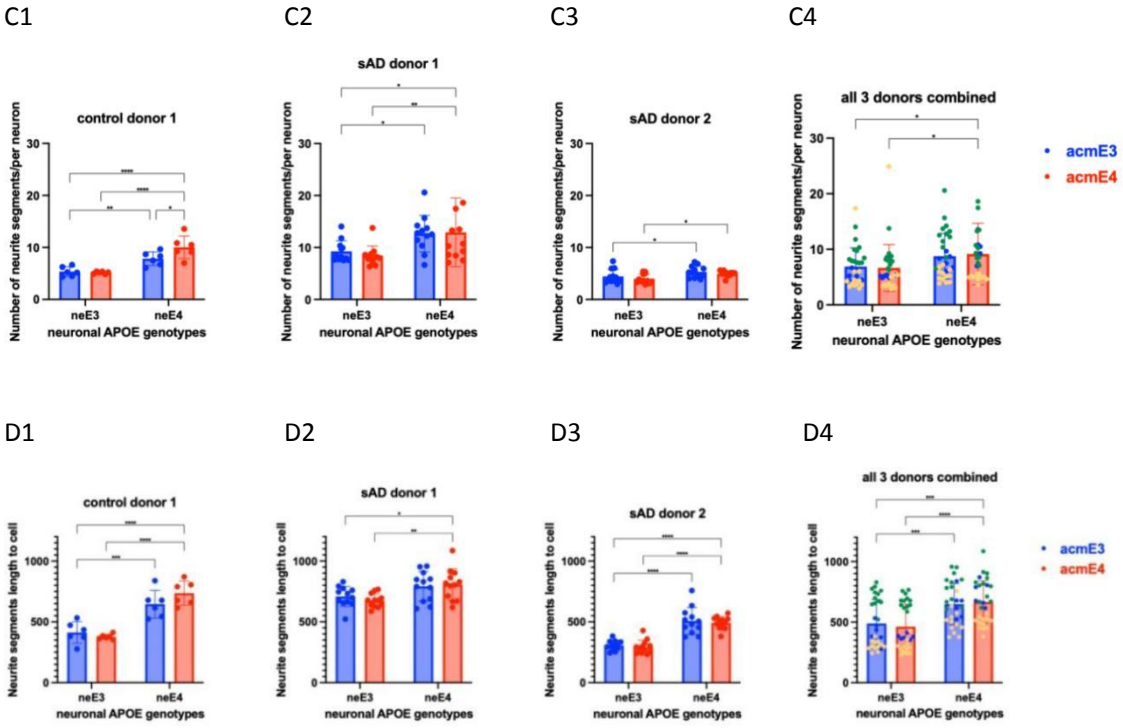



***Fig. 5.5. Neurites changes to ACM treatment using astrocytes derived via lentiviral induction.*** *Two-way ANOVA results are presented on selected features extracted by Harmony software from ACM experiments with lentiviral astrocytes. Rows C and D represent neuronal morphology - neurite number and length, respectively. The 1st panel in each row corresponds to control donor 1; the 2nd, sAD donor 1; the 3rd, sAD donor 2; and the 4th panel presents pooled data from all three donors. Dot colors indicate donor identity: blue = control donor 1, green = sAD donor 1, yellow = sAD donor 2. In each panel, bar colour denotes neuronal APOE genotype (blue bars = APOE3 neurons [neE3]; red bars = APOE4 neurons [neE4]). Error bars represent ±1 SD. Asterisks indicate significant difference from the control group (*p < .05,** p < .01, ***p < .001).*

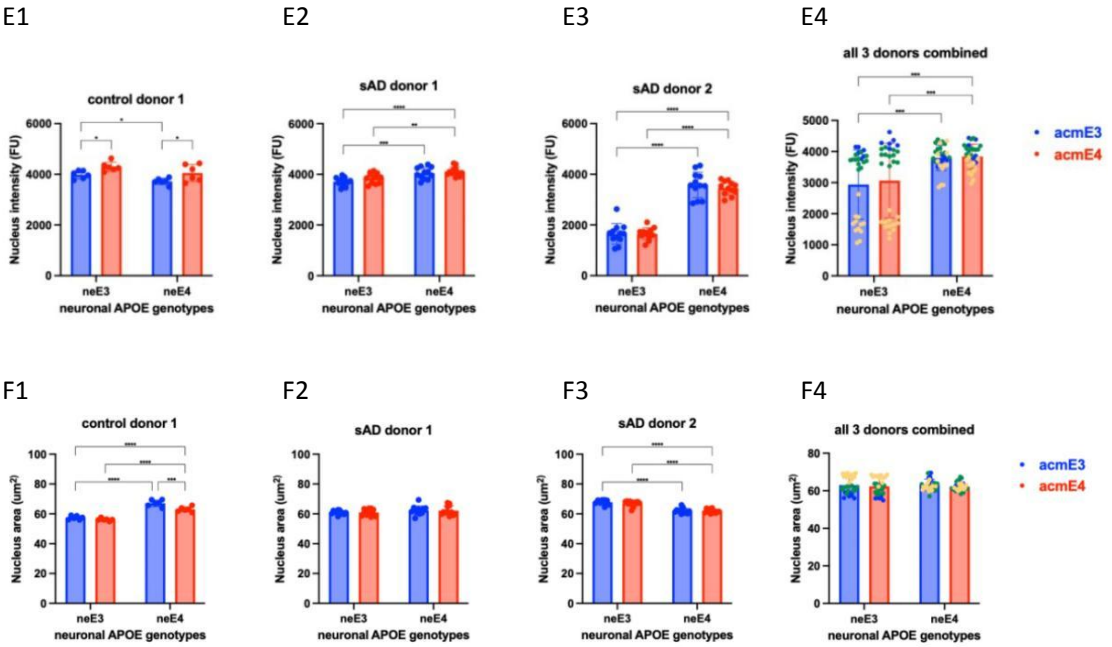



***Fig. 5.6. Neuronal nucleus changes to ACM treatment using astrocytes derived via lentiviral induction.*** *Two-way ANOVA results are presented on selected features extracted by Harmony software from ACM experiments with lentiviral astrocytes. Rows E and F represent nuclear properties - nucleus intensity and size, respectively. The 1st panel in each row corresponds to control donor 1; the 2nd, sAD donor 1; the 3rd, sAD donor 2; and the 4th panel presents pooled data from all three donors. Dot colors indicate donor identity: blue = control donor 1, green = sAD donor 1, yellow = sAD donor 2. In each panel, bar colour denotes neuronal APOE genotype (blue bars = APOE3 neurons [neE3]; red bars = APOE4 neurons [neE4]). Error bars represent ±1 SD. Asterisks indicate significant difference from the control group (*p < .05,** p < .01, ***p < .001).*

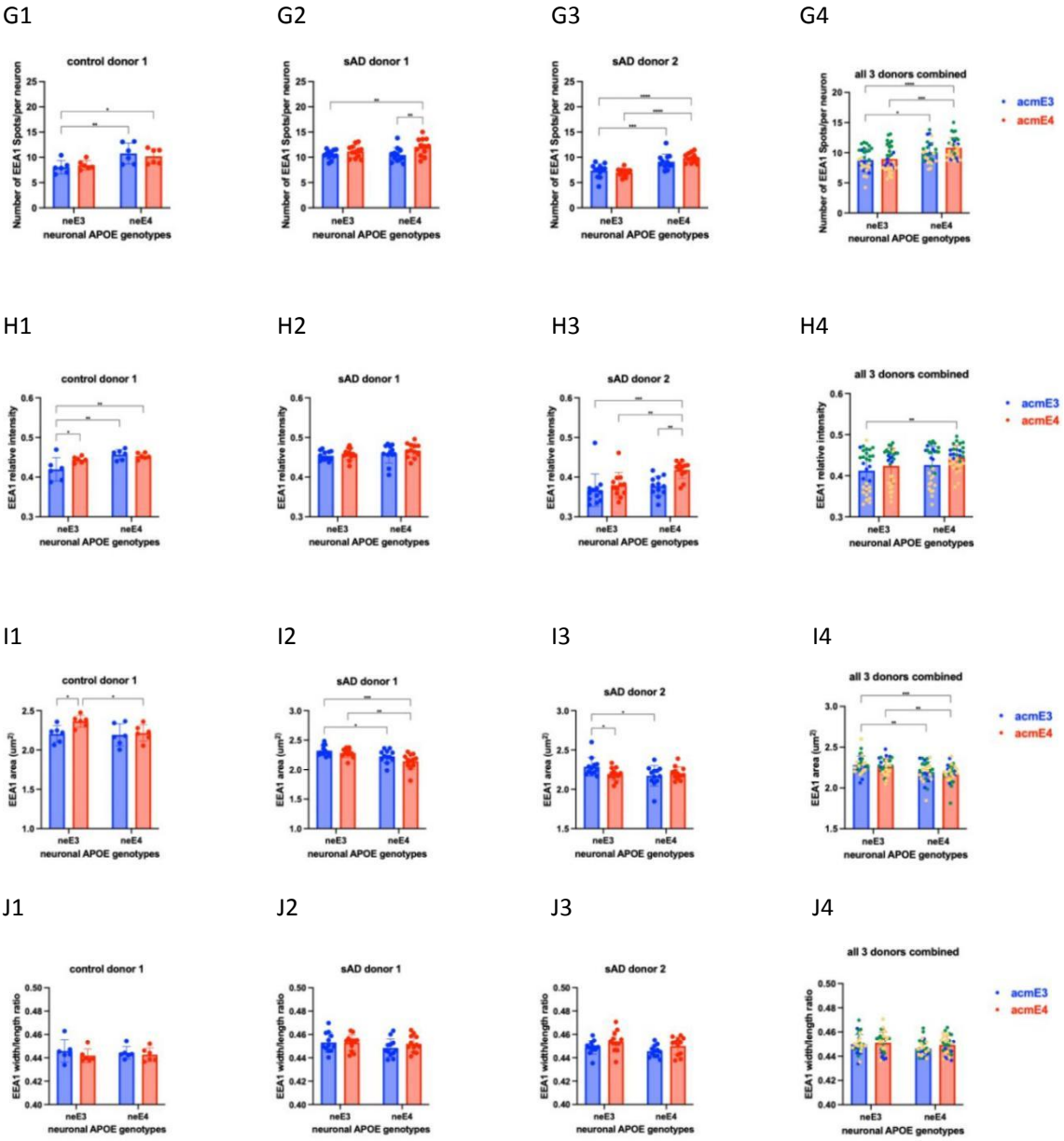



***Fig. 5.7. Early endosomal changes to ACM treatment using astrocytes derived via lentiviral induction.*** *Two-way ANOVA results are presented on selected features extracted by Harmony software from ACM experiments with lentiviral astrocytes. Rows G, H, I and J represent early endosomal proprieties - EEA1 number, intensity, area, and width-to-length ratio, respectively. The 1st panel in each row corresponds to control donor 1; the 2nd, sAD donor 1; the 3rd, sAD donor 2; and the 4th panel presents pooled data from all three donors. Dot colors indicate donor identity: blue = control donor 1, green = sAD donor 1, yellow = sAD donor 2. In each panel, bar colour denotes neuronal APOE genotype (blue bars = APOE3 neurons [neE3]; red bars = APOE4 neurons [neE4]. Error bars represent ±1 SD. Asterisks indicate significant difference from the control group (*p < .05,** p < .01, ***p < .001).*

### *5.2.3. Is this impact determined by the genotype of the astrocytes?*

As mentioned above, under the effect of secreted factors, neuronal genotype-specific differences were not substantially altered by the genotype of astrocytes. In other words, differences persisted regardless of the type of ACM, with one exception: only under APOE3 ACM did APOE4 neurons exhibit a higher number of early endosomes (Fig.5.7G - G1, G3).

When comparing the impact of APOE3 versus APOE4 astrocytes on neuronal baseline differences in co-culture, APOE4 neurons paired with APOE4 astrocytes expressed higher numbers of SYP puncta, EEA1 spots, and neurites (Fig. 5.8A - A2, A3; Fig. 5.11G - G1, G3; Fig.5.9C - C1, C3) than APOE3 neurons under the same condition. Conversely, when co-cultured with APOE3 astrocytes, APOE4 neurons displayed larger SYP puncta area (Fig.5.8B - B2, B3) and reduced EEA1 intensity (Fig.5.11H - H1, H3).

When examining neurons of the same genotype under different astrocytic conditions, no feature-level changes were observed in ACM treatment. However, in co-culture experiments, astrocyte genotype exerted clearer effects. Both APOE3 and APOE4 neurons co-cultured with APOE4 astrocytes showed smaller SYP puncta area (Fig.5.8B - B1, B2) and brighter EEA1 intensity (Fig.5.11H - H2, H3) compared to those co-cultured with APOE3 astrocytes. Notably, for APOE4 neurons specifically, co-culture with APOE4 astrocytes also led to larger nuclear area (Fig.5.10F - F2, F3), smaller early endosomes (Fig.5.11I - I2, I3), and greater width-to-length ratios of early endosomes (Fig.5.11J -J1, J2, J3) compared to co-culture with

APOE3 astrocytes.

Together, these findings suggest that astrocytic APOE genotype modulates neuronal phenotypes in a contact-dependent manner, with APOE4 neurons being particularly sensitive to APOE4 astrocytes. This genotype–genotype interaction highlights how astrocytic APOE4 can amplify neuronal APOE4-related vulnerabilities, especially in pathways linked to synaptic structure and endosomal function-mechanisms thought to underlie the selective susceptibility of APOE4 carriers in AD.

#### *5.2.4. Is this impact determined by the genotype of the neurons?*

The data show that the impact of neuronal genotype is stronger than the impact of the genotype of the ACM, such that, as previously mentioned, the neuronal baseline differences were maintained mainly after either APOE3 or APOE4 ACM treatment.

However, the number of neuronal feature responses to astrocytes showed marked genotype-specific differences, such that APOE4 neurons seem to have higher sensitivity. In the co-culture condition, only two neuronal features in APOE3 neurons met the threshold of significance (≥2 out of 3 donors) when comparing APOE3 versus APOE4 astrocyte co-culture. Specifically, APOE3 neurons co-cultured with APOE4 astrocytes exhibited larger SYP puncta area (Fig.5.8B - B2, B3) and reduced EEA1 intensity (Fig.5.11H - H1, H3) compared to those co-cultured with APOE3 astrocytes. In contrast, APOE4 neurons displayed a broader and more pronounced response to astrocytic genotype. When co-cultured with APOE4

astrocytes, APOE4 neurons showed reduced SYP area (Fig. 5.9B - B2, B3), enlarged nuclear area (Fig. 5.10F - F2, F3), brighter but smaller EEA1 spots (Fig. 5.11H - H2, H3; Fig. 5.11I - I2, I3), and an increased width-to-length ratio of early endosomes (Fig. 5.11J - J1, J2, J3).

These findings reinforce the genotype-dependent vulnerability of APOE4 neurons to astrocyte-mediated influence, particularly under direct contact conditions. Overall, these neuronal genotype-specific differences emerged only in co-culture, indicating that direct astrocytic contact is required to reveal the heightened susceptibility of APOE4 neurons.

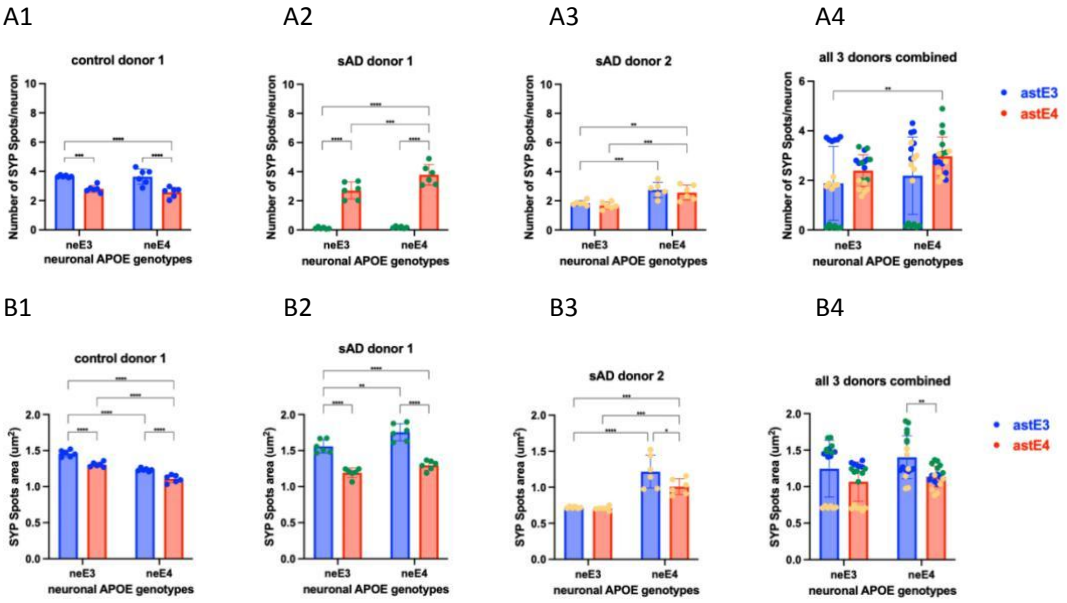



***Fig. 5.8. Synaptic morphology changes to co-culture treatment using astrocytes derived via lentiviral induction.*** *Two-way ANOVA results are presented on selected features extracted by Harmony software from co-culture experiments with lentiviral astrocytes. Rows A and B represent synaptic features - synaptophysin number and size, respectively. The 1st panel in each row corresponds to control donor 1 (MITCTL); the 2nd, sAD donor 1 (MITsAD); the 3rd, sAD donor 2 (UKBio); and the 4th panel presents pooled data from all three donors. Dot colors indicate donor identity: blue = control donor 1 (MITCTL), green = sAD donor 1 (MITsAD), yellow = sAD donor 2 (UKBio). In each panel, bar colour denotes neuronal APOE genotype (blue bars = APOE3 neurons [neE3]; red bars = APOE4 neurons [neE4]). Error bars represent ±1 SD. Asterisks indicate significant difference from the control group (*p < .05,** p < .01, ***p < .001).*

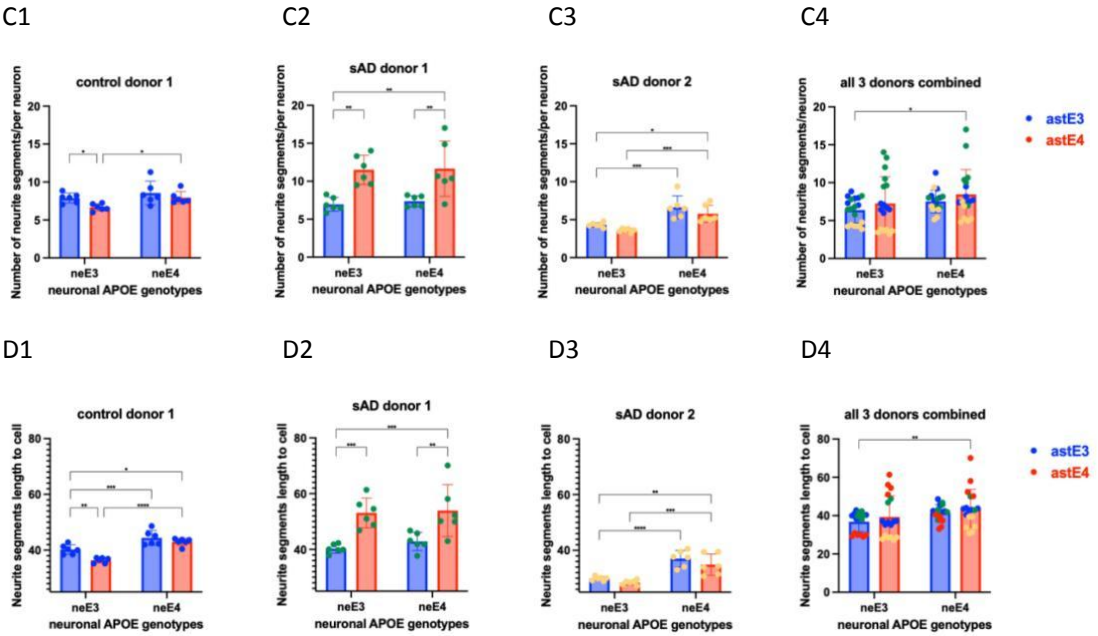



***Fig. 5.9. Neurites changes to co-culture treatment using astrocytes derived via lentiviral induction.*** *Two-way ANOVA results are presented on selected features extracted by Harmony software from co-culture experiments with lentiviral astrocytes. Rows C and D represent neuronal morphology - neurite number and length, respectively. The 1st panel in each row corresponds to control donor 1; the 2nd, sAD donor 1; the 3rd, sAD donor 2; and the 4th panel presents pooled data from all three donors. Dot colors indicate donor identity: blue = control donor 1, green = sAD donor 1, yellow = sAD donor 2. In each panel, bar colour denotes neuronal APOE genotype (blue bars = APOE3 neurons [neE3]; red bars = APOE4 neurons [neE4]). Error bars represent ±1 SD. Asterisks indicate significant difference from the control group (*p < .05,** p < .01, ***p < .001).*

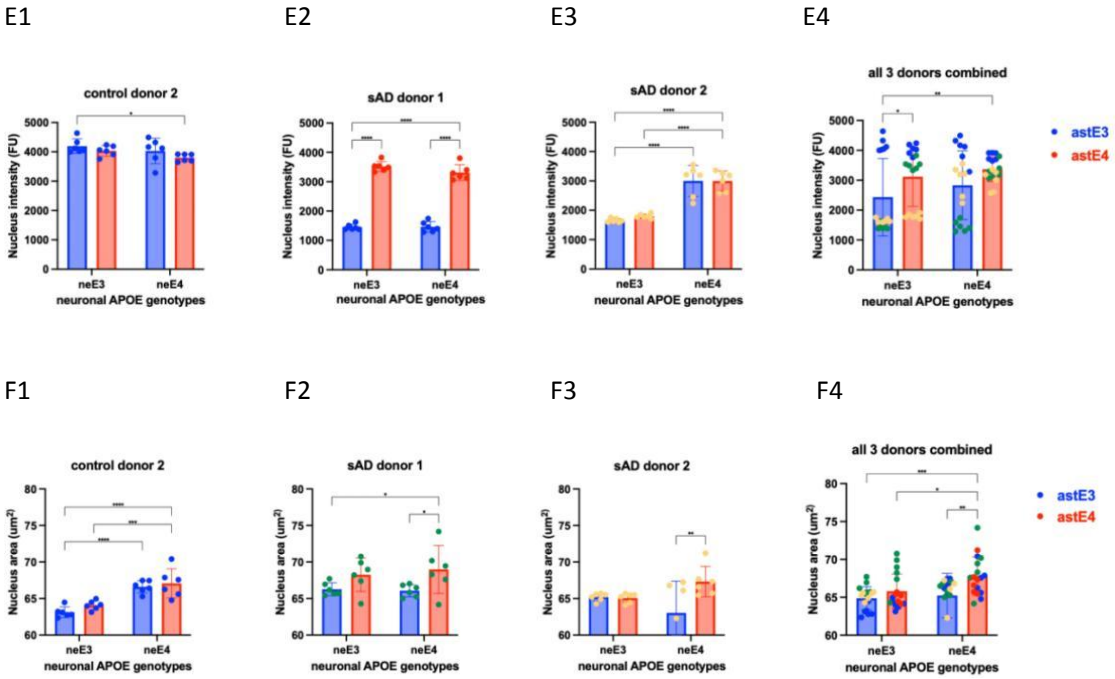



***Fig. 5.10. Neuronal nucleus changes to co-culture treatment using astrocytes derived via lentiviral induction.*** *Two-way ANOVA results are presented on selected features extracted by Harmony software from co-culture experiments with lentiviral astrocytes. Rows E and F represent nuclear properties - nucleus intensity and size, respectively. The 1st panel in each row corresponds to control donor 1; the 2nd, sAD donor 1; the 3rd, sAD donor 2; and the 4th panel presents pooled data from all three donors. Dot colors indicate donor identity: blue = control donor 1, green = sAD donor 1, yellow = sAD donor 2. In each panel, bar colour denotes neuronal APOE genotype (blue bars = APOE3 neurons [neE3]; red bars = APOE4 neurons [neE4]). Error bars represent ±1 SD. Asterisks indicate significant difference from the control group (*p < .05,** p < .01, ***p < .001).*

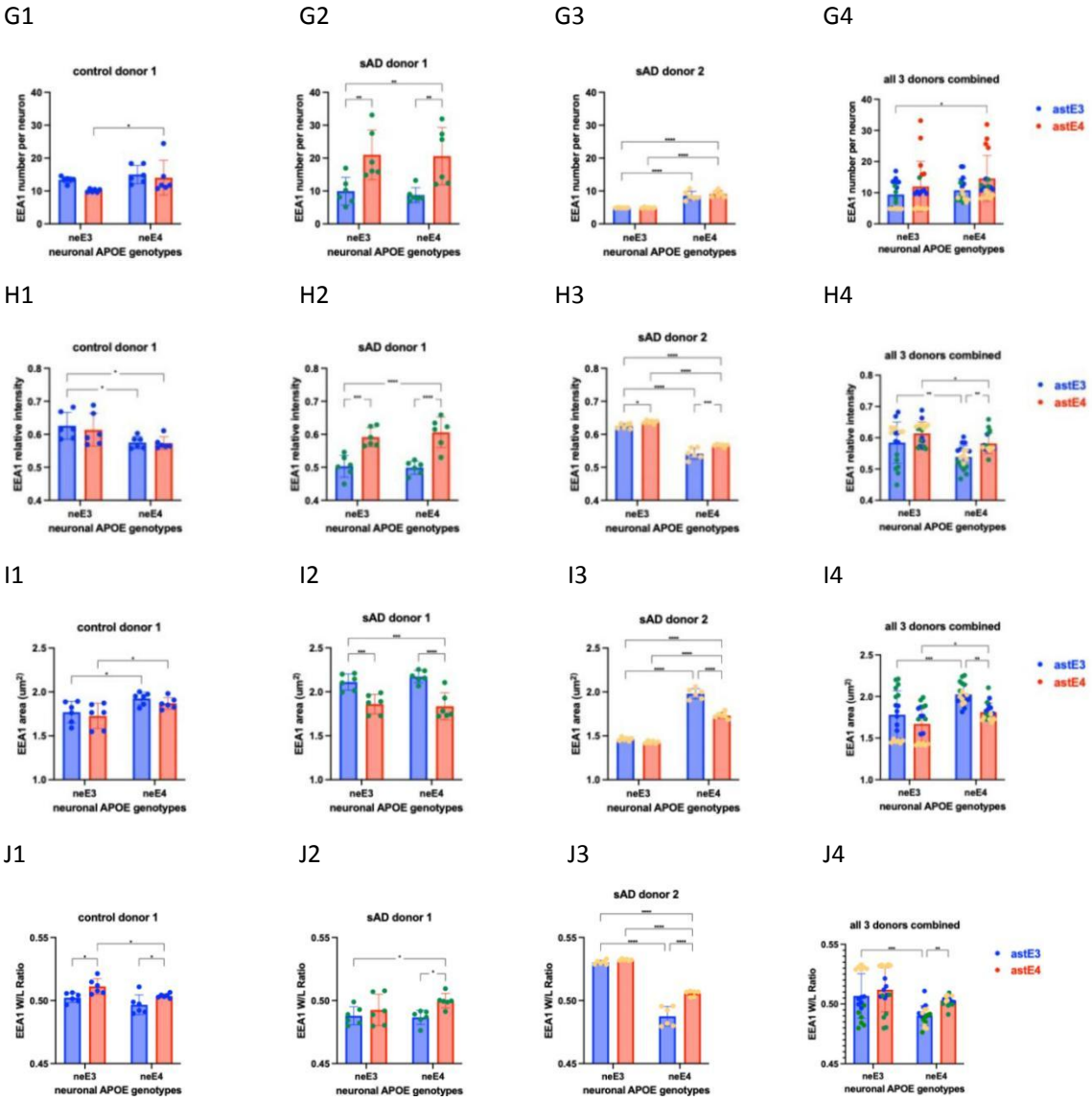



***Fig. 5.11. Early endosomal changes to co-culture treatment using astrocytes derived via lentiviral induction.*** *Two-way ANOVA results are presented on selected features extracted by Harmony software from co-culture experiments with lentiviral astrocytes. Rows G, H, I and J represent early endosomal proprieties - EEA1 number, intensity, area, and width-to-length (w/l) ratio, respectively. The 1st panel in each row corresponds to control donor 1; the 2nd, sAD donor 1; the 3rd, sAD donor 2; and the 4th panel presents pooled data from all three donors. Dot colors indicate donor identity: blue = control donor 1, green = sAD donor 1, yellow = sAD donor 2. In each panel, bar colour denotes neuronal APOE genotype (blue bars = APOE3 neurons [neE3]; red bars = APOE4 neurons [neE4]). Error bars represent ±1 SD. Asterisks indicate significant difference from the control group (*p < .05,** p < .01, ***p < .001).*

| 10 neuronal features treated with astrocytes/Ab | | E3 vs. E4 co-cultures | E3 neu vs. E4 neu @NMM | E3 neu vs. E4 neu @ACM E3 | E3 neu vs. E4 neu @ACM E4 | E3 neu @ACM E3 vs. ACM E4 | E4 neu @ACM E3 vs. ACM E4 | E3 neu vs. E4 neu co-cultured with E3 ast | E3 neu vs. E4 neu co-cultured with E4 ast | E3 neu co-cultured with E3 ast vs E4 ast | E4 neu co-cultured with E3 ast vs E4 ast | E3 neu vs. E4 neu @NMM + Ab | E3 neu @ NMM vs. @NMM+ Ab | E4 neu @ NMM vs. @NMM+ Ab | E3 neu vs. E4 neu @ACM+Ab |
|---|---|---|---|---|---|---|---|---|---|---|---|---|---|---|---|
| | | lentiviral-astrocytes | | | | | | | | | | | | | |
| 0 | Variables | baseline | | same astrocyte APOE | | same neuronal APOE | | same astrocyte APOE | | same neuronal APOE | | baseline | same astrocyte APOE | | same neuronal APOE |
| 1 | SYP # | E4>E3 (2,3) | ns. | ns. | ns. | ns. | ns. | ns. | E4>E3 (2,3) | ns. | ns. | ns. | ns. | ns. | ns. |
| 2 | SYP area | E4<E3 (1,2) | E4<E3 (1,2) | ns. | ns. | ns. | ns. | E4>E3 (2,3) | ns. | E4<E3 (1,2) | E4<E3 (1,2,3) | ns. | ns. | NMM < NMM+Ab | ns. |
| 3 | Neurite # | E4>E3 (2,3) | E4>E3 (1,3) | E4>E3 (1,2,3) | E4>E3 (1,2,3) | ns. | ns. | ns. | E4>E3 (1,3) | ns. | ns. | ns. | NMM < NMM+Ab | NMM < NMM+Ab | E4<E3 |
| 4 | Neurite length | E4>E3 (1,2,3) | E4>E3 (1,3) | E4>E3 (1,3) | E4>E3 (1,2,3) | ns. | ns. | E4>E3 (1,3) | E4>E3 (1,3) | ns. | ns. | E4>E3 | ns. | ns. | E4>E3 |
| 5 | Nucleus intensity | E4>E3 (2,3) | E4>E3 (2,3) | E4>E3 (2,3) | E4>E3 (2,3) | ns. | ns. | ns. | ns. | ns. | ns. | ns. | ns. | ns. | ns. |
| 6 | Nucleus area | E4>E3 (1,2) | ns. | ns. | ns. | ns. | ns. | ns. | ns. | ns. | E4>E3 (2,3) | ns. | ns. | ns. | ns. |
| 7 | EEA1 # | E4>E3 (2,3) | ns. | E4>E3 (1,3) | ns. | ns. | ns. | ns. | E4>E3 (1,3) | ns. | ns. | ns. | ns. | ns. | ns. |
| 8 | EEA1 intensity | E4<E3 (1,3) | E4>E3 (1,3) | ns. | ns. | ns. | ns. | E4<E3 (1,3) | ns. | E4>E3 (2,3) | E4>E3 (2,3) | ns. | ns. | NMM < NMM+Ab | ns. |
| 9 | EEA1 area | E4>E3 (1,3) | E4>E3 (1,3) | E4<E3 (2,3) | E4<E3 (1,2) | ns. | ns. | E4>E3 (1,3) | E4>E3 (1,3) | ns. | E4<E3 (2,3) | ns. | ns. | ns. | ns. |
| 10 | EEA1 (W/L) morphology | ns. | ns. | ns. | ns. | ns. | ns. | ns | ns. | ns. | E4>E3 (1,2,3) | ns. | ns. | NMM < NMM+Ab | ns. |

***Table 5.1. Matrix summary of APOE- and context-dependent neuronal phenotypes affected by lentiviral-induced astrocytes.***

*Direction and significance of pairwise differences for 10 neuronal readouts across conditions including neuronal APOE genotype (E3 vs E4) and astrocyte context (ACM from E3 or E4 astrocytes or co-culture with E3 or E4 astrocytes). Each cell reports the direction of the effect for the row feature under the column comparison.*

*Notation:*

*Baseline - E3 vs E4 neurons in monocultures or co-cultures. ACM - neurons exposed to astrocyte-conditioned medium from E3 or E4 astrocytes (noted as @ACM E3/E4). Co-culture - neurons directly co-cultured with E3 or E4 astrocytes (co-cultured with E3/E4 astrocytes). NMM - neuronal maturation medium. NMM+Ab - indicates $A\beta_{25-35}$ stress added to NMM (see Methods). E4 > E3 or E4 < E3 - direction of a significant difference (E4 relative to E3). ns - not significant. Numbers in parentheses (e.g.,(1,2,3)) - in which donor the effect was significant (see figures for mapping). EEA1 W/L morphology - early endosome width/length ratio.*

## 5.3. Discussion

The results of this section show that *APOE* genotype influences both neuronal and astrocytic features (Table 5.1). These neuronal differences are further modulated by astrocytic genotype and the mode of interaction with lentiviral-derived astrocytes. In monoculture, APOE4 astrocytes consistently exhibited lower nuclear intensity and reduced endosome roundness, but increased cytoplasmic width-to-length ratio, higher BODIPY intensity, and higher EEA1 intensity compared to APOE3 astrocytes. These phenotypes may reflect altered nuclear organization, cytoplasmic morphology, lipid metabolism, and endosomal activity driven by APOE-related cellular mechanisms. For example, reduced nucleus roundness has been associated with cellular stress (Frey et al., 2022). Higher BODIPY intensity suggests greater neutral lipid accumulation, which could indicate shifts in lipid storage or turnover (Windham et al., 2024). Increased EEA1 intensity is in line with the previous finding that APOE4 is associated with enlarged or increased accumulation EEA1-positive early endosomes and delayed recycling (Lin et al., 2018). Since proper acidification is crucial for early-endosomal maturation, cargo sorting, and timely transition to late endosomes, the observed enlargement/accumulation suggests a potential dysfunction in the endosomal acidification process. This is consistent with studies implicating dysregulated endosomal pH and altered cargo processing (Narayan et al., 2020; Prasad & Rao, 2018a). Although these changes are consistent with cellular processes previously implicated in APOE4 biology, their functional significance in astrocytes remains to be further investigated using functional assays, including endosomal pH measurements, Aβ uptake and

clearance, ABCA1-dependent cholesterol efflux, and lipid droplets turnover/lipophagy flux analyses.

In co-culture, comparing APOE4 neuron–astrocyte co-cultures with APOE3 neuron–astrocyte co-cultures showed a similar pattern to monocultures of APOE3 vs. APOE4 neurons, such as brighter and larger nuclei (consistent with findings from small molecule-derived astrocytes), more and longer neurites, higher numbers of SYP puncta and EEA1-positive vesicles, and enlarged endosomal area, but smaller SYP puncta and reduced endosomal intensity compared with neurons grown with APOE3 astrocytes. Among these features, nucleus area, the number of SYP puncta, and the number of early endosomes were not significantly different in monoculture, but became significant when co-cultured with astrocytes bearing the corresponding genotype. These findings suggest that *APOE* genotype influences neuron–astrocyte interactions, particularly in pathways related to neurite development, synaptic structure, and endosomal function. Alternatively, it may imply that direct astrocyte contact and local signaling could amplify genotype-specific effects (Watanabe et al., 2023). Moreover, the differences between ACM and co-culture may reflect the role of contact-dependent mechanisms such as gap junction communication, extracellular matrix interactions, or localized signaling at the tripartite synapse, which cannot be fully recapitulated by secreted factors in ACM (Shan et al., 2021). Such context-dependent sensitivity may underlie the greater vulnerability of APOE4-bearing circuits to stress and could help explain why interventions targeting astrocytic lipidation, endosomal recycling, or

extracellular matrix (ECM) remodeling show selective benefit in APOE4 models. Thus, these co-culture data highlight APOE-dependent astrocyte-neuron crosstalk as a mechanistic bridge between molecular dysfunction and network fragility. This interaction identifies specific pathways (e.g., cholesterol transfer, inflammatory signaling) that serve as promising targets for functional rescue as well as a basis for screening compounds that rescue these specific pathologies.

Although fewer features reached statistical significance, astrocyte treatment (ACM or co-culture) largely preserved the baseline differences observed between APOE3 and APOE4 neurons. For example, APOE4 neurons consistently showed higher numbers of early endosomes and longer, more numerous neurites under both ACM and co-culture conditions. However, astrocyte treatment also introduced genotype-specific and contact-dependent modifications in certain features. When treated with APOE3 ACM, APOE4 neurons exhibited more early endosomes, while in co-culture with APOE4 astrocytes, APOE4 neurons expressed higher numbers of EEA1 spots, SYP puncta, and neurites.

It is worth noting that although most baseline differences remained, there were two features that were altered by astrocyte treatments. Under both APOE3 and APOE4 ACM conditions, APOE4 neurons displayed smaller early endosomes compared to APOE3 neurons, reversing the pattern observed in monoculture. It could indicate faster maturation or higher recycling flux (Kamentseva et al., 2020) rescued by the astrocytes. In co-culture with APOE3

astrocytes, APOE4 neurons showed larger SYP puncta area compared to APOE3 neurons under the same condition, again representing a reversal of baseline differences. It could suggest presynaptic maturation or astrocyte-induced assembly through ECM cues, such as hevin/thrombospondins (Allen & Eroglu, 2017). These results suggest that both secreted astrocytic factors and direct contact, while not eliminating all intrinsic genotype-dependent phenotypes, can selectively modulate them, sometimes counteracting baseline differences. Such modulation of endosomal and synaptic features is of particular interest, as endosomal–lysosomal pathways are among the earliest cellular systems affected in AD (Nyberg et al., 2025), although the precise role of APOE isoforms in these processes remains incompletely understood.

The impact of astrocytic genotype appeared stronger in co-culture than in ACM. For both APOE3 and APOE4 neurons, co-culture with APOE4 astrocytes led to smaller SYP puncta area and brighter EEA1 intensity compared with co-culture with APOE3 astrocytes, a difference not seen in ACM experiments. For APOE4 neurons specifically, additional effects were observed, including enlarged nuclear area, smaller but brighter early endosomes, and increased endosome width-to-length ratio under APOE4 co-culture. The larger and, in some cases, directionally different neuronal phenotypes observed in direct co-culture compared with ACM suggest that soluble astrocyte-derived factors alone do not capture the full neuron – astrocyte interaction. Rather than demonstrating that physical cell-cell contact itself is necessary, these findings are consistent with additional local communication

mechanisms present in co-culture, including ECM/matrisome cues, locally retained or concentrated secreted factors, cell-surface juxtacrine signalling, connexin/hemichannel-associated communication, and reciprocal neuron – astrocyte feedback.

ECM-related signalling is particularly relevant in the context of APOE genotype. TCW et al. (2022) identified APOE4-associated lipid metabolic dysfunction in human astrocytes and microglia, including increased cholesterol synthesis despite intracellular cholesterol accumulation in astrocytes. Importantly, they also identified dysregulation of matrisome-associated pathways in APOE4 astrocytes co-cultured with neurons, associated with chemotaxis, glial activation and lipid-biosynthetic programmes, and showed that these changes recapitulated altered astrocytic matrisome signalling observed in human brain. These findings indicate that neuronal context can reveal APOE4-associated astrocytic programmes that are less apparent in isolated glial cultures, providing a relevant precedent for the stronger genotype-associated effects observed in the present direct co-culture model.

A more direct link between APOE4 astrocytic ECM regulation and neuronal synaptic morphology has also been demonstrated by Watanabe et al. (2023). In an isogenic human iPSC-derived astrocyte model, APOE4 astrocytes showed increased expression of the extracellular-matrix glycoprotein EDIL3 and reduced dendritic spine density in co-cultured

neurons; importantly, reduction of EDIL3 in APOE4 astrocytes ameliorated the neuronal spine phenotype. This supports the possibility that APOE-dependent astrocytic matrisome changes can influence neuronal structural phenotypes and is particularly relevant to the SYP-associated differences observed in the present study.

Other local signalling mechanisms may additionally contribute. Connexin43 (GJA1), a major astrocytic connexin, has been implicated in AD-associated astrocyte states and in regulation of Aβ metabolism. Experimental manipulation of astrocytic GJA1 alters neuronal A β -associated phenotypes in co-culture, while connexin43 hemichannel activation in an AD mouse model promotes ATP and glutamate release and contributes to neuronal stress (Yi et al., 2016; Kajiwara et al., 2018). Co-culture also permits membrane-associated receptor – ligand and adhesion interactions that are absent or markedly reduced in transferred ACM, providing a potential route for juxtacrine regulation of neuronal morphology. However, none of these mechanisms was directly isolated in the present experiments. The co-culture findings therefore support the presence of additional local or contact-associated communication layers, but do not establish ECM, connexin signalling or physical contact as the causal mechanism. Matched Transwell experiments, defined or decellularised ECM conditions, and targeted perturbation of adhesion/integrin or connexin pathways would be required to distinguish these contributions.

When comparing the relative contributions of neuronal versus astrocytic genotype, neuronal genotype exerted the stronger influence on neuronal morphology in certain features. *APOE*4 neurons consistently maintained longer neurites and brighter nuclei, regardless of astrocytic genotype, especially in ACM treatment, with the exceptions in co-culture conditions with APOE3 or APOE4 astrocytes, such as SYP area, nucleus intensity, neurite, and EEA1 numbers (summarized in Table 3.6). However, APOE4 neurons also showed greater sensitivity to astrocytic treatment, such that they exhibited broader feature-level responses when paired with APOE4 astrocytes, whereas APOE3 neurons showed only minor changes under the same conditions. Together with Ramakrishna et al. (2021) showing sustained $Ca^{2+}$/translation inhibition in APOE4-treated neurons than transient change in APOE3 neurons and Konings et al. (2021) demonstrated that astrocytic APOE4 acutely boosts firing while neuronal APOE3 maximizes activity, these data support the interpretation that APOE4 neurons are intrinsically more responsive to environmental cues (astrocyte treatment) and that APOE4 -APOE4 paired interaction can amplify phenotypic differences.

In summary, the use of lentiviral-induced astrocytes highlights that APOE genotype shapes neuronal and astrocytic features, and that direct astrocyte-neuron contact might play a critical role for revealing the heightened sensitivity of APOE4 neurons. While astrocytic factors alone preserve most baseline neuronal differences, co-culture with APOE4 astrocytes accentuates them, particularly in synaptic and endosomal pathways. These results emphasize that APOE4-related neuronal phenotypes are not purely cell-autonomous

but are modulated through astrocytic interactions, with the strongest effects emerged in direct co-culture conditions, consistent with contributions from local, matrix-associated, juxtacrine and/or bidirectional signalling mechanisms that are not fully captured by ACM.

Comparing astrocyte induction methods revealed that lentiviral- and small molecule–derived astrocytes converged on broadly similar outcomes (Table 5.2). Across both protocols, APOE4 astrocytes reinforced neuronal vulnerabilities, while APOE3 astrocytes sometimes buffered or stabilized neuronal features. Nonetheless, specific readouts differed, with occasional reversals in feature direction depending on induction strategy (EEA1 area and nuclear size). These subtle discrepancies could lead to hypothesize that they reflect underlying differences in the developmental state or subtypes of the astrocytes produced by each protocol. This hypothesis could be tested in future work by directly comparing transcriptomic profiles, maturation markers, or temporal dynamics of the two astrocyte populations.

| 10 neuronal features treated with astrocytes/Ab | | E3 vs. E4 co-cultures<br>lentiviral-astrocytes<br>small molecules-astrocytes | E3 neu vs. E4 neu @NMM | E3 neu vs. E4 neu @ACM E3 | E3 neu vs. E4 neu @ACM E4 | E3 neu @ACM E3 vs. ACM E4 | E4 neu @ACM E3 vs. ACM E4 | E3 neu vs. E4 neu co-cultured with E3 ast | E3 neu vs. E4 neu co-cultured with E4 ast | E3 neu co-cultured with E3 ast vs E4 ast | E4 neu co-cultured with E3 ast vs E4 ast |
|---|---|---|---|---|---|---|---|---|---|---|---|
| 0 | **Variables** | **baseline** | | **same astrocyte APOE** | | **same neuronal APOE** | | **same astrocyte APOE** | | **same neuronal APOE** | |
| 1 | SYP # | E4>E3 (2,3) | ns. | E4>E3 (1,3) | ns. | ns. | E4<E3 (2,3) | ns. | E4>E3 (2,3) | ns. | ns. |
| 2 | SYP area | E4<E3 (1,2) | E4<E3 (1,2) | E4>E3 (2,3) | E4>E3 (2,3) | ns. | ns. | E4>E3 (2,3) | ns. | E4<E3 (1,2) | E4<E3 (1,2,3) |
| 3 | Neurite # | E4>E3 (2,3) | E4>E3 (1,3) | E4>E3 (1,2,3) | E4>E3 (1,2,3) | ns. | E4<E3 (2,3) | ns. | E4>E3 (1,3) | ns. | E4>E3 (2,3) |
| 4 | Neurite length | E4>E3 (1,2,3) | E4>E3 (1,3) | E4>E3 (2,3)<br>E4>E3 (1,3) | E4>E3 (1,2,3) | ns. | E4<E3 (2,3) | E4>E3 (1,3) | E4>E3 (1,3) | ns. | E4>E3 (2,3) |
| 5 | Nucleus intensity | E4>E3 (2,3)<br>E4>E3 (3/3) | E4>E3 (2,3) | E4>E3 (2,3)<br>E4>E3 (2,3) | E4>E3 (2,3)<br>E4>E3 (2,3) | ns. | E4<E3 (2,3) | ns. | E4>E3 (2,3) | ns. | E4>E3 (1,3) |
| 6 | Nucleus area | E4>E3 (1,2)<br>E4<E3 (1,2) | ns. | ns. | E4<E3 (2,3) | ns. | ns. | ns. | ns. | E4>E3 (2,3) | E4>E3 (2,3)<br>E4>E3 (2,3) |
| 7 | EEA1 # | E4>E3 (2,3) | ns. | E4>E3 (1,3) | ns. | ns. | E4<E3 (2,3) | E4<E3 (2,3) | E4>E3 (1,3) | ns. | E4>E3 (2,3) |
| 8 | EEA1 intensity | E4<E3 (1,3) | E4>E3 (1,3) | E4<E3 (2,3) | ns. | ns. | ns. | E4<E3 (1,2,3)<br>E4<E3 (1,3) | ns. | E4>E3 (2,3) | E4>E3 (2,3) |
| 9 | EEA1 area | E4>E3 (1,3) | E4>E3 (1,3) | E4<E3 (2,3) | E4<E3 (1,2) | ns. | ns. | E4<E3 (2,3)<br>E4>E3 (1,3) | E4>E3 (1,3) | ns. | E4>E3 (2,3)<br>E4<E3 (2,3) |
| 10 | EEA1 (W/L) morphology | ns. | ns. | E4<E3 (2,3) | E4<E3 (1,2,3) | ns. | ns. | ns | ns. | ns. | E4>E3 (1,2,3) |

***Table 5.2. Summary of neuronal phenotypic comparisons between lentiviral- and small molecule-induced astrocytes.*** *This table summarizes consistencies and differences in neuronal responses to two astrocyte treatments, comparing lentiviral-induced (blue font) and small molecules-induced astrocytes (green font). Ten key neuronal readouts include neurite length and number, synaptic marker (SYP) size and number, early endosome morphology and intensity (EEA1), and nuclear features (size and intensity). The summary comparisons highlight how neuronal phenotype was affected by APOE genotypes, astrocyte treatments (co-culture or ACM), astrocytes induction methods. Abbreviations: ns., not significant; NMM, neuronal maintenance medium; ACM, astrocyte conditioned medium.*

# Chapter 6: The effects of Aβ stress on astrocytic and neuronal phenotype

## 6.1. Introduction

### *6.1.1. Astrocyte–neuron communication under Aβ stress is influenced by APOE genotypes*

In sAD, the interplay between astrocyte-derived APOE and Aβ significantly contributes to disease pathology (Wisniewski & Drummond, 2020). While Aβ is predominantly produced by neurons, studies have revealed that a small subset of iPSC-derived astrocytes can also secrete substantial levels of Aβ (M.-C. Liao et al., 2016). APOE is not only co-deposited with Aβ in plaques but also critically regulates its clearance, aggregation, and uptake.

APOE and Aβ interact through common receptors such as LRP1, LDLR, and HSPGs, mediating their cellular uptake (Dias et al., 2025). These interactions are modulated by APOE isoform, lipidation status, and Aβ aggregation state. Compared to APOE3, APOE4 forms fewer stable complexes with Aβ and is less effective at promoting Aβ degradation, partly due to impaired lipidation and altered receptor binding (Tai et al., 2015). It was also reported that there are fewer APOE-Aβ complexes from the CSF in APOE4 carriers, who also have higher levels of Aβ oligomers and induce a greater burden of cellular stress (Long & Holtzman, 2019). Additionally, APOE4 has been associated with impaired autophagy in astrocytes, further reducing Aβ clearance capacity (Simonovitch et al., 2019).

Because internalized Aβ predominantly traffics through early and late endosomes toward lysosomal degradation, disruptions in these pathways, especially in APOE4 contexts, may contribute to Aβ accumulation and neuronal vulnerability. This study therefore focuses on how *APOE* genotype and Aβ exposure together influence neuronal phenotype in human iPSC-derived fetal-stage cortical neurons. By applying $A\beta_{25-35}$ as a stressor, we aim to mimic early AD-related cellular pathology and investigate how APOE3 and APOE4 backgrounds differentially shape neuronal responses under neurodegenerative stress conditions.

### *6.1.2. Using $A\beta_{25-35}$ as a rapid and reproducible stressor*

Not only do Aβ plaques accumulate in the brain, but soluble Aβ oligomers also play a toxic role by disrupting synaptic functions and triggering pathways that lead to neuronal damage and cognitive decline even before plaque deposition becomes evident (Mucke & Selkoe, 2012). While full-length peptides such as $A\beta_{1-42}$ are commonly studied, they often require prolonged incubation to form aggregates and careful aggregation control, which introduces variability between experiments.

To create a faster and more consistent stress model in vitro, this study uses 10 μM $A\beta_{25-35}$, a short synthetic peptide that retains a region of Aβ associated with neurotoxicity. $A\beta_{25-35}$ contains methionine-35 (Met35), a residue that has been implicated in oxidative stress and membrane damage. The peptide can also adopt β-sheet-rich aggregated structures under appropriate experimental conditions (Friedemann et al., 2015). Compared with full-length $A\beta_{1-42}$, $A\beta_{25-35}$ provides a practical acute stress paradigm for short-term experiments, with

reported cellular effects occurring within 24-48 hours. In the present study, 10 μM $A\beta_{25-35}$ was selected during preliminary optimisation because 1 μM produced only a delayed morphological response, whereas 10 μM generated a reproducible morphological phenotype without marked loss of cell number. Nuclease-free water was used as the vehicle control.

Although $A\beta_{25-35}$ is not naturally present in the brain, its consistent and well-characterized toxic effects allow us to model synaptotoxic stress efficiently. In this study, it was applied to iPSC-derived neurons co-cultured with astrocytes carrying *APOE*3 or *APOE*4 genotypes, enabling us to investigate how astrocyte genotype influences neuronal vulnerability under controlled Aβ challenge with the following questions:

(1) How does $A\beta_{25-35}$ exposure alter the morphology of monoculture of neurons and astrocytes?

(2) How does $A\beta_{25-35}$ affect the baseline difference between APOE3 and APOE4 in neurons and astrocytes?

(3) How do neurons treated with ACM respond to $A\beta_{25-35}$ stress?

## 6.2. Results

### *6.2.1. How Aβ$_{25–35}$ affects the baseline difference between APOE3 and APOE4 in neurons*

Representative ICC images of the lentiviral-induced astrocyte monoculture and neuron – astrocyte co-culture conditions analysed in this chapter are provided in Figure 3.3. The corresponding image-analysis and segmentation examples are shown in Section 2.8 (Figures 2.4 & 2.5). Overall, Aβ$_{25-35}$-induced stress does not amplify the baseline phenotypic differences between APOE3 and APOE4 neurons. In fact, despite previously observed genotype-specific differences under non-stressed conditions in NMM as baseline, most neuronal features become less distinct following Aβ exposure, with only a limited number of changes consistently reported across donors.

Neurite number remains a robust distinguishing feature between genotypes, with APOE4 neurons consistently exhibiting a higher neurite count than APOE3 neurons (Fig. 6.2D - D1, D2, D3). In contrast, all other genotype-dependent differences observed at baseline were no longer statistically significant following Aβ treatment.

### *6.2.2. Is the neuronal response to Aβ$_{25–35}$ genotype-dependent between APOE3 and APOE4*

Aβ$_{25-35}$ exposure affects APOE4 neurons more profoundly than APOE3 neurons. While APOE3 neurons show only reduced neurite length upon stress (Fig. 6.2C - C1, C2, C3), APOE4 neurons display decreased SYP puncta area (Fig. 6.1B - B1, B2, B3), shorter neurites (Fig. 6.2C - C1, C2, C3), reduced EEA1 intensity (Fig. 6.4H - H1, H2, H3), and lower early endosome

width-to-length ratio (Fig. 6.4J - J1, J2, J3) under stress. Notably, Aβ exposure increases neurite number but reduces neurite length in APOE4 neurons, suggesting possible neurite fragmentation. These findings indicate selective, genotype-specific vulnerability rather than a uniform amplification of APOE-related phenotypes.

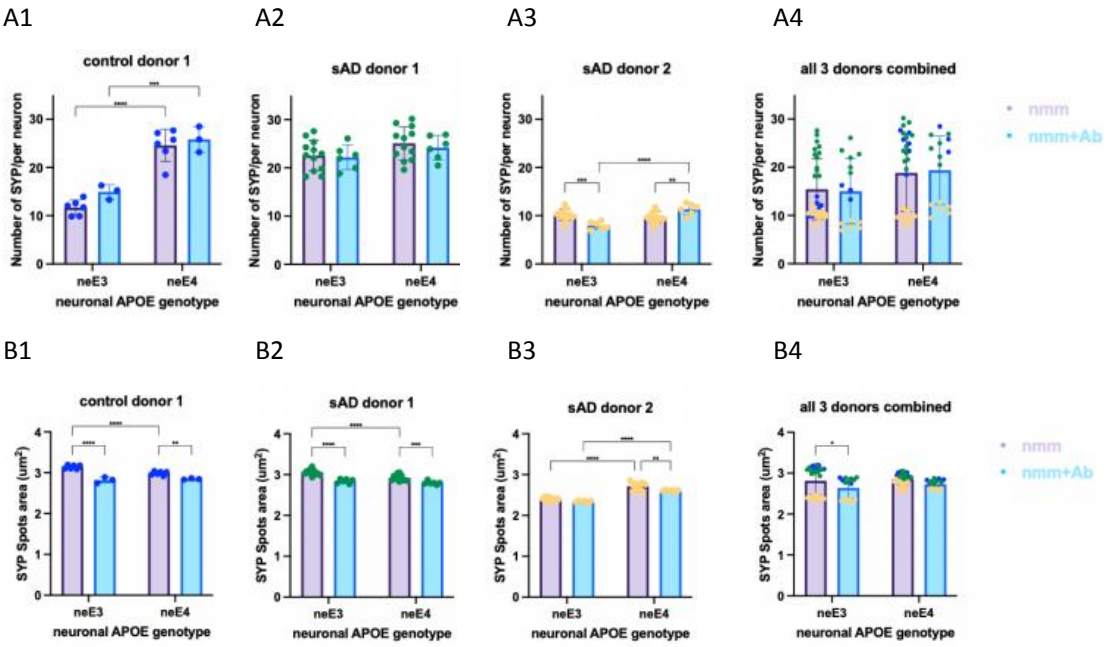



***Fig. 6.1 Neuronal synaptic morphology changes to Aβ$_{25-35}$ exposure in APOE3 and APOE4 monoculture neurons.*** *Two-way ANOVA results are presented on selected features extracted by Harmony software from monoculture experiments comparing APOE3 and APOE4 neurons with or without Aβ$_{25-35}$ treatment. Rows A and B represent synaptic features-synaptophysin (SYP) number and size, respectively. The 1st panel in each row shows results from control donor #1; the 2nd from control donor 1; the 3rd from sAD donor 2. The 4th panel presents pooled data across all four donors, with dot color indicating the donor source: blue = control donor 2; green = sAD donor 1; yellow = sAD donor 2. In each panel, bar colour denotes treatment condition (purple bars = neuronal maintenance medium [nmm]; light blue bars = nmm supplemented with Aβ [nmm + Aβ]). Error bars represent ±1 SD. Asterisks indicate significant difference from the control group (*p < .05,** p < .01, ***p < .001).*

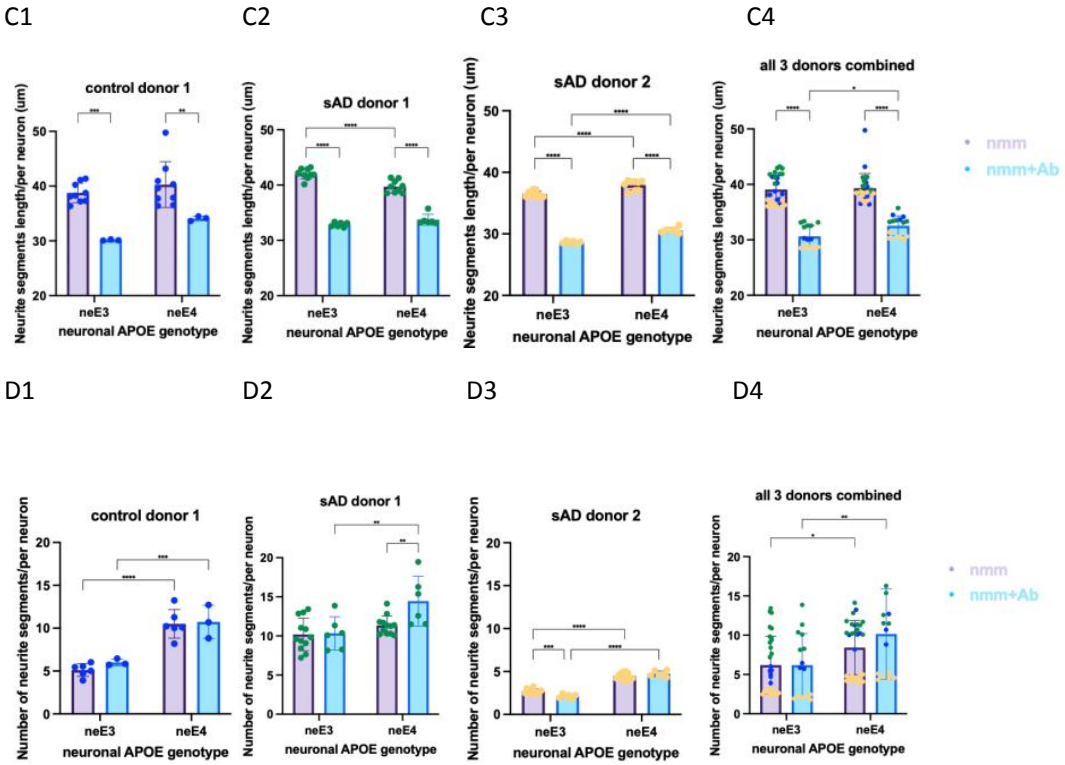



***Fig. 6.2 Neurite changes to Aβ$_{25-35}$ exposure in APOE3 and APOE4 monoculture neurons.*** *Two-way ANOVA results are presented on selected features extracted by Harmony software from monoculture experiments comparing APOE3 and APOE4 neurons with or without Aβ$_{25-35}$ treatment. Rows C and D represent morphological features—neurite length and neurite number, respectively. The 1st panel in each row shows results from control donor 1; the 2nd from control donor 1; the 3rd from sAD donor 2. The 4th panel presents pooled data across all four donors, with dot color indicating the donor source: blue = control donor 2; green = sAD donor 1; yellow = sAD donor 2. In each panel, bar colour denotes treatment condition (purple bars = neuronal maintenance medium [nmm]; light blue bars = nmm supplemented with Aβ [nmm + Aβ]). Error bars represent ±1 SD. Asterisks indicate significant difference from the control group (*p < .05,** p < .01, ***p < .001).*

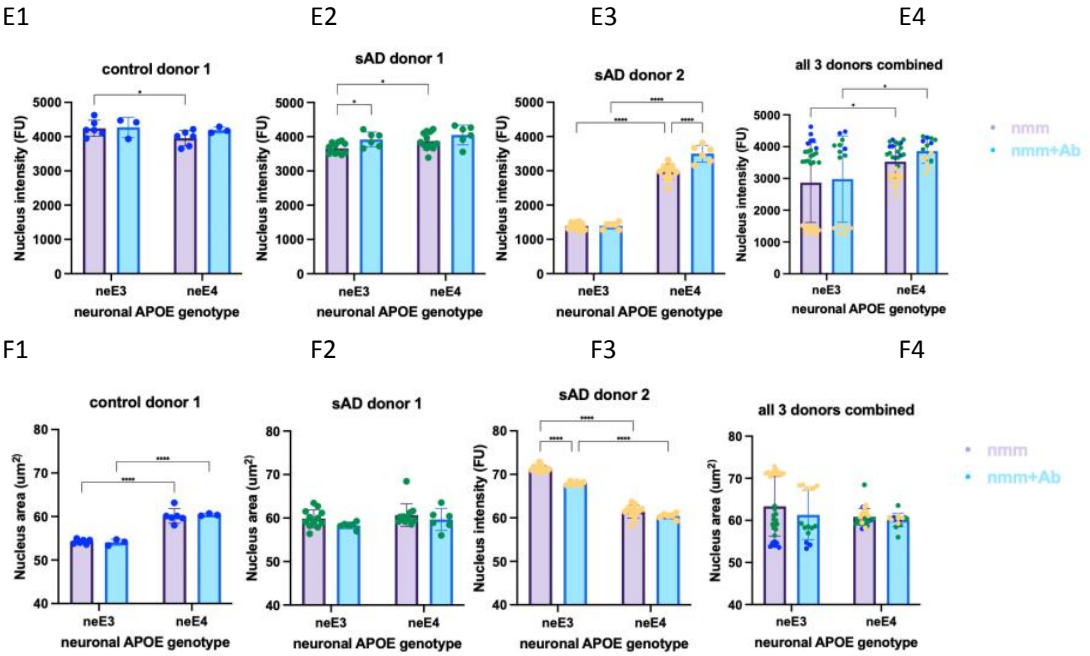



***Fig. 6.3 Neuronal nucleus changes after Aβ$_{25-35}$ exposure in APOE3 and APOE4 monoculture neurons.*** *Two-way ANOVA results are presented on selected features extracted by Harmony software from monoculture experiments comparing APOE3 and APOE4 neurons with or without Aβ$_{25-35}$ treatment. Rows E and F represent morphological features-nucleus expression intensity and the size of the nucleus, respectively. The 1st panel in each row shows results from control donor 1; the 2nd from control donor 1; the 3rd from sAD donor 2. The 4th panel presents pooled data across all four donors, with dot color indicating the donor source: blue = control donor 2; green = sAD donor 1; yellow = sAD donor 2. In each panel, bar colour denotes treatment condition (purple bars = neuronal maintenance medium [nmm]; light blue bars = nmm supplemented with Aβ [nmm + Aβ]). Error bars represent ±1 SD. Asterisks indicate significant difference from the control group (*p < .05,** p < .01, ***p < .001).*

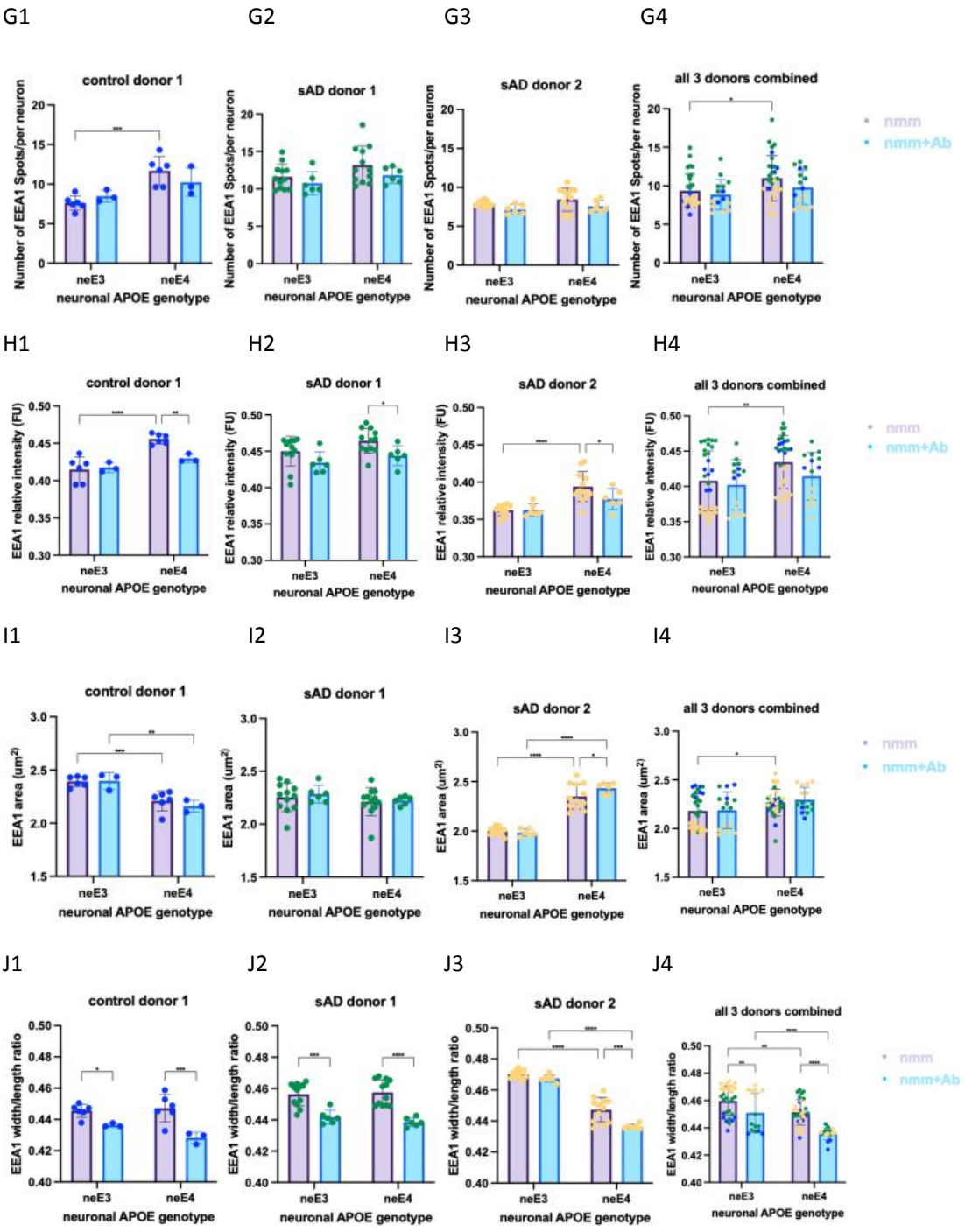



***Fig. 6.4 Neuronal early endosome changes after Aβ$_{25-35}$ exposure in APOE3 and APOE4 monoculture neurons.*** *Two-way ANOVA results are presented on selected features extracted by Harmony software from monoculture experiments comparing APOE3 and APOE4 neurons with or without Aβ$_{25-35}$ treatment. Rows G to J represent early endosomal features-EEA1 number, intensity, area, and width-to-length ratio, respectively. The 1st panel in each row shows results from control donor 1; the 2nd from control donor 1; the 3rd from sAD donor 2. The 4th panel presents pooled data across all four donors, with dot color indicating the donor source: blue =*

*control donor 2; green = sAD donor 1; yellow = sAD donor 2. In each panel, bar colour denotes treatment condition (purple bars = neuronal maintenance medium [nmm]; light blue bars = nmm supplemented with Aβ [nmm + Aβ]). Error bars represent ±1 SD. Asterisks indicate significant difference from the control group (*p < .05,** p < .01, ***p < .001).*

### *6.2.3. How do neurons treated with ACM respond to Aβ$_{25–35}$ stress?*

The influence of Aβ$_{25-35}$ on how ACM modifies neuronal phenotype appears largely independent of the *APOE* genotype of the astrocyte-conditioned media. Regardless of whether neurons were treated with ACM derived from APOE3 or APOE4 astrocytes, Aβ-stressed APOE4 neurons consistently exhibited a higher neurite count (Fig. 6.6C - C1, C2, C3) but shorter neurite length (Fig. 6.6D - D1, D2, D3) compared to APOE3 neurons. Other features that showed genotype-related differences under non-stressed ACM conditions, or that were previously influenced by neuronal genotype, no longer displayed significant differences.

### *6.2.4. How does Aβ$_{25–35}$ affect the baseline difference between monoculture of APOE3 and APOE4 astrocytes?*

A total of 43 astrocytic morphological features were extracted using Harmony, of which 10 were selected for further analysis. These included cytoplasmic area and width-to-length ratio (Fig. 6.9 A&B), nuclear intensity, area and roundness (Fig. 6.10 C, D&E), BODIPY intensity, number and area (Fig. 6.11 F, G&H), and EEA1 intensity and roundness (Fig. 6.12 I&J).

Aβ$_{25-35}$ stress appears to attenuate the genotype-specific differences observed at baseline. Under stress conditions, only one feature that previously distinguished APOE3 from APOE4 astrocytes remained significantly different, such that APOE4 astrocytes still have larger cell

width/length ratio than APOE3 astrocytes even after $A\beta_{25-35}$ stress (Fig. 6.9B - B1, B3). Moreover, the baseline difference in nucleus roundness is reversed under stress, such that APOE4 astrocytes express smaller nucleus roundness than APOE3 astrocytes (Fig. 6.10E - E2, E3). The rest baseline differences are no longer significant. Specifically, BODIPY intensity (Fig. 6.11F -F1, F2, F3), higher in APOE4 astrocytes at baseline, became indistinguishable from APOE3 after $A\beta_{25-35}$ exposure. EEA1 intensity, which was elevated in APOE4 astrocytes (Fig. 6.12I - I2, I3), and EEA1 roundness, which was initially reduced (Fig. 6.12J - J1, J2, J3), also do not show genotype-specific differences under Aβ-induced stress. In other words, features that originally reported significance during baseline comparison between APOE3 and APOE4 astrocytes were not significant anymore after adding Aβ. This suggests that $A\beta_{25-35}$ imposes a general stress response that overrides baseline APOE-dependent differences.

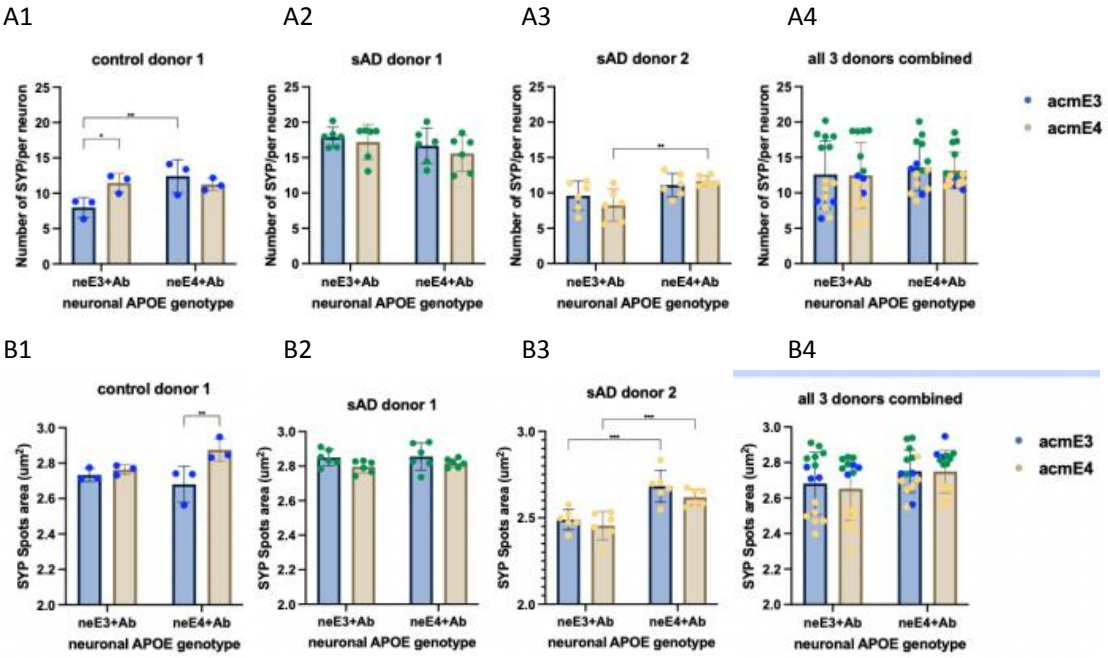



***Fig. 6.5 Neuronal synaptic changes after Aβ$_{25-35}$ exposure in APOE3 and APOE4 neurons treated with APOE3 or APOE4 ACM.*** *Two-way ANOVA results are presented on selected features extracted by Harmony software from ACM treatment experiments comparing APOE3 and APOE4 neurons with or without Aβ$_{25-35}$. Rows A and B represent the size and number of the synaptophysin (SYP), respectively. The 1st panel in each row shows results from control donor 1; the 2nd from control donor 1; the 3rd from sAD donor 2. The 4th panel presents pooled data across all donors, with dot color indicating the donor source: blue = control donor 2; green = sAD donor 1; yellow = sAD donor 2. In each panel, bar colour denotes the ACM source genotype (blue bars = ACM derived from APOE3 astrocytes [acmE3]; beige bars = ACM derived from APOE4 astrocytes [acmE4]). Neuronal APOE genotype (neE3 vs neE4) and Aβ exposure are indicated on the x-axis. Error bars represent ±1 SD. Asterisks indicate significant difference from the control group (*p < .05,** p < .01, ***p < .001).*

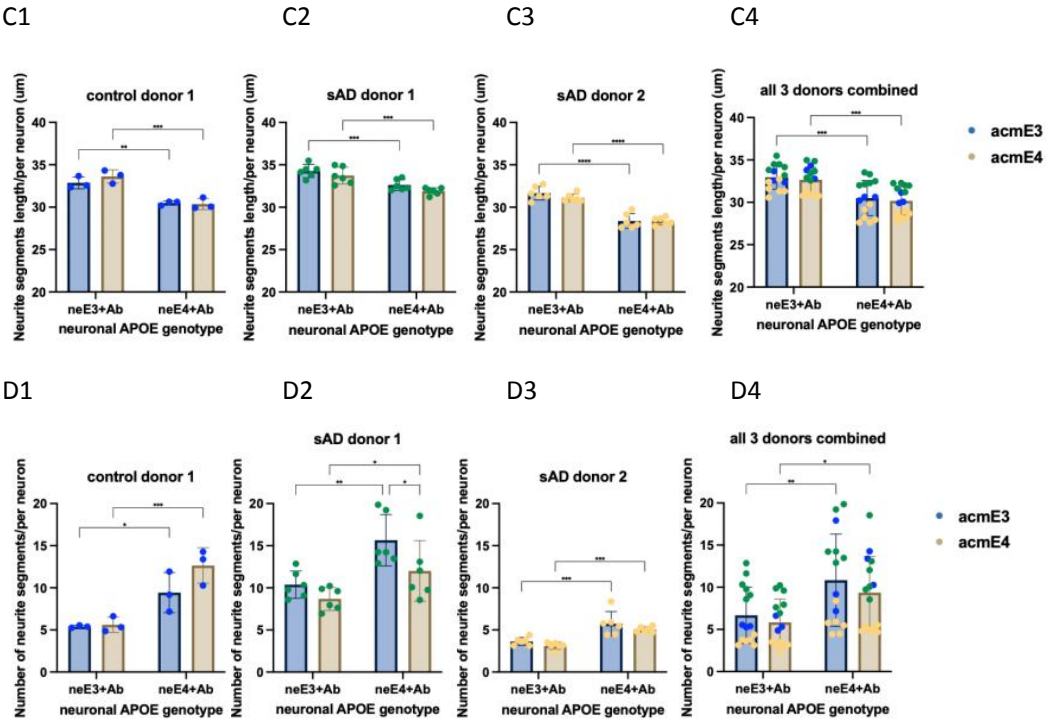



***Fig. 6.6 Neurite changes after Aβ$_{25-35}$ exposure in APOE3 and APOE4 neurons treated with APOE3 or APOE4 ACM.*** *Two-way ANOVA results are presented on selected features extracted by Harmony software from ACM treatment experiments comparing APOE3 and APOE4 neurons with or without Aβ$_{25-35}$. Rows C and D represent the length and number of neurite segments, respectively. The 1st panel in each row shows results from control donor 1; the 2nd from control donor 1; the 3rd from sAD donor 2. The 4th panel presents pooled data across all donors, with dot color indicating the donor source: blue = control donor 2; green = sAD donor 1; yellow = sAD donor 2. In each panel, bar colour denotes the ACM source genotype (blue bars = ACM derived from APOE3 astrocytes [acmE3]; beige bars = ACM derived from APOE4 astrocytes [acmE4]). Neuronal APOE genotype (neE3 vs neE4) and Aβ exposure are indicated on the x-axis. Error bars represent ±1 SD. Asterisks indicate significant difference from the control group (*p < .05,** p < .01, ***p < .001).*

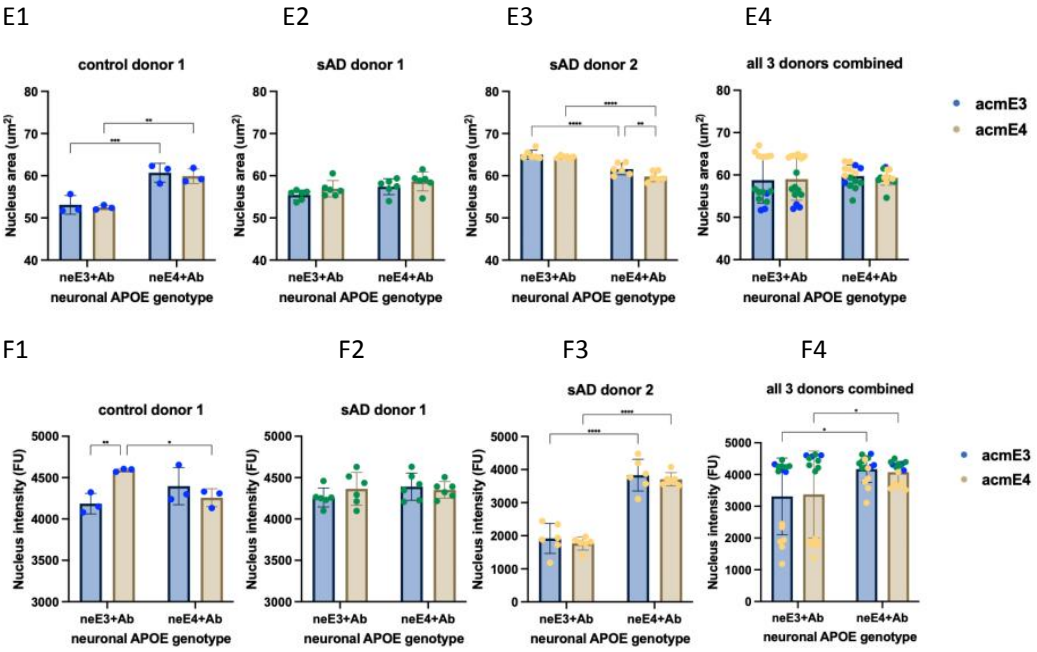



***Fig. 6.7 Neuronal nucleus changes after Aβ$_{25-35}$ exposure in APOE3 and APOE4 neurons treated with APOE3 or APOE4 ACM.*** *Two-way ANOVA results are presented on selected features extracted by Harmony software from ACM treatment experiments comparing APOE3 and APOE4 neurons with or without Aβ$_{25-35}$. Rows E and F represent the size and expression intensity of the nucleus, respectively. The 1st panel in each row shows results from control donor 1; the 2nd from control donor 1; the 3rd from sAD donor 2. The 4th panel presents pooled data across all donors, with dot color indicating the donor source: blue = control donor 2; green = sAD donor 1; yellow = sAD donor 2. In each panel, bar colour denotes the ACM source genotype (blue bars = ACM derived from APOE3 astrocytes [acmE3]; beige bars = ACM derived from APOE4 astrocytes [acmE4]). Neuronal APOE genotype (neE3 vs neE4) and Aβ exposure are indicated on the x-axis. Error bars represent ±1 SD. Asterisks indicate significant difference from the control group (*p < .05,** p < .01, ***p < .001).*

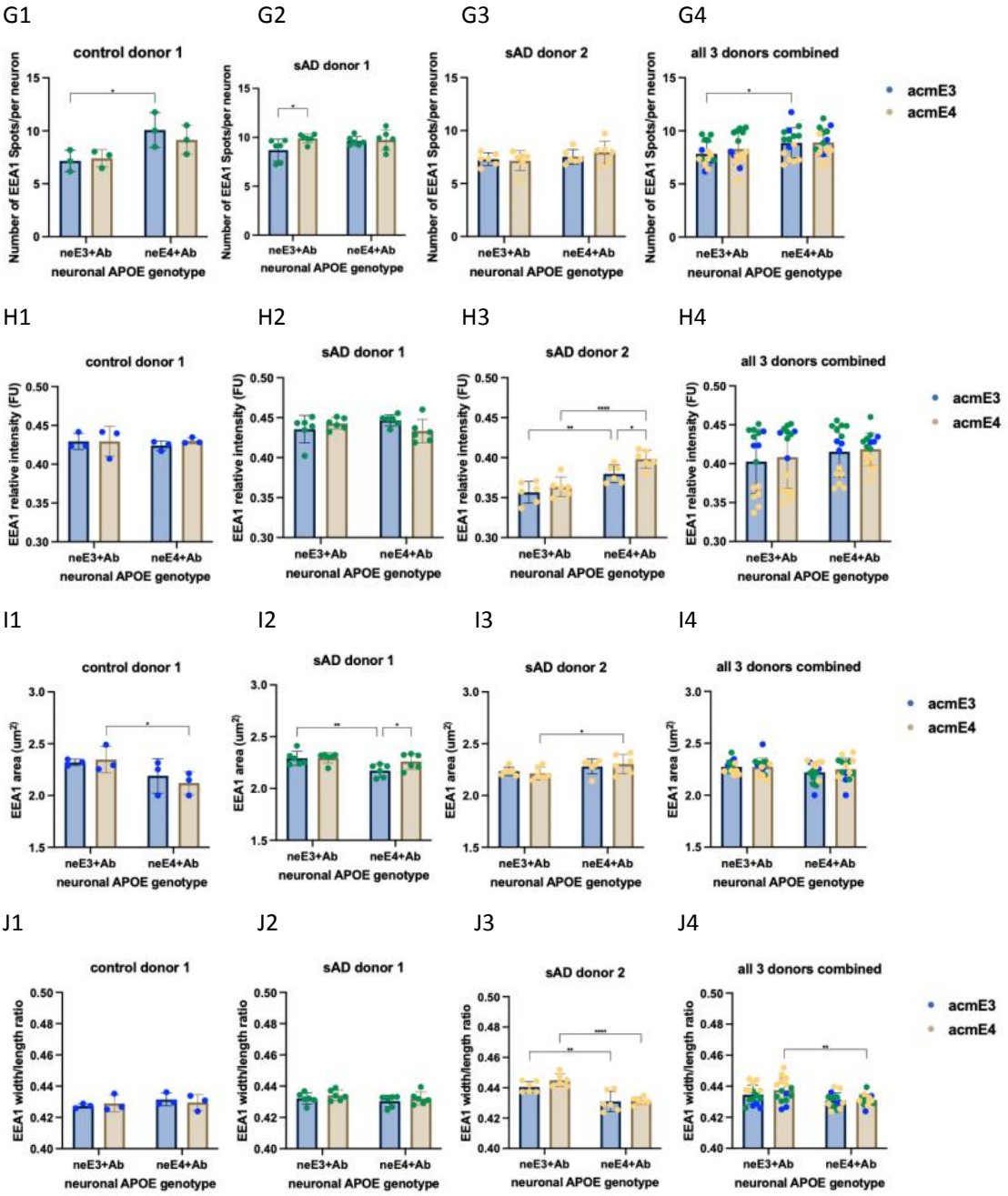



***Fig. 6.8 Neuronal early endosomal changes after Aβ$_{25-35}$ exposure in APOE3 and APOE4 neurons treated with APOE3 or APOE4 ACM.*** *Two-way ANOVA results are presented on selected features extracted by Harmony software from ACM treatment experiments comparing APOE3 and APOE4 neurons with or without Aβ$_{25-35}$. Rows G, H, I, and J represent early endosome features-EEA1 puncta number, intensity, area, and width-to-length ratio, respectively. The 1st panel in each row shows results from control donor 1; the 2nd from control donor 1; the 3rd from sAD donor 2. The 4th panel presents pooled data across all donors, with dot color indicating the donor source: blue = control donor 2; green = sAD donor 1; yellow = sAD donor 2. In each panel, bar colour denotes the ACM source genotype (blue bars = ACM derived from APOE3 astrocytes [acmE3];*

*beige bars = ACM derived from APOE4 astrocytes [acmE4]). Neuronal APOE genotype (neE3 vs neE4) and Aβ exposure are indicated on the x-axis. Error bars represent ±1 SD. Asterisks indicate significant difference from the control group (*p < .05,** p < .01, ***p < .001).*

### *6.2.5. Is this effect dependent on astrocyte genotype?*

Both APOE3 and APOE4 astrocytes responded to $A\beta_{25-35}$ exposure, but the affected features differed between genotypes. In APOE4 astrocytes, Aβ stress led to reduced cytoplasmic area (Fig. 6.9A – A1, A2, A3), decreased EEA1 intensity (Fig. 6.12I – I1, I2, I3), and lower endosomal roundness (Fig. 6.12J – J1, J2, J3) compared to untreated controls. In contrast, APOE3 astrocytes showed reductions in cytoplasmic area (Fig. 6.9A – A2, A3), EEA1 intensity (Fig. 6.12I – I1, I2, I3), and cytoplasmic width-to-length ratio (Fig. 6.9B – B2, B3).

This indicates that while both genotypes are sensitive to $A\beta_{25-35}$, APOE4 astrocytes undergo more pronounced endosomal remodeling, whereas APOE3 astrocytes primarily exhibit cytoplasmic and structural alterations. Such differential vulnerabilities may reflect genotype-specific mechanisms of stress adaptation, with APOE4 astrocytes particularly prone to disruptions in endolysosomal trafficking and morphology.

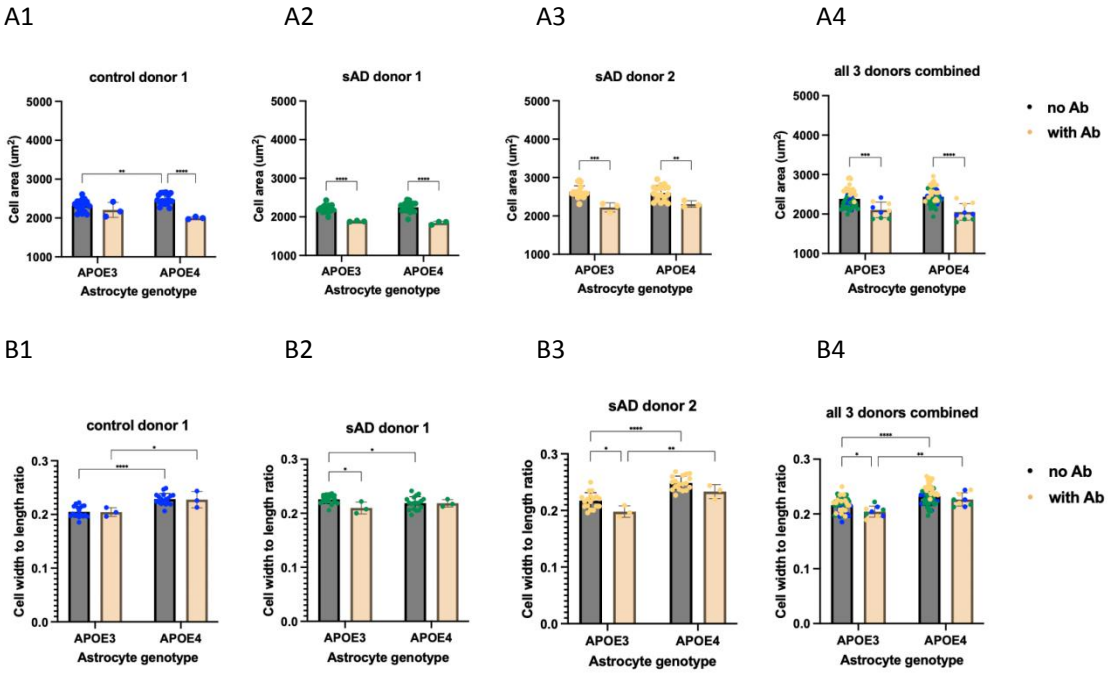



***Fig. 6.9 Cytoplasmic morphology of lentiviral-induced astrocytes in monoculture under Aβ$_{25–35}$ treatment.*** *Two-way ANOVA results are presented for cytoplasmic features extracted by Harmony software. Row A shows the cytoplasmic area, and Row B shows the cytoplasmic width-to-length ratio. The 1st panel in each row corresponds to control donor 1; the 2nd, sAD donor 1; the 3rd, sAD donor 2; and the 4th panel presents pooled data from all three donors. Dot colors indicate donor identity: blue = control donor 1, green = sAD donor 1, yellow = sAD donor 2. Dot colour indicates donor identity (blue = control donor 1; green = sAD donor 1; yellow = sAD donor 2). In each panel, bar colour denotes Aβ exposure (dark grey bars = no Aβ; beige bars = with Aβ). Astrocyte APOE genotype (APOE3 vs APOE4) is indicated on the x-axis. Comparisons were made between APOE3 and APOE4 astrocytes with or without Aβ$_{25–35}$ treatment. Error bars represent ±1 SD. Asterisks indicate significant difference from the control group (*p < .05,** p < .01, ***p < .001).*

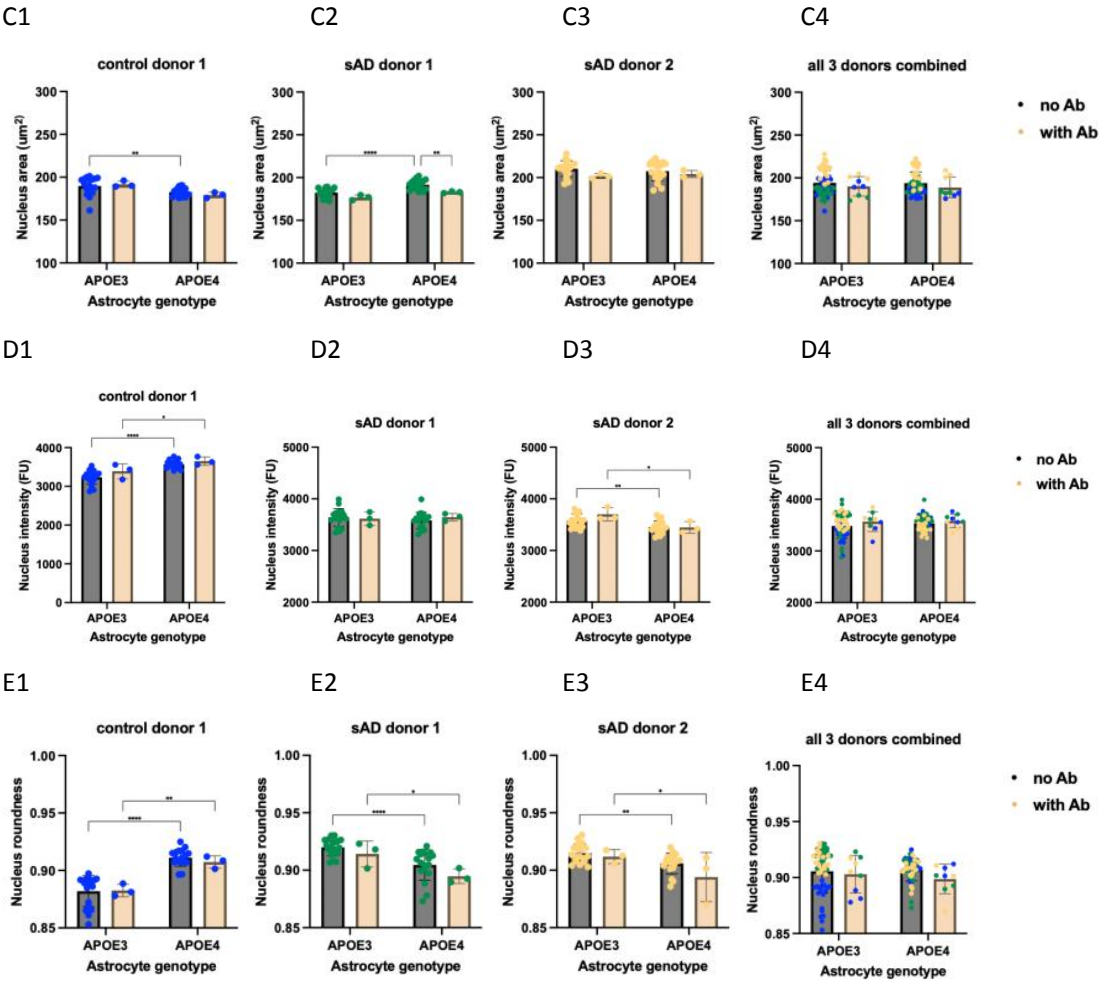



***Fig. 6.10 Nuclear morphological features of lentiviral-induced astrocytes in monoculture under Aβ$_{25–35}$ treatment.*** *Two-way ANOVA results are presented for selected nuclear features extracted by Harmony software. Row C shows nuclear intensity, Row D shows nuclear area, and Row E presents nuclear roundness. The 1st panel in each row corresponds to control donor 1; the 2nd, sAD donor 1; the 3rd, sAD donor 2; and the 4th panel presents pooled data from all three donors. Dot colors indicate donor identity: blue = control donor 1, green = sAD donor 1, yellow = sAD donor 2. Dot colour indicates donor identity (blue = control donor 1; green = sAD donor 1; yellow = sAD donor 2). In each panel, bar colour denotes Aβ exposure (dark grey bars = no Aβ; beige bars = with Aβ). Astrocyte APOE genotype (APOE3 vs APOE4) is indicated on the x-axis. Comparisons were made between APOE3 and APOE4 astrocytes with or without Aβ$_{25–35}$ treatment. Error bars represent ±1 SD. Asterisks indicate significant difference from the control group (*p < .05,** p < .01, ***p < .001).*

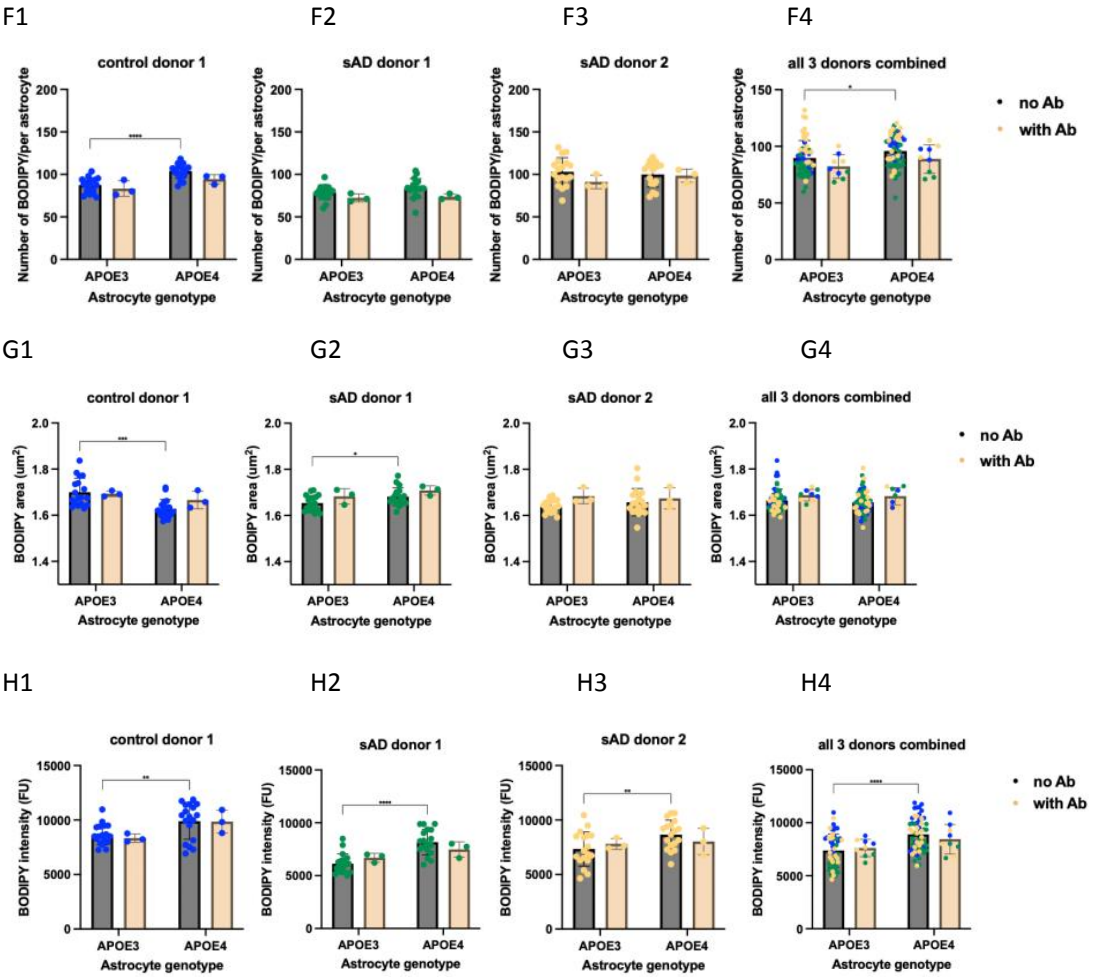



***Fig. 6.11 Astrocytic lipid droplet profiles in monoculture under Aβ$_{25–35}$ treatment.*** *Two-way ANOVA results are presented on selected lipid-associated features extracted by Harmony software from lentiviral-induced astrocyte monocultures. Row F shows BODIPY intensity, Row G represents lipid droplet number, and Row H displays lipid droplet area. The 1st panel in each row corresponds to control donor 1; the 2nd, sAD donor 1; the 3rd, sAD donor 2; and the 4th panel presents pooled data from all three donors. Dot colors indicate donor identity: blue = control donor 1, green = sAD donor 1, yellow = sAD donor 2. Dot colour indicates donor identity (blue = control donor 1; green = sAD donor 1; yellow = sAD donor 2). In each panel, bar colour denotes Aβ exposure (dark grey bars = no Aβ; beige bars = with Aβ). Astrocyte APOE genotype (APOE3 vs APOE4) is indicated on the x-axis. Comparisons were made between APOE3 and APOE4 astrocytes with or without Aβ$_{25–35}$ treatment. Error bars represent ±1 SD. Asterisks indicate significant difference from the control group (*p < .05,** p < .01, ***p < .001).*

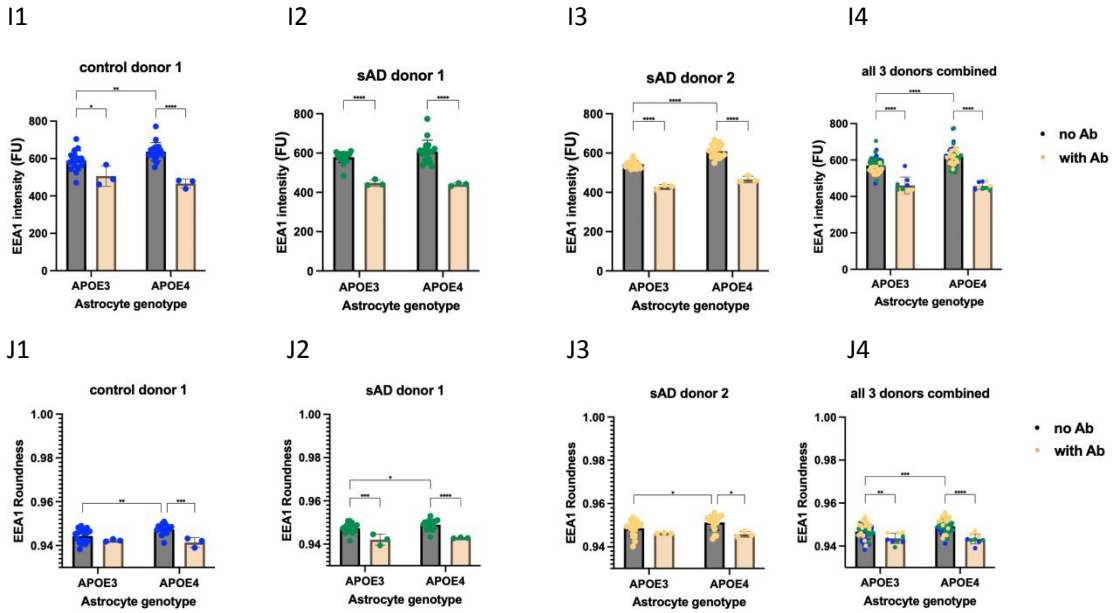



***Fig. 6.12 Astrocytic early endosomal features in monoculture under Aβ$_{25–35}$ treatment.*** *Two-way ANOVA results are presented on selected endosomal features extracted by Harmony software from monocultured astrocytes derived via lentiviral induction. Row I displays EEA1 intensity, and Row J shows EEA1 morphology (width-to-length ratio). The 1st panel in each row corresponds to control donor 1; the 2nd, sAD donor 1; the 3rd, sAD donor 2; and the 4th panel presents pooled data from all three donors. Dot colors indicate donor identity: blue = control donor 1, green = sAD donor 1, yellow = sAD donor 2. Dot colour indicates donor identity (blue = control donor 1; green = sAD donor 1; yellow = sAD donor 2). In each panel, bar colour denotes Aβ exposure (dark grey bars = no Aβ; beige bars = with Aβ). Astrocyte APOE genotype (APOE3 vs APOE4) is indicated on the x-axis. Comparisons were made between APOE3 and APOE4 astrocytes, with or without Aβ$_{25–35}$ treatment. Error bars represent ±1 SD. Asterisks indicate significant difference from the control group (*p < .05,** p < .01, ***p < .001).*

## 6.3. Discussion

Exposure to $A\beta_{25-35}$ substantially altered neuronal morphology in ways that blurred many of the baseline differences between APOE3 and APOE4 neurons. Features that had previously distinguished the two genotypes, such as synaptic puncta size and endosomal parameters, were no longer significant under stress conditions, suggesting that the toxic impact of Aβ imposes a dominant effect on neuronal structure. One difference that persisted was the higher neurite number in APOE4 neurons, indicating that not all genotype-related traits are abolished by Aβ, and that some APOE4-specific morphological trends remain resilient even in the face of acute stress.

Although many baseline distinctions were diminished, the overall neuronal response to $A\beta_{25-35}$ was not equivalent across genotypes. APOE4 neurons exhibited a broader and more complex set of changes than APOE3 neurons, consistent with the idea of selective vulnerability. Whereas APOE3 neurons primarily showed a reduction in neurite length, APOE4 neurons underwent multidimensional remodeling, including loss of synaptic puncta, shortening of neurites, and changes in endosomal intensity and morphology. These observations suggest that Aβ does not uniformly exacerbate pre-existing APOE-dependent differences but instead reveals the heightened susceptibility of APOE4 neurons to additional stressors. In this sense, APOE4 neurons appear to be less able to maintain structural homeostasis, which aligns with their well-established risk profile in AD.

The influence of ACM was also diminished under Aβ stress. In untreated conditions, ACM preserved or even modified certain APOE-dependent differences. However, after Aβ exposure, these influences were largely overridden. Regardless of astrocyte genotype, APOE4 neurons consistently showed more, but shorter, neurites compared to APOE3 neurons, a pattern that may reflect neurite fragmentation or impaired maintenance under stress. Other previously genotype-associated features disappeared altogether, underscoring the idea that Aβ exerts a unifying pathological pressure that eclipses more subtle modulatory effects of astrocytes.

Taken together, these findings indicate that $A\beta_{25-35}$ exposure shifts the balance from genotype-specific differences toward a stress-dominated phenotype, while at the same time unmasking the greater vulnerability of APOE4 neurons. Rather than amplifying baseline APOE-dependent traits, Aβ stress selectively destabilizes APOE4 neurons across multiple cellular domains, including synaptic, neurite, and endosomal pathways. The loss of ACM-mediated modulation further emphasizes that under conditions of acute stress, the intrinsic susceptibility of APOE4 neurons prevails over astrocytic support. This integrated view highlights that the interplay between APOE genotype and Aβ stress is not simply additive but reflects a complex hierarchy in which Aβ exerts dominant effects while exposing genotype-specific weaknesses.

Exposure to $A\beta_{25-35}$ markedly altered astrocytic morphology and largely diminished the baseline differences previously observed between APOE3 and APOE4 astrocytes. Under control conditions, APOE4 astrocytes exhibited distinctive features including higher BODIPY intensity, altered nuclear and endosomal morphology, and increased cytoplasmic width-to-length ratio. However, after Aβ stress, nearly all of these genotype-specific differences disappeared. For example, BODIPY intensity and EEA1 parameters, which distinguished APOE4 astrocytes at baseline, became indistinguishable from APOE3 levels. The only baseline feature that persisted under stress was the increased cytoplasmic width-to-length ratio in APOE4 astrocytes, while nucleus roundness even reversed direction, becoming lower in APOE4 than APOE3 astrocytes. These findings suggest that $A\beta_{25-35}$ imposes a dominant stress program that overrides or masks most APOE-dependent morphological signatures.

Although Aβ reduced the overall contrast between genotypes, both *APOE*3 and *APOE*4 astrocytes reported stress responses, with partially overlapping but also genotype-specific features. Specifically, both APOE3 and APOE4 astrocytes showed reductions in cytoplasmic area and EEA1 intensity, indicating a shared vulnerability affecting cell size and endosomal activity. However, the rest of the changes are diverged. APOE4 astrocytes displayed more pronounced endosomal remodeling, with reductions in EEA1 intensity and roundness that point to impaired endosomal cargo processing and vesicle maturation. By contrast, APOE3 astrocytes exhibited structural shifts, including decreases in cytoplasmic area and

cytoplasmic width-to-length ratio, consistent with altered cell morphology rather than endosomal reorganization.

To probe lipid–metabolic coupling, neuron-to-astrocyte fatty-acid transfer can be traced (e.g., BODIPY-FA pulse–chase or clickable FA labeling) and astrocytic lipid droplets quantified with BODIPY 493/503; observation of larger or more numerous LDs under APOE4 or stress would be consistent with evidence that astrocytes buffer neuron-derived fatty acids in LDs and that APOE4 biases this axis toward inefficient detoxification/usage with reduced neuronal support (Qi et al., 2021c; Smolič et al., 2022). In parallel, early-endosomal pH can be measured and the co-internalization/retention of APOER2 with AMPA/NMDA receptors within EEA1-positive compartments quantified to determine whether APOE4 promotes pH-dependent recycling delays; such delays have been reversed by re-acidifying early endosomes, restoring receptor recycling and synaptic responses (Pohlkamp et al., 2021; Xian et al., 2018). Complementarily in astrocytes, APOE4-linked down-regulation of NHE6 produces hyper-acidified endosomes with LRP1 trapping and impaired Aβ clearance, which has been normalized by restoring NHE6 via HDAC-dependent epigenetic correction (Prasad & Rao, 2018). Collectively, these assays position lipid handling and endosomal pH-recycling as tractable, APOE-dependent determinants of neuroglial coupling and provide testable levers for causal rescue.

Taken together, these results indicate that while $A\beta_{25\text{-}35}$ elicits a general astrocytic stress

response, the specific features affected depend on *APOE* genotype. APOE4 astrocytes appear more prone to perturbations of the endosomal–lysosomal system, a pathway implicated as an early vulnerability in AD, whereas APOE3 astrocytes respond with broader cytoplasmic and nuclear structural changes. These genotype-dependent patterns may reflect distinct strategies of stress adaptation, with APOE4 astrocytes particularly sensitive to disruptions in intracellular trafficking, while APOE3 astrocytes show greater structural plasticity.

# Chapter 7: Drug screening using lentiviral-induced astrocytes reveals feature-specific and genotype-dependent rescue of APOE4-associated phenotypes

## 7.1. Introduction

Baseline characterization established that APOE4 astrocytes consistently diverge from APOE3 astrocytes across several image-derived features that capture nuclear architecture, lipid metabolism, endosomal biology and general cell morphology which could imply potential mechanistic link to pathways implicated in AD (Section 6.2.4). Five endpoints were selected from the baseline APOE3 – APOE4 astrocyte comparisons: nuclear roundness, BODIPY intensity, EEA1 intensity, EEA1 roundness, and cytoplasmic width-to-length ratio. Endpoint selection was based on three complementary criteria: (i) evidence of a reproducible APOE genotype-associated difference across the donor panel; (ii) representation of distinct, non-redundant morphological domains, including nuclear shape, neutral-lipid signal, early-endosomal signal and morphology, and whole-cell geometry; and (iii) readiness to be detected and measured from the images. The selected endpoints therefore balanced cross-donor reproducibility, biological interpretability, and technical suitability for phenotypic screening (Table 7.2). These endpoints were interpreted as morphological proxies for cellular processes implicated in APOE4 biology rather than as direct functional measurements of those pathways.

Specifically, nuclear abnormalities have been linked to chromatin reorganization and stress responses (Iatrou et al., 2021); BODIPY intensity reflects the accumulation of neutral lipids and lipid droplets, which are increasingly recognized as pathological hallmarks in APOE4 contexts (Cashikar et al., 2023); and early endosome morphology (intensity and roundness) reflects endolysosomal trafficking dysfunction which is a central early pathology in sAD (Hu et al., 2015; Kaur & Lakkaraju, 2018). Finally, the cytoplasmic width-to-length ratio represents alterations in cytoskeletal organization and astrocytic morphology, features that mirror key aspects of patient-derived pathophysiology and may carry functional consequences involved in Aβ responses (Rowland et al., 2025). Because the astrocytic cytoskeleton is closely linked to astrocytes' ability to extend fine processes, regulate extracellular space, and maintain contact with synapses, shifts in width-to-length ratio may translate into impaired neuronal support and altered synaptic regulation. Moreover, because APOE is primarily expressed by astrocytes, and astrocytes orchestrate lipid metabolism, synaptic support, and Aβ clearance, these cellular signatures from isogenic iPSCs-derived astrocytes provide a disease-relevant window on APOE4 biology and a principled set of targets for phenotypic rescue.

Building on the robust APOE4-associated phenotypes identified at baseline, a phenotype-based drug screening strategy was implemented in collaboration with GSK. This screening leverages the scalability of iPSC-derived astrocyte models combined with high-content imaging. Specifically, following compound exposure, astrocytes were subjected to the same ICC staining panel used in baseline characterization, imaged and analyzed with

the same pipeline to ensure direct comparability. Specifically, human iPSC-derived astrocytes were generated by lentiviral over-expression of NfiB, producing morphology and marker profiles compatible with a mature astrocytic state. Three independent donors were used. For each donor, isogenic *APOE*3 and *APOE*4 lines were plated and treated with a panel of compounds plus a DMSO vehicle; for exposition in this section, five representative compounds are analyzed in *depth*. Cells were immunostained with the same panel used for baseline characterization, imaged under identical settings, and processed with the same Harmony pipeline. Well-level cellular features were used directly as distributions after quality control; no variance-stabilizing transforms were required because the non-parametric statistics do not assume normality.

The purpose of this screen was to test whether reproducible APOE4-associated astrocyte morphology could serve as tractable phenotypic endpoints for compound prioritisation. It was not designed to identify development-ready therapeutic candidates or to determine which patients would benefit from existing clinical therapies. Rather, the screen was intended as a proof-of-concept assessment of whether selected compounds could shift APOE4 astrocyte morphology towards the donor-matched APOE3 reference, thereby identifying compound–feature relationships for subsequent dose–response, mechanistic and functional validation. Accordingly, rescue in this chapter refers to morphological normalisation towards the APOE3 reference and does not imply restoration of cellular function or clinical efficacy.

The central rationale of this approach is that APOE4-specific abnormalities provide measurable phenotypic readouts that can serve as drug-responsive biomarkers. If treatment with a small molecule normalizes these features and renders APOE4 astrocytes statistically indistinguishable from untreated APOE3 astrocytes, this could be potentially interpreted as a phenotypic rescue. Such a shift would not only validate the relevance of these features as disease-relevant markers but may also highlight the therapeutic potential of candidate compounds. As mentioned, altered lipid handling, cytoskeletal remodeling, and endosomal dysfunction have been repeatedly observed in AD models. The astrocytic phenotypes identified are not only robust *in vitro* markers but also reflect cellular pathways implicated in AD pathology. Additionally, since astrocytes regulate lipid metabolism, synaptic maintenance, and Aβ clearance, rescuing these APOE4-driven phenotypes may alleviate downstream neuronal dysfunction. Thus, identifying compounds that rescue these APOE4-driven abnormalities may alleviate downstream neuronal dysfunction and provide a translational link between cellular pathology and candidate therapeutics in sAD.

To systematically explore this, 42 small molecules including $A\beta_{25-35}$ and DMSO control were tested on APOE3 and APOE4 astrocytes from three donors. These compounds were selected to cover a broad range of mechanisms relevant to AD by GSK. The compound panel was selected to target multiple pathways previously implicated in APOE-associated AD biology, including inflammatory and stress-response pathways. By using APOE4 astrocytes as a disease-prone model and APOE3 astrocytes as controls, the following questions are asked: (1)

which morphological and molecular features of APOE4 astrocytes can be pharmacologically reversed toward an APOE3-like state? (2) are certain features more amenable to drug-induced rescue than others?

Therefore, to answer these questions directly, the phenotypic rescue was operationally defined as a compound-induced shift in APOE4 morphology that reduced APOE4 divergence from the untreated APOE3 reference. At first, a baseline distance between APOE4+vehicle and APOE3+vehicle was quantified for each donor and feature, followed by the research question of whether the compound brings APOE4 closer to the APOE3 reference distribution.

## 7.2. Results

### *7.2.1. APOE4-associated phenotypes exhibit a hierarchy of responsiveness to drug treatment*

Representative ICC images of the lentiviral-induced astrocyte model used for the compound screen are provided in Figure 3.3. Representative examples of the image-analysis workflow used to identify and quantify nuclear, cytoplasmic, EEA1 and BODIPY features are provided in Section 2.8 (Figures 2.5), providing visual context for the five screening endpoints analysed below. Across the three donors, 42 compounds per donor were evaluated across five cellular features using two-sample, two-tailed t-tests comparing APOE4 astrocytes treated with each compound to APOE3 astrocytes receiving vehicle (DMSO). When the ratio

of group standard deviations was < 2, the pooled-variance (Student's) t-test was applied; when the ratio was ≥ 2, Welch's unequal-variances t-test was used.

The results revealed clear heterogeneity in drug responses across the five selected APOE4-associated astrocytic features. Among them, EEA1 roundness emerged as the most pharmacologically sensitive parameter, with 31 compounds capable of restoring this feature toward APOE3-like morphology across all three donors (Table 7.1). Nuclear roundness was the second most drug-sensitive phenotype, rescued by 20 compounds in all donors. This suggests that although nuclear architecture is disrupted in APOE4 astrocytes, it remains relatively plastic and responsive to external modulation. Features associated with EEA1 intensity displayed intermediate sensitivity, with 13 compounds able to normalize this phenotype and partially restore trafficking capacity. By contrast, the cytoplasmic width-to-length ratio and cytoskeletal organization, proved to be the most resistant feature. No compound achieved full rescue across all three donors, and only 13 compounds partially restored this phenotype in two donors, with high variability. BODIPY intensity, reflecting lipid droplet accumulation, was the second most resistant feature. Only 8 compounds significantly reduced lipid droplet burden in APOE4 astrocytes.

Having established that certain features are more readily rescued than others, the next question is to ask whether any compounds could broadly correct multiple aspects of APOE4 pathology simultaneously.

### *7.2.2. Compounds exert pathway-selective rescue effects across APOE4-associated phenotypes*

To further dissect the pharmacological effects, a systematic quantification was performed to assess how many features were reversed across all donors for each small molecule. The analysis revealed a tiered distribution of rescue outcomes: 5 compounds were able to rescue three features as marked in pink in Table 7.1, compounds #220, #660, #033, #085 and #581. Specifically, #220, #660, and #085 change nuclear roundness, EEA1 intensity, and EEA1 roundness of APOE4 astrocytes and make them indistinguishable from APOE3 astrocytes in control across all 3 donors. Compounds #033 and #581 rescue BODIPY intensity, EEA1 intensity, and EEA1 roundness of APOE4 astrocytes. 18 compounds corrected two out of the five, and 16 compounds normalized only a single feature. This pattern indicates that broad-spectrum rescue across all phenotypes represented by the five features is uncommon, whereas partial rescue of selected features is more frequent, consistent with pathway-specific drug actions.

In a parallel validation, the rescue effects were further evaluated under stress conditions using $A\beta_{25-35}$ treatment as a negative control. The same screening pipeline was applied to APOE4 astrocytes exposed to $A\beta_{25-35}$ and compared to APOE3 untreated astrocytes, and across all three donors, no APOE4-associated features were rescued. In other words, the differences between APOE3 astrocytes in DMSO and APOE4 astrocytes in $A\beta_{25-35}$ were significant. This inability of $A\beta_{25-35}$ to normalize any APOE4 phenotypes provides a critical

internal control, reinforcing both the specificity and the validity of the features identified as pharmacologically reversible under baseline conditions.

| donor ID / compound | Nucleus Roundness | | | BODIPY Intensity | | | EEA1 Intensity | | | EEA1 Roundness | | | Cell W/L Ratio | | |
|---|---|---|---|---|---|---|---|---|---|---|---|---|---|---|---|
| | ctrl#1 | sAD#1 | sAD#2 | ctrl#1 | sAD#1 | sAD#2 | ctrl#1 | sAD#1 | sAD#2 | ctrl#1 | sAD#1 | sAD#2 | ctrl#1 | sAD#1 | sAD#2 |
| #233 | 0.003123333 | 0.378104981 | 0.553292052 | 0.944943979 | 0.015398809 | 0.633711451 | 0.579685008 | 0.094035348 | 0.000852378 | 0.302647829 | 0.815399547 | 0.677884974 | 0.006955674 | 1 | 0.0015946 |
| #470 | 0.003546447 | 0.206947423 | 0.291939693 | 0.990977521 | 0.012173475 | 0.667880936 | 0.759650861 | 0.912640519 | 0.026884589 | 1 | 0.524003322 | 0.735241517 | 0.005946921 | 0.613817476 | 0.004302311 |
| #636 | 0.004245944 | 0.060876921 | 0.64451104 | 0.323791535 | 0.015123363 | 0.657972002 | 0.584731625 | 0.838436444 | 0.005154794 | 0.322598578 | 0.691985543 | 0.648967057 | 0.009445478 | 1 | 0.04781057 |
| #101 | 0.004750243 | 1 | 0.260768993 | 0.281852506 | 0.000593647 | 0.717854963 | 0.755203736 | 0.92209077 | 0.00045844 | 0.52444036 | 0.447732723 | 0.62309128 | 0.001872227 | 0.731714996 | 0.001455358 |
| #664 | 0.00335658 | 0.293486221 | 0.80693458 | 0.272608991 | 0.00706909 | 0.631646198 | 0.73781415 | 0.079554714 | 0.052828338 | 0.296808011 | 0.685558098 | 0.338671037 | 0.01016313 | 1 | 0.001364969 |
| #411 | 0.004135234 | 0.214616205 | 0.17729079 | 0.839772876 | 0.480390837 | 0.690696687 | 0.388758761 | 0.075487075 | 0.000527958 | 0.419857503 | 0.88274479 | 0.387395972 | 0.049835253 | 0.708174072 | 0.002569673 |
| #105 | 0.003891422 | 0.029592576 | 0.554197676 | 0.691676472 | 0.03236083 | 0.993940231 | 0.403227641 | 0.611718902 | 0.03118924 | 0.303331956 | 0.719250435 | 0.596819658 | 0.017424411 | 0.114915832 | 0.216237937 |
| #934 | 0.061714139 | 0.019107919 | 0.443614025 | 0.637631684 | 0.056280011 | 0.90249115 | 0.870583949 | 0.008780174 | 0.413455224 | 0.86338424 | 0.633925586 | 0.793919609 | 0.276662329 | 0.052060728 | 0.762620097 |
| #781 | 0.004649475 | 0.104698904 | 0.828593361 | 0.886950013 | 0.008797405 | 0.710906425 | 0.628952567 | 0.882925374 | 0.316860154 | 0.318429356 | 1 | 0.464683949 | 0.002723174 | 1 | 0.195427296 |
| #907 | 0.005305134 | 0.279675817 | 0.835239291 | 0.718730824 | 0.00437147 | 0.698388153 | 0.752805733 | 1 | 0.280233923 | 0.317749052 | 0.736387397 | 0.011593794 | 0.877236056 | 0.778740647 | 0.048365084 |
| #153 | 0.004524841 | 0.220243659 | 0.987231133 | 0.113133687 | 0.018823975 | 0.647206459 | 0.401108783 | 0.905489537 | 0.01135586 | 0.41399464 | 0.739203476 | 0.620479499 | 0.006445006 | 1 | 0.002171842 |
| #769 | 0.003341314 | 0.482091033 | 0.825212948 | 0.232568436 | 0.000581102 | 0.813876248 | 0.773898073 | 0.108730817 | 0.008040498 | 0.309237426 | 0.827367101 | 0.319052018 | 0.001609789 | 1 | 0.001873506 |
| #965 | 0.014315015 | 0.102445703 | 0.080715723 | 0.324054931 | 0.004401649 | 0.788280218 | 0.326249691 | 0.829397911 | 0.277732475 | 0.418924862 | 0.7601903 | 0.74977837 | 0.005686708 | 0.396517756 | 0.12562944 |
| #488 | 0.004524396 | 0.021512442 | 0.191372824 | 0.816498877 | 0.005305803 | 0.475773096 | 0.575640669 | 0.730832753 | 0.001550278 | 0.384048759 | 0.725139833 | 0.493850101 | 0.005709621 | 0.279323532 | 0.031665646 |
| #563 | 0.004701743 | 0.02828787 | 0.087738979 | 0.142062355 | 0.023202803 | 0.693941479 | 0.295960118 | 0.06952967 | 0.273399636 | 0.368730503 | 0.932857521 | 0.950987364 | 0.007021802 | 0.756302909 | 0.007393947 |
| #48L | 0.008620136 | 0.024715433 | 0.08373039 | 0.361376569 | 0.138670308 | 0.828625727 | 0.548767005 | 0.148267335 | 0.073819179 | 0.94213828 | 0.909337729 | 0.784107497 | 0.014298471 | 0.193039001 | 0.003464876 |
| #12X | 0.010841556 | 0.032620392 | 0.258258832 | 0.306654433 | 0.006635932 | 0.64851467 | 0.47709118 | 0.944629717 | 0.191454112 | 0.370797483 | 0.70484281 | 0.989543811 | 0.005741287 | 0.730942101 | 0.009244023 |
| #307 | 0.008193642 | 0.023454547 | 0.487097569 | 0.818179259 | 0.086237315 | 0.904102497 | 0.776623436 | | 0.034675942 | 0.797031139 | 0.654333666 | 1 | 0.008650581 | 0.145047223 | 0.005219329 |
| #053 | 0.038555204 | 0.067298887 | 0.09687876 | 0.644123272 | 0.011871463 | 0.722414466 | 0.494409403 | 0.874985175 | 0.005112234 | 0.775428137 | 0.684955611 | 0.607521273 | 0.011758696 | 0.446557948 | 0.008443599 |
| #906 | 0.038634324 | 0.024807112 | 0.57086258 | 0.95043198 | 0.414119253 | 0.665860523 | 0.348095471 | 0.886203374 | 0.015333829 | 0.4194131 | 0.97518141 | 0.752200414 | 0.007036447 | 0.851553044 | 0.009170296 |
| #983 | 0.003731699 | 0.113828107 | 0.672510197 | 0.15248384 | 0.011898245 | 0.962525178 | 0.776837549 | 0.955112697 | 0.030398507 | 0.300009572 | 0.738299936 | 0.478528087 | 0.009953775 | 1 | 0.002238414 |
| #763 | 0.003772976 | 0.018409678 | 0.133544898 | 0.80060806 | 0.144666232 | 0.706325812 | 0.522556137 | 0.922039268 | 0.00169823 | 0.348532858 | 0.952142035 | 1 | 0.016063554 | 0.452326133 | 0.008663774 |
| #835 | 0.037657145 | 0.03828773 | 0.030792409 | 0.77072259 | 0.015928182 | 0.710996872 | 0.994146994 | 0.599363863 | 0.715632027 | 0.41924349 | 0.649460224 | 0.940001995 | 0.161781556 | 0.024079936 | 0.488493689 |
| #901 | 0.004318134 | 0.217363452 | 0.626942191 | 0.125417028 | 0.015162654 | 0.92887448 | 0.393310406 | 0.926289634 | 0.345658849 | 0.30796345 | 0.682517054 | 0.921353738 | 0.036874111 | 0.929331573 | 0.1580221 |
| #695 | 0.004123139 | 0.196223524 | 0.445610619 | 0.141105243 | 0.032595727 | 0.772260812 | 0.491860272 | 0.885903221 | 0.418881845 | 0.735649823 | 0.794372326 | 0.76522588 | 0.006169286 | 0.449318406 | 0.255509239 |
| #706 | 0.003411131 | 0.115375952 | 0.806044226 | 0.505129683 | 0.003220054 | 0.784115088 | 0.387871276 | 0.083502566 | 0.291813171 | 0.355099081 | 0.711327553 | 1 | 0.028490875 | 1 | 0.361531317 |
| #211 | 0.004626803 | 0.020923471 | 0.445591145 | 0.212871716 | 0.077398079 | 0.904634947 | 0.357389551 | 0.924324898 | 0.299825763 | 0.316387413 | 0.966655227 | 0.740077975 | 0.00649503 | 0.813143626 | 0.400794695 |
| #154 | 0.009405502 | 0.035153696 | 0.28915403 | 0.793344579 | 0.192585235 | 0.8427749 | 0.748511972 | 0.473048928 | 0.000819908 | 0.7746069 | 1 | 1 | 0.028557683 | 1 | 0.00778048 |
| #645 | 0.003894696 | 0.117581693 | 0.781186727 | 0.155968139 | 0.109689311 | 0.662003345 | 0.759492877 | 0.93132348 | 0.005305088 | 0.334947595 | 0.988648646 | 0.360326908 | 0.009645472 | 1 | 0.004058979 |
| #766 | 0.002488012 | 0.285597601 | 0.633856194 | 0.161934673 | 0.002619479 | 0.748724287 | 0.729508916 | 0.995454159 | 0.03127868 | 0.331665935 | 0.688339194 | 0.584778686 | 0.002317315 | 0.742250236 | 0.00186159 |
| #956 | 0.014731998 | 0.234689163 | 0.385362678 | 0.2852229 | 0.001909228 | 0.931475821 | 0.312365413 | 0.899094732 | 0.016061444 | 0.312405825 | 0.898513102 | 0.451241885 | 0.003800993 | 1 | 0.005335793 |
| #448 | 0.004795131 | 0.11855353 | 0.293127822 | 0.816971684 | 0.028913617 | 0.675449752 | 1 | 0.579694224 | 0.101353956 | 0.997463748 | 0.787488937 | 1 | 0.033730732 | 0.995322535 | 0.360712442 |
| #077 | 0.005573628 | 0.363884704 | 0.327991269 | 0.69863706 | 0.010537369 | 0.604433148 | 0.352428443 | 0.972898973 | 0.016344359 | 0.964196434 | 0.708756099 | 0.543100027 | 0.019765995 | 1 | 0.000402498 |
| #220 | 0.050292933 | 0.28502213 | 0.310679379 | 0.6465011 | 0.055571637 | 0.809089521 | 0.478816598 | 0.925346522 | 0.497840535 | 0.857392108 | 1 | 1 | 0.088084044 | 0.988700045 | 0.021022151 |
| #660 | 0.003263486 | 0.735896865 | 0.865784102 | 0.85548338 | 0.002378821 | 0.735567483 | 0.913979636 | 0.822453781 | 0.304408527 | 0.321949138 | 0.65155293 | 0.353488203 | 0.001367895 | 0.418295043 | 0.007979057 |
| #033 | 0.004703739 | 0.08018345 | 0.856230636 | 0.63020799 | 0.592081037 | 0.749406269 | 0.521713021 | 0.918582422 | 0.424407617 | 0.333777722 | 1 | 0.561889684 | 0.019623591 | 0.887587536 | 0.582226307 |
| #085 | 0.005675353 | 0.982895241 | 0.829859042 | 0.654447129 | 0.005001387 | 0.658155742 | 0.877908618 | 0.231695204 | 0.765641868 | 0.411748306 | 0.996012558 | 0.995996355 | 0.006230986 | 0.958189247 | 0.215592674 |
| #581 | 0.009679049 | 0.371145957 | 0.270171293 | 0.876000892 | 0.01440563 | 0.671628205 | 1 | 0.851369917 | 0.335807107 | 0.803273591 | 0.697847144 | 1 | 0.049110206 | 1 | 0.003687376 |

***Table 7.1. Statistical summary of drug-induced phenotypic rescue across three donors and five cellular features (with BH–FDR correction).***
*The table lists q-values (Benjamini-Hochberg False Discovery Rates (BH-FDR) adjusted p-values) from two-sample, two-tailed t-tests comparing each cellular feature in drug-treated APOE4 astrocytes to that of the untreated APOE3 (DMSO vehicle) control, for each of the three donors (control donor 1 – ctrl#1,* sAD donor 1 – sAD#1, *,* sAD donor 2 – sAD#2*). Representative features include nuclear roundness, BODIPY intensity*

*(neutral lipid droplets), EEA1 intensity, EEA1 roundness (early endosomes), and cytoplasmic width: length (cell geometry). The unit of analysis is well-level feature distributions from high-content images (identical ICC panel and acquisition settings as baseline assays). When the ratio of group standard deviations was < 2, a pooled-variance (Student's) t-test was used; when ≥ 2, Welch's unequal-variances t-test was applied. Multiple comparisons were controlled with BH-FDR across all donor × feature × compound contrasts in this table (family-wise FDR target 0.05); the table displays the resulting q-values. Red text denotes comparisons where the baseline APOE4-APOE3 phenotypic gap was maintained, indicating a lack of rescue. Pink highlighting identifies compounds that normalized three out of the five APOE4-associated features across 3 donors.*

### *7.2.3. Validating candidate compounds with distribution-based analysis*

Following the initial screening, 5 compounds were identified that altered at least three of the five predefined cellular features in APOE4 astrocytes relative to APOE3 vehicle controls. To determine whether the mean-level shifts detected by t-tests reflected genuine distributional normalization toward APOE3, a donor-resolved, non-parametric analysis was performed using two-sample, two-tailed Kolmogorov–Smirnov (KS) tests. To quantify the degree of this phenotypic rescue, rescue indices were calculated. Conceptually, these indices measure how much a treatment 'closes the gap' between the APOE4 and APOE3 states with a scale from 0 (no rescue) to 1 (perfect APOE3-like state). The distribution-level rescue index ($R_{KS}$) assesses whether the entire shape of the APOE4 cell population's distribution becomes more like the APOE3 population. The location-level rescue index ($R_{median}$) specifically measures the convergence of the median toward the APOE3 reference. This approach allowed us to distinguish between partial and full rescue, and to detect whether a drug affected all cells or only a subset of cells strongly.

The baseline measurements, summarized in Table 7.2, were essential for interpreting rescue directionality. BODIPY intensity, EEA1 intensity, and EEA1 roundness were consistently higher in APOE4 than in APOE3 across all donors, so successful rescue is expected to reduce these values. The cell width-to-length ratio also shows APOE4 exceeding APOE3 in control donor 1 and sAD donor 2. Nuclear roundness shows APOE3 > APOE4 in sAD donor 1 and sAD donor 2, so rescue implies an increase of nuclear roundness in APOE4. These baselines are

essential for interpreting the empirical cumulative distribution function (ECDF) overlays and for excluding when a treatment effect that looks 'large' is actually moving in the wrong direction, making treated APOE4 more deviated from untreated APOE3.

| donor | feature | D_base | p_base | med_E4_base | med_E3_base | delta_base |
|---|---|---|---|---|---|---|
| control 1 | Nucleus_Roundness | 0.888889 | 1.33E-06 | 0.93425 | 0.92045 | 0.0138 |
| control 1 | BODIPY_Intensity | 0.555556 | 0.007732 | 10142 | 8506 | 1636 |
| control 1 | EEA1_Intensity | 0.444444 | 0.05713 | 621.1 | 597.7 | 23.4 |
| control 1 | EEA1_Roundness | 0.555556 | 0.007732 | 0.9475 | 0.9455 | 0.002 |
| control 1 | Cell_Ratio_Width_to_Length | 0.777778 | 3.73E-05 | 0.2263 | 0.20395 | 0.02235 |
| sAD 1 | Nucleus_Roundness | 0.666667 | 0.000671 | 0.93605 | 0.9415 | -0.00545 |
| sAD 1 | BODIPY_Intensity | 0.722222 | 0.000167 | 8294.5 | 5878.5 | 2416 |
| sAD 1 | EEA1_Intensity | 0.444444 | 0.05713 | 606.55 | 587.65 | 18.9 |
| sAD 1 | EEA1_Roundness | 0.444444 | 0.05713 | 0.94905 | 0.94765 | 0.0014 |
| sAD 1 | Cell_Ratio_Width_to_Length | 0.333333 | 0.27 | 0.21935 | 0.22665 | -0.0073 |
| sAD 2 | Nucleus_Roundness | 0.5 | 0.022218 | 0.93055 | 0.9368 | -0.00625 |
| sAD 2 | BODIPY_Intensity | 0.5 | 0.022218 | 8828 | 6815.5 | 2012.5 |
| sAD 2 | EEA1_Intensity | 0.833333 | 7.45E-06 | 606.3 | 545.65 | 60.65 |
| sAD 2 | EEA1_Roundness | 0.5 | 0.022218 | 0.9524 | 0.94975 | 0.00265 |

***Table 7.2. Baseline separation of APOE3 and APOE4 astrocytes across donors quantified by Kolmogorov–Smirnov (KS) tests.***

*High-content imaging features were extracted from isogenic iPSC-derived astrocytes (APOE3 vs APOE4) for each donor (control 1, sAD 1, sAD 2) under vehicle (DMSO) conditions. For every donor–feature pair (Nucleus_Roundness, BODIPY_Intensity, EEA1_Intensity, EEA1_Roundness, Cell_Ratio_Width_to_Length), two-sample KS tests were used to assess distributional differences between APOE4 and APOE3 astrocytes. D_base ($D_{base}$) denotes the KS test statistic; p_base reports the corresponding p-value for the null hypothesis of identical distributions; med_E4_base and med_E3_base give the median baseline values for APOE4 and APOE3 astrocytes, respectively. delta_base ($\Delta_{base}$) represents the median shift (med_E4_base – med_E3_base), indicating the direction and magnitude of the APOE4 effect for each feature. Together, these metrics summarize the robustness and consistency of APOE4-associated morphological differences across donors and guide selection of features for downstream drug-rescue analyses.*

### *7.2.4. Compound-specific rescue profiles reveal feature selectivity and donor heterogeneity*

The five candidate compounds were re-evaluated across the five focal features within each donor, inducing a significant distributional shift in APOE4 astrocytes toward the APOE3 reference. This convergence is visualized by the ECDFs in Figures 4.1-4.5, where successful rescue is evidenced by the APOE4 curve overlapping with the APOE3 curve, accompanied by a reduction in the area between them and convergence of the medians. The distribution-level ($R_{KS}$) and location-level ($R_{median}$) rescue indices, along with combined and adjusted p-values, quantitatively confirmed these effects for specific compound-feature pairs.

Compound #085 produced the most compelling and coherent rescue on nuclear roundness (Fig. 4.1A). In sAD donor 1 and 2, ECDFs of APOE4 + #085 shifted toward APOE3 + DMSO vehicle, with medians shifting in the correct direction and the area between curves appreciably reduced and the Fisher-combined permutation q-value crossed conventional thresholds for significance. Bootstrap intervals excluded zero for the primary indices in the donors that contributed most strongly, and trimming analyses retained positive rescue, indicating that the result is not an artifact of a few extreme cells. The control donor 1 contributed less to the combined signal, which is consistent with the donor's modest and even inverted baseline direction for this feature.

The same compound also tended to improve EEA1 roundness (Fig. 7.1D), with positive mean rescue indices and concordant ECDF shifts, although combined significance was not reached.

In contrast, BODIPY intensity did not improve for this compound at the overall level, and the combined KS analysis suggested movement away from APOE3 (Fig. 7.1B).

Compound #220 exhibited feature-selective rescue with clear donor-specificity (Fig. 7.2). The strongest pattern was observed for EEA1 roundness, where ECDFs showed narrowing of the APOE4–APOE3 gap across 3 donors, especially in the control donor 1 (Fig. 7.2D). Distribution rescue index was moderate to large, and the permutation-combined q-value approached significance after BH correction. The location rescue index was also positive for BODIPY intensity, with particularly clean rescue patterns in the control donor 1, although the distribution-level index was smaller and donor heterogeneity larger. EEA1 intensity showed a robust improvement in sAD donor 2 with weaker or absent shifts in the other donors (Fig. 7.2C). Nuclear roundness did not show consistent benefits for this compound (Fig. 7.2A), and the cytoplasmic width-to-length ratio exhibited modest average rescue with sAD donor 1 contributing the majority of the effect, the control donor 1 remaining equivocal and sAD donor 2 showing no clear improvement (Fig. 7.2E).

Compound #660 also yielded a feature-selective profile (Fig. 7.3). The most favorable result was for EEA1 intensity, particularly in the sAD donor 1, where APOE4 distributions moved substantially toward the APOE3 reference and medians converged accordingly (Fig. 7.3C). The donor-combined level permutation combination supported this effect with near-significant q-values. At the same time, EEA1 roundness (Fig. 7.3D) and the cell

width-to-length ratio (Fig. 7.3E) did not support a rescue claim, and the nuclear roundness (Fig. 7.3A) and BODIPY intensity (Fig. 7.3B) were largely unchanged on average.

Compound #033 produced mixed outcomes dominated by donor-specific signals (Fig. 7.4). EEA1 intensity improved convincingly in sAD donor 1, with ECDF overlays and per-donor permutation results consistent with rescue, whereas the other 2 donors did not move appreciably (Fig. 7.4C). For the cell width-to-length ratio, sAD donor 2 suggested improvement but other donors did not (Fig. 7.4E), and for BODIPY intensity the median shifted toward APOE3 while the distribution index remained near zero, yielding a modest overall effect (Fig. 7.4B). Nuclear roundness (Fig. 7.4A) and EEA1 roundness (Fig. 7.4D) showed no consistent changes when combining donors together. These findings place #033 in a category of compounds that can partially normalize early endosomal intensity in specific donor contexts without effects on nuclear and early endosomal shape.

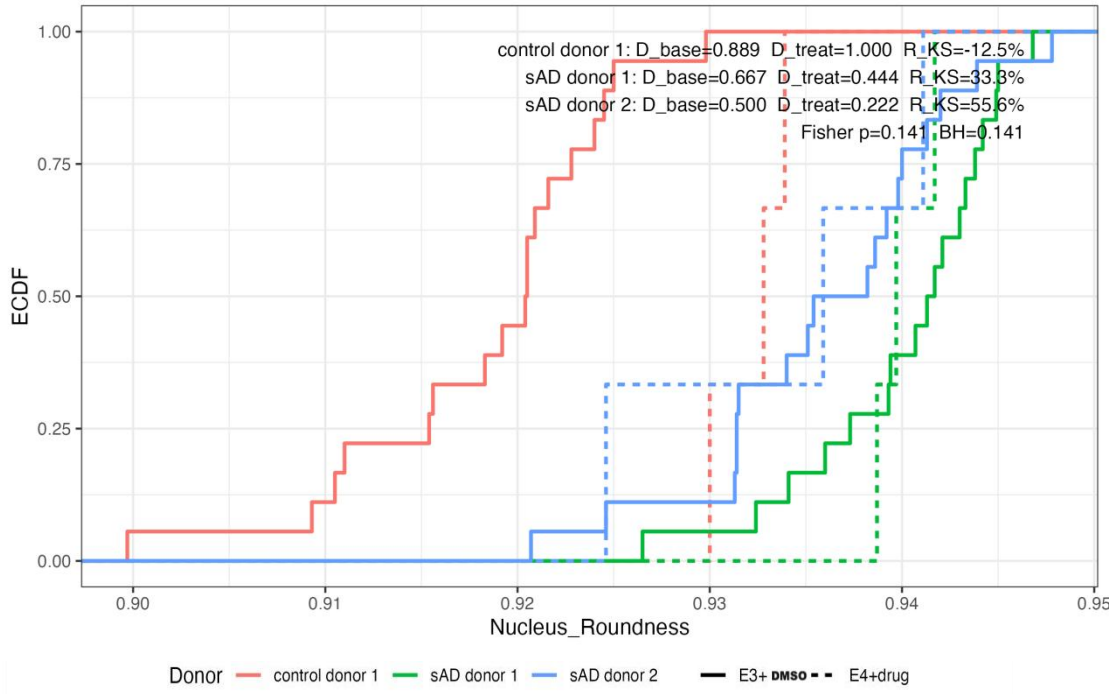
Compound #581 displayed improvements across multiple features predominantly for control donor 1 (Fig. 7.5). Positive but modest median-level rescue was observed for nuclear roundness, BODIPY intensity, EEA1 intensity and EEA1 roundness (Fig. 7.5A, B, C & D), with distributional indices close to zero and study-level permutation q-values above significance thresholds. The cytoplasmic width-to-length ratio behaved similarly (Fig.7.5E).

A key finding across all compounds was that rescue was feature-specific and often donor-dependent, highlighting the influence of individual genetic background on drug

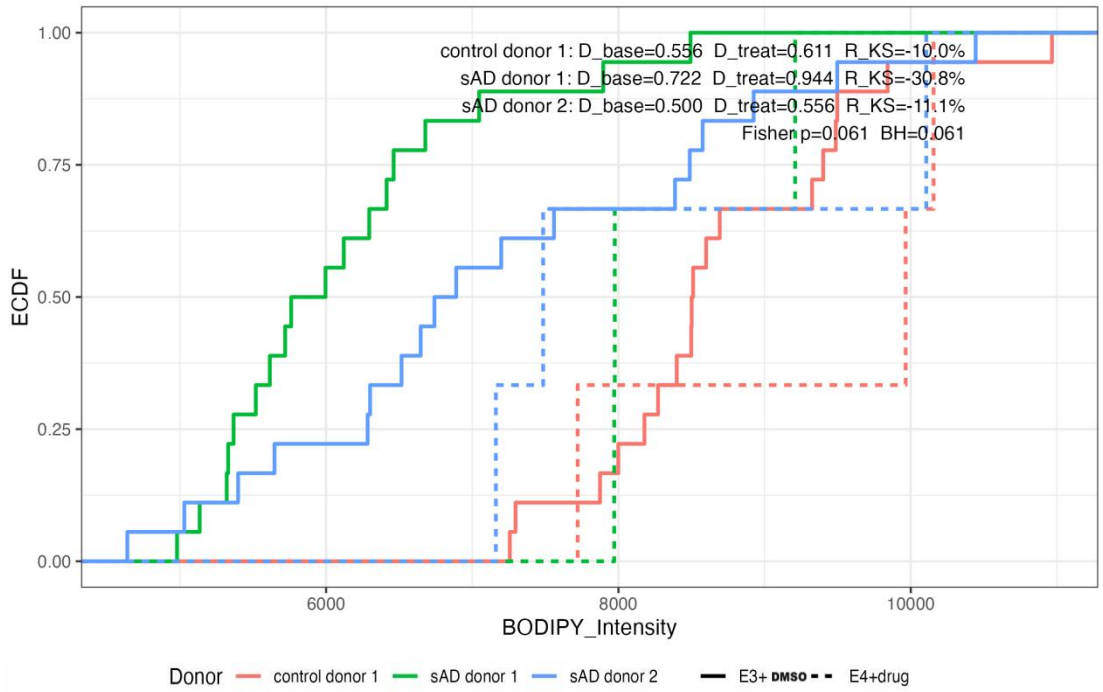
response.

Figure 7.1.

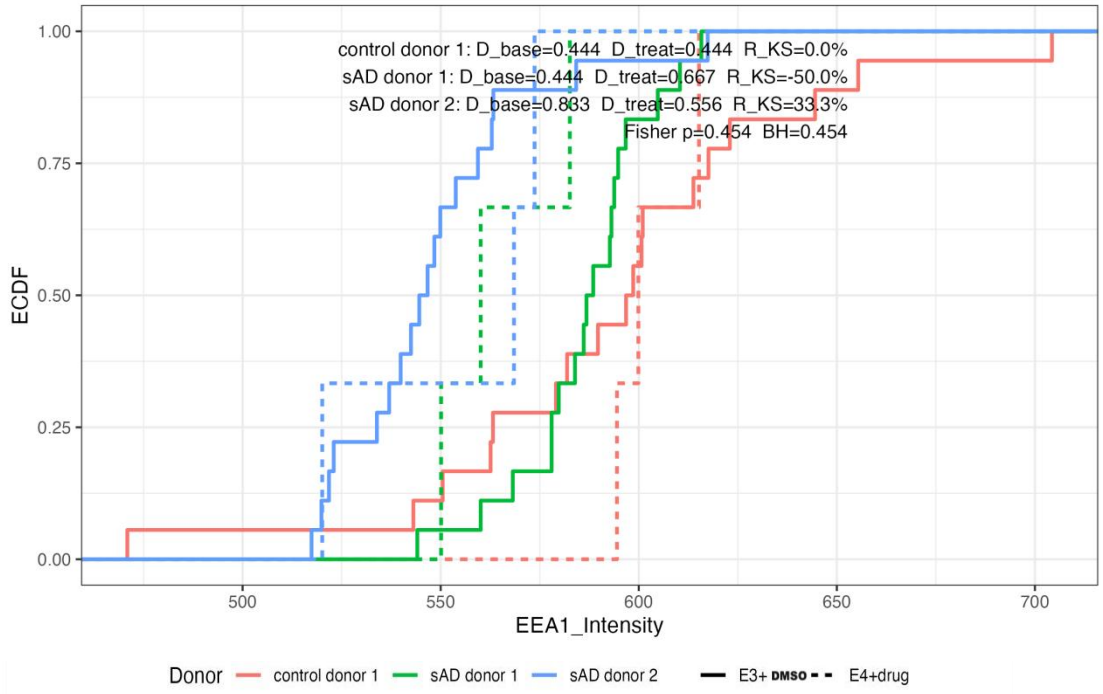
A. ECDF - Compound #085 Feature: Nucleus_Roundness



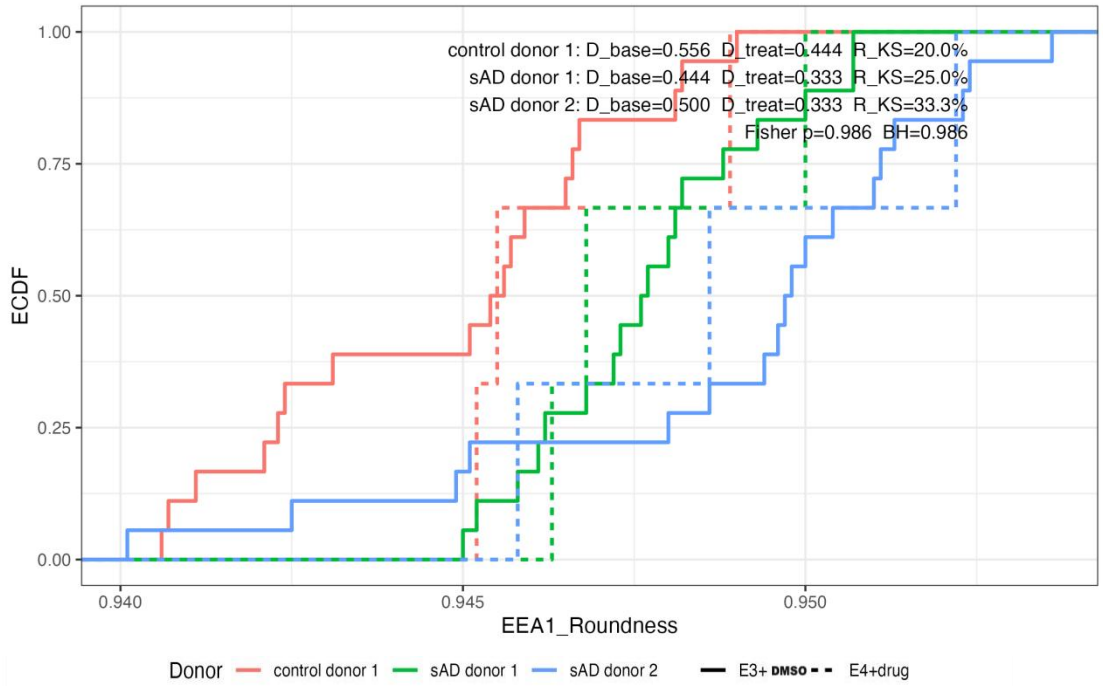

B. ECDF - Compound #085 Feature: BODIPY_Intensity



C. ECDF - Compound #085 Feature: EEA1_Intensity




D. ECDF - Compound #085 Feature: EEA1_Roundness



E. ECDF - Compound #085 Feature: Cell_Ratio_Width_to_Length

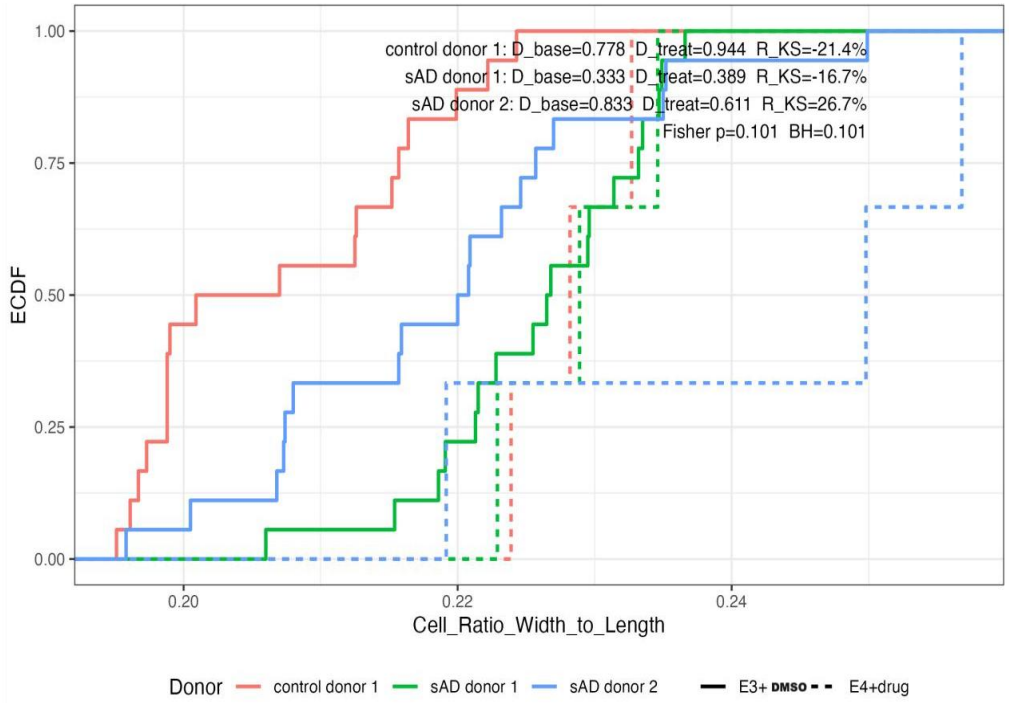



***Figure 7.1. Empirical cumulative distribution functions (ECDFs) for APOE4 + Compound #085 compared to the APOE3 + vehicle (DMSO).*** *The figure shows the comparison within each donor (control donor 1, sAD donor 1, sAD donor 2). Donor-matched APOE4 + vehicle curves are overlaid to show the baseline APOE4–APOE3 gap for that same donor. Colored/linetyped curves denote donor-specific APOE4 + drug and their corresponding APOE4 + vehicle controls; dotted vertical lines mark per-curve medians. The inset in each panel reports per-donor Kolmogorov–Smirnov distance D and the one-sided permutation p (adjusted by BH within panel) testing whether the drug reduces the APOE4–APOE3 distance relative to baseline; the combined (Fisher) value summarizes evidence across donors.*

*Panels (A–E) correspond to the five features:*

*(A) Nucleus roundness—rescue corresponds to a rightward shift of the APOE4 + drug curve toward the APOE3 reference (baseline: APOE3 > APOE4).*

*(B) BODIPY intensity—rescue corresponds to a leftward shift (baseline: APOE4 > APOE3).*

*(C) EEA1 intensity—rescue corresponds to a leftward shift.*

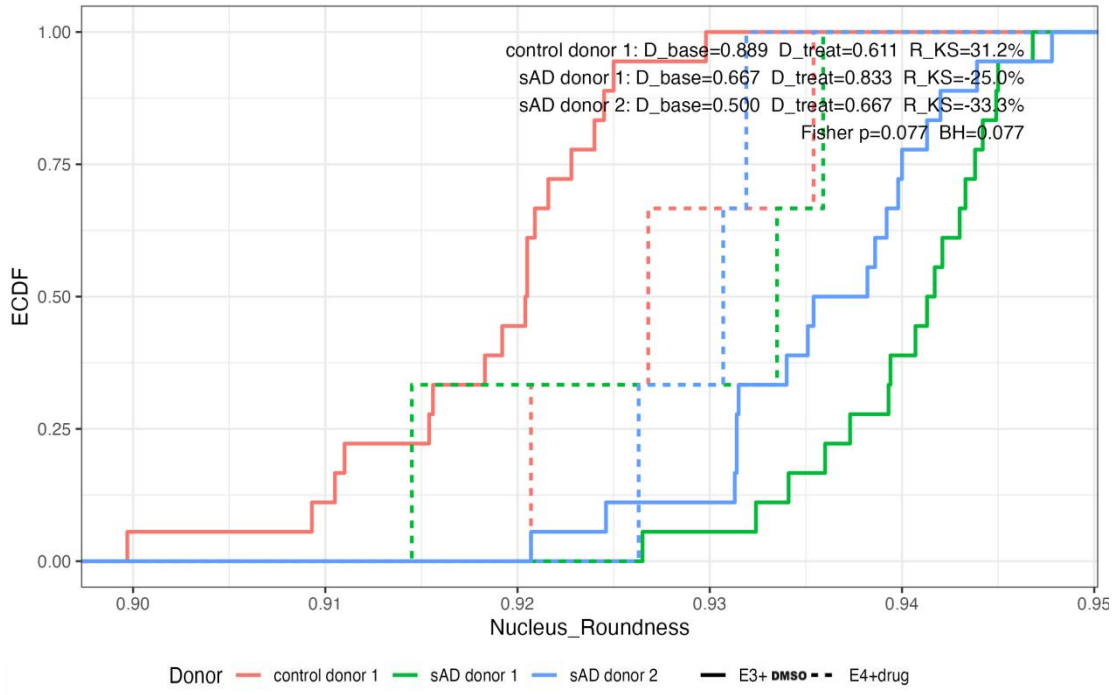
*(D) EEA1 roundness—rescue corresponds to a leftward shift.*

*(E) Cell width-to-length ratio —rescue corresponds to a leftward shift.*

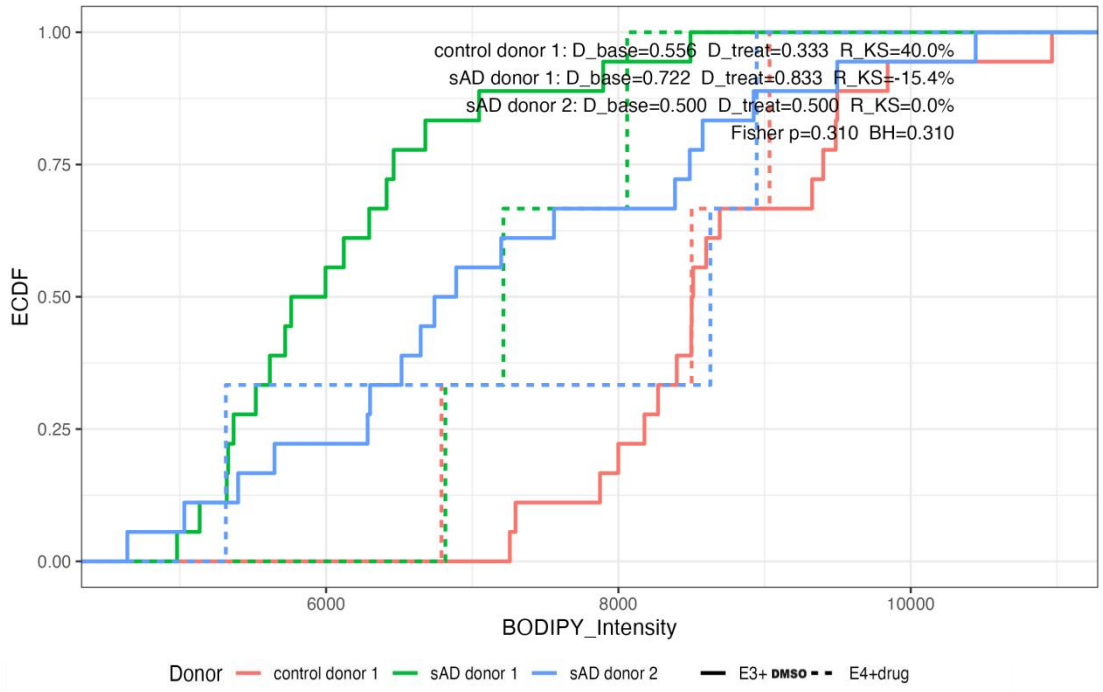
*Definition of rescue: $D_{treat}$ =KS (APOE4+drug, APOE3+vehicle) < $D_{base}$ =KS (APOE4+DMSO, APOE3+DMSO) in the same donor and feature. P-values are BH-adjusted within the panel; Fisher combination is across donors.*

Figure 7.2.

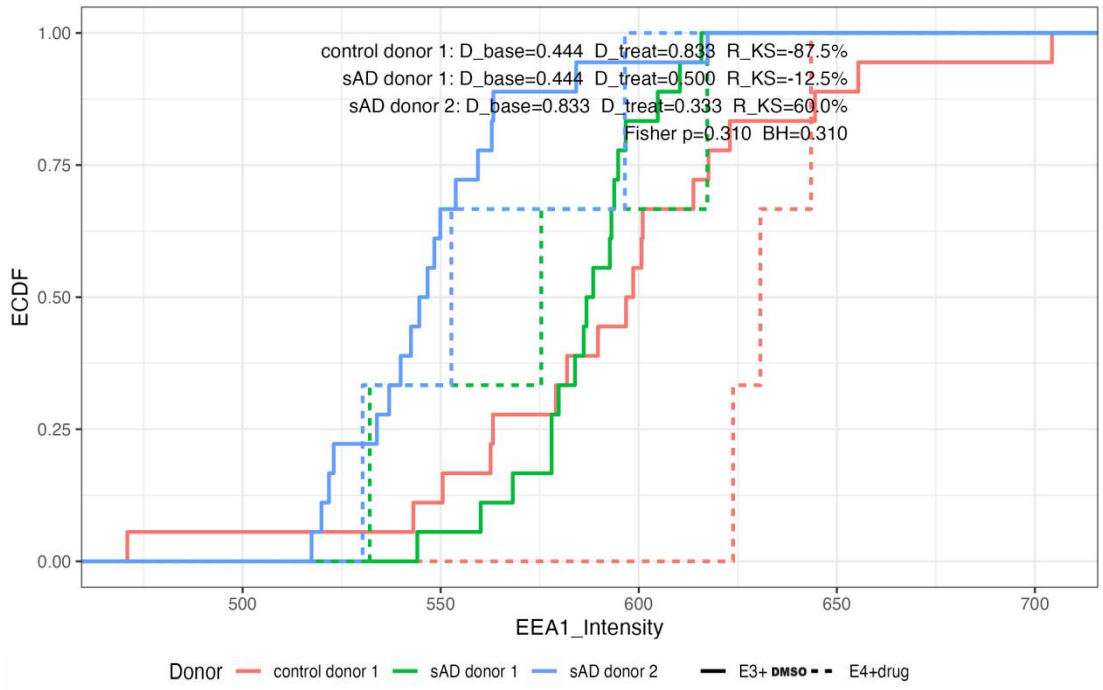
A. ECDF - Compound #220 Feature: Nucleus_Roundness



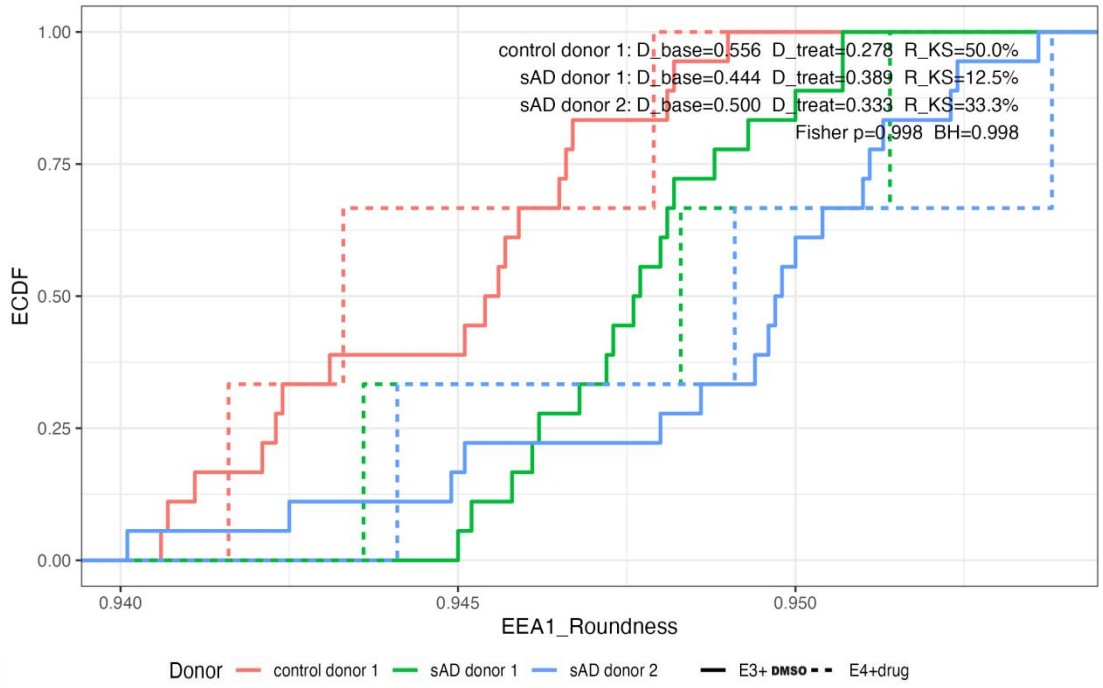

B. ECDF - Compound #220 Feature: BODIPY_Intensity



C. ECDF - Compound #220 Feature: EEA1_Intensity




D. ECDF - Compound #220 Feature: EEA1_Roundness



E. ECDF - Compound #220  Feature: Cell_Ratio_Width_to_Length

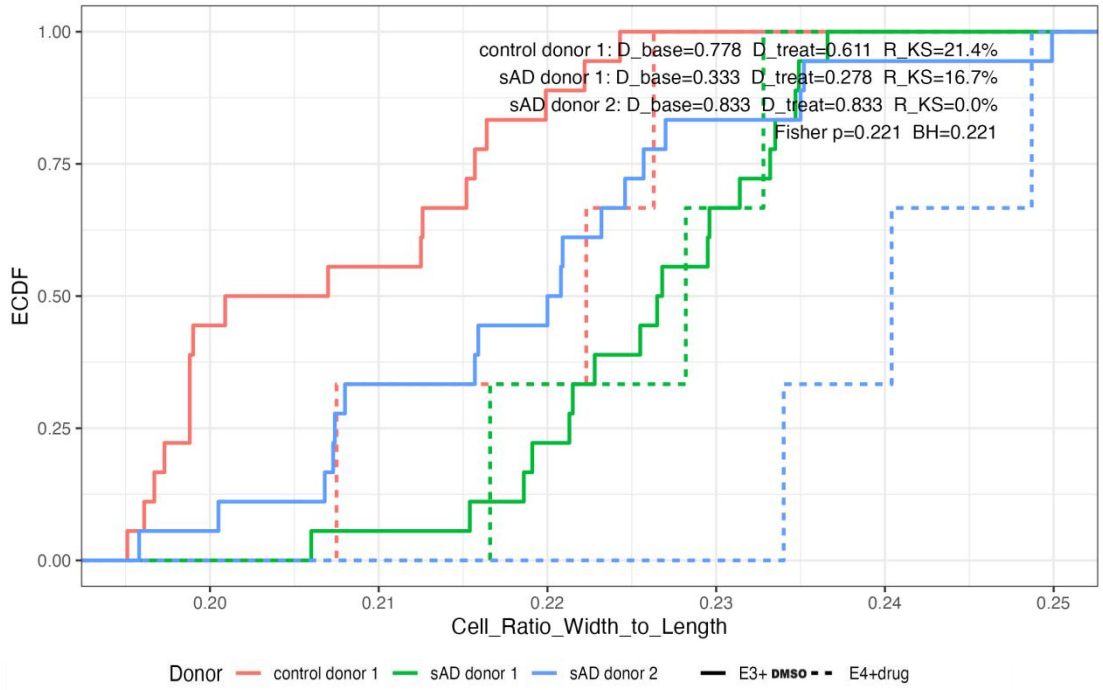



***Figure 7.2. Empirical cumulative distribution functions (ECDFs) for APOE4 + #220 compared to the APOE3 + vehicle (DMSO).*** *The figure shows the comparison within each donor. Donor-matched APOE4 + vehicle curves are overlaid to show the baseline APOE4–APOE3 gap within the same donor. Colored/linetyped curves denote donor-specific APOE4 + drug and their corresponding APOE4 + vehicle controls; dotted vertical lines mark per-curve medians. The inset in each panel reports per-donor Kolmogorov–Smirnov distance D and the one-sided permutation p (adjusted by BH within panel) testing whether the drug reduces the APOE4–APOE3 distance relative to baseline; the combined (Fisher) value summarizes evidence across donors.*

*Panels (A–E) correspond to the five features:*

*(A) Nucleus roundness—rescue = rightward shift toward APOE3 (baseline: APOE3 > APOE4).*

*(B) BODIPY intensity—rescue = leftward shift (baseline: APOE4 > APOE3).*

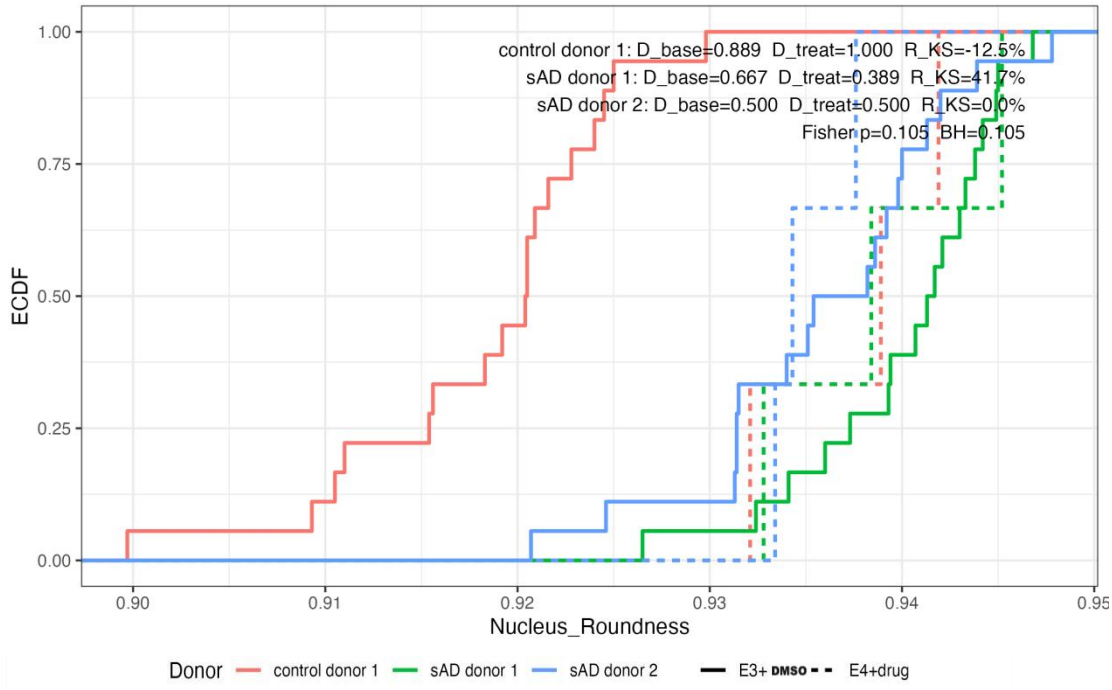
*(C) EEA1 intensity—rescue = leftward shift.*

*(D) EEA1 roundness—rescue = leftward shift.*

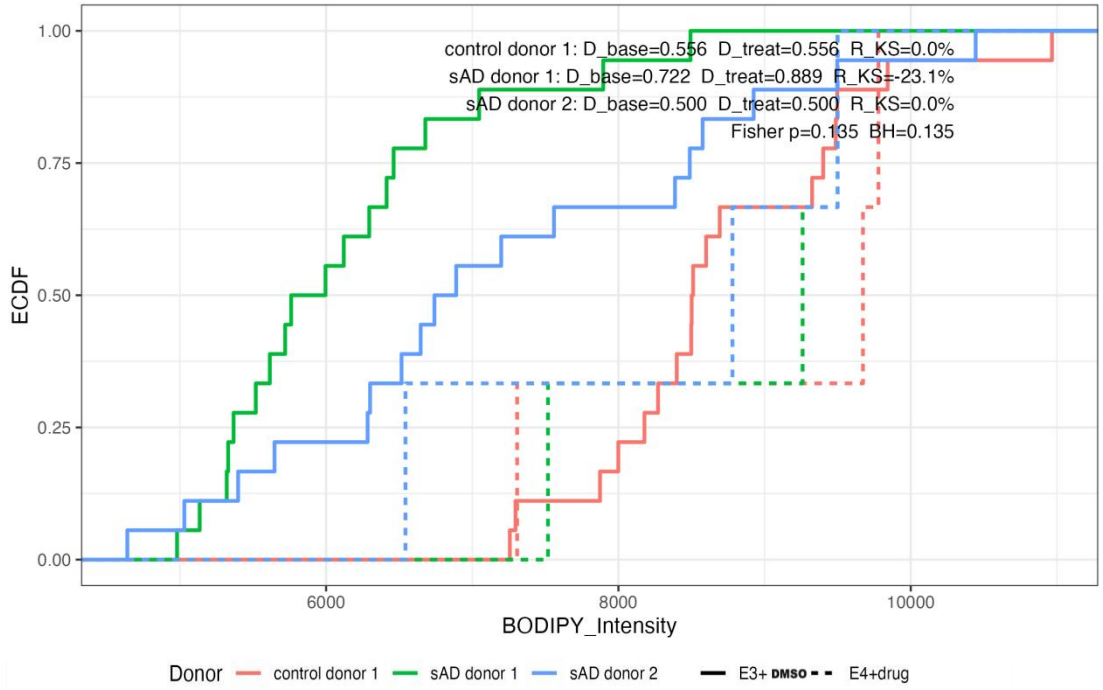
(E) *Cell width-to-length ratio—rescue = leftward shift.*

Figure 7.3.

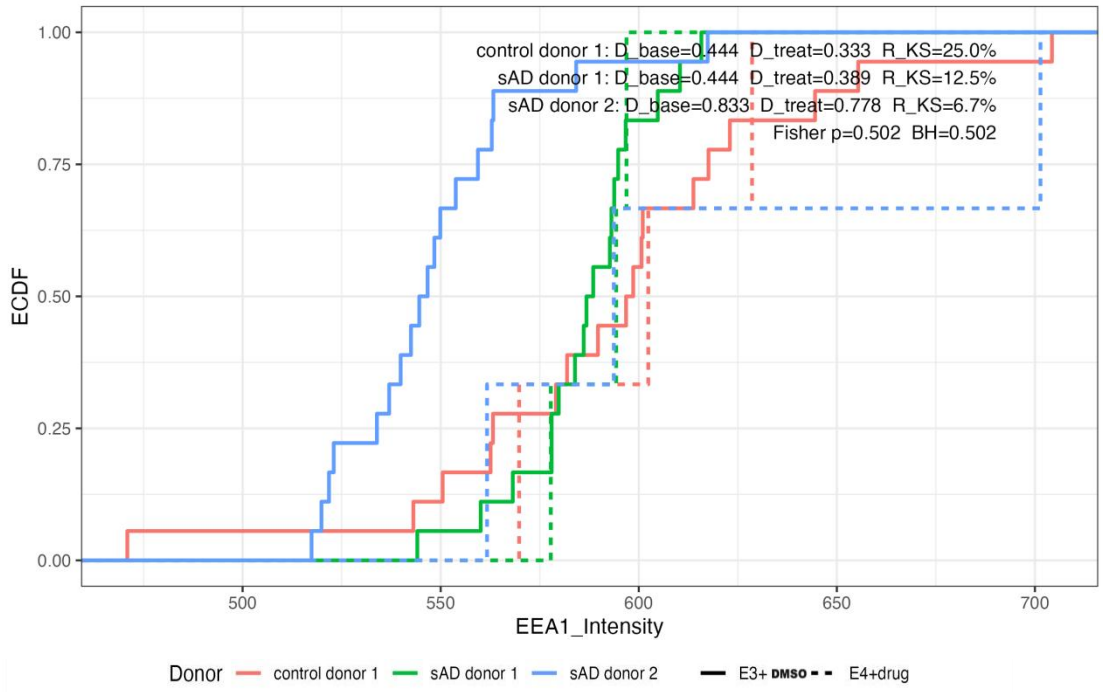
A. ECDF - Compound #660 Feature: Nucleus_Roundness



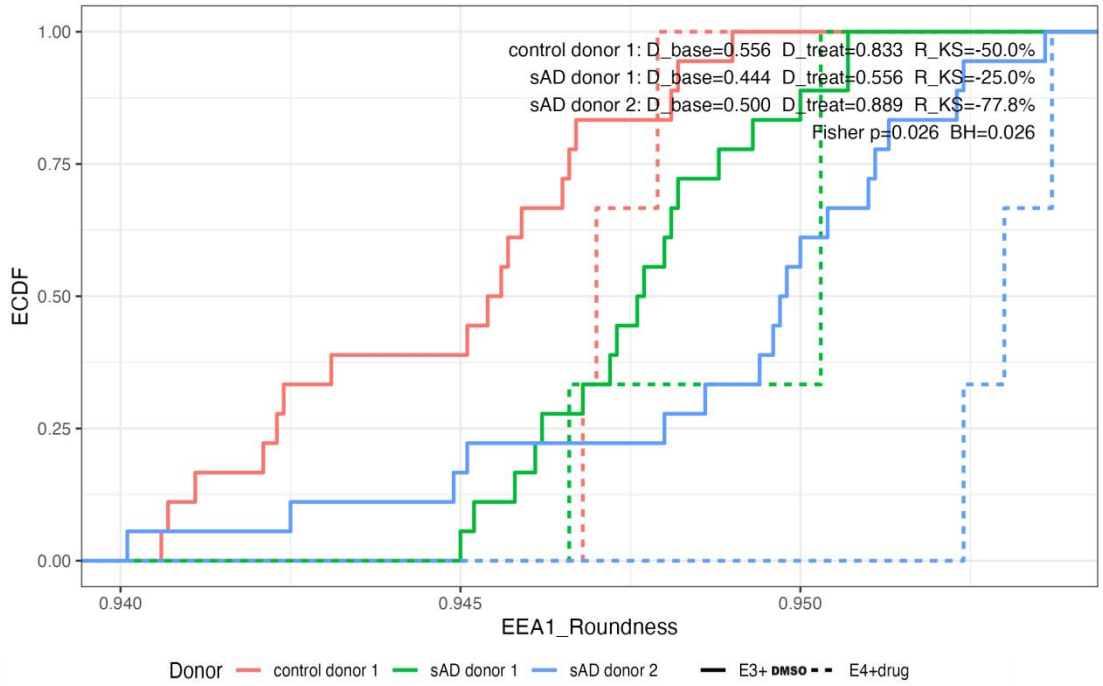

B. ECDF - Compound #660 Feature: BODIPY_Intensity



C. ECDF - Compound #660 Feature: EEA1_Intensity




D. ECDF - Compound #660 Feature: EEA1_Roundness



E. ECDF - Compound #660 Feature: Cell_Ratio_Width_to_Length

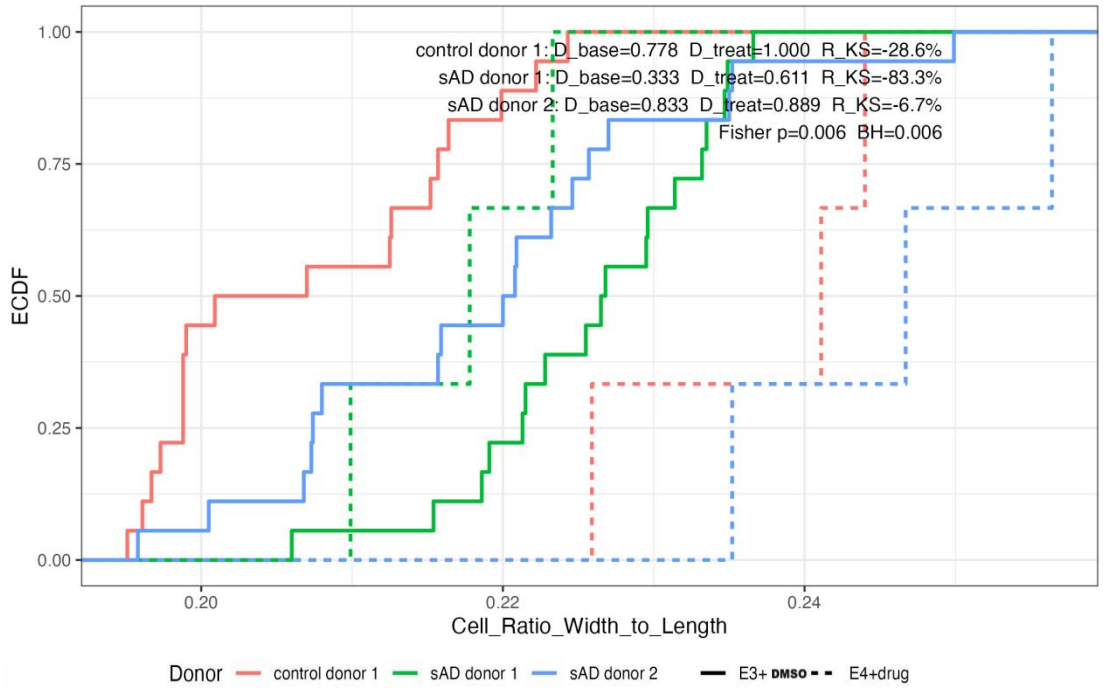



***Figure 7.3. Empirical cumulative distribution functions (ECDFs) for APOE4 + #660 compared to the APOE3 + vehicle (DMSO).*** *The figure shows the comparison within each donor (control donor 1, sAD donor 1, sAD donor 2), with donor-matched APOE4 + vehicle curves overlaid. Colored/linetyped curves denote donor-specific APOE4 + drug and APOE4 + vehicle; dotted vertical lines mark medians. Insets show per-donor KS distance D and the one-sided permutation p (adjusted by BH within panel) testing whether the drug reduces the APOE4–APOE3 distance relative to baseline; the combined (Fisher) value summarizes evidence across donors.*

*Panels (A–E) correspond to the five features:*

*(A) Nucleus roundness—rescue = rightward shift (baseline: APOE3 > APOE4).*

*(B) BODIPY intensity—rescue = leftward shift (baseline: APOE4 > APOE3).*

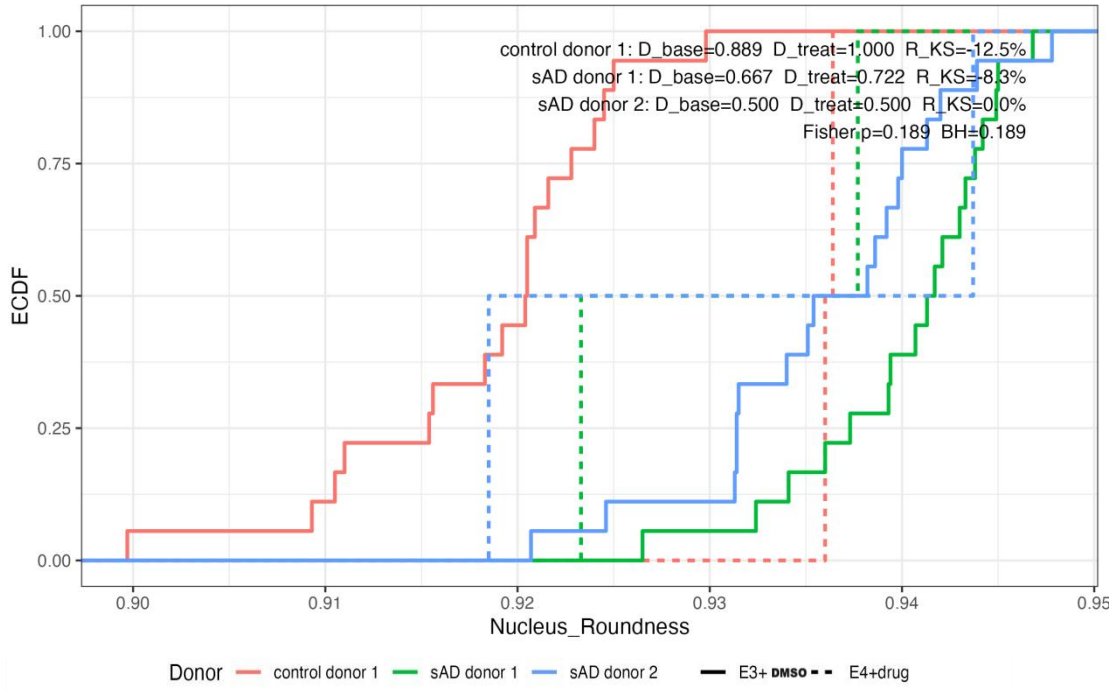
*(C) EEA1 intensity—rescue = leftward shift.*

*(D) EEA1 roundness—rescue = leftward shift.*

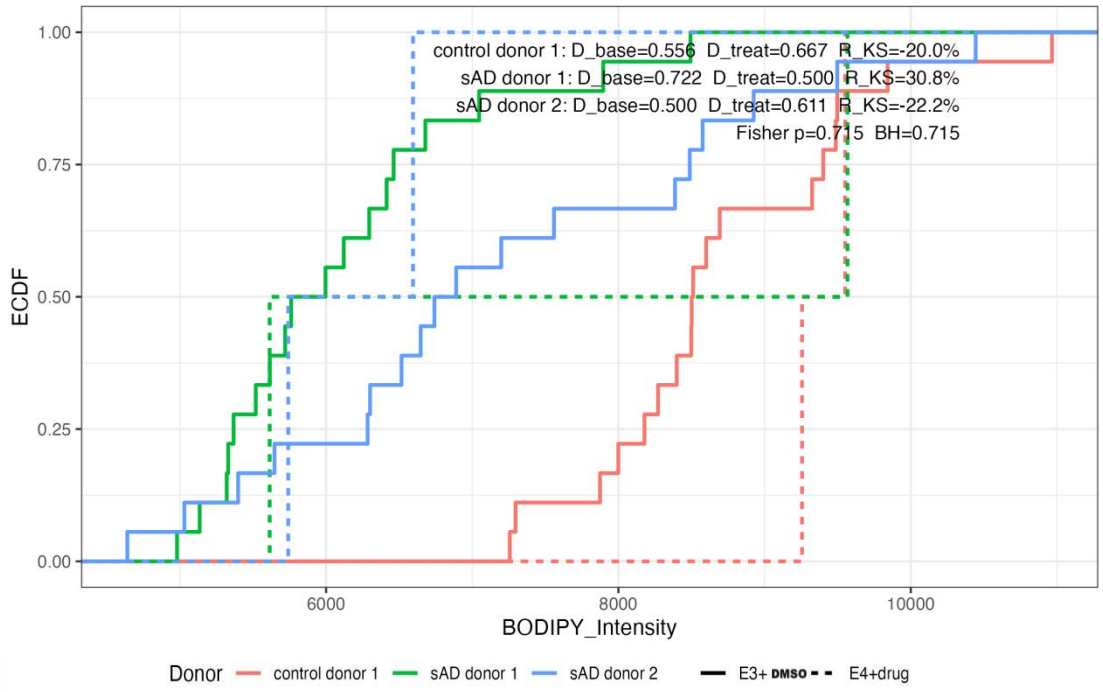
*(E) Cell width-to-length ratio—rescue = leftward shift.*

Figure 7.4.

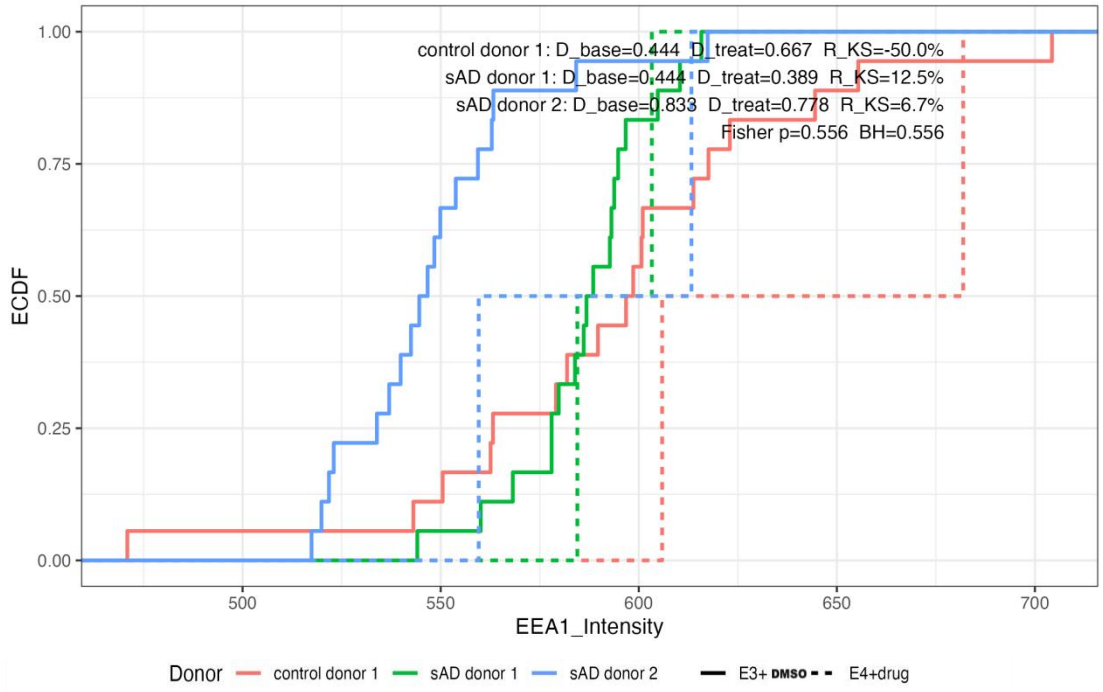
A. ECDF - Compound #033 Feature: Nucleus_Roundness



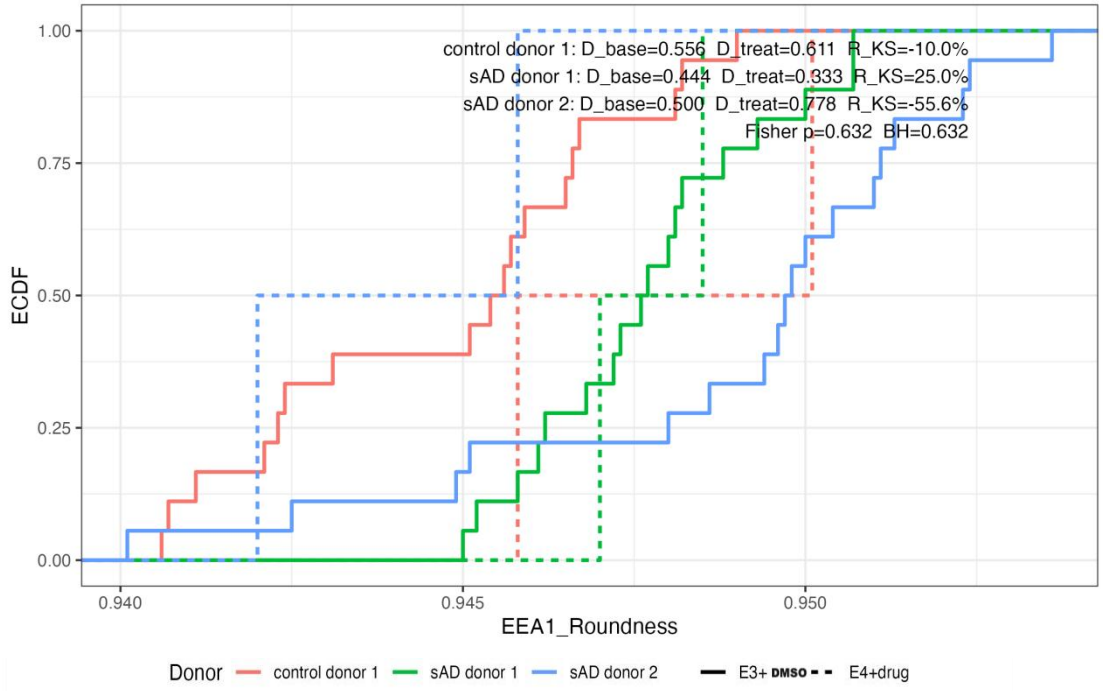

B. ECDF - Compound #033 Feature: BODIPY_Intensity



C. ECDF - Compound #033 Feature: EEA1_Intensity




D. ECDF - Compound #033 Feature: EEA1_Roundness



E. ECDF - Compound #033 Feature: Cell_Ratio_Width_to_Length

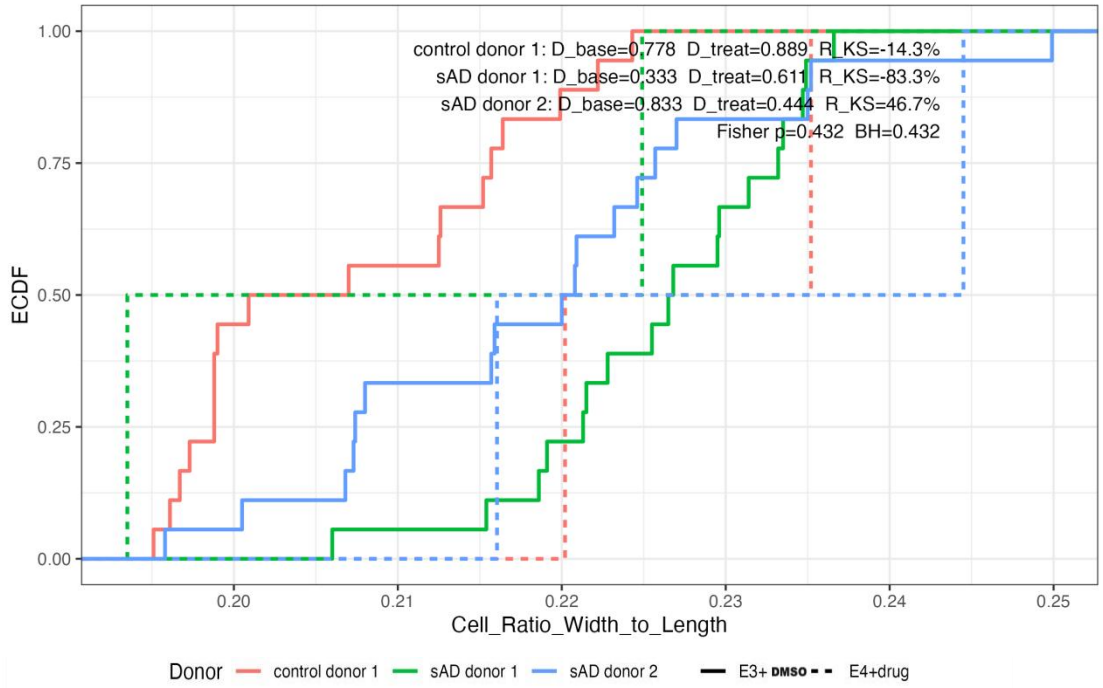



***Figure 7.4. Empirical cumulative distribution functions (ECDFs) for APOE4 + #033 versus APOE3 + vehicle (DMSO).*** *The figure shows the comparison within each donor (control donor 1, sAD donor 1, sAD donor 2), with donor-matched APOE4 + vehicle overlays. Colored/linetyped curves identify donor-specific APOE4 + drug and APOE4 + vehicle; dotted lines mark medians. Insets report per-donor KS D and the one-sided permutation p (adjusted by BH within panel) testing whether the drug reduces the APOE4–APOE3 distance relative to baseline; the combined (Fisher) value summarizes evidence across donors.*

*Panels (A–E) correspond to the five features:*

*(A) Nucleus roundness—rescue = rightward shift (baseline: APOE3 > APOE4).*

*(B) BODIPY intensity—rescue = leftward shift (baseline: APOE4 > APOE3).*

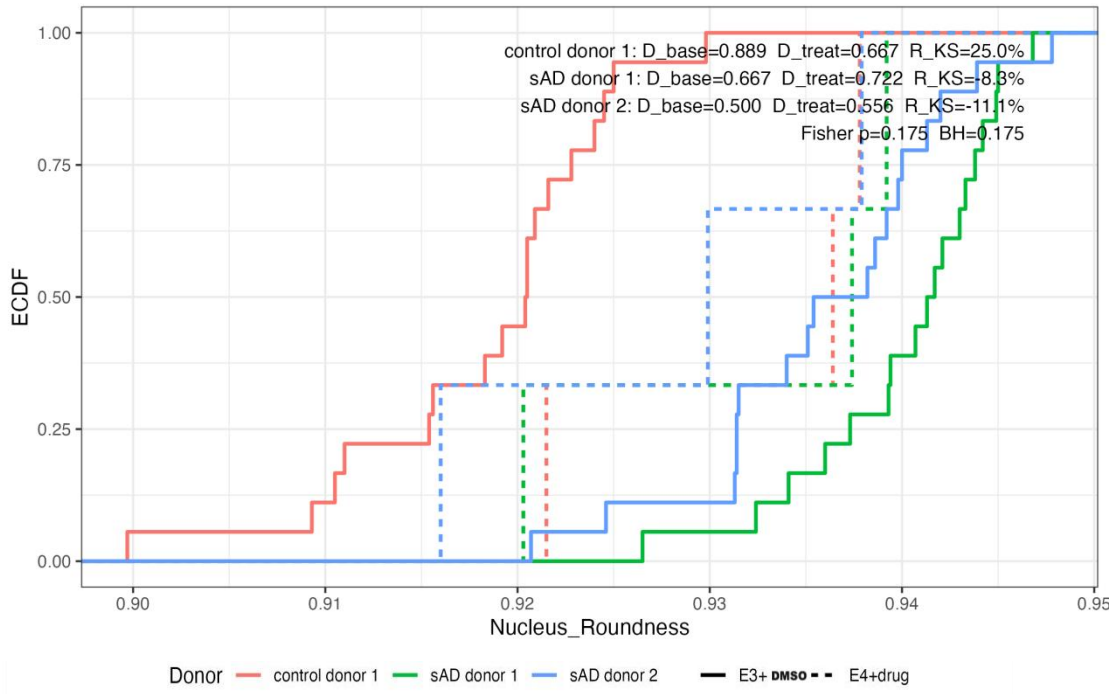
*(C) EEA1 intensity—rescue = leftward shift.*

*(D) EEA1 roundness—rescue = leftward shift.*

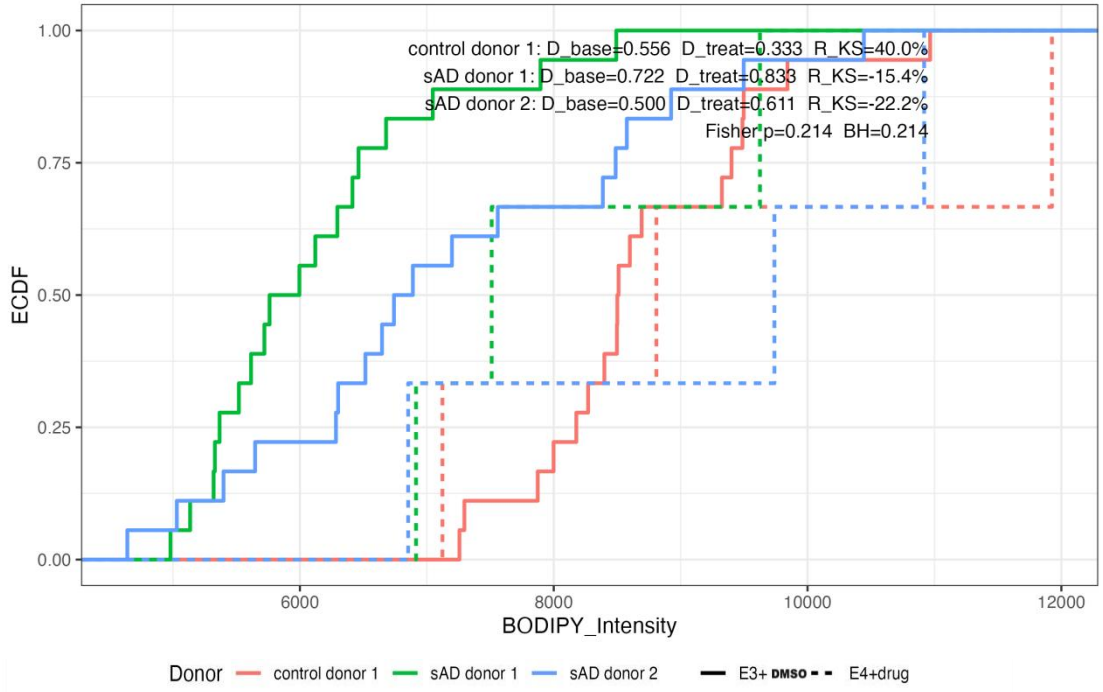
*(E) Cell width-to-length ratio—rescue = leftward shift.*

Figure 7.5.

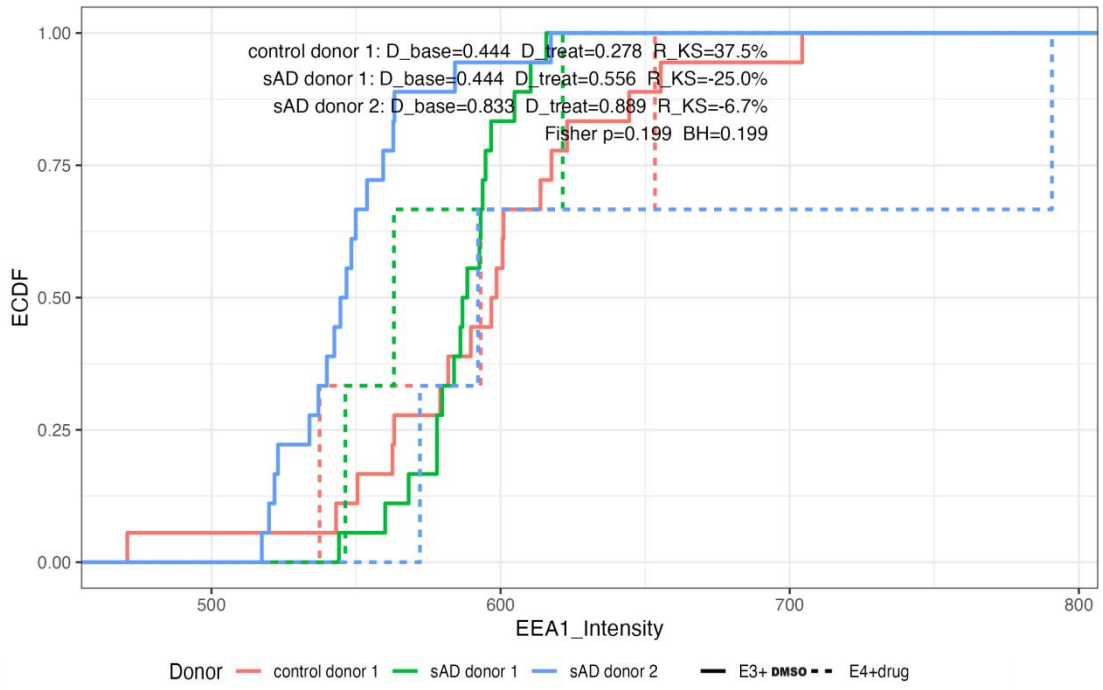
A. ECDF - Compound #581 Feature: Nucleus_Roundness



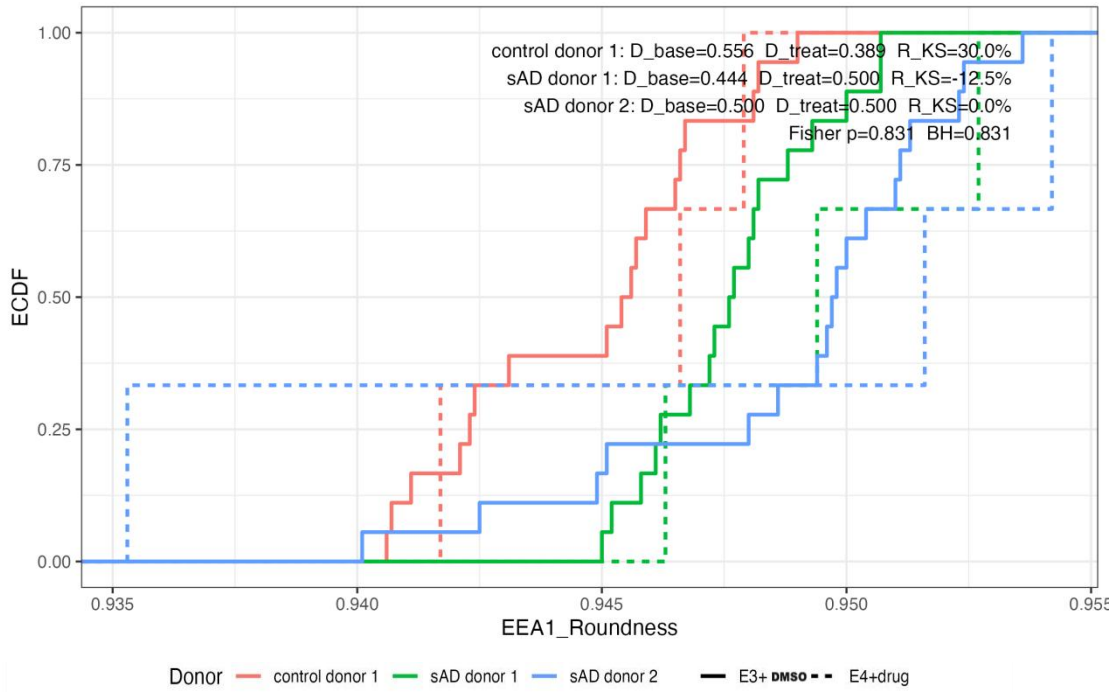

B. ECDF - Compound #581 Feature: BODIPY_Intensity



C. ECDF - Compound #581 Feature: EEA1_Intensity




D. ECDF - Compound #581 Feature: EEA1_Roundness



E. ECDF - Compound #581 Feature: Cell_Ratio_Width_to_Length

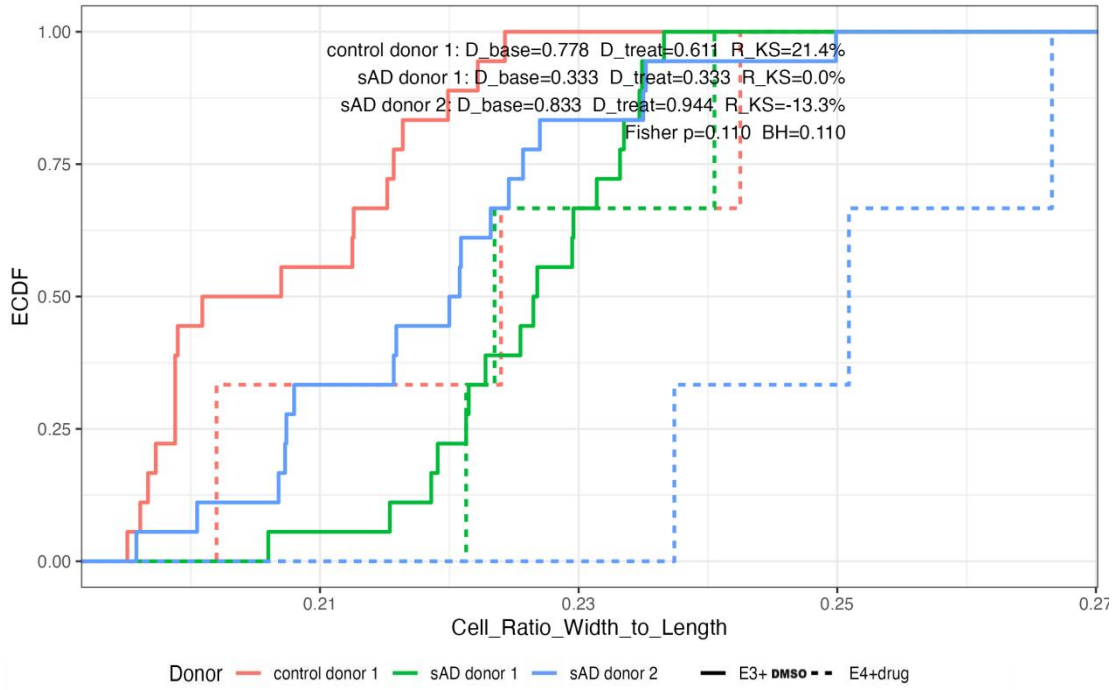



***Figure 7.5. Empirical cumulative distribution functions (ECDFs) for APOE4 + #581 compared to APOE3 + vehicle (DMSO).*** *The figure shows the comparison within each donor (control donor 1, sAD donor 1, sAD donor 2), with donor-matched APOE4 + vehicle curves overlaid. Colored/linetyped curves denote donor-specific APOE4 + drug and APOE4 + vehicle; dotted vertical lines mark per-curve medians. Insets show per-donor KS distance D and the one-sided permutation p (adjusted by BH within panel) testing whether the drug reduces the APOE4–APOE3 distance relative to baseline; the combined (Fisher) value summarizes evidence across donors.*

*Panels (A–E) correspond to the five features:*

*(A) Nucleus roundness—rescue = rightward shift (baseline: APOE3 > APOE4).*

*(B) BODIPY intensity—rescue = leftward shift (baseline: APOE4 > APOE3).*

*(C) EEA1 intensity—rescue = leftward shift.*

*(D) EEA1 roundness—rescue = leftward shift.*

*(E) Cell width-to-length ratio—rescue = leftward shift.*

### *7.2.5. Control analysis rules out cytotoxicity as a confounder*

To exclude the possibility that treatment effects on cellular phenotypes were secondary to cell death, astrocyte nuclei per well were compared across the five drug conditions and the DMSO control by one-way ANOVA (Fig. 7.6). Normality of residuals and equality of variances were verified by diagnostic tests and QQ plots; therefore, the parametric ANOVA model was retained. No significant effect of treatment on cell number was observed across the 3 donors after Tukey correction. These results confirmed that observed differences are not attributable to variation in cell loss.

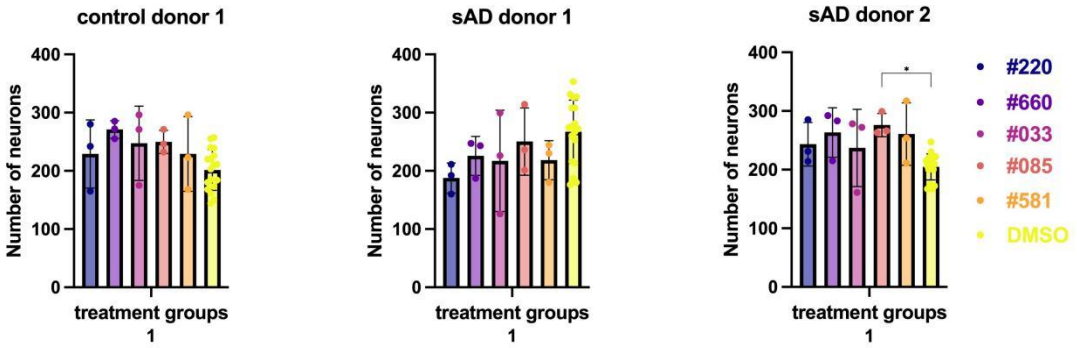



***Figure 7.6. Cell count per well of the neurons in five selected drug treatments and vehicle control across three donors.*** *Number of astrocytes per well for (left) control donor 1, (middle) sAD donor 1, and (right) sAD donor 2 following exposure to five selected compounds (#220, #660, #033, #085, #581) or DMSO vehicle. Bars show mean cell count per condition; individual dots represent replicate wells quantified from high-content images using the nucleus marker–based segmentation pipeline. Group comparisons were performed using One-way ANOVA. Across donors, cell counts are broadly comparable between drug-treated and vehicle conditions, with no consistent reduction indicative of toxicity (a minor increase is observed for one compound in sAD donor 2). These data indicate that treatment-associated morphological changes reported elsewhere are unlikely to be driven by drug-induced cell loss.*

### *7.2.6. AIML reveals donor and genotype signals in astrocyte morphology for screening*

To further advance the drug screening platform directly from raw immunocytochemistry images, rather than from manually-engineered cellular features, an AIML workflow was established. In detail, image analysis was performed at the following two spatial granularities chosen to probe complementary biological context: (i) field-of-view (FOV) tiles based on microscope resolution that contain multiple cells and (ii) nucleocentric region that focuses on chromatin/lamina morphology while retaining minimal cytoplasmic context (Heckenbach et al., 2022; Belhadj et al., 2023; Beuckeleer et al., 2024).

At first, two baseline classifications were performed to test whether genotype and donor information are present in morphology and to quantify how strongly they are expressed using two complementary learning settings. A weakly supervised classification using untreated astrocytes from the DMSO group was performed using image-level labels available at the donor level (no manual cell-by-cell annotation). In this context, weakly supervised indicates that the models receive minimal labels (e.g., donor identity per image) and learns to discover discriminative features without explicit annotation of subcellular structures. Moreover, with the aim of distinguishing donors, DINO, a self-supervised model, was trained based on the general-purpose embeddings using all astrocytes regardless of drug treatments and genotypes (Caron et al., 2021). After model training, the results of well- and FOV level embeddings were projected for each donor using UMAP (Fig. 7.7 & Fig. 7.8, respectively). At the FOV level, the weakly supervised classifier achieved 81% accuracy for

*APOE* genotype prediction and 93% accuracy for donor identity. Accuracy here denotes the proportion of correctly classified images among all test images. Embeddings extracted from both the weakly supervised and trained by self-supervised models supported downstream genotype and donor classification, indicating that general morphological representations contain genotype signal even when models are trained without genotype supervision. The accuracy results for FOV and nucleocentric region were summarized in the table for tach donor (Table. 7.3). To better aid interpretability, two-dimensional UMAP projections were also generated from the embeddings. UMAP visualization of astrocyte morphology showed that clustering by donor identity has higher accuracy than which drug treatment (Fig. 7.9). This indicates that the inter-individual baseline morphological differences between donors exert a stronger influence on the overall cellular state than the effects induced by the tested compounds under these conditions. This pattern is consistent with the feature-based results reported earlier in section 7.2.2, where only a subset of the five morphological axes, rather than all axes simultaneously, showed drug responsiveness in astrocytes.

### *7.2.7. A quantitative profile of treatment-induced morphological shifts*

Building on the baseline classification analyses, a treatment-level distance analysis was performed to quantify the degree of morphological convergence or divergence across all conditions in the drug screen (Fig. 7.10). Image embeddings were computed as described above and compared at the drug treatment level, such that larger treatment-control distances indicated stronger morphology-level effects. Under these metrics, $A\beta_{25–35}$ produced the largest morphological shifts, consistent with its role as a control inducing

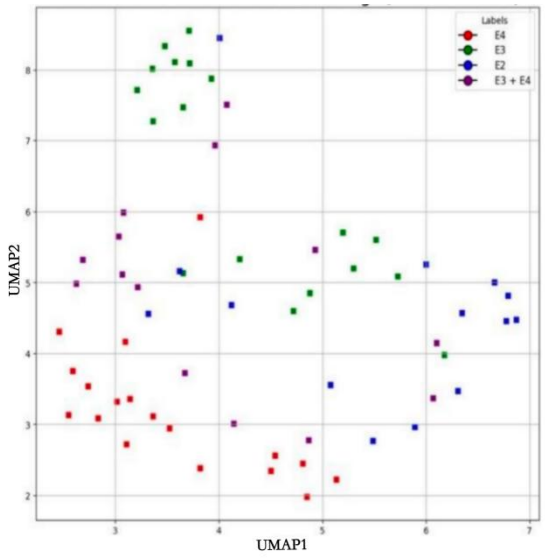
perturbation in this system. By contrast, the five candidate compounds mentioned above did not form separable clusters from other drugs nor from the vehicle, indicating that compound-induced effects in astrocytes were modest under the current doses and exposure windows. This pattern aligns with the earlier feature-based results, in which only a subset of the five morphological axes showed drug responsiveness in astrocytes, rather than concerted shifts across all axes simultaneously.

These findings indicate that, in the present astrocyte context, variance attributable to donor and genotype was stronger, yielding 60–80% classification accuracy. By contrast, compound effects were comparatively restricted and tended to be confined to endosomal or nuclear metrics rather than to global morphology. As a result, although $A\beta_{25–35}$ provided a clear benchmark for detectable morphological change and supported the sensitivity and accuracy of the image-based screening platform for capturing treatment-induced effects, discrimination among the five candidate compounds was limited, and at the applied doses and exposure windows, the compounds did not elicit strong astrocytic responses.

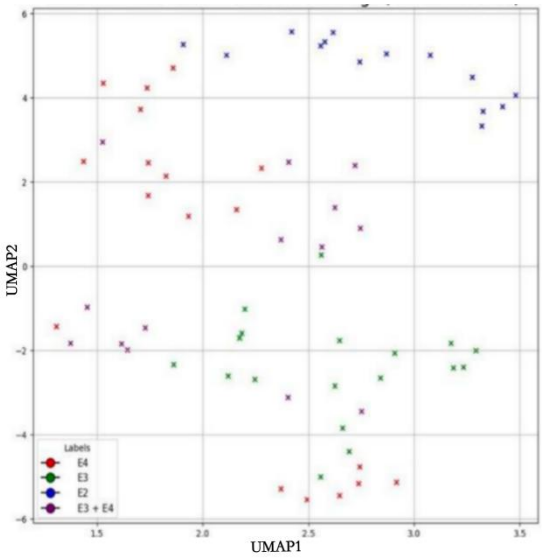
| cell_type | donor | training | FOV | nucleocentric region |
|---|---|---|---|---|
| Astro | control donor 1 | Classify_donors | 56.5 | 56.4 |
| Astro | control donor 1 | Classify_genotypes | 57.1 | 55.1 |
| Astro | sAD donor 1 | Classify_donors | 58.8 | 55.0 |
| Astro | sAD donor 1 | Classify_genotypes | 58.8 | 58.2 |
| Astro | sAD donor 2 | Classify_donors | 58.7 | 55.1 |
| Astro | sAD donor 2 | Classify_genotypes | 58.0 | 55.0 |
| Astro | average | Classify_donors | 57.9 | 55.5 |
| Astro | average | Classify_genotypes | 54.7 | 56.0 |

***Table 7.3. Information content in astrocyte embeddings: SVM readouts for donor/genotype classification.*** *Table reports validation accuracy (%) of a linear SVM that uses neural-network image embeddings as inputs. Embeddings were computed at two spatial granularities: FOV (field-of-view tiles) and nucleocentric region. Rows indicate the donor and the objective used to obtain the embeddings (Classify_donors or Classify_genotypes). Across donors (control donor 1, sAD donor 1, sAD donor 2), astrocyte embeddings contain detectable but modest information about genotype/donor, with performance depending on both the donor and the spatial representation. (Credit: for the following results, astrocytes cell culture, plating and ICC staining were performed by the dissertation author; drug application and image acquisition were performed by Dr Helen Rowland; AIML analysis pipelines were developed by Ying Chen, Prof. Alejo Nevado-Holgado, and Dr Andrey Kormilitzin)*

A. UMAP of control donor 1 - well level




B. UMAP of sAD donor 1 - well level




C. UMAP of sAD donor 1 - well level

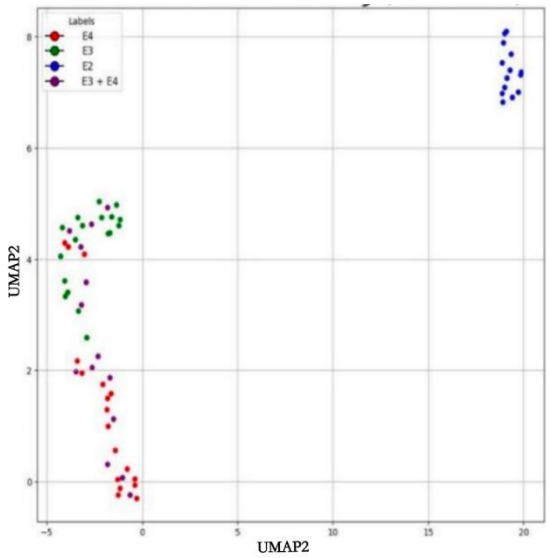
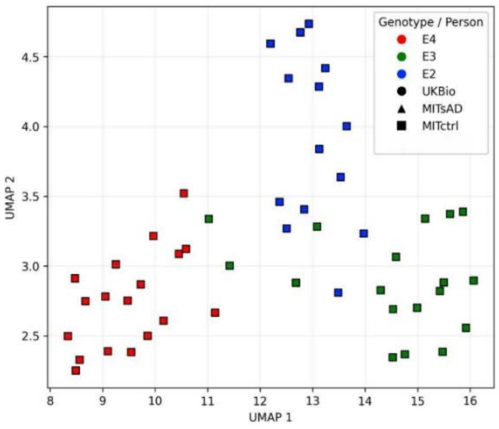


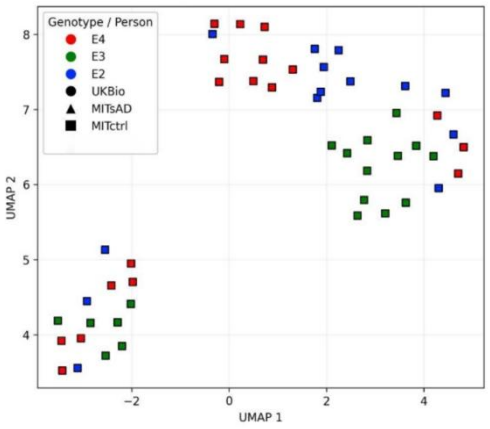

***Fig 7.7. Genotype structure in well-level image embeddings within donors.*** *(A-C) UMAP projections of well-level embeddings from the validation split for individual donors: (A) control donor 1, (B) sAD donor 1, (C) sAD donor 2. Each point represents a single well of isogenic iPSC-derived astrocytes imaged under vehicle (DMSO) conditions in the high-content ICC assay. Colours indicate APOE genotype (E2 blue, E3 green, E4 red, E3 + E4, a 1:1 mixture of E3 and E4, purple). Well-level embeddings were obtained by aggregating field-of-view using the trained image encoder, providing an image-native summary of astrocyte morphology. Within each donor, APOE genotype–dependent separation is visible, indicating that genotype-linked morphological signatures are distinguishable directly from raw images. These untreated distributions served as donor-matched baselines for subsequent treatment-effect analyses. Axes represent UMAP*

*components.(**Credit**: for the following results, astrocytes cell culture, plating and ICC staining were performed by the dissertation author; drug application and image acquisition were performed by Dr Helen Rowland; AIML analysis pipelines were developed by Ying Chen, Prof. Alejo Nevado-Holgado, and Dr Andrey Kormilitzin)*

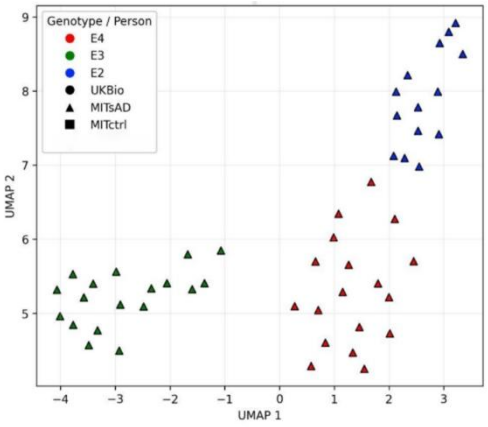
Astro FOV; control donor 1



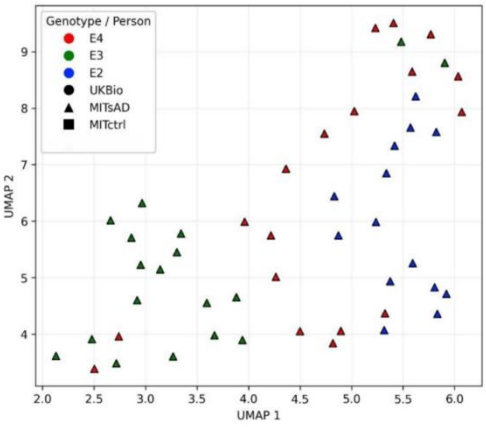

Astro nucleocentric region; control donor 1



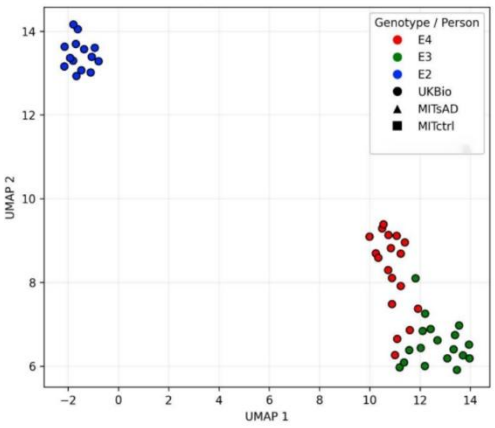

Astro FOV; sAD donor 1




Astro nucleocentric region; sAD donor 1




Astro FOV; sAD donor 2




Astro nucleuscentric region; sAD donor 2

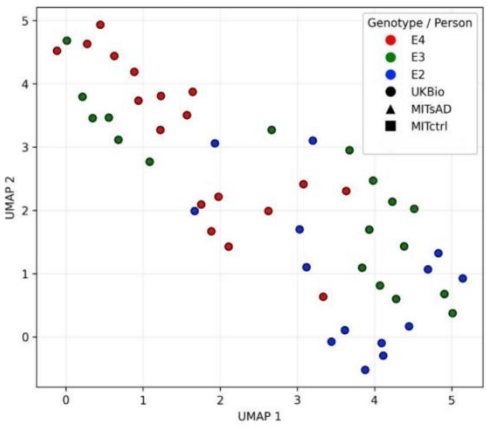



***Figure 7.8. Self-supervised FOV-level embeddings of untreated astrocyte reveal genotype-dependent structure.***

*UMAP projections of field-of-view (FOV) and nucleocentric region embeddings from untreated (vehicle) astrocyte are shown separately for each donor: top, control donor 1; middle, sAD donor 1; bottom, sAD donor 2. Each point represents a single image tile from the high-content ICC assay. Embeddings were generated using a self-supervised DINO encoder trained without access to APOE genotype labels and then reduced to two dimensions with UMAP. Colours indicate APOE genotype (E2, blue; E3, green; E4, red), illustrating that genotype-related morphology can be recovered even in the absence of supervised labels. All three donors show distinguishable genotype structure, with the sharpest separation in sAD donor 2, clear but partially overlapping clusters in control donor 1, and a more graded transition in sAD donor 1. Axes represent UMAP components. (**Credit**: for the following results, astrocytes cell culture, plating and ICC staining were performed by the dissertation author; drug application and image acquisition were performed by Dr Helen Rowland; AIML analysis pipelines were developed by Ying Chen, Prof. Alejo Nevado-Holgado, and Dr Andrey Kormilitzin)*

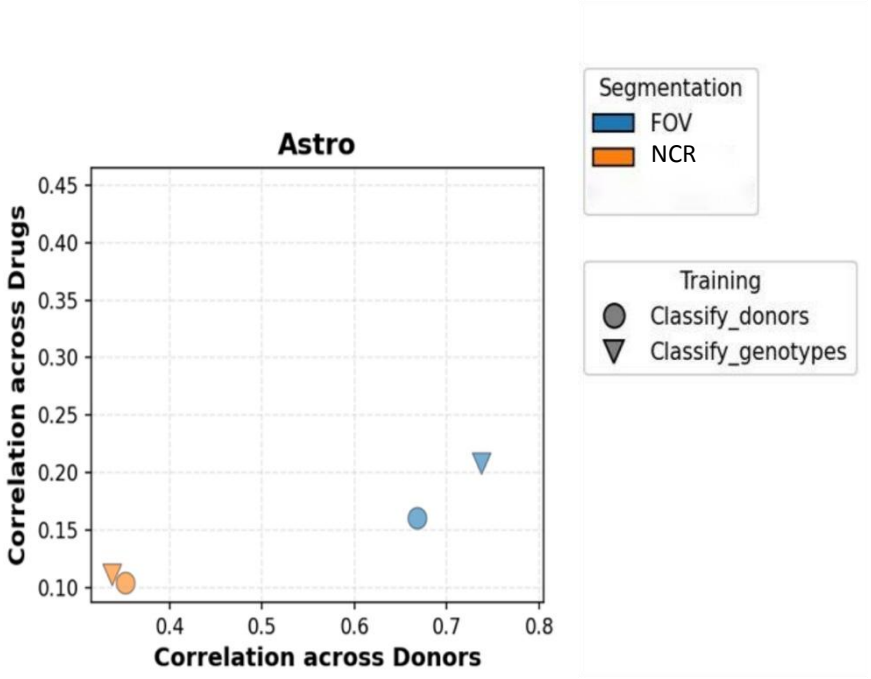



***Figure 7.9. Embedding-based projection shows strong donor influence and modest compound responses in astrocytes.***

*Scatter plot summarizing the correlation of drugs and donors' distance profiles computed from neural-network image embeddings. Each marker corresponds to a representation variant defined by segmentation (colour: FOV = blue, nucleuscentric region (NCR) = orange) and training objective (shape: circle-Classify_donors, trangle-Classify_genotypes). For each variant, per-treatment effects were quantified as distances of well embeddings from the donor-matched vehicle centroid; the x-axis shows the correlation of these distance profiles across donors, and the y-axis shows the correlation across drugs. FOV representations exhibited higher cross-donor concordance (~0.67–0.75) than perinuclear representations (~0.33–0.36), whereas cross-drug concordance was low for all variants (~0.10–0.21). These results indicate that, in astrocytes, donor identity dominates variance and compound-induced morphological shifts are modest under the current conditions. (**Credit**: for the following results, astrocytes cell culture, plating and ICC staining were performed by the dissertation author; drug application and image acquisition were performed by Dr Helen Rowland; AIML analysis pipelines were developed by Ying Chen, Prof. Alejo Nevado-Holgado, and Dr Andrey Kormilitzin)*

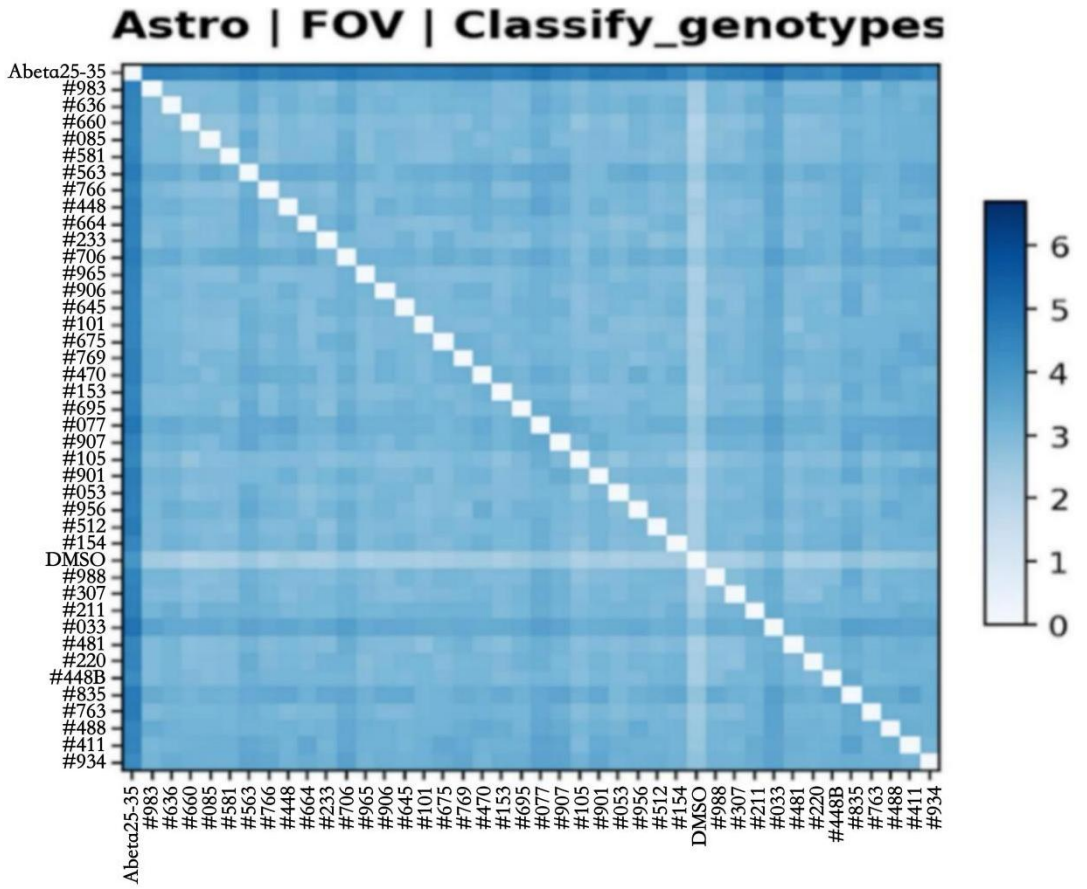



***Figure 7.10. Treatment–treatment distance matrix from astrocyte FOV embeddings.***

*Heatmap showing pairwise distances in embedding space between treatments. For each treatment, well-level embeddings were obtained from astrocyte FOV images using the neural encoder trained on the Classify genotypes objective, then aggregated to a treatment centroid (pooled across wells and donors). Matrix entries represent the distance between treatment centroids; the diagonal is zero by definition, and darker shades indicate greater dissimilarity (colour scale in arbitrary distance units). Aβ$_{25–35}$ displays the largest average separation from other conditions, serving as a clear positive perturbation. In contrast, the small-molecule candidates (e.g., the GSK series) show modest, partially overlapping shifts, yielding limited mutual separability under the present dosing and exposure windows. (**Credit**: for the following results, astrocytes cell culture, plating and ICC staining were performed by the dissertation author; drug application and image acquisition were performed by Dr Helen Rowland; AIML analysis pipelines were developed by Ying Chen, Prof. Alejo Nevado-Holgado, and Dr Andrey Kormilitzin)*

## 7.3. Discussion

### *7.3.1. Feature-specific drug responses reveal underlying mechanisms of APOE4 pathology*

These results suggest that APOE4 astrocytic phenotypes are both feature-specific and pharmacologically targetable, though with significant variability. Nuclear roundness, endosomal roundness emerged as the relative drug-responsive features, supporting the idea that cytoskeletal and trafficking pathways are promising therapeutic entry points. EEA1 intensity occupied an intermediate position, with credible rescue in specific drug–donor combinations. In contrast, lipid droplet accumulation (BODIPY intensity) and cell shape (width-to-length ratio) were the least responsive. Lipid droplet burden likely integrates tightly regulated cholesterol trafficking and lipidation states that cannot be returned by short exposures of the drug treatment for 24hrs, and the cell aspect ratio could reflect multiple downstream pathways working together, including lipid, cytoskeletal, and trafficking perturbations, which may require multi-pathway or chronic interventions to normalize.

Specifically, the differential sensitivity of features also provides insights into APOE4-related biology. Nuclear roundness, which is dynamically linked to transcriptional activity and chromatin accessibility, may respond to drugs that modulate nuclear architecture or epigenetic state (Flores et al., 2021). Notably, APOE, particularly APOE4, has been found to act as a transcriptional factor, binding to DNA and influencing the expression of genes related to synaptic function with implications for AD and aging (Theendakara et al., 2018). Moreover, because nuclear morphology is closely linked to transcriptional activity, chromatin

accessibility, and stress adaptation, its sensitivity may reflect the dynamic regulation of nuclear-cytoskeletal interactions and the potential for drugs to stabilize nuclear integrity.

The observed endosomal phenotypes in the APOE4 astrocytes are consistent with *in vivo* evidence, strengthening their relevance to disease mechanisms. Transcriptomic analyses in APOE4 mouse brains have shown significant enrichment of genes involved in endosomal-lysosomal processing, alongside age-dependent increases in both the number and size of early endosomes, even in the absence of overt AD pathology (Nuriel et al., 2017). This links APOE4 to endosomal-lysosomal dysregulation *in vivo* and suggests that endosomal phenotypes observed in the iPSC models may reflect a correlated mechanism in the heightened AD risk of APOE4 carriers. Within the current screening data, it is interesting to note that EEA1 intensity can improve independently even when EEA1 shape does not, such that the endosome roundness appeared more easily modulated than intensity. It is likely because pharmacological treatments can rapidly influence molecular remodeling and organelle shape, whereas changes in cargo accumulation or protein turnover require longer timescales.

Conversely, the resilience of lipid metabolism and global cell shape to rescue underscores their role as convergent, downstream phenotypes. Lipid droplet accumulation reflects a core impairment in APOE4-related cholesterol efflux and lipid homeostasis, which are recognized hallmarks of APOE4 astrocytic dysfunction. The resistance of this phenotype to pharmacological reversal could also highlight the difficulty of directly targeting lipid

metabolism in APOE4 carriers. Additionally, the resistance also suggests that cytoplasmic morphology represents the integration of multiple disrupted pathways, including lipid handling, cytoskeletal remodeling, and endosomal regulation. The cytoplasmic width-to-length ratio represents an integrated morphological outcome of multiple disrupted pathways, including lipid metabolism, cytoskeletal remodeling, and endosomal trafficking, likely requiring broad restoration of astrocytic physiology rather than single-pathway correction. Therefore, it reflects a downstream phenotype rather than a single directly targetable mechanism. Moreover, its persistence could also underscore its role as a convergent readout of APOE4 pathology.

Taken together, these findings indicate that some *APOE*4-associated phenotypes, such as nuclear or endosomal morphology, remain relatively plastic and drug-responsive, while others, particularly those related to lipid metabolism and general cytoplasmic morphology, reflect more deeply embedded aspects of astrocytic dysfunction.

#### *7.3.2. Biological implications for APOE4-targeted therapeutic strategy*

The drug screening experiments using isogenic iPSCs-induced astrocytes extend the findings from baseline and Aβ stress conditions by demonstrating that APOE4-associated cellular phenotypes are pharmacologically targetable in a feature-specific manner. By selecting five morphological features that consistently distinguished APOE4 from APOE3 astrocytes across donors, a set of robust disease-relevant readouts was established, including nuclear roundness, BODIPY intensity, EEA1 intensity, EEA1 roundness, and cytoplasmic

width-to-length ratio. These markers not only reflect structural differences but also map onto well-established AD pathways, including nuclear stress responses, lipid droplet accumulation, endosomal trafficking dysfunction, and cytoskeletal alterations.

An important observation from this study is that APOE4-associated features differed in their response to the 24 hour drug treatment, with some features showing greater normalisation towards the APOE3 reference than others. Nuclear roundness and endosomal features (particularly EEA1 roundness) were readily normalized by multiple compounds across donors, suggesting that nuclear integrity and EEA1 organelle morphology are relatively dynamic states influenced by cytoskeletal remodeling and transcriptional plasticity. These tractable phenotypes point to chromatin organization and trafficking machinery as promising therapeutic targets in APOE4 astrocytes. In contrast, BODIPY intensity exhibited significant resistance to pharmacological modulation compared to other cellular readouts. While this preliminary finding cannot conclusively identify targeted pathways, it aligns with the extensively documented role of APOE4 in disrupting cerebral lipid metabolism and cholesterol homeostasis. Future high-throughput screens with libraries enriched for lipid-modulating compounds are warranted to validate this association and identify specific rescue mechanisms. The cytoplasmic width-to-length ratio was the least reversible by any drug across all donors, likely reflecting its role as an integrative endpoint of multiple dysregulated pathways. This hierarchy of drug sensitivity highlights the layered nature of APOE4 pathology,

suggesting that some pathways are reversible under short-term perturbation, while others may require longer or combined interventions.

Differences in drug response between donors may also reflect factors beyond APOE genotype. Although the isogenic design controls the APOE locus within each donor pair, the wider genetic background remains different between donors. The two sAD pairs retain the genetic backgrounds of individuals with sporadic AD even when APOE4 is edited to APOE3. Genetic variants outside APOE may therefore affect both baseline phenotype and drug responses. Polygenic risk scores were not available for these donors, so this could not be tested directly.

Sex and iPSC origin may also contribute to donor-specific differences. The control and sAD1 pairs were derived from female fibroblasts, whereas sAD2 was derived from blood from a male donor (Table 2.1). Because the only male donor was also the only blood-derived donor, the effects of sex and cell origin cannot be separated in this study. Larger donor panels with known polygenic risk scores, balanced sex representation and matched iPSC origins will be required to determine their contributions to drug response.

As mentioned above, each of the five phenotypic features represents a convergent pathway of AD pathology with distinct biological implications. Nuclear roundness reflects chromatin organization and nuclear stability. Reduced nuclear roundness in APOE4 astrocytes may indicate increased cellular stress, DNA damage responses, or altered transcriptional states (dos Santos, 2021). BODIPY intensity quantifies neutral lipid accumulation. Elevated levels in APOE4 astrocytes are consistent with impaired cholesterol trafficking and excess lipid droplet

formation, a hallmark of metabolic dysregulation in AD brains (Qi et al., 2021a). EEA1 intensity captures endosomal activity. Increased staining in APOE4 astrocytes suggests hyperactivation or congestion of the early endosomal pathway, in line with reports of early endosome enlargement as one of the earliest cytopathological signatures of AD (Cataldo et al., 2000). EEA1 roundness reflects vesicular morphology and trafficking fidelity. Less round endosomes in APOE4 astrocytes may indicate defects in vesicle scission, recycling, or fusion, potentially disrupting receptor-mediated Aβ uptake and lipid recycling. Cytoplasmic width-to-length ratio serves as a measure of overall astrocytic morphology and cytoskeletal organization. Higher ratios in APOE4 astrocytes suggest hypertrophic or dysmorphic processes, reminiscent of reactive astrocytosis observed in AD (Smit et al., 2021).

From a therapeutic perspective, the observed phenotypic plasticity along specific axes suggests a path toward modulating astrocyte-neuron interactions. For instance, if nuclear and endosomal rescue shifts APOE4 astrocytes phenotype towards APOE3, providing appropriate uptake and recycling of neurotransmitters, metabolic support, and regulation of the extracellular milieu, then the downstream neuronal morphology and synaptic maintenance may benefit. The hypothesis can be tested in co-culture models by assessing whether APOE4 neurons are rescued toward an APOE3 state when cultured with drug-treated APOE4 astrocytes.

### *7.3.3. Compounds show distinct rescue patterns in APOE4 astrocytes*

The screening framework, anchored to APOE3 as the reference, demonstrates that rescue is both feature-specific and donor-dependent. The most robust and statistically supported rescue was #085. It significantly increased the nuclear roundness of APOE4 astrocytes and reversed the baseline difference observed, such that untreated APOE4 has significantly less rounded nuclei than APOE3 astrocytes. #220 coherently normalized EEA1 roundness and BODIPY intensity in 2 out of 3 donors. #660 minimized the APOE-specific difference of EEA1 intensity in a donor-specific manner but also showed a limited effect on EEA1 roundness and the cell width-to-length ratio. #033 produced limited reversal of EEA1 intensity and cytoplasmic width to length ratio, while #581 yielded mild effects largely in the control donor 1.

This compound profiling validates the feasibility of using high-content imaging and ICC-derived features as a scalable phenotypic screening platform. By directly linking cellular morphology to disease-relevant phenotypes, it is possible to achieve high-throughput screening while maintaining biological implications. Although only preliminary, this approach enables rapid identification of compounds that shift APOE4 astrocytes toward an APOE3-like state. The finding that APOE4 astrocytes are pharmacologically pliable in specific dimensions but resistant in others parallels clinical observations: while some pathways (e.g., cholesterol lowering with statins) yield modest benefits, others (e.g., lipid droplet clearance) remain elusive.

### *7.3.4. A scalable AIML platform captures donor and genotype signals*

These phenotypic analyses were supported by an image-based AIML platform that enabled scalable classification and representation learning. The platform works by constructing a compact, high-dimensional representation from the images, which constitutes an integrated morphological profile encompassing features of the cytoplasm, endosomes, lipid droplets, and nucleus. The representation in turns enables the inference of donor- and genotype-related cellular states.

The models accurately distinguished genotypes and donors, with morphological variance attributable to donor and genotype being strong. By contrast, compound effects were more restricted, confined largely to endosomal or nuclear metrics rather than global morphology. As a result, although $A\beta_{25–35}$ provided a clear benchmark for detectable morphological change and supported the sensitivity and accuracy of the image-based screening platform for capturing treatment-induced effects, discrimination among the five candidate compounds was limited, and at the applied doses and exposure windows, the compounds did not elicit strong astrocytic responses.

Moreover, the pronounced donor-specific effects underscore the necessity of controlling for donor variability in experimental design, for example, through cross-donor train/test splits or mixed-donor batching.

### *7.3.5. Limitations and plans for mechanistic validation*

The principal limitations emerge from the scope and timescale. The current feature readouts are from well-level resolution, if single-cell counts are extracted and analyzed, or increased sample size, the KS distances could be less influenced by tails and will improve precision. Moreover, treatments here were acute for 24 hours. Phenotypes that proved resistant in this short-term setting, such as lipid droplets and global morphology, might only be modified by longer or repeated drug exposures.

Thirdly, the readouts, while strongly disease relevant, are morphological surrogates from ICC images; therefore, mechanistic validation remains essential. These morphological readouts are indirect proxies for cellular function. For example, while nuclear roundness may reflect transcriptional state, it does not necessarily confirm gene regulatory changes without complementary assays such as RNA-seq. Nuclear rescue should be paired with ATAC-seq or lamina-associated domain profiling to evaluate chromatin accessibility and nuclear organization. Similarly, endosomal morphology provides a structural correlate of trafficking, but does not capture dynamic cargo turnover, pH changes or degradative capacity in live cells. Lipid droplet accumulation is a reliable marker of impaired lipid handling, yet without direct lipidomic profiling or efflux assays, the underlying metabolic imbalance remains speculative. Thus, while these features provide valuable and scalable surrogates for APOE4 pathology, further validation at the molecular and functional levels will be essential to establish causality and therapeutic relevance.

The next step will be to learn the identity of the small molecules tested, and determine whether their annotated mechanisms of action of each compound correspond to the pathways implicated by the rescued features. This will allow targeted validation of whether the compounds indeed act on transcriptional regulation, endosomal–lysosomal dynamics, cytoskeletal remodeling, or lipid metabolism, and will provide mechanistic confirmation that the morphological rescue reflects pathway-specific therapeutic potential.

Based on these findings, three practical improvements should be made for the screening approach. First, not only increase sample number or use single object level resolution cellular features as mentioned above, but also perform dose–response and time-course experiments for the strongest pairs, such as #085 with nuclear roundness, #220 with EEA1 roundness, and #660 with EEA1 intensity. This will help us determine the optimal dosage and see if the beneficial effects last over time, while watching for any negative effects at higher concentrations. Second, since single compounds could not reverse all APOE4 phenotypes, drug combinations could be introduced, such as coupling nuclear/trafficking modulators with lipid-centric agents to target resistant phenotypes such as BODIPY intensity and the width-to-length ratio. Third, extend to neuron–astrocyte co-cultures to ask whether astrocytic rescue translates into neuronal morphology and synaptic function, and, if successful, to 3D organoids or *in vivo* contexts for translational alignment. Throughout these steps, methodological consistency could be maintained to ensure results remain comparable across scaling steps.

# Chapter 8: Discussion

This study investigates how the major sporadic AD risk allele, APOE4, perturbs human brain cell biology, especially in astrocytes. The overarching questions are: (i) define how APOE4 alters astrocyte-neuron interactions under amyloid stress, and (ii) establish a phenotype-driven drug screening platform. These questions are especially relevant to sporadic AD, where *APOE* is the strongest common genetic risk factor, but the cell-type specificity and molecular mechanisms that translate *APOE* genotype into increased vulnerability and the routes of intercellular propagation remain debated (Liu et al., 2013).

Using isogenic human iPSCs, astrocyte-neuron crosstalk is modeled via astrocyte-conditioned media (ACM) and direct co-culture, with and without an acute Aβ25–35 challenge. High-content imaging revealed that astrocytes are a key cellular site of *APOE4* risk and showed that mode of interaction (ACM vs co-culture) changes neuronal outcomes differently, therefore highlighting the importance for model choice. This work also identified drug-sensitive cellular features (endosomal/nuclear) for rapid drug screening and provided a scalable drug screen workflow that links image features to pathways and nominates targets testable with further functional validation.

The discussion focuses on the following: (i) strengths and unique value of isogenic human iPSC lines; (ii) APOE as a network-level perturbation of neuroglia crosstalk and choice of models; (iii) limitations, alternative research models and the functional validations; and (iv)

drug-responsiveness of phenotypes and insights for drug screening strategies.

## 8.1. Strengths and unique value of isogenic human iPSC lines

Research on familial AD has progressed quickly because clear, causal gene variants enable strong models in immortalized cell lines and transgenic mice (Drummond & Wisniewski, 2017). By contrast, the most common dementia, sporadic AD is polygenic and environmentally modulated, so no single model captures its complexity. As a result, the field relies on a portfolio of complementary systems: primary rodent and transgenic lines for circuit-level physiology and *in vivo* pharmacology (Ganesan et al., 2024); drosophila and C. elegans for rapid, whole-organism dissection and behavioral readouts (Jiang & MacNeil, 2023); clinical records for real life human information (Wang et al., 2020). Within this landscape, human iPSC-derived cortical cell models offer distinctive advantages for sAD because they better reproduce the human genetic context (e.g., APOE4) and species-specific disease pathophysiology, thereby providing a more clinically relevant platform for studying pathogenic mechanisms and evaluating drug efficacy while mitigating translational risks arising from species differences (Kanekiyo et al., 2014; Liu et al., 2013).

In addition, isogenic iPSC pairs improve genetic control, and standardized differentiation protocols make these models comparatively scalable and reproducible across experiments (Cerneckis et al., 2024). Together, these features give iPSC neuron–astrocyte models higher human relevance and practical throughput, making them well suited both for dissecting

mechanisms and for phenotypic drug screening grounded in quantitative, image-based readouts. Building on these complementary systems, CRISPR-edited, isogenic human iPSC lines provide an especially powerful framework for sAD biology. By generating *APOE* pairs within the same donor background, isogenic designs minimize donor-to-donor genetic variation, which is a major confound in complex, polygenic conditions like sAD, so that observed effects can be attributed to the APOE isoform itself rather than background noise. This genetic control sharpens signal detection, increases reproducibility across experiments, and enables tighter statistical inference on genotype effects.

Equally important, the platform allows independent differentiation of neurons and astrocytes from the same isogenic pairs, followed by controlled mixing across genotypes (e.g., APOE3 neurons with APOE4 astrocytes from the same donor and vice versa). This design also separates cell-autonomous (within-cell) from non–cell-autonomous (across-cell) mechanisms and supports factorial experiments that test how neuronal and astrocytic *APOE* genotypes interact. Moreover, implementing two interaction modes of ACM to isolate secreted-factor effects from contact-dependent pathways maps mechanism onto phenotype with greater precision.

Because all readouts are collected with standardized immunocytochemistry and high-content imaging, the pipeline scales readily to multi-donor replication and phenotype-rescue drug screening, while maintaining human cellular context. In sum, CRISPR-generated isogenic iPSCs

plus controlled neuron–astrocyte mixing convert a heterogeneous, multifactorial problem into a tractable, hypothesis-driven system for dissecting APOE-dependent biology and for prioritizing therapeutic levers.

## 8.2. The relevance and importance of studying neuro-glial cross talk.

Neuro–glia crosstalk is now understood as a bidirectional, circuit-level dialogue in which glia shape synapse formation, elimination, excitability, metabolism, and immune tone, replacing the older notion of glia as passive support (Chavda et al., 2022). At excitatory synapses, astrocytes form perisynaptic processes that create a bona fide tripartite synapse, promote synaptogenesis through thrombospondins and hevin/glypicans, and fine-tune transmission via $Ca^{2+}$-dependent gliotransmitters and high-capacity glutamate/$K^+$ buffering (Allen & Eroglu, 2017; Christopherson et al., 2005; Kucukdereli et al., 2011). They also provide metabolic support through the astrocyte–neuron lactate shuttle and deliver lipid cargo in APOE-containing lipoproteins whose lipidation depends on ABCA1/LCAT, thereby impacting receptor trafficking and synaptic stability (Liu et al., 2017; Pellerin & Magistretti, 1994; Vitali et al., 2014). Endosomal–lysosomal pathways integrate much of this traffic. As mentioned, early endosomal enlargement and cargo-handling defects are early features of AD, and astrocytic handling of Aβ and lipids converges on LRP1/LDLR/HSPG-mediated uptake and EEA1-marked endosomes (Cataldo et al., 2000; Kanekiyo et al., 2014; Nixon et al., 2005). In inflammatory contexts, astrocytes adopt context-specific reactive states that can become

synaptotoxic, illustrating how immune cues remodel neuron–glia communication (Escartin et al., 2021). Beside astrocytes, microglia also complement this axis by tagging and engulfing synapses via C1q/C3–CR3 and by sensing lipidated debris through the TREM2–APOE pathway, linking immune surveillance to lipid metabolism and synapse fate (Atagi et al., 2015; Liddelow et al., 2017). Moreover, oligodendroglia and NG2 glia add metabolic and conduction control, coupling axonal demands to glial support (Philips & Rothstein, 2017).

Not only are multiple cell types involved, evidence from single-nucleus and spatial transcriptomics underscores the heterogeneity within the cell types in AD where APOE also plays a role. Cortex-level atlases reveal disease-associated astrocyte and microglial states enriched for programs in lipid handling, complement, and endosomal biology (Mathys et al., 2019). APOE itself is selectively repressed in specific oligodendrocyte progenitor and astrocyte subpopulations in AD, highlighting lineage- and state-dependent regulation (Grubman et al., 2019). Converging mechanistic work indicates that APOE isoforms differentially modulate Aβ aggregation and clearance in brain, while also influencing synaptic plasticity, cell signaling, lipid transport/metabolism, and neuroinflammation (Kanekiyo et al., 2014). The direction and magnitude of these effects vary with APOE isoform, lipidation state, Aβ aggregation state, receptor usage, and cellular context.

Taken together, these data support a model in which astrocytes, including other glia, actively set the neuronal habitat, rather than merely responding to neuronal injury. In AD, isoform-specific disturbances in APOE lipidation and endosomal–lysosomal flux within glia

can propagate to synaptic structure and function, linking genetic risk to circuit-level dysfunction and cognitive decline (Escartin et al., 2021; Farhy-Tselnicker & Allen, 2018; Mahley & Huang, 2012). This neuron–glia interaction network and the local microenvironment it establishes therefore represent a compelling focus for mechanistic study and therapeutic targeting, with direct implications for drug delivery, biomarker design and patient stratification in AD.

## 8.3. APOE as a network-level perturbation of neuroglia crosstalk

In **chapter 4 & 5,** APOE isoform effects in neuronal monocultures were observed to be subtler and more variable across donors than in astrocyte monocultures, which as detailed in Chapter 6 displayed the strongest and most reproducible APOE4-dependent differences across multiple donors. By contrast, more pronounced neuronal baseline differences were observed when neurons were co-cultured with astrocytes of the corresponding *APOE* genotype. The pattern is biologically coherent because astrocytes are the main source of APOE in the CNS and orchestrate cholesterol efflux and lipoprotein delivery to neurons (Holtzman et al., 2011).

ACM captured the impact of soluble factors, including APOE-lipoproteins, cytokines/complement, EV cargo. In the presence of ACM, some neuronal baseline genotype differences persisted, consistent with partial buffering by diffusible signals. By contrast,

co-culture, including secretome and local mechanics exerted larger remodeling of neurites and endosomes and sometimes equalized *APOE* genotype differences. This indicates contact-dependent mechanisms, including matrix composition, integrins, connexins, juxtacrine signaling, contribute materially to neuron remodeling (Allen & Eroglu, 2017). Across paradigms, APOE4 neurons exhibited greater sensitivity to astrocytic influence and $A\beta_{25–35}$. This matches prior observations that APOE4 lowers the homeostatic reserve of circuits (Nuriel et al., 2017).

APOE genotype may influence phenotypes at both cell-autonomous and intercellular interaction levels. Together, these findings are consistent with a network-level perturbation of neuroglial crosstalk. The data indicate that APOE4 is unlikely to act as a proximal pathological trigger. Instead, relative to APOE3, APOE4 destabilizes the neural milieu, diminishing the capacity of astrocytes to maintain homeostasis and thereby priming neurons for stress-induced dysfunction. Converging evidence from genetics, transcriptomics, and glial biology similarly argues that APOE4 orchestrates a shared pathological program centered on lipid handling, endolysosomal trafficking, and neuroinflammatory signaling (Shvetcov et al., 2025). Cross-disease analyses highlight convergent astrocyte–microglia states and receptor pathways (e.g., LRP1/LDLR/HSPG axes) modulated by APOE4 that track with synaptic vulnerability. Thus, APOE4 is best viewed as a broad susceptibility allele that perturbs neuroglial crosstalk, with astrocytes as the primary locus of effect and neurons rendered more stress-prone—a network-level disturbance consistent with the present study's findings.

## 8.4. Limitations alternative research models and the functional validations

This dissertation was intentionally scoped to platform establishment and phenotype nomination, with astrocyte-centered assays prioritized initially to leverage the strongest APOE-linked phenotypes and maximize assay sensitivity for drug screening. This design was done to create a screening method that can be scaled up and has little bias. Its purpose was also to identify drug responses that are linked to specific biological pathways for more detailed follow-up study. It has been well shown that morphological profiling can be used to capture changes at the pathway level and to screen many different treatments at once (Caicedo et al., 2017). Therefore, its use is justified as the first step in discovery. Even so, the primary readouts are high-content imaging (HCI)-derived morphological proxies, which remain a central limitation. Having established that these endpoints (neurite number, length and branching/MAP2, synaptic puncta/SYP, endosomes/EEA1, lipid droplets/BODIPY, nuclear size/shape/intensity/Hoechst map onto plausible biology, it is acknowledged that they do not by themselves demonstrate functional consequences. Accordingly, after rapid nomination of the affected pathways, the next phase should explicitly pair the morphological axis with the orthogonal functional assays. Validation will begin with the most drug-responsive axes and, with longer, longitudinal studies reserved for assessing combined treatments..

For the neurite–synapse axis, spontaneous and evoked network activity on multi-electrode

arrays (MEA) can quantify firing rates, synchrony and bursting (Spira & Hai, 2013). This can also be complemented by whole-cell patch clamp to measure intrinsic excitability and synaptic currents. Vesicle cycling could be assayed using FM1-43 dye uptake/release to directly read out endo-exocytosis activity in neurons (Betz et al., 1992). For the endosomal pathway, live imaging of Rab5/Rab7/LAMP1 reporters can capture early-to-late endosome maturation and lysosomal delivery; LDL uptake/recycling assays will functionally anchor the EEA1 phenotypes we detected (Scott et al., 2014). To delineate the lipid axis, two complementary approaches would be employed, including cholesterol efflux assays to APOA-I (specifically probing ABCA1/HDL functionality) and unbiased lipidomics. This combined strategy will determine whether the elevated BODIPY intensity in APOE4 astrocytes stems primarily from impaired cholesterol efflux or from global alterations in lipid synthesis and turnover. Furthermore, targeted perturbation of ABCA1 and LCAT will establish a causal link between the efflux/lipidation capacity and the observed imaging phenotypes (Zannis et al., 2017). For the nuclear axis, ATAC-seq and RNA-seq can relate nuclear shape/intensity to chromatin accessibility and transcriptional state that may underlie the APOE4-specific nuclear morphology we observed (Buenrostro et al., 2015). Collectively, this phased strategy embodies the core premise of cellular phenomics: that high-dimensional morphological signatures and multimodal assays serve as a predictive gestalt of the underlying cell state (Nam et al., 2024; Tegtmeyer et al., 2025). The power of this approach is amplified by data integration. High-content imaging provides quantitative, morphological insights for specific cellular processes. And measurable functional phenotypes could potentially then enable the

investigation of the underlying activity. Having established this validated, scalable platform, its direct application in designing a mechanism-aware drug screen for APOE4 pathology will be detailed in the following discussion.

A second priority is to define the astrocyte secretome and extracellular environment underlying the neuronal changes observed in this study. The ACM experiments showed that soluble factors released by astrocytes were sufficient to alter neuronal morphology, whereas direct co-culture generally produced broader and sometimes directionally different effects. This suggests that ACM captures only part of the astrocyte influence on neurons. This interpretation is consistent with TCW et al. (2022), who showed that APOE4 disrupts cholesterol homeostasis in human astrocytes and microglia and alters astrocytic matrisome-associated pathways, particularly in the presence of neuronal signals. Their findings therefore provide a relevant link between APOE genotype, lipid metabolism and the extracellular environment.

In the present study, ACM contains soluble and released astrocyte-derived factors, whereas direct co-culture additionally includes locally concentrated signals, ECM-associated factors, cell-surface interactions and reciprocal neuron-astrocyte signalling. These additional components may contribute to the stronger phenotypic differences observed in co-culture, although they were not directly measured here. Future studies using proteomic and lipidomic analysis of ACM, together with ECM profiling and matched Transwell experiments, could

identify which APOE-dependent soluble or matrix-associated signals contribute to the EEA1, SYP and neurite phenotypes observed in this thesis. LC–MS/MS proteomics on ACM can quantify APOE lipidation state, complement components, cytokines (e.g., IL-6, TNF-α), and ECM/glycoproteins that plausibly drive the EEA1 and SYP changes measured (Habib et al., 2020). Cell-type-specific sorting of co-cultures (e.g., via astrocytic ACSA-2 or GLAST) followed by RNA-seq and proteomics will delineate APOE4-driven alterations in direct contact. On the neuronal side, receptor-centric assays (blocking antibodies or CRISPRi/CRISPRa) targeting LRP1, LDLR, HSPGs can evaluate whether specific APOE–receptor interactions mediate the EEA1 and SYP shifts in the ACM and co-culture paradigms (Kanekiyo et al., 2014).

To disentangle secreted vs. contact-dependent mechanisms, the research model can also be refined with Transwell (shared media, no contact), and microfluidic chambers that compartmentalize axons/dendrites from somata to localize astrocyte influence (Kurmashev et al., 2024; Taylor et al., 2005). These systems will test whether the convergence of APOE3 versus APOE4 neuronal phenotypes in co-culture reflects juxtacrine cues (e.g., heparan-sulfate proteoglycans, adhesion molecules), gap-junctional signaling, or matrix-bound factors not captured in bulk ACM. In parallel, introducing 3D context/cortical organoids and subtype-specific identity of the astrocytes can better approximate morphogen gradients, extracellular space, and astrocyte heterogeneity that influence synaptic and endosomal phenotypes *in vivo* (Paşca et al., 2015; Sloan et al., 2017).

The Aβ modality is another boundary condition. $A\beta_{25-35}$ was used to impose reproducible, short-term stress **in chapter 6**. However, to bridge from the acute stress model to the chronic features of the disease, future work should compare $A\beta_{1-42}$ oligomers vs. fibrils with controlled aggregation states and chronic exposure regimens, and even incorporate tau seeding to model the dual pathologies that drive clinical decline (Benilova et al., 2012; Guo & Lee, 2011; Lambert et al., 1998).

Moreover, a complete understanding of the system also requires incorporating microglia and oligodendrocyte lineage cells. This is critical because microglia regulate synaptic pruning and inflammatory tone, while oligodendrocytes and myelin exhibit well-established vulnerability in AD (Hickman et al., 2018; Nasrabady et al., 2018). As introduced in Section 1.3.3, microglia respond to lipid and damage signals partly through the TREM2-APOE axis. TREM2 is a microglial receptor involved in sensing lipid-associated and cellular damage signals, while APOE is closely linked to the downstream transition towards disease-associated microglial states. This pathway influences microglial lipid metabolism, phagocytosis and inflammatory responses in neurodegenerative conditions (Krasemann et al., 2017; Nugent et al., 2020). The absence of microglia is therefore an important limitation of the present astrocyte-centred model. Although the simplified neuron-astrocyte system allowed these two cell types to be studied more directly, it cannot capture the effects of TREM2-APOE signalling or reciprocal communication between microglia and astrocytes. This is particularly relevant to the lipid and endosomal phenotypes identified in this thesis, as both processes are also strongly regulated

in microglia. Therefore, some APOE-associated phenotypes observed here may differ when microglia are present. Future studies could incorporate isogenic microglia into the neuron-astrocyte co-culture to directly examine three-way neuron-astrocyte-microglia interactions and the contribution of TREM2-APOE signalling.

## 8.5. Potential for future drug screen development

Drug screen considerations also follow directly from the current results. The pipeline in this study demonstrates a fast, objective, scalable HCI platform, including fixed imaging/staining, standardized cell segmentation pipeline, and pre-specified feature sets enable quantitative assessment of compounds across hundreds of wells with minimal subjective bias. Specifically, the phenotypes provided by the morphological layer bridges multiple modalities. For example, nuclear and endosomal morphology changes can be tracked alongside omics signatures of chromatin remodeling or lipid trafficking repair, creating a multidimensional picture of drug action. Integrating these metrics through systems-level frameworks and linking imaging features to pathway modules enables more accurate identification of synergistic compound pairs and compensatory network effects (Zhang et al., 2013; Kiddle et al., 2018; Johnson et al., 2020). This approach parallels advances in oncology and immunology, where combination regimens are tailored by converging biomarkers across cell function and omics state (Napoli et al., 2022). The fundamental challenge in dissecting complex genetic disorders like sAD is bridging the gap between a static genetic variant and its dynamic, multifaceted pathological cascade. More broadly, phenomics, which includes the systematic, large-scale acquisition and

analysis of phenotypic data, has emerged as a pivotal discipline to address this challenge (Ying, 2023). It operates on the core premise that cellular morphology is not a mere static outcome but a rich, information-dense readout of the underlying mechanistic state of the cells and the pathways engaged. Foundational studies and large-scale Cell Painting resources have demonstrated that image-based morphological profiles can accurately discriminate pharmacological perturbations, recover biological similarity structure, and enable computational inference of mechanism at scale (Chandrasekaran et al., 2023; Way et al., 2022). Under matched conditions (e.g., Cell Painting and L1000 transcriptomics), morphology often captures a broader diversity of cell states, capturing changes that transcriptomics alone may miss (Caicedo et al., 2017; Severin et al., 2022). This map enables a highly practical screening paradigm: a primary screen can be run using images alone, while a smaller, paired subset supplies the multimodal reference needed to turn morphology into mechanism. This approach transforms a gestalt view of the cell state, where a holistic morphological signature into a first-pass, predictive layer that nominates pathways for functional confirmation. the study embodies this integrated strategy: by applying a high-content, phenomic approach to an isogenic *APOE*4 model, we aim to decode the pathway-level disruptions driving AD risk and position them within a standardized discovery pipeline.

Because APOE4 acts as a risk-shaping allele with pleiotropic effects on astrocytic lipid handling, endosomal-lysosomal trafficking, and inflammatory tone, compounds that shift APOE4 phenotypes toward APOE3-like states in human astrocytes have dual significance. For

sAD, such agents target upstream cellular programs that condition Ab handling and synaptic resilience, complementary to Ab-centric approaches and potentially effective earlier in disease (Wilcock & Colton, 2008). Beyond AD, similar APOE4-conditioned glial states appear across disorders with glia-synapse vulnerability; therefore, APOE4-normalizing agents may carry cross-indication value wherever the same astrocytic programs are stressed. Within this framework the astrocyte screen uncovered a hierarchy of drug responsiveness in **chapter 7**, such that endosomal and nuclear shape are highly sensitive (numerous compounds 'rescue' toward APOE3-like), EEA1 intensity shows intermediate sensitivity, lipid load is less responsive, and cytoplasmic width-to-length is most refractory. This stratification suggests a pragmatic two-tier strategy: deploy endosomal/nuclear features as primary screening endpoints to identify active chemotypes quickly, then confirm lipid/cytoskeletal remodeling in secondary, longer-term assays (chronic dosing, combination therapy) where slower, integrative biology may shift. Therefore, in complex, multifactorial disorders such as sAD, single-target therapies have faced significant challenges and demonstrated limited efficacy. This is because the pathology arises from intersecting disruptions across lipid metabolism, endosomal trafficking, synaptic signaling, and neuroinflammation, rather than a single linear cascade. Even the recent modest successes of monoclonal antibodies, which exhibit limited efficacy in broad populations, underscore the necessity of addressing the disease's multifaceted nature (Cummings et al., 2019; De Strooper & Karran, 2016). Combination strategies that act on multiple pathways would be beneficial for successful interventions.

Notably, the pathological effects of APOE4 extend beyond sAD. There are literatures support APOE4 as a glia-first susceptibility allele that tunes lipidation endolysosomal and immune set-points in astrocytes and microglia for other neurological conditions including cerebral amyloid angiopathy, dementia with Lewy bodies, tauopathy, and poor recovery after traumatic brain injury (Fernandez et al., 2019). Specifically, in primary tauopathy, APOE4 accelerates tau-mediated neurodegeneration independent of Aβ, largely via non-neuronal mechanisms (Shi et al., 2017), aligning with endolysosomal/lipid signatures seen in the APOE4 astrocytes. In Lewy body diseases, APOE4 increases the risk and severity of dementia and cortical Lewy pathology, and modulates α-synuclein burden, with glial lipid and inflammatory programs implicated in human post-mortem and snRNA-seq datasets (Kaivola et al., 2021; Sekiya et al., 2025; Zhao et al., 2020). In cerebral amyloid angiopathy and lobar ICH, APOE4 (and E2 in distinct patterns) modifies vascular Aβ deposition and hemorrhage risk, pointing to perivascular glia–vascular interactions and lipidated APOE particles in Aβ handling (Biffi & Greenberg, 2011; Greenberg, 1998). After traumatic brain injury, APOE4 carriers show worse cognitive outcomes and heightened amyloid/tau pathology, consistent with an APOE4-conditioned reactive glial milieu that impairs debris clearance and amplifies synaptic stress. Associations in PD dementia and DLB (risk/severity), and mixed evidence in MS and ALS, converge on the same axis: APOE4 biases glia toward lipid-overloaded, lysosome-engaged, complement-positive states that correlate with synaptic vulnerability (Belloy et al., 2023; Escartin et al., 2021; Mahley & Huang, 2012). Thus, therapeutic strategies designed to counteract the core cellular dysfunctions of APOE4, particularly in astrocytes,

could have broad translational relevance across multiple disorders sharing APOE4-related pathophysiology.

Finally, even with carefully engineered isogenic APOE3 versus APOE4 pairs, inter-individual background still measurably shapes phenotype and sometimes the direction of effects. In the dataset, multiple neuronal readouts were '2-of-3 donors significant,' but the two donors were not always the same two across features. For example, under ACM we observed that APOE3 neurons from the two sAD donors often showed reduced intensity of nuclei and smaller SYP puncta than APOE4 neurons, whereas control donor #1 showed the opposite pattern (brighter nuclei, larger SYP area in APOE3) under the same exposure. These cross-over effects indicate that donor background and disease status (control vs. sAD) can also modulate effect sizes and even directions, despite the strong noise reduction afforded by isogenic editing. This observation aligns with large-scale iPSC studies showing that common genetic variation and donor-specific factors introduce substantial molecular and phenotypic heterogeneity across lines, even when culture conditions are standardized (Panopoulos et al., 2017; Volpato & Webber, 2020). Similar donor-dependent response profiles have been documented after differentiation into multiple neural subtypes (Schwartzentruber et al., 2018) and are also a hallmark of clinical heterogeneity in sAD, where *APOE*4's effect sizes vary with background genetics, environment, and comorbidity (Belloy et al., 2019). It follows that isogenic designs, while necessary, are not sufficient. They control the genotype at the *APOE* locus within a single donor background but cannot eliminate inter-individual variance stemming from

polygenic backgrounds or disease history. A key practical implication for future drug screening is that replication across multiple donor lines would be a crucial even in isogenic models.

In short, the results suggest that isogenic editing localizes the question and multi-donor sampling answers it reliably. Future screens and mechanistic experiments, particularly those probing neuron-glia crosstalk should combine isogenic pairs with multiple donors and explicitly report donor-wise concordance to align preclinical readouts with the true heterogeneity seen in sAD cohorts.

## Concluding remarks

Sporadic AD accounts for the vast majority of dementia cases worldwide, imposing profound personal, caregiver, and healthcare burdens as populations age, while truly disease-modifying therapies remain limited. It currently affects tens of millions globally and contributes to a major share of years lived with disability in late life; as populations age, incidence and total economic costs are projected to rise substantially, underscoring the urgency of pinpointing tractable cellular mechanisms and therapeutic entry points (Lin et al., 2025). Sporadic AD is driven by risk architecture rather than single-gene determinism, and *APOE*4 is the most robust genetic contributor to that risk. Using human isogenic iPSC models that disentangle neuronal and astrocytic contributions, this work pinpoints the impact of astrocytes on neuronal phenotypes across *APOE* variants. Across multiple donors, APOE4 astrocytes consistently exhibited altered morphology features that were weaker and less reproducible in neurons alone. Notably, when neurons were co-cultured with astrocytes of the same *APOE* genotype, the baseline APOE differences became more pronounced than in neuronal monoculture, indicating that astrocytic context amplifies genotype effects. The results suggest that APOE4 is more likely to disrupt astrocytic homeostasis, and neuronal vulnerability follows rather than intrinsically from the neurons themselves. Framing APOE4 as a glia-first network perturbation aligns with clinical genetics, where APOE4 increases risk and lowers age of onset rather than acting as a deterministic mutation. It provides a mechanistic bridge between population risk and synaptic failure in AD.

We then asked how astrocytes promote risk to neurons. ACM altered specific neuronal features, but direct co-culture exerted the larger effect, indicating that contact-dependent mechanisms shape neuronal phenotypes beyond what soluble cues can explain. In this context, APOE4 neurons showed greater vulnerability to astrocyte treatments and to $A\beta_{25–35}$ stress. These observations support a network model in which APOE4 does not act as a direct toxic factor; instead, it destabilizes neuroglial homeostasis, lowering the threshold for synaptic dysfunction, particularly in the presence of amyloid or inflammation. This network view is consistent with contemporary AD pathophysiology, in which synaptic loss or brain atrophy, rather than plaque burden itself, best tracks cognitive decline, and in which glial states modulate clearance, lipidation, and endosomal–lysosomal trafficking that together shape neuronal resilience.

Translationally, we converted these image-based phenotypes into high-content screening platform. A compound phenotype-rescue screen in *APOE*-isogenic astrocytes showed feature-specific reversibility: nuclear and endosomal features were drug-responsive across donors, whereas lipid burden and cytoplasmic geometry were more resistant, likely representing slower, integrative biology. This stratification suggests a practical roadmap: target trafficking and nuclear architecture for early rescue, while treating lipid remodeling as a chronic or combination-therapy goal. The pipeline from standardized image acquisition, cell segmentation, feature extraction to statistical modeling, provides a quick and scalable framework that links 'pixels to pathways' and can be paired with subsequent

functional/omics confirmation.

AD is a disorder of neural circuits and their neuronal support cells. This work locates the impact of APOE within neuron-astrocyte interactions, where the *APOE*4 genotype destabilizes the neural microenvironment. By integrating isogenic human iPSCs with HCI, we operationalize this genetic risk into a drug-screening platform. This framework may be useful in leveraging astrocytic trafficking to raise circuit resilience, offering a pathway to interrupt the progression from molecular imbalance to cognitive decline. Ultimately, by converting a common genetic risk factors into functionally relevant, quantifiable cellular features that are amenable to therapeutic screening, this work supports a shift from neuron-centric pathology toward neuroglial systems biology, with the goal of delivering interventions that meaningfully delay loss of independence for patients and families.

# References

2025 Alzheimer's disease facts and figures. (2025). *Alzheimer's & Dementia*, *21*(4), e70235. https://doi.org/10.1002/alz.70235

Aborode, A. T., Emmanuel, O. A., Onifade, I. A., Olotu, E., Otorkpa, O. J., Mehmood, Q., Abdulai, S. I., Jamiu, A., Osinuga, A., Oko, C. I., Fakorede, S., Mangdow, M., Babatunde, O., Olapade, Z., Victoria, A. G., Salami, A., Usman, I. A., Agboli, V. I., & Adesola, R. O. (2025). The role of machine learning in discovering biomarkers and predicting treatment strategies for neurodegenerative diseases: A narrative review. *NeuroMarkers*, *2*(1), 100034. https://doi.org/10.1016/j.neumar.2024.100034

Abushakra S, Power A, Watson D, et al. (2025). Clinical efficacy, safety and imaging effects of oral valiltramiprosate in APOE $\varepsilon$ 4/ $\varepsilon$ 4 homozygotes with early Alzheimer's disease: Results of the Phase III, randomized, double-blind, placebo-controlled, 78-week APOLLOE4 trial. Drugs, 85, 1455-1472.

Abushakra S, et al. (2026). Effects of oral valiltramiprosate on clinical efficacy, safety, and brain volume outcomes in APOE4/4 homozygotes with early Alzheimer's disease: Topline results of the 78-week Phase 3 APOLLOE4 trial (P1-12.001). Neurology, 106(11 Suppl 1), 4443.

Aizenstein, H. J., Nebes, R. D., Saxton, J. A., Price, J. C., Mathis, C. A., Tsopelas, N. D., Ziolko, S. K., James, J. A., Snitz, B. E., Houck, P. R., Bi, W., Cohen, A. D., Lopresti, B. J., DeKosky, S. T., Halligan, E. M., & Klunk, W. E. (2008). Frequent amyloid deposition without significant cognitive impairment among the elderly. *Archives of Neurology*, *65*(11), 1509–1517. https://doi.org/10.1001/archneur.65.11.1509

Allen, N. J. (2020). Chapter 33—Astrocyte–neuron interactions in synaptic development. In J. Rubenstein, P. Rakic, B. Chen, & K. Y. Kwan (Eds), *Patterning and Cell Type Specification in the Developing CNS and PNS (Second Edition)* (pp. 829–846). Academic Press. https://doi.org/10.1016/B978-0-12-814405-3.00033-3

Allen, N. J., & Eroglu, C. (2017). Cell Biology of Astrocyte-Synapse Interactions. *Neuron*, *96*(3), 697–708. https://doi.org/10.1016/j.neuron.2017.09.056

Al-Qahtani, A. A., Alhamlan, F. S., & Al-Qahtani, A. A. (2024). Pro-Inflammatory and Anti-Inflammatory Interleukins in Infectious Diseases: A Comprehensive Review. *Tropical Medicine and Infectious Disease*, *9*(1), Article 1. https://doi.org/10.3390/tropicalmed9010013

Altshuler, D., Donnelly, P., & The International HapMap Consortium. (2005). A haplotype map of the human genome. *Nature*, *437*(7063), 1299–1320. https://doi.org/10.1038/nature04226

Andersen, J. V., Markussen, K. H., Jakobsen, E., Schousboe, A., Waagepetersen, H. S., Rosenberg, P. A., & Aldana, B. I. (2021). Glutamate metabolism and recycling at the excitatory synapse in health and neurodegeneration. *Neuropharmacology*, *196*, 108719.

https://doi.org/10.1016/j.neuropharm.2021.108719

Araque, A., Parpura, V., Sanzgiri, R. P., & Haydon, P. G. (1999). Tripartite synapses: Glia, the unacknowledged partner. *Trends in Neurosciences*, *22*(5), 208–215. https://doi.org/10.1016/s0166-2236(98)01349-6

Atagi, Y., Liu, C.-C., Painter, M. M., Chen, X.-F., Verbeeck, C., Zheng, H., Li, X., Rademakers, R., Kang, S. S., Xu, H., Younkin, S., Das, P., Fryer, J. D., & Bu, G. (2015). Apolipoprotein E Is a Ligand for Triggering Receptor Expressed on Myeloid Cells 2 (TREM2). *Journal of Biological Chemistry*, *290*(43), 26043–26050. https://doi.org/10.1074/jbc.M115.679043

Athanasopoulou, K., Daneva, G. N., Adamopoulos, P. G., & Scorilas, A. (2022). Artificial Intelligence: The Milestone in Modern Biomedical Research. *BioMedInformatics*, *2*(4), Article 4. https://doi.org/10.3390/biomedinformatics2040049

Azevedo, F. A. C., Carvalho, L. R. B., Grinberg, L. T., Farfel, J. M., Ferretti, R. E. L., Leite, R. E. P., Jacob Filho, W., Lent, R., & Herculano-Houzel, S. (2009). Equal numbers of neuronal and nonneuronal cells make the human brain an isometrically scaled-up primate brain. *The Journal of Comparative Neurology*, *513*(5), 532–541. https://doi.org/10.1002/cne.21974

Balu, D., Karstens, A. J., Loukenas, E., Weng, J. M., York, J. M., Valencia-Olvera, A. C., & LaDu, M. J. (2019). The role of APOE in transgenic mouse models of AD. *Neuroscience Letters*, *707*, 134285. https://doi.org/10.1016/j.neulet.2019.134285

Barbar, L., Jain, T., Zimmer, M., Kruglikov, I., Sadick, J. S., Wang, M., Kalpana, K., Rose, I. V. L., Burstein, S. R., Rusielewicz, T., Nijsure, M., Guttenplan, K. A., Domenico, A. di, Croft, G., Zhang, B., Nobuta, H., Hébert, J. M., Liddelow, S. A., & Fossati, V. (2020). CD49f Is a Novel Marker of Functional and Reactive Human iPSC-Derived Astrocytes. *Neuron*, *107*(3), 436-453.e12. https://doi.org/10.1016/j.neuron.2020.05.014

Barker, A. J., Koch, S. M., Reed, J., Barres, B. A., & Ullian, E. M. (2008). Developmental Control of Synaptic Receptivity. *Journal of Neuroscience*, *28*(33), 8150–8160. https://doi.org/10.1523/JNEUROSCI.1744-08.2008

Bellenguez, C., Küçükali, F., Jansen, I. E., Kleineidam, L., Moreno-Grau, S., Amin, N., Naj, A. C., Campos-Martin, R., Grenier-Boley, B., Andrade, V., Holmans, P. A., Boland, A., Damotte, V., van der Lee, S. J., Costa, M. R., Kuulasmaa, T., Yang, Q., de Rojas, I., Bis, J. C., … Lambert, J.-C. (2022). New insights into the genetic etiology of Alzheimer's disease and related dementias. *Nature Genetics*, *54*(4), 412–436. https://doi.org/10.1038/s41588-022-01024-z

Belloy, M. E., Andrews, S. J., Le Guen, Y., Cuccaro, M., Farrer, L. A., Napolioni, V., & Greicius, M. D. (2023). APOE Genotype and Alzheimer Disease Risk Across Age, Sex, and Population Ancestry. *JAMA Neurology*, *80*(12), 1284–1294. https://doi.org/10.1001/jamaneurol.2023.3599

Belloy, M. E., Napolioni, V., & Greicius, M. D. (2019). A Quarter Century of APOE and Alzheimer's

Disease: Progress to Date and the Path Forward. *Neuron*, *101*(5), 820–838. https://doi.org/10.1016/j.neuron.2019.01.056

Benilova, I., Karran, E., & De Strooper, B. (2012). The toxic Aβ oligomer and Alzheimer's disease: An emperor in need of clothes. *Nature Neuroscience*, *15*(3), 349–357. https://doi.org/10.1038/nn.3028

Berghoff, S. A., Spieth, L., Sun, T., Hosang, L., Depp, C., Sasmita, A. O., Vasileva, M. H., Scholz, P., Zhao, Y., Krueger-Burg, D., Wichert, S., Brown, E. R., Michail, K., Nave, K.-A., Bonn, S., Odoardi, F., Rossner, M., Ischebeck, T., Edgar, J. M., & Saher, G. (2021). Neuronal cholesterol synthesis is essential for repair of chronically demyelinated lesions in mice. *Cell Reports*, *37*(4), 109889. https://doi.org/10.1016/j.celrep.2021.109889

Betz, W. J., Mao, F., & Bewick, G. S. (1992). Activity-dependent fluorescent staining and destaining of living vertebrate motor nerve terminals. *The Journal of Neuroscience: The Official Journal of the Society for Neuroscience*, *12*(2), 363–375. https://doi.org/10.1523/JNEUROSCI.12-02-00363.1992

Biffi, A., & Greenberg, S. M. (2011). Cerebral amyloid angiopathy: A systematic review. *Journal of Clinical Neurology (Seoul, Korea)*, *7*(1), 1–9. https://doi.org/10.3988/jcn.2011.7.1.1

Birger, A., Ben-Dor, I., Ottolenghi, M., Turetsky, T., Gil, Y., Sweetat, S., Perez, L., Belzer, V., Casden, N., Steiner, D., Izrael, M., Galun, E., Feldman, E., Behar, O., & Reubinoff, B. (2019). Human iPSC-derived astrocytes from ALS patients with mutated C9ORF72 show increased oxidative stress and neurotoxicity. *EBioMedicine*, *50*, 274–289. https://doi.org/10.1016/j.ebiom.2019.11.026

Black, J. E., Kueper, J. K., & Williamson, T. S. (2023). An introduction to machine learning for classification and prediction. *Family Practice*, *40*(1), 200–204. https://doi.org/10.1093/fampra/cmac104

Blanchard, J. W., Akay, L. A., Davila-Velderrain, J., von Maydell, D., Mathys, H., Davidson, S. M., Effenberger, A., Chen, C.-Y., Maner-Smith, K., Hajjar, I., Ortlund, E. A., Bula, M., Agbas, E., Ng, A., Jiang, X., Kahn, M., Blanco-Duque, C., Lavoie, N., Liu, L., … Tsai, L.-H. (2022). APOE4 impairs myelination via cholesterol dysregulation in oligodendrocytes. *Nature*, *611*(7937), Article 7937. https://doi.org/10.1038/s41586-022-05439-w

Blanchard, J. W., Bula, M., Davila-Velderrain, J., Akay, L. A., Zhu, L., Frank, A., Victor, M. B., Bonner, J. M., Mathys, H., Lin, Y.-T., Ko, T., Bennett, D. A., Cam, H. P., Kellis, M., & Tsai, L.-H. (2020). Reconstruction of the human blood-brain barrier in vitro reveals a pathogenic mechanism of APOE4 in pericytes. *Nature Medicine*, *26*(6), 952–963. https://doi.org/10.1038/s41591-020-0886-4

Blumenfeld, J., Yip, O., Kim, M. J., & Huang, Y. (2024). Cell type-specific roles of APOE4 in Alzheimer disease. *Nature Reviews Neuroscience*, *25*(2), 91–110. https://doi.org/10.1038/s41583-023-00776-9

Brezovakova, V., Sykova, E., & Jadhav, S. (2022). Astrocytes Derived from Familial and Sporadic Alzheimer's Disease iPSCs Show Altered Calcium Signaling and Respond Differently to Misfolded Protein Tau. *Cells*, *11*(9), 1429. https://doi.org/10.3390/cells11091429

Buenrostro, J. D., Wu, B., Chang, H. Y., & Greenleaf, W. J. (2015). ATAC-seq: A Method for Assaying Chromatin Accessibility Genome-Wide. *Current Protocols in Molecular Biology*, *109*, 21.29.1-21.29.9. https://doi.org/10.1002/0471142727.mb2129s109

Busche, M. A., & Konnerth, A. (2016). Impairments of neural circuit function in Alzheimer's disease. *Philosophical Transactions of the Royal Society B: Biological Sciences*, *371*(1700), 20150429. https://doi.org/10.1098/rstb.2015.0429

Butterfield, D. A., & Mattson, M. P. (2020). Apolipoprotein E and Oxidative Stress in Brain with Relevance to Alzheimer Disease. *Neurobiology of Disease*, *138*, 104795. https://doi.org/10.1016/j.nbd.2020.104795

Cai, Q., & Tammineni, P. (2017). Mitochondrial Aspects of Synaptic Dysfunction in Alzheimer's Disease. *Journal of Alzheimer's Disease : JAD*, *57*(4), 1087–1103. https://doi.org/10.3233/JAD-160726

Caicedo, J. C., Cooper, S., Heigwer, F., Warchal, S., Qiu, P., Molnar, C., Vasilevich, A. S., Barry, J. D., Bansal, H. S., Kraus, O., Wawer, M., Paavolainen, L., Herrmann, M. D., Rohban, M., Hung, J., Hennig, H., Concannon, J., Smith, I., Clemons, P. A., … Carpenter, A. E. (2017). Data-analysis strategies for image-based cell profiling. *Nature Methods*, *14*(9), 849–863. https://doi.org/10.1038/nmeth.4397

Calero-Cuenca, F. J., Janota, C. S., & Gomes, E. R. (2018). Dealing with the nucleus during cell migration. *Current Opinion in Cell Biology*, *50*, 35–41. https://doi.org/10.1016/j.ceb.2018.01.014

Camargo, N., Goudriaan, A., van Deijk, A.-L. F., Otte, W. M., Brouwers, J. F., Lodder, H., Gutmann, D. H., Nave, K.-A., Dijkhuizen, R. M., Mansvelder, H. D., Chrast, R., Smit, A. B., & Verheijen, M. H. G. (2017). Oligodendroglial myelination requires astrocyte-derived lipids. *PLoS Biology*, *15*(5), e1002605. https://doi.org/10.1371/journal.pbio.1002605

Canals, I., Ginisty, A., Quist, E., Timmerman, R., Fritze, J., Miskinyte, G., Monni, E., Hansen, M. G., Hidalgo, I., Bryder, D., Bengzon, J., & Ahlenius, H. (2018). Rapid and efficient induction of functional astrocytes from human pluripotent stem cells. *Nature Methods*, *15*(9), 693–696. https://doi.org/10.1038/s41592-018-0103-2

Canessa, E., Chaigneau, S. E., Moreno, S., & Lagos, R. (2020). Informational content of cosine and other similarities calculated from high-dimensional Conceptual Property Norm data. *Cognitive Processing*, *21*(4), 601–614. https://doi.org/10.1007/s10339-020-00985-5

Carter, J. L., Halmai, J. A. N. M., & Fink, K. D. (2020). The iNs and Outs of Direct Reprogramming to Induced Neurons. *Frontiers in Genome Editing*, *2*. https://doi.org/10.3389/fgeed.2020.00007

Casati, M., Ferri, E., Gussago, C., Mazzola, P., Abbate, C., Bellelli, G., Mari, D., Cesari, M., & Arosio, B. (2018). Increased expression of TREM2 in peripheral cells from mild cognitive impairment patients who progress into Alzheimer's disease. *European Journal of Neurology*, *25*(6), 805–810. https://doi.org/10.1111/ene.13583

Cash, J. G., Kuhel, D. G., Basford, J. E., Jaeschke, A., Chatterjee, T. K., Weintraub, N. L., & Hui, D. Y. (2012). Apolipoprotein E4 Impairs Macrophage Efferocytosis and Potentiates Apoptosis by Accelerating Endoplasmic Reticulum Stress *. *Journal of Biological Chemistry*, *287*(33), 27876–27884. https://doi.org/10.1074/jbc.M112.377549

Cashikar, A. G., Toral-Rios, D., Timm, D., Romero, J., Strickland, M., Long, J. M., Han, X., Holtzman, D. M., & Paul, S. M. (2023). Regulation of astrocyte lipid metabolism and ApoE secretion by the microglial oxysterol, 25-hydroxycholesterol. *Journal of Lipid Research*, *64*(4). https://doi.org/10.1016/j.jlr.2023.100350

Castellano, J. M., Kim, J., Stewart, F. R., Jiang, H., DeMattos, R. B., Patterson, B. W., Fagan, A. M., Morris, J. C., Mawuenyega, K. G., Cruchaga, C., Goate, A. M., Bales, K. R., Paul, S. M., Bateman, R. J., & Holtzman, D. M. (2011). Human apoE isoforms differentially regulate brain amyloid-β peptide clearance. *Science Translational Medicine*, *3*(89), 89ra57. https://doi.org/10.1126/scitranslmed.3002156

Cataldo, A. M., Barnett, J. L., Pieroni, C., & Nixon, R. A. (1997). Increased Neuronal Endocytosis and Protease Delivery to Early Endosomes in Sporadic Alzheimer's Disease: Neuropathologic Evidence for a Mechanism of Increased β-Amyloidogenesis. *Journal of Neuroscience*, *17*(16), 6142–6151. https://doi.org/10.1523/JNEUROSCI.17-16-06142.1997

Cataldo, A. M., Peterhoff, C. M., Troncoso, J. C., Gomez-Isla, T., Hyman, B. T., & Nixon, R. A. (2000). Endocytic Pathway Abnormalities Precede Amyloid β Deposition in Sporadic Alzheimer's Disease and Down Syndrome: Differential Effects of APOE Genotype and Presenilin Mutations. *The American Journal of Pathology*, *157*(1), 277–286. https://doi.org/10.1016/S0002-9440(10)64538-5

Cerneckis, J., Cai, H., & Shi, Y. (2024). Induced pluripotent stem cells (iPSCs): Molecular mechanisms of induction and applications. *Signal Transduction and Targeted Therapy*, *9*(1), 112. https://doi.org/10.1038/s41392-024-01809-0

Chandrasekaran, S. N., Ackerman, J., Alix, E., Ando, D. M., Arevalo, J., Bennion, M., Boisseau, N., Borowa, A., Boyd, J. D., Brino, L., Byrne, P. J., Ceulemans, H., Ch'ng, C., Cimini, B. A., Clevert, D.-A., Deflaux, N., Doench, J. G., Dorval, T., Doyonnas, R., … Carpenter, A. E. (2023). *JUMP Cell Painting dataset: Morphological impact of 136,000 chemical and genetic perturbations* (p. 2023.03.23.534023). bioRxiv. https://doi.org/10.1101/2023.03.23.534023

Chavda, V., Singh, K., Patel, V., Mishra, M., & Mishra, A. K. (2022). Neuronal Glial Crosstalk: Specific and Shared Mechanisms in Alzheimer's Disease. *Brain Sciences*, *12*(1), 75. https://doi.org/10.3390/brainsci12010075

Chen, Y., Durakoglugil, M. S., Xian, X., & Herz, J. (2010). ApoE4 reduces glutamate receptor function and synaptic plasticity by selectively impairing ApoE receptor recycling. *Proceedings of the National Academy of Sciences of the United States of America*, *107*(26), 12011–12016. https://doi.org/10.1073/pnas.0914984107

Chiareli, R. A., Carvalho, G. A., Marques, B. L., Mota, L. S., Oliveira-Lima, O. C., Gomes, R. M., Birbrair, A., Gomez, R. S., Simão, F., Klempin, F., Leist, M., & Pinto, M. C. X. (2021). The Role of Astrocytes in the Neurorepair Process. *Frontiers in Cell and Developmental Biology*, *9*. https://doi.org/10.3389/fcell.2021.665795

Christopherson, K. S., Ullian, E. M., Stokes, C. C. A., Mullowney, C. E., Hell, J. W., Agah, A., Lawler, J., Mosher, D. F., Bornstein, P., & Barres, B. A. (2005). Thrombospondins are astrocyte-secreted proteins that promote CNS synaptogenesis. *Cell*, *120*(3), 421–433. https://doi.org/10.1016/j.cell.2004.12.020

Christou, Y. A., Ohyama, K., Placzek, M., Monk, P. N., & Shaw, P. J. (2013). Wild-type but not mutant SOD1 transgenic astrocytes promote the efficient generation of motor neuron progenitors from mouse embryonic stem cells. *BMC Neuroscience*, *14*(1), 126. https://doi.org/10.1186/1471-2202-14-126

Cloak, N., Schoo, C., & Al Khalili, Y. (2025). Behavioral and Psychological Symptoms in Dementia. In *StatPearls*. StatPearls Publishing. http://www.ncbi.nlm.nih.gov/books/NBK551552/

Cole, S. L., & Vassar, R. (2007). The Alzheimer's disease β-secretase enzyme, BACE1. *Molecular Neurodegeneration*, *2*, 22. https://doi.org/10.1186/1750-1326-2-22

Congdon, E. E., Ji, C., Tetlow, A. M., Jiang, Y., & Sigurdsson, E. M. (2023). Tau-targeting therapies for Alzheimer disease: Current status and future directions. *Nature Reviews. Neurology*, *19*(12), 715–736. https://doi.org/10.1038/s41582-023-00883-2

Corder, E. H., Saunders, A. M., Strittmatter, W. J., Schmechel, D. E., Gaskell, P. C., Small, G. W., Roses, A. D., Haines, J. L., & Pericak-Vance, M. A. (1993). Gene dose of apolipoprotein E type 4 allele and the risk of Alzheimer's disease in late onset families. *Science (New York, N.Y.)*, *261*(5123), 921–923. https://doi.org/10.1126/science.8346443

Cummings, J., Lee, G., Ritter, A., Sabbagh, M., & Zhong, K. (2019). Alzheimer's disease drug development pipeline: 2019. *Alzheimer's & Dementia : Translational Research & Clinical Interventions*, *5*, 272–293. https://doi.org/10.1016/j.trci.2019.05.008

Dai, Y., Sun, F., Zhu, H., Liu, Q., Xu, X., Gong, P., Jiang, R., Jin, G., Qin, J., Chen, J., Zhang, X., & Shi, W. (2019). Effects and Mechanism of Action of Neonatal Versus Adult Astrocytes on Neural Stem Cell Proliferation After Traumatic Brain Injury. *Stem Cells*, *37*(10), 1344–1356. https://doi.org/10.1002/stem.3060

Danbolt, N. C. (2001). Glutamate uptake. *Progress in Neurobiology*, *65*(1), 1–105. https://doi.org/10.1016/s0301-0082(00)00067-8

de Ceglia, R., Ledonne, A., Litvin, D. G., Lind, B. L., Carriero, G., Latagliata, E. C., Bindocci, E., Di Castro, M. A., Savtchouk, I., Vitali, I., Ranjak, A., Congiu, M., Canonica, T., Wisden, W., Harris, K., Mameli, M., Mercuri, N., Telley, L., & Volterra, A. (2023). Specialized astrocytes mediate glutamatergic gliotransmission in the CNS. *Nature*, *622*(7981), 120–129. https://doi.org/10.1038/s41586-023-06502-w

De Strooper, B., & Karran, E. (2016). The Cellular Phase of Alzheimer's Disease. *Cell*, *164*(4), 603–615. https://doi.org/10.1016/j.cell.2015.12.056

Deane, R., Sagare, A., Hamm, K., Parisi, M., Lane, S., Finn, M. B., Holtzman, D. M., & Zlokovic, B. V. (2008). apoE isoform-specific disruption of amyloid beta peptide clearance from mouse brain. *The Journal of Clinical Investigation*, *118*(12), 4002–4013. https://doi.org/10.1172/JCI36663

DeGiosio, R. A., Grubisha, M. J., MacDonald, M. L., McKinney, B. C., Camacho, C. J., & Sweet, R. A. (2022). More than a marker: Potential pathogenic functions of MAP2. *Frontiers in Molecular Neuroscience*, *15*. https://doi.org/10.3389/fnmol.2022.974890

Degl'Innocenti, E., & Dell'Anno, M. T. (2023). Human and mouse cortical astrocytes: A comparative view from development to morphological and functional characterization. *Frontiers in Neuroanatomy*, *17*, 1130729. https://doi.org/10.3389/fnana.2023.1130729

Dias, D., Portugal, C. C., Relvas, J., Socodato, R., Dias, D., Portugal, C. C., Relvas, J., & Socodato, R. (2025). From Genetics to Neuroinflammation: The Impact of ApoE4 on Microglial Function in Alzheimer's Disease. *Cells*, *14*(4). https://doi.org/10.3390/cells14040243

Djukic, B., Casper, K. B., Philpot, B. D., Chin, L.-S., & McCarthy, K. D. (2007). Conditional Knock-Out of Kir4.1 Leads to Glial Membrane Depolarization, Inhibition of Potassium and Glutamate Uptake, and Enhanced Short-Term Synaptic Potentiation. *Journal of Neuroscience*, *27*(42), 11354–11365. https://doi.org/10.1523/JNEUROSCI.0723-07.2007

dos Santos, Á. (2021). *Spatial and Physical Organisation of the Mammalian Nucleus* [Phd, University of Sheffield]. https://etheses.whiterose.ac.uk/id/eprint/30579/

Dossi, E., Vasile, F., & Rouach, N. (2018). Human astrocytes in the diseased brain. *Brain Research Bulletin*, *136*, 139–156. https://doi.org/10.1016/j.brainresbull.2017.02.001

Drummond, E., & Wisniewski, T. (2017). Alzheimer's Disease: Experimental Models and Reality. *Acta Neuropathologica*, *133*(2), 155–175. https://doi.org/10.1007/s00401-016-1662-x

Ebenau, J. L., van der Lee, S. J., Hulsman, M., Tesi, N., Jansen, I. E., Verberk, I. M. W., van Leeuwenstijn, M., Teunissen, C. E., Barkhof, F., Prins, N. D., Scheltens, P., Holstege, H., van Berckel, B. N. M., & van der Flier, W. M. (2021). Risk of dementia in APOE $\varepsilon$4 carriers is mitigated by a polygenic risk score. Alzheimer's & Dementia: Diagnosis, Assessment & Disease Monitoring, 13(1), e12229.

Escartin, C., Galea, E., Lakatos, A., O'Callaghan, J. P., Petzold, G. C., Serrano-Pozo, A., Steinhäuser, C., Volterra, A., Carmignoto, G., Agarwal, A., Allen, N. J., Araque, A., Barbeito, L., Barzilai, A., Bergles, D. E., Bonvento, G., Butt, A. M., Chen, W.-T., Cohen-Salmon, M., … Verkhratsky, A. (2021). Reactive astrocyte nomenclature, definitions, and future directions. *Nature Neuroscience*, *24*(3), 312–325. https://doi.org/10.1038/s41593-020-00783-4

Fan, J., Liu, J., Liu, J., Chen, C., Koutalos, Y., & Crosson, C. E. (2021). Evidence for ceramide induced cytotoxicity in retinal ganglion cells. *Experimental Eye Research*, *211*, 108762. https://doi.org/10.1016/j.exer.2021.108762

Farhy-Tselnicker, I., & Allen, N. J. (2018). Astrocytes, neurons, synapses: A tripartite view on cortical circuit development. *Neural Development*, *13*(1), 7. https://doi.org/10.1186/s13064-018-0104-y

Farrer, L. A., Cupples, L. A., Haines, J. L., Hyman, B., Kukull, W. A., Mayeux, R., Myers, R. H., Pericak-Vance, M. A., Risch, N., & van Duijn, C. M. (1997). Effects of age, sex, and ethnicity on the association between apolipoprotein E genotype and Alzheimer disease. A meta-analysis. APOE and Alzheimer Disease Meta Analysis Consortium. *JAMA*, *278*(16), 1349–1356.

Fedele, E. (2023). Anti-Amyloid Therapies for Alzheimer's Disease and the Amyloid Cascade Hypothesis. *International Journal of Molecular Sciences*, *24*(19), 14499. https://doi.org/10.3390/ijms241914499

Feng, S., Zhuang, M., & Wu, R. (2012). Secretion of nerve growth factor, brain-derived neurotrophic factor, and glial cell-line derived neurotrophic factor in co-culture of four cell types in cerebrospinal fluid-containing medium. *Neural Regeneration Research*, *7*(36), 2907–2914. https://doi.org/10.3969/j.issn.1673-5374.2012.36.008

Fernandez, C. G., Hamby, M. E., McReynolds, M. L., & Ray, W. J. (2019). The Role of APOE4 in Disrupting the Homeostatic Functions of Astrocytes and Microglia in Aging and Alzheimer's Disease. *Frontiers in Aging Neuroscience*, *11*, 14. https://doi.org/10.3389/fnagi.2019.00014

Fernández-Calle, R., Konings, S. C., Frontiñán-Rubio, J., García-Revilla, J., Camprubí-Ferrer, L., Svensson, M., Martinson, I., Boza-Serrano, A., Venero, J. L., Nielsen, H. M., Gouras, G. K., & Deierborg, T. (2022). APOE in the bullseye of neurodegenerative diseases: Impact of the APOE genotype in Alzheimer's disease pathology and brain diseases. *Molecular Neurodegeneration*, *17*(1), 62. https://doi.org/10.1186/s13024-022-00566-4

Fleeman, R. M., Kuhn, M. K., Chan, D. C., & Proctor, E. A. (2023). Apolipoprotein E ε4 modulates astrocyte neuronal support functions in the presence of amyloid-β. *Journal of Neurochemistry*, jnc.15781. https://doi.org/10.1111/jnc.15781

Flores, L. F., Tader, B. R., Tolosa, E. J., Sigafoos, A. N., Marks, D. L., & Fernandez-Zapico, M. E. (2021). Nuclear Dynamics and Chromatin Structure: Implications for Pancreatic Cancer. *Cells*, *10*(10), 2624. https://doi.org/10.3390/cells10102624

Fortea, J., Pegueroles, J., Alcolea, D., et al. (2024). APOE4 homozygosity represents a distinct genetic form of Alzheimer's disease. Nature Medicine, 30, 1284–1291. https://doi.org/10.1038/s41591-024-02931-w

Friedemann, M., Helk, E., Tiiman, A., Zovo, K., Palumaa, P., & Tõugu, V. (2015). Effect of methionine-35 oxidation on the aggregation of amyloid-β peptide. *Biochemistry and Biophysics Reports*, *3*, 94–99. https://doi.org/10.1016/j.bbrep.2015.07.017

Fritschi, L., Lindmar, J. H., Scheidl, F., & Lenk, K. (2021). Neuronal and Astrocytic Regulations in Schizophrenia: A Computational Modelling Study. *Frontiers in Cellular Neuroscience*, *15*. https://doi.org/10.3389/fncel.2021.718459

Fulton, E. A. (2010). Approaches to end-to-end ecosystem models. *Journal of Marine Systems*, *81*(1), 171–183. https://doi.org/10.1016/j.jmarsys.2009.12.012

Ganesan, K., Rentsch, P., Langdon, A., Milham, L. T., & Vissel, B. (2024). Modeling sporadic Alzheimer's disease in mice by combining Apolipoprotein E4 risk gene with environmental risk factors. *Frontiers in Aging Neuroscience*, *16*. https://doi.org/10.3389/fnagi.2024.1357405

Garcia, A. R., Finch, C., Gatz, M., Kraft, T., Rodriguez, D. E., Cummings, D., Charifson, M., Buetow, K., Beheim, B. A., Allayee, H., Thomas, G. S., Stieglitz, J., Gurven, M. D., Kaplan, H., & Trumble, B. C. (2021). Apoe4 is associated with elevated blood lipids and lower levels of innate immune biomarkers in a tropical amerindian subsistence population. *eLife*, *10*(e68231). https://doi.org/10.7554/eLife.68231

Garcia, V. J., Rushton, D. J., Tom, C. M., Allen, N. D., Kemp, P. J., Svendsen, C. N., & Mattis, V. B. (2019). Huntington's Disease Patient-Derived Astrocytes Display Electrophysiological Impairments and Reduced Neuronal Support. *Frontiers in Neuroscience*, *13*. https://doi.org/10.3389/fnins.2019.00669

Gascón, S., Masserdotti, G., Russo, G. L., & Götz, M. (2017). Direct Neuronal Reprogramming: Achievements, Hurdles, and New Roads to Success. *Cell Stem Cell*, *21*(1), 18–34. https://doi.org/10.1016/j.stem.2017.06.011

Górriz, J. M., Álvarez-Illán, I., Álvarez-Marquina, A., Arco, J. E., Atzmueller, M., Ballarini, F., Barakova, E., Bologna, G., Bonomini, P., Castellanos-Dominguez, G., Castillo-Barnes, D., Cho, S. B., Contreras, R., Cuadra, J. M., Domínguez, E., Domínguez-Mateos, F., Duro, R. J., Elizondo, D., Fernández-Caballero, A., … Ferrández-Vicente, J. M. (2023). Computational approaches to Explainable Artificial Intelligence: Advances in theory, applications and trends. *Information Fusion*, *100*, 101945. https://doi.org/10.1016/j.inffus.2023.101945

Greco, T. M., Seeholzer, S. H., Mak, A., Spruce, L., & Ischiropoulos, H. (2010). Quantitative Mass Spectrometry-based Proteomics Reveals the Dynamic Range of Primary Mouse Astrocyte Protein Secretion. *Journal of Proteome Research*, *9*(5), 2764–2774. https://doi.org/10.1021/pr100134n

Greenberg, S. M. (1998). Cerebral amyloid angiopathy. *Neurology*, *51*(3), 690–694. https://doi.org/10.1212/WNL.51.3.690

Grubman, A., Chew, G., Ouyang, J. F., Sun, G., Choo, X. Y., McLean, C., Simmons, R. K., Buckberry, S., Vargas-Landin, D. B., Poppe, D., Pflueger, J., Lister, R., Rackham, O. J. L., Petretto, E., & Polo, J. M. (2019). A single-cell atlas of entorhinal cortex from individuals with Alzheimer's disease reveals cell-type-specific gene expression regulation. *Nature Neuroscience*, *22*(12), 2087–2097. https://doi.org/10.1038/s41593-019-0539-4

Guo, J. L., & Lee, V. M.-Y. (2011). Seeding of normal Tau by pathological Tau conformers drives

pathogenesis of Alzheimer-like tangles. *The Journal of Biological Chemistry*, *286*(17), 15317–15331. https://doi.org/10.1074/jbc.M110.209296

Habib, N., McCabe, C., Medina, S., Varshavsky, M., Kitsberg, D., Dvir-Szternfeld, R., Green, G., Dionne, D., Nguyen, L., Marshall, J. L., Chen, F., Zhang, F., Kaplan, T., Regev, A., & Schwartz, M. (2020). Disease-associated astrocytes in Alzheimer's disease and aging. *Nature Neuroscience*, *23*(6), 701–706. https://doi.org/10.1038/s41593-020-0624-8

Hajjo, R., Sabbah, D. A., Abusara, O. H., & Al Bawab, A. Q. (2022). A Review of the Recent Advances in Alzheimer's Disease Research and the Utilization of Network Biology Approaches for Prioritizing Diagnostics and Therapeutics. *Diagnostics*, *12*(12), 2975. https://doi.org/10.3390/diagnostics12122975

Hama, H., Hara, C., Yamaguchi, K., & Miyawaki, A. (2004). PKC signaling mediates global enhancement of excitatory synaptogenesis in neurons triggered by local contact with astrocytes. *Neuron*, *41*(3), 405–415. https://doi.org/10.1016/s0896-6273(04)00007-8

Hampel, H., Hardy, J., Blennow, K., Chen, C., Perry, G., Kim, S. H., Villemagne, V. L., Aisen, P., Vendruscolo, M., Iwatsubo, T., Masters, C. L., Cho, M., Lannfelt, L., Cummings, J. L., & Vergallo, A. (2021). The Amyloid-β Pathway in Alzheimer's Disease. *Molecular Psychiatry*, *26*(10), 5481–5503. https://doi.org/10.1038/s41380-021-01249-0

Hawkes, C. A., Sullivan, P. M., Hands, S., Weller, R. O., Nicoll, J. A. R., & Carare, R. O. (2012). Disruption of Arterial Perivascular Drainage of Amyloid-β from the Brains of Mice Expressing the Human APOE ε4 Allele. *PLoS ONE*, *7*(7), e41636. https://doi.org/10.1371/journal.pone.0041636

He, K., Li, B., Wang, J., Wang, Y., You, Z., Chen, X., Chen, H., Li, J., Huang, Q., Guo, Q., Huang, Y. H., Guan, Y., Chen, K., Zhao, J., Deng, Y., & Xie, F. (2024). APOE ε4 is associated with decreased synaptic density in cognitively impaired participants. *Alzheimer's & Dementia*, *20*(5), 3157–3166. https://doi.org/10.1002/alz.13775

Heinzelmann, E., Piraino, F., Costa, M., Roch, A., Norkin, M., Garnier, V., Homicsko, K., & Brandenberg, N. (2024). iPSC-derived and Patient-Derived Organoids: Applications and challenges in scalability and reproducibility as pre-clinical models. *Current Research in Toxicology*, *7*, 100197. https://doi.org/10.1016/j.crtox.2024.100197

Heneka, M. T. (2023). ApoE4 makes microglia trem2bling. *Neuron*, *111*(2), 142–144. https://doi.org/10.1016/j.neuron.2022.12.032

Herz, J., & Chen, Y. (2006). Reelin, lipoprotein receptors and synaptic plasticity. *Nature Reviews. Neuroscience*, *7*(11), 850–859. https://doi.org/10.1038/nrn2009

Hickman, S., Izzy, S., Sen, P., Morsett, L., & El Khoury, J. (2018). Microglia in neurodegeneration. *Nature Neuroscience*, *21*(10), 1359–1369. https://doi.org/10.1038/s41593-018-0242-x

Hicks, D. A., Nalivaeva, N. N., & Turner, A. J. (2012). Lipid Rafts and Alzheimer's Disease: Protein-Lipid

Interactions and Perturbation of Signaling. *Frontiers in Physiology*, *3*. https://doi.org/10.3389/fphys.2012.00189

Holtzman, D. M., Morris, J. C., & Goate, A. M. (2011). Alzheimer's Disease: The Challenge of the Second Century. *Science Translational Medicine*, *3*(77). https://doi.org/10.1126/scitranslmed.3002369

Hosny, A., Parmar, C., Quackenbush, J., Schwartz, L. H., & Aerts, H. J. W. L. (2018). Artificial intelligence in radiology. *Nature Reviews. Cancer*, *18*(8), 500–510. https://doi.org/10.1038/s41568-018-0016-5

Hossain, E., Rana, R., Higgins, N., Soar, J., Barua, P. D., Pisani, A. R., & Turner, K. (2023). Natural Language Processing in Electronic Health Records in relation to healthcare decision-making: A systematic review. *Computers in Biology and Medicine*, *155*, 106649. https://doi.org/10.1016/j.compbiomed.2023.106649

Hu, Y.-B., Dammer, E. B., Ren, R.-J., & Wang, G. (2015). The endosomal-lysosomal system: From acidification and cargo sorting to neurodegeneration. *Translational Neurodegeneration*, *4*(1), 18. https://doi.org/10.1186/s40035-015-0041-1

Huang, C.-Y., Liu, C.-L., Ting, C.-Y., Chiu, Y.-T., Cheng, Y.-C., Nicholson, M. W., & Hsieh, P. C. H. (2019). Human iPSC banking: Barriers and opportunities. *Journal of Biomedical Science*, *26*(1), 87. https://doi.org/10.1186/s12929-019-0578-x

Huang, Y.-W. A., Zhou, B., Wernig, M., & Südhof, T. C. (2017). ApoE2, ApoE3, and ApoE4 Differentially Stimulate APP Transcription and Aβ Secretion. *Cell*, *168*(3), 427-441.e21. https://doi.org/10.1016/j.cell.2016.12.044

Iatrou, A., Clark, E. M., & Wang, Y. (2021). Nuclear dynamics and stress responses in Alzheimer's disease. *Molecular Neurodegeneration*, *16*(1), 65. https://doi.org/10.1186/s13024-021-00489-6

Iliff, J. J., Wang, M., Liao, Y., Plogg, B. A., Peng, W., Gundersen, G. A., Benveniste, H., Vates, G. E., Deane, R., Goldman, S. A., Nagelhus, E. A., & Nedergaard, M. (2012). A paravascular pathway facilitates CSF flow through the brain parenchyma and the clearance of interstitial solutes, including amyloid β. *Science Translational Medicine*, *4*(147), 147ra111. https://doi.org/10.1126/scitranslmed.3003748

Israel, M. A., Yuan, S. H., Bardy, C., Reyna, S. M., Mu, Y., Herrera, C., Hefferan, M. P., Van Gorp, S., Nazor, K. L., Boscolo, F. S., Carson, C. T., Laurent, L. C., Marsala, M., Gage, F. H., Remes, A. M., Koo, E. H., & Goldstein, L. S. B. (2012). Probing sporadic and familial Alzheimer's disease using induced pluripotent stem cells. *Nature*, *482*(7384), 216–220. https://doi.org/10.1038/nature10821

Jiang, P., Chen, C., Liu, X.-B., Pleasure, D. E., Liu, Y., & Deng, W. (2016). Human iPSC-derived Immature Astroglia Promote Oligodendrogenesis by increased TIMP-1 Secretion. *Cell Reports*, *15*(6), 1303–1315. https://doi.org/10.1016/j.celrep.2016.04.011

Jiang, Y., & MacNeil, L. T. (2023). Simple model systems reveal conserved mechanisms of Alzheimer's disease and related tauopathies. *Molecular Neurodegeneration*, *18*(1), 82.

https://doi.org/10.1186/s13024-023-00664-x

Jiang-Xie, L.-F., Drieu, A., Bhasiin, K., Quintero, D., Smirnov, I., & Kipnis, J. (2024). Neuronal dynamics direct cerebrospinal fluid perfusion and brain clearance. *Nature*, *627*(8002), 157–164. https://doi.org/10.1038/s41586-024-07108-6

Jinek, M., Chylinski, K., Fonfara, I., Hauer, M., Doudna, J. A., & Charpentier, E. (2012). A Programmable Dual-RNA–Guided DNA Endonuclease in Adaptive Bacterial Immunity. *Science*, *337*(6096), 816–821. https://doi.org/10.1126/science.1225829

Jusop, A. S., Thanaskody, K., Tye, G. J., Dass, S. A., Wan Kamarul Zaman, W. S., & Nordin, F. (2023). Development of brain organoid technology derived from iPSC for the neurodegenerative disease modelling: A glance through. *Frontiers in Molecular Neuroscience*, *16*. https://doi.org/10.3389/fnmol.2023.1173433

Kaivola, K., Shah, Z., Chia, R., & Scholz, S. W. (2021). Genetic evaluation of dementia with Lewy bodies implicates distinct disease subgroups. *Brain*, *145*(5), 1757–1762. https://doi.org/10.1093/brain/awab402

Kamentseva, R., Kosheverova, V., Kharchenko, M., Zlobina, M., Salova, A., Belyaeva, T., Nikolsky, N., & Kornilova, E. (2020). Functional cycle of EEA1-positive early endosome: Direct evidence for pre-existing compartment of degradative pathway. *PloS One*, *15*(5), e0232532. https://doi.org/10.1371/journal.pone.0232532

Kanekiyo, T., Xu, H., & Bu, G. (2014). ApoE and Aβ in Alzheimer's disease: Accidental encounters or partners? *Neuron*, *81*(4), 740–754. https://doi.org/10.1016/j.neuron.2014.01.045

Kaur, G., & Lakkaraju, A. (2018). Early Endosome Morphology in Health and Disease. *Advances in Experimental Medicine and Biology*, *1074*, 335–343. https://doi.org/10.1007/978-3-319-75402-4_41

Keren-Shaul, H., Spinrad, A., Weiner, A., Matcovitch-Natan, O., Dvir-Szternfeld, R., Ulland, T. K., David, E., Baruch, K., Lara-Astaiso, D., Toth, B., Itzkovitz, S., Colonna, M., Schwartz, M., & Amit, I. (2017). A Unique Microglia Type Associated with Restricting Development of Alzheimer's Disease. *Cell*, *169*(7), 1276-1290.e17. https://doi.org/10.1016/j.cell.2017.05.018

Kerkering, J., Muinjonov, B., Rosiewicz, K. S., Diecke, S., Biese, C., Schiweck, J., Chien, C., Zocholl, D., Conrad, T., Paul, F., Alisch, M., & Siffrin, V. (2023). iPSC-derived reactive astrocytes from patients with multiple sclerosis protect cocultured neurons in inflammatory conditions. *The Journal of Clinical Investigation*, *133*(13), e164637. https://doi.org/10.1172/JCI164637

Khakh, B. S., & Sofroniew, M. V. (2015). Diversity of astrocyte functions and phenotypes in neural circuits. *Nature Neuroscience*, *18*(7), 942–952. https://doi.org/10.1038/nn.4043

Kim, J., Basak, J. M., & Holtzman, D. M. (2009). The Role of Apolipoprotein E in Alzheimer's Disease. *Neuron*, *63*(3), 287–303. https://doi.org/10.1016/j.neuron.2009.06.026

Kim, Y., Park, J., & Choi, Y. K. (2019). The Role of Astrocytes in the Central Nervous System Focused on BK Channel and Heme Oxygenase Metabolites: A Review. *Antioxidants*, *8*(5), 121. https://doi.org/10.3390/antiox8050121

Kok, F. K., van Leerdam, S. L., & de Lange, E. C. M. (n.d.). Potential Mechanisms Underlying Resistance to Dementia in Non-Demented Individuals with Alzheimer's Disease Neuropathology. *Journal of Alzheimer's Disease*, *87*(1), 51–81. https://doi.org/10.3233/JAD-210607

Konings, S. C., Nyberg, E., Martinsson, I., Torres-Garcia, L., Klementieva, O., Almeida, C. G., & Gouras, G. K. (2023). Apolipoprotein E intersects with amyloid-β within neurons. *Life Science Alliance*, *6*(8). https://doi.org/10.26508/lsa.202201887

Konings, S. C., Torres-Garcia, L., Martinsson, I., & Gouras, G. K. (2021). Astrocytic and Neuronal Apolipoprotein E Isoforms Differentially Affect Neuronal Excitability. *Frontiers in Neuroscience*, *15*, 734001. https://doi.org/10.3389/fnins.2021.734001

Krasemann, S., Madore, C., Cialic, R., et al. (2017). The TREM2-APOE pathway drives the transcriptional phenotype of dysfunctional microglia in neurodegenerative diseases. Immunity, 47(3), 566 – 581.e9. https://doi.org/10.1016/j.immuni.2017.08.008

Krencik, R., & Zhang, S.-C. (2011). Directed differentiation of functional astroglial subtypes from human pluripotent stem cells. *Nature Protocols*, *6*(11), 1710–1717. https://doi.org/10.1038/nprot.2011.405

Kucukdereli, H., Allen, N. J., Lee, A. T., Feng, A., Ozlu, M. I., Conatser, L. M., Chakraborty, C., Workman, G., Weaver, M., Sage, E. H., Barres, B. A., & Eroglu, C. (2011). Control of excitatory CNS synaptogenesis by astrocyte-secreted proteins Hevin and SPARC. *Proceedings of the National Academy of Sciences*, *108*(32), E440–E449. https://doi.org/10.1073/pnas.1104977108

Kumar, A., Sidhu, J., Lui, F., & Tsao, J. W. (2025). Alzheimer Disease. In *StatPearls*. StatPearls Publishing. http://www.ncbi.nlm.nih.gov/books/NBK499922/

Kumar, Y., Koul, A., Singla, R., & Ijaz, M. F. (2023). Artificial intelligence in disease diagnosis: A systematic literature review, synthesizing framework and future research agenda. *Journal of Ambient Intelligence and Humanized Computing*, *14*(7), 8459–8486. https://doi.org/10.1007/s12652-021-03612-z

Kurmashev, A., Boos, J. A., Laventie, B.-J., Swart, A. L., Sütterlin, R., Junne, T., Jenal, U., & Hierlemann, A. (2024). Transwell-Based Microfluidic Platform for High-Resolution Imaging of Airway Tissues. *Advanced Materials Technologies*, *9*(20), 2400326. https://doi.org/10.1002/admt.202400326

Kushwaha, R., Sinha, A., Makarava, N., Molesworth, K., & Baskakov, I. V. (2021). Non-cell autonomous astrocyte-mediated neuronal toxicity in prion diseases. *Acta Neuropathologica Communications*, *9*(1), 22. https://doi.org/10.1186/s40478-021-01123-8

Kuszczyk, M. A., Sanchez, S., Pankiewicz, J., Kim, J., Duszczyk, M., Guridi, M., Asuni, A. A., Sullivan, P. M.,

Holtzman, D. M., & Sadowski, M. J. (2013). Blocking the Interaction between Apolipoprotein E and Aβ Reduces Intraneuronal Accumulation of Aβ and Inhibits Synaptic Degeneration. *The American Journal of Pathology*, *182*(5), 1750–1768. https://doi.org/10.1016/j.ajpath.2013.01.034

Kwon, C.-Y., & Lee, B. (2021). Prevalence of Behavioral and Psychological Symptoms of Dementia in Community-Dwelling Dementia Patients: A Systematic Review. *Frontiers in Psychiatry*, *12*. https://doi.org/10.3389/fpsyt.2021.741059

Lambert, J.-C., Ibrahim-Verbaas, C. A., Harold, D., Naj, A. C., Sims, R., Bellenguez, C., Jun, G., DeStefano, A. L., Bis, J. C., Beecham, G. W., Grenier-Boley, B., Russo, G., Thornton-Wells, T. A., Jones, N., Smith, A. V., Chouraki, V., Thomas, C., Ikram, M. A., Zelenika, D., … Amouyel, P. (2013). Meta-analysis of 74,046 individuals identifies 11 new susceptibility loci for Alzheimer's disease. *Nature Genetics*, *45*(12), 1452–1458. https://doi.org/10.1038/ng.2802

Lambert, M. P., Barlow, A. K., Chromy, B. A., Edwards, C., Freed, R., Liosatos, M., Morgan, T. E., Rozovsky, I., Trommer, B., Viola, K. L., Wals, P., Zhang, C., Finch, C. E., Krafft, G. A., & Klein, W. L. (1998). Diffusible, nonfibrillar ligands derived from Abeta1-42 are potent central nervous system neurotoxins. *Proceedings of the National Academy of Sciences of the United States of America*, *95*(11), 6448–6453. https://doi.org/10.1073/pnas.95.11.6448

Lane-Donovan, C., & Herz, J. (2017). ApoE, ApoE receptors, and the Synapse in Alzheimer's Disease. *Trends in Endocrinology and Metabolism: TEM*, *28*(4), 273–284. https://doi.org/10.1016/j.tem.2016.12.001

Lastuka, A., Bliss, E., Breshock, M. R., Iannucci, V. C., Sogge, W., Taylor, K. V., Pedroza, P., & Dieleman, J. L. (n.d.). Societal Costs of Dementia: 204 Countries, 2000–2019. *Journal of Alzheimer's Disease*, *101*(1), 277–292. https://doi.org/10.3233/JAD-240163

Lee, H., Cho, S., Kim, M.-J., Park, Y. J., Cho, E., Jo, Y. S., Kim, Y.-S., Lee, J. Y., Thoudam, T., Woo, S.-H., Lee, S.-I., Jeon, J., Lee, Y.-S., Suh, B.-C., Yoon, J. H., Go, Y., Lee, I.-K., & Seo, J. (2023). ApoE4-dependent lysosomal cholesterol accumulation impairs mitochondrial homeostasis and oxidative phosphorylation in human astrocytes. *Cell Reports*, *42*(10). https://doi.org/10.1016/j.celrep.2023.113183

Lee, H.-G., Wheeler, M. A., & Quintana, F. J. (2022). Function and therapeutic value of astrocytes in neurological diseases. *Nature Reviews. Drug Discovery*, *21*(5), 339–358. https://doi.org/10.1038/s41573-022-00390-x

Lee, S.-I., Jeong, W., Lim, H., Cho, S., Lee, H., Jang, Y., Cho, J., Bae, S., Lin, Y.-T., Tsai, L.-H., Moon, D. W., & Seo, J. (2021). APOE4-carrying human astrocytes oversupply cholesterol to promote neuronal lipid raft expansion and Aβ generation. *Stem Cell Reports*, *16*(9), 2128–2137. https://doi.org/10.1016/j.stemcr.2021.07.017

Lexeo Therapeutics. (2024). *A 52-Week, Multicenter, Phase 1/2 Open-label Study to Evaluate the Safety of LX1001 in Participants With APOE4 Homozygote Alzheimer's Disease* (Clinical Trial

Registration No. NCT03634007). clinicaltrials.gov. https://clinicaltrials.gov/study/NCT03634007

Li, L. (2009). Identification of Astrocyte Secreted Proteins with a Combination of Shotgun Proteomics and Bioinformatics. *Journal of Proteome Research*. https://doi.org/10.1021/PR900248Y

LI, M., SUN, L., LUO, Y., XIE, C., PANG, Y., & LI, Y. (2014). High-mobility group box 1 released from astrocytes promotes the proliferation of cultured neural stem/progenitor cells. *International Journal of Molecular Medicine*, *34*(3), 705–714. https://doi.org/10.3892/ijmm.2014.1820

Li, Z., Shue, F., Zhao, N., Shinohara, M., & Bu, G. (2020). APOE2: Protective mechanism and therapeutic implications for Alzheimer's disease. *Molecular Neurodegeneration*, *15*(1), 63. https://doi.org/10.1186/s13024-020-00413-4

Liang, T., Hang, W., Chen, J., Wu, Y., Wen, B., Xu, K., Ding, B., & Chen, J. (2021). ApoE4 (Δ272–299) induces mitochondrial-associated membrane formation and mitochondrial impairment by enhancing GRP75-modulated mitochondrial calcium overload in neuron. *Cell & Bioscience*, *11*, 50. https://doi.org/10.1186/s13578-021-00563-y

Liao, C., Chen, Y., Peng, D., Li, S., Liu, L., Li, Q., Huang, R., Huang, L., Jiang, T., Hu, H., & Li, Y. (2024). Neuron-like lineage differentiation induced by exogenous Neurexin-1 as a potential therapeutic strategy for glioma. *Cancer Letters*, *611*, 217387. https://doi.org/10.1016/j.canlet.2024.217387

Liao, F., Li, A., Xiong, M., Bien-Ly, N., Jiang, H., Zhang, Y., Finn, M. B., Hoyle, R., Keyser, J., Lefton, K. B., Robinson, G. O., Serrano, J. R., Silverman, A. P., Guo, J. L., Getz, J., Henne, K., Leyns, C. E., Gallardo, G., Ulrich, J. D., … Holtzman, D. M. (2018). Targeting of nonlipidated, aggregated apoE with antibodies inhibits amyloid accumulation. *The Journal of Clinical Investigation*, *128*(5), 2144–2155. https://doi.org/10.1172/JCI96429

Liao, M.-C., Muratore, C. R., Gierahn, T. M., Sullivan, S. E., Srikanth, P., De Jager, P. L., Love, J. C., & Young-Pearse, T. L. (2016). Single-Cell Detection of Secreted Aβ and sAPPα from Human IPSC-Derived Neurons and Astrocytes. *The Journal of Neuroscience*, *36*(5), 1730–1746. https://doi.org/10.1523/JNEUROSCI.2735-15.2016

Liddelow, S. A., Guttenplan, K. A., Clarke, L. E., Bennett, F. C., Bohlen, C. J., Schirmer, L., Bennett, M. L., Münch, A. E., Chung, W.-S., Peterson, T. C., Wilton, D. K., Frouin, A., Napier, B. A., Panicker, N., Kumar, M., Buckwalter, M. S., Rowitch, D. H., Dawson, V. L., Dawson, T. M., … Barres, B. A. (2017). Neurotoxic reactive astrocytes are induced by activated microglia. *Nature*, *541*(7638), 481–487. https://doi.org/10.1038/nature21029

Lin, C.-Y., Zhai, Y.-J., An, H.-H., Wu, F., Qiu, H.-N., Li, J.-B., & Lin, J.-N. (2025). Global trends in prevalence, disability adjusted life years, and risk factors for early onset dementia from 1990 to 2021. *Scientific Reports*, *15*, 13488. https://doi.org/10.1038/s41598-025-97404-6

Lin, Y.-T., Seo, J., Gao, F., Feldman, H. M., Wen, H.-L., Penney, J., Cam, H. P., Gjoneska, E., Raja, W. K., Cheng, J., Rueda, R., Kritskiy, O., Abdurrob, F., Peng, Z., Milo, B., Yu, C. J., Elmsaouri, S., Dey, D., Ko,

T., … Tsai, L.-H. (2018). APOE4 causes widespread molecular and cellular alterations associated with Alzheimer's disease phenotypes in human iPSC-derived brain cell types. *Neuron*, *98*(6), 1141-1154.e7. https://doi.org/10.1016/j.neuron.2018.05.008

Liu, C.-C., Kanekiyo, T., Xu, H., & Bu, G. (2013). Apolipoprotein E and Alzheimer disease: Risk, mechanisms, and therapy. *Nature Reviews. Neurology*, *9*(2), 106–118. https://doi.org/10.1038/nrneurol.2012.263

Liu, L., MacKenzie, K. R., Putluri, N., Maletić-Savatić, M., & Bellen, H. J. (2017). The glia-neuron lactate shuttle and elevated ROS promote lipid synthesis in neurons and lipid droplet accumulation in glia via APOE/D. *Cell Metabolism*, *26*(5), 719-737.e6. https://doi.org/10.1016/j.cmet.2017.08.024

Loch, R. A., Wang, H., Perálvarez-Marín, A., Berger, P., Nielsen, H., Chroni, A., & Luo, J. (2023). Cross interactions between Apolipoprotein E and amyloid proteins in neurodegenerative diseases. *Computational and Structural Biotechnology Journal*, *21*, 1189–1204. https://doi.org/10.1016/j.csbj.2023.01.022

Long, J. M., & Holtzman, D. M. (2019). Alzheimer Disease: An Update on Pathobiology and Treatment Strategies. *Cell*, *179*(2), 312–339. https://doi.org/10.1016/j.cell.2019.09.001

Lu, A., Chen, W.-T., Dalby, M., et al. (2026). Human microglial transitions at the A $\beta$ – tau inflection point associate with divergent pathways to dementia and resilience. Nature Medicine, 32(6), 2047 – 2059. https://doi.org/10.1038/s41591-026-04393-8

Lynch, J. R., Tang, W., Wang, H., Vitek, M. P., Bennett, E. R., Sullivan, P. M., Warner, D. S., & Laskowitz, D. T. (2003). APOE Genotype and an ApoE-mimetic Peptide Modify the Systemic and Central Nervous System Inflammatory Response *. *Journal of Biological Chemistry*, *278*(49), 48529–48533. https://doi.org/10.1074/jbc.M306923200

MacVicar, B. A., & Newman, E. A. (2015). Astrocyte Regulation of Blood Flow in the Brain. *Cold Spring Harbor Perspectives in Biology*, *7*(5), a020388. https://doi.org/10.1101/cshperspect.a020388

Madill, M., McDonagh, K., Ma, J., Vajda, A., McLoughlin, P., O'Brien, T., Hardiman, O., & Shen, S. (2017). Amyotrophic lateral sclerosis patient iPSC-derived astrocytes impair autophagy via non-cell autonomous mechanisms. *Molecular Brain*, *10*(1), 22. https://doi.org/10.1186/s13041-017-0300-4

Magistretti, P. J., & Allaman, I. (2018). Lactate in the brain: From metabolic end-product to signalling molecule. *Nature Reviews. Neuroscience*, *19*(4), 235–249. https://doi.org/10.1038/nrn.2018.19

Mahley, R. W., & Huang, Y. (2012). Apolipoprotein e sets the stage: Response to injury triggers neuropathology. *Neuron*, *76*(5), 871–885. https://doi.org/10.1016/j.neuron.2012.11.020

Marton, S., Miquel, E., Acosta-Rodríguez, J., Fontenla, S., Libisch, G., & Cassina, P. (2023). SOD1G93A Astrocyte-Derived Extracellular Vesicles Induce Motor Neuron Death by a miRNA-155-5p-Mediated Mechanism. *ASN NEURO*, *15*, 17590914231197527. https://doi.org/10.1177/17590914231197527

Masopust, D., Sivula, C. P., & Jameson, S. C. (2017). Of Mice, Dirty Mice, and Men: Using Mice to Understand Human Immunology. *Journal of Immunology (Baltimore, Md. : 1950)*, *199*(2), 383–388. https://doi.org/10.4049/jimmunol.1700453

Mathys, H., Davila-Velderrain, J., Peng, Z., Gao, F., Mohammadi, S., Young, J. Z., Menon, M., He, L., Abdurrob, F., Jiang, X., Martorell, A. J., Ransohoff, R. M., Hafler, B. P., Bennett, D. A., Kellis, M., & Tsai, L.-H. (2019). Single-cell transcriptomic analysis of Alzheimer's disease. *Nature*, *570*(7761), 332–337. https://doi.org/10.1038/s41586-019-1195-2

Mauch, D. H., Nägler, K., Schumacher, S., Göritz, C., Müller, E. C., Otto, A., & Pfrieger, F. W. (2001). CNS synaptogenesis promoted by glia-derived cholesterol. *Science (New York, N.Y.)*, *294*(5545), 1354–1357. https://doi.org/10.1126/science.294.5545.1354

Melková, K., Zapletal, V., Jansen, S., Nomilner, E., Zachrdla, M., Hritz, J., Nováček, J., Zweckstetter, M., Jensen, M. R., Blackledge, M., & Žídek, L. (2018). Functionally specific binding regions of microtubule-associated protein 2c exhibit distinct conformations and dynamics. *The Journal of Biological Chemistry*, *293*(34), 13297–13309. https://doi.org/10.1074/jbc.RA118.001769

Meyer-Acosta, K. K., Diaz-Guerra, E., Varma, P., Aruk, A., Mirsadeghi, S., Muniz-Perez, A., Rafati, Y., Hosseini, A., Nieto-Estevez, V., Giugliano, M., Navara, C., & Hsieh, J. (2025). *APOE4* impacts cortical neurodevelopment and alters network formation in human brain organoids. *Stem Cell Reports*, *20*(7), 102537. https://doi.org/10.1016/j.stemcr.2025.102537

Mucke, L., & Selkoe, D. J. (2012). Neurotoxicity of Amyloid β-Protein: Synaptic and Network Dysfunction. *Cold Spring Harbor Perspectives in Medicine*, *2*(7), a006338. https://doi.org/10.1101/cshperspect.a006338

Mummery, C. J., Börjesson-Hanson, A., Blackburn, D. J., et al. (2023). Tau-targeting antisense oligonucleotide MAPTRx in mild Alzheimer's disease: A phase 1b, randomized, placebo-controlled trial. Nature Medicine, 29(6), 1437–1447. https://doi.org/10.1038/s41591-023-02326-3

Nagai, J., Yu, X., Papouin, T., Cheong, E., Freeman, M. R., Monk, K. R., Hastings, M. H., Haydon, P. G., Rowitch, D., Shaham, S., & Khakh, B. S. (2021). Behaviorally consequential astrocytic regulation of neural circuits. *Neuron*, *109*(4), 576–596. https://doi.org/10.1016/j.neuron.2020.12.008

Nägler, K., Mauch, D. H., & Pfrieger, F. W. (2001). Glia-derived signals induce synapse formation in neurones of the rat central nervous system. *The Journal of Physiology*, *533*(Pt 3), 665–679. https://doi.org/10.1111/j.1469-7793.2001.00665.x

Nakayama, T., Momoki-Soga, T., Yamaguchi, K., & Inoue, N. (n.d.). *E/cient production of neural stem cells and neurons from embryonic stem cells*. 5.

Nam, Y., Kim, J., Jung, S.-H., Woerner, J., Suh, E. H., Lee, D.-G., Shivakumar, M., Lee, M. E., & Kim, D. (2024). Harnessing Artificial Intelligence in Multimodal Omics Data Integration: Paving the Path for the

Next Frontier in Precision Medicine. *Annual Review of Biomedical Data Science*, *7*(1), 225–250. https://doi.org/10.1146/annurev-biodatasci-102523-103801

Namba, Y., Tomonaga, M., Kawasaki, H., Otomo, E., & Ikeda, K. (1991). Apolipoprotein E immunoreactivity in cerebral amyloid deposits and neurofibrillary tangles in Alzheimer's disease and kuru plaque amyloid in Creutzfeldt-Jakob disease. *Brain Research*, *541*(1), 163–166. https://doi.org/10.1016/0006-8993(91)91092-F

Napoli, G. C., Figg, W. D., & Chau, C. H. (2022). Functional Drug Screening in the Era of Precision Medicine. *Frontiers in Medicine*, *9*. https://doi.org/10.3389/fmed.2022.912641

Narayan, P., Sienski, G., Bonner, J. M., Lin, Y.-T., Seo, J., Baru, V., Haque, A., Milo, B., Akay, L. A., Graziosi, A., Freyzon, Y., Landgraf, D., Hesse, W. R., Valastyan, J., Barrasa, M. I., Tsai, L.-H., & Lindquist, S. (2020). PICALM Rescues Endocytic Defects Caused by the Alzheimer's Disease Risk Factor APOE4. *Cell Reports*, *33*(1), 108224. https://doi.org/10.1016/j.celrep.2020.108224

Nasrabady, S. E., Rizvi, B., Goldman, J. E., & Brickman, A. M. (2018). White matter changes in Alzheimer's disease: A focus on myelin and oligodendrocytes. *Acta Neuropathologica Communications*, *6*(1), 22. https://doi.org/10.1186/s40478-018-0515-3

Ng, B., Rowland, H. A., Wei, T., Arunasalam, K., Hayes, E. M., Koychev, I., Hedegaard, A., Ribe, E. M., Chan, D., Chessell, T., Ffytche, D., Gunn, R. N., Kocagoncu, E., Lawson, J., Malhotra, P. A., Ridha, B. H., Rowe, J. B., Thomas, A. J., Zamboni, G., … Wade-Martins, R. (2022). Neurons derived from individual early Alzheimer's disease patients reflect their clinical vulnerability. *Brain Communications*, *4*(6), fcac267. https://doi.org/10.1093/braincomms/fcac267

Nishida, H., & Okabe, S. (2007). Direct Astrocytic Contacts Regulate Local Maturation of Dendritic Spines. *Journal of Neuroscience*, *27*(2), 331–340. https://doi.org/10.1523/JNEUROSCI.4466-06.2007

Nixon, R. A. (2017). Amyloid precursor protein and endosomal-lysosomal dysfunction in Alzheimer's disease: Inseparable partners in a multifactorial disease. *FASEB Journal: Official Publication of the Federation of American Societies for Experimental Biology*, *31*(7), 2729–2743. https://doi.org/10.1096/fj.201700359

Nixon, R. A., Wegiel, J., Kumar, A., Yu, W. H., Peterhoff, C., Cataldo, A., & Cuervo, A. M. (2005). Extensive Involvement of Autophagy in Alzheimer Disease: An Immuno-Electron Microscopy Study. *Journal of Neuropathology & Experimental Neurology*, *64*(2), 113–122. https://doi.org/10.1093/jnen/64.2.113

Nugent, A. A., Lin, K., Lengerich, B. van, Lianoglou, S., Przybyla, L., Davis, S. S., Llapashtica, C., Wang, J., Kim, D. J., Xia, D., Lucas, A., Baskaran, S., Haddick, P. C. G., Lenser, M., Earr, T. K., Shi, J., Dugas, J. C., Andreone, B. J., Logan, T., … Paolo, G. D. (2020). TREM2 Regulates Microglial Cholesterol Metabolism upon Chronic Phagocytic Challenge. *Neuron*, *105*(5), 837-854.e9. https://doi.org/10.1016/j.neuron.2019.12.007

Nuriel, T., Peng, K. Y., Ashok, A., Dillman, A. A., Figueroa, H. Y., Apuzzo, J., Ambat, J., Levy, E., Cookson, M. R., Mathews, P. M., & Duff, K. E. (2017). The Endosomal–Lysosomal Pathway Is Dysregulated by APOE4 Expression in Vivo. *Frontiers in Neuroscience*, *11*, 702. https://doi.org/10.3389/fnins.2017.00702

Nyberg, E., Konings, S. C., Lindblom, N., Israelsson, B., Klementieva, O., Martinsson, I., & Gouras, G. K. (2025). Neuronal endolysosomal alterations induced by Apolipoprotein E4 emerge over time in primary neurons. *Journal of Biological Chemistry*, *301*(8), 110479. https://doi.org/10.1016/j.jbc.2025.110479

Orr, A. L., Kim, C., Jimenez-Morales, D., Newton, B. W., Johnson, J. R., Krogan, N. J., Swaney, D. L., & Mahley, R. W. (2019). Neuronal Apolipoprotein E4 Expression Results in Proteome-Wide Alterations and Compromises Bioenergetic Capacity by Disrupting Mitochondrial Function. *Journal of Alzheimer's Disease: JAD*, *68*(3), 991–1011. https://doi.org/10.3233/JAD-181184

Panopoulos, A. D., D'Antonio, M., Benaglio, P., Williams, R., Hashem, S. I., Schuldt, B. M., DeBoever, C., Arias, A. D., Garcia, M., Nelson, B. C., Harismendy, O., Jakubosky, D. A., Donovan, M. K. R., Greenwald, W. W., Farnam, K., Cook, M., Borja, V., Miller, C. A., Grinstein, J. D., … Frazer, K. A. (2017). iPSCORE: A Resource of 222 iPSC Lines Enabling Functional Characterization of Genetic Variation across a Variety of Cell Types. *Stem Cell Reports*, *8*(4), 1086–1100. https://doi.org/10.1016/j.stemcr.2017.03.012

Paşca, A. M., Sloan, S. A., Clarke, L. E., Tian, Y., Makinson, C. D., Huber, N., Kim, C. H., Park, J.-Y., O'Rourke, N. A., Nguyen, K. D., Smith, S. J., Huguenard, J. R., Geschwind, D. H., Barres, B. A., & Paşca, S. P. (2015). Functional cortical neurons and astrocytes from human pluripotent stem cells in 3D culture. *Nature Methods*, *12*(7), 671–678. https://doi.org/10.1038/nmeth.3415

Pellerin, L., & Magistretti, P. J. (1994). Glutamate uptake into astrocytes stimulates aerobic glycolysis: A mechanism coupling neuronal activity to glucose utilization. *Proceedings of the National Academy of Sciences of the United States of America*, *91*(22), 10625–10629. https://doi.org/10.1073/pnas.91.22.10625

Penney, J., Ralvenius, W. T., & Tsai, L.-H. (2020). Modeling Alzheimer's disease with iPSC-derived brain cells. *Molecular Psychiatry*, *25*(1), Article 1. https://doi.org/10.1038/s41380-019-0468-3

Perea, G., Navarrete, M., & Araque, A. (2009). Tripartite synapses: Astrocytes process and control synaptic information. *Trends in Neurosciences*, *32*(8), 421–431. https://doi.org/10.1016/j.tins.2009.05.001

Perriot, S., Mathias, A., Perriard, G., Canales, M., Jonkmans, N., Merienne, N., Meunier, C., El Kassar, L., Perrier, A. L., Laplaud, D.-A., Schluep, M., Déglon, N., & Du Pasquier, R. (2018). Human Induced Pluripotent Stem Cell-Derived Astrocytes Are Differentially Activated by Multiple Sclerosis-Associated Cytokines. *Stem Cell Reports*, *11*(5), 1199–1210. https://doi.org/10.1016/j.stemcr.2018.09.015

Pfaffl, M. W. (2001). A new mathematical model for relative quantification in real-time RT–PCR. *Nucleic Acids Research*, *29*(9), e45. https://doi.org/10.1093/nar/29.9.e45

Pflanzner, T., Janko, M. C., André-Dohmen, B., Reuss, S., Weggen, S., Roebroek, A. J. M., Kuhlmann, C. R. W., & Pietrzik, C. U. (2011). LRP1 mediates bidirectional transcytosis of amyloid-β across the blood-brain barrier. *Neurobiology of Aging*, *32*(12), 2323.e1-2323.e11. https://doi.org/10.1016/j.neurobiolaging.2010.05.025

Phatnani, H., & Maniatis, T. (2015). Astrocytes in Neurodegenerative Disease. *Cold Spring Harbor Perspectives in Biology*, *7*(6), a020628. https://doi.org/10.1101/cshperspect.a020628

Philips, T., & Rothstein, J. D. (2017). Oligodendroglia: Metabolic supporters of neurons. *The Journal of Clinical Investigation*, *127*(9), 3271–3280. https://doi.org/10.1172/JCI90610

Pires, M., Rego, A. C., Pires, M., & Rego, A. C. (2023). Apoe4 and Alzheimer's Disease Pathogenesis—Mitochondrial Deregulation and Targeted Therapeutic Strategies. *International Journal of Molecular Sciences*, *24*(1). https://doi.org/10.3390/ijms24010778

Pohlkamp, T., Xian, X., Wong, C. H., Durakoglugil, M. S., Werthmann, G. C., Saido, T. C., Evers, B. M., White, C. L., Connor, J., Hammer, R. E., & Herz, J. (n.d.). NHE6 depletion corrects ApoE4-mediated synaptic impairments and reduces amyloid plaque load. *eLife*, *10*, e72034. https://doi.org/10.7554/eLife.72034

Prasad, H., & Rao, R. (2018a). Amyloid clearance defect in ApoE4 astrocytes is reversed by epigenetic correction of endosomal pH. *Proceedings of the National Academy of Sciences*, *115*(28), E6640–E6649. https://doi.org/10.1073/pnas.1801612115

Prasad, H., & Rao, R. (2018b). Histone deacetylase-mediated regulation of endolysosomal pH. *The Journal of Biological Chemistry*, *293*(18), 6721–6735. https://doi.org/10.1074/jbc.RA118.002025

Preman, P., Alfonso-Triguero, M., Alberdi, E., Verkhratsky, A., & Arranz, A. M. (2021). Astrocytes in Alzheimer's Disease: Pathological Significance and Molecular Pathways. *Cells*, *10*(3), 540. https://doi.org/10.3390/cells10030540

Qi, G., Mi, Y., Shi, X., Gu, H., Brinton, R. D., & Yin, F. (2021a). ApoE4 Impairs Neuron-Astrocyte Coupling of Fatty Acid Metabolism. *Cell Reports*, *34*(1), 108572. https://doi.org/10.1016/j.celrep.2020.108572

Qi, G., Mi, Y., Shi, X., Gu, H., Brinton, R. D., & Yin, F. (2021b). ApoE4 Impairs Neuron-Astrocyte Coupling of Fatty Acid Metabolism. *Cell Reports*, *34*(1), 108572. https://doi.org/10.1016/j.celrep.2020.108572

Qi, G., Mi, Y., Shi, X., Gu, H., Brinton, R. D., & Yin, F. (2021c). ApoE4 Impairs Neuron-Astrocyte Coupling of Fatty Acid Metabolism. *Cell Reports*, *34*(1), 108572. https://doi.org/10.1016/j.celrep.2020.108572

Raiders, S., Han, T., Scott-Hewitt, N., Kucenas, S., Lew, D., Logan, M. A., & Singhvi, A. (2021). Engulfed by Glia: Glial Pruning in Development, Function, and Injury across Species. *Journal of Neuroscience*, *41*(5), 823–833. https://doi.org/10.1523/JNEUROSCI.1660-20.2020

Rajmohan, R., & Reddy, P. H. (2017). Amyloid Beta and Phosphorylated Tau Accumulations Cause

Abnormalities at Synapses of Alzheimer's disease Neurons. *Journal of Alzheimer's Disease : JAD*, *57*(4), 975–999. https://doi.org/10.3233/JAD-160612

Ramakrishna, S., Jhaveri, V., Konings, S. C., Nawalpuri, B., Chakraborty, S., Holst, B., Schmid, B., Gouras, G. K., Freude, K. K., & Muddashetty, R. S. (2021). APOE4 Affects Basal and NMDAR-Mediated Protein Synthesis in Neurons by Perturbing Calcium Homeostasis. *The Journal of Neuroscience: The Official Journal of the Society for Neuroscience*, *41*(42), 8686–8709. https://doi.org/10.1523/JNEUROSCI.0435-21.2021

Reas, E. T., Solders, S. K., Tsiknia, A., Triebswetter, C., Shen, Q., Rivera, C. S., Andrews, M. J., Alderson-Myers, A., & Brewer, J. B. (2024). APOE $\varepsilon$4-related blood–brain barrier breakdown is associated with microstructural abnormalities. *Alzheimer's & Dementia*, *20*(12), 8615–8624. https://doi.org/10.1002/alz.14302

Riddell, D. R., Zhou, H., Atchison, K., Warwick, H. K., Atkinson, P. J., Jefferson, J., Xu, L., Aschmies, S., Kirksey, Y., Hu, Y., Wagner, E., Parratt, A., Xu, J., Li, Z., Zaleska, M. M., Jacobsen, J. S., Pangalos, M. N., & Reinhart, P. H. (2008). Impact of apolipoprotein E (ApoE) polymorphism on brain ApoE levels. *The Journal of Neuroscience: The Official Journal of the Society for Neuroscience*, *28*(45), 11445–11453. https://doi.org/10.1523/JNEUROSCI.1972-08.2008

Rojas, F., Aguilar, R., Almeida, S., Fritz, E., Corvalán, D., Ampuero, E., Abarzúa, S., Garcés, P., Amaro, A., Diaz, I., Arredondo, C., Cortes, N., Sanchez, M., Mercado, C., Varela-Nallar, L., Gao, F.-B., Montecino, M., & van Zundert, B. (2023). Mature iPSC-derived astrocytes of an ALS/FTD patient carrying the TDP43A90V mutation display a mild reactive state and release polyP toxic to motoneurons. *Frontiers in Cell and Developmental Biology*, *11*. https://doi.org/10.3389/fcell.2023.1226604

Rowland, H. A., Miller, G., Liu, Q., Li, S., Sharp, N. R., Ng, B., Wei, T., Arunasalam, K., Koychev, I., Hedegaard, A., Ribe, E. M., Chan, D., Chessell, T., Kocagoncu, E., Lawson, J., Malhotra, P., Ridha, B. H., Rowe, J. B., Thomas, A. J., … Buckley, N. J. (2025). Changes in iPSC-astrocyte morphology reflect Alzheimer's disease patient clinical markers. *Stem Cells*, *43*(3), sxae085. https://doi.org/10.1093/stmcls/sxae085

Ryan, N. S., & Rossor, M. N. (2010). Correlating familial Alzheimer's disease gene mutations with clinical phenotype. *Biomarkers in Medicine*, *4*(1), 99–112.

Salomon-Zimri, S., Glat, M. J., Barhum, Y., Luz, I., Boehm-Cagan, A., Liraz, O., Ben-Zur, T., Offen, D., & Michaelson, D. M. (2016). Reversal of ApoE4-Driven Brain Pathology by Vascular Endothelial Growth Factor Treatment. *Journal of Alzheimer's Disease: JAD*, *53*(4), 1443–1458. https://doi.org/10.3233/JAD-160182

Sarker, I. H. (2021). Machine Learning: Algorithms, Real-World Applications and Research Directions. *SN Computer Science*, *2*(3), 160. https://doi.org/10.1007/s42979-021-00592-x

Scharp, D., Hobensack, M., Davoudi, A., & Topaz, M. (2024). Natural Language Processing Applied to

Clinical Documentation in Post-acute Care Settings: A Scoping Review. *Journal of the American Medical Directors Association*, *25*(1), 69–83. https://doi.org/10.1016/j.jamda.2023.09.006

Schwartzentruber, J., Foskolou, S., Kilpinen, H., Rodrigues, J., Alasoo, K., Knights, A. J., Patel, M., Goncalves, A., Ferreira, R., Benn, C. L., Wilbrey, A., Bictash, M., Impey, E., Cao, L., Lainez, S., Loucif, A. J., Whiting, P. J., Gutteridge, A., & Gaffney, D. J. (2018). Molecular and functional variation in iPSC-derived sensory neurons. *Nature Genetics*, *50*(1), 54–61. https://doi.org/10.1038/s41588-017-0005-8

Scott, C. C., Vacca, F., & Gruenberg, J. (2014). Endosome maturation, transport and functions. *Seminars in Cell & Developmental Biology*, *31*, 2–10. https://doi.org/10.1016/j.semcdb.2014.03.034

Sekiya, H., Matsubara, T., DeTure, M. A., & Dickson, D. W. (2025). Neuropathology of Lewy body dementia: Lewy-related pathology, α-synuclein oligomers, and comorbid pathologies. *Molecular Neurodegeneration*, *20*, 117. https://doi.org/10.1186/s13024-025-00900-6

Seo, M.-S., Kang, K.-K., Oh, S.-K., Sung, S.-E., Kim, K.-S., Kwon, Y.-S., Yun, S., Seo, M.-S., Kang, K.-K., Oh, S.-K., Sung, S.-E., Kim, K.-S., Kwon, Y.-S., & Yun, S. (2021). Isolation and Characterization of Feline Wharton's Jelly-Derived Mesenchymal Stem Cells. *Veterinary Sciences*, *8*(2). https://doi.org/10.3390/vetsci8020024

Serrano-Pozo, A., Das, S., & Hyman, B. T. (2021). APOE and Alzheimer's Disease: Advances in Genetics, Pathophysiology, and Therapeutic Approaches. *The Lancet. Neurology*, *20*(1), 68–80. https://doi.org/10.1016/S1474-4422(20)30412-9

Severin, Y., Hale, B. D., Mena, J., Goslings, D., Frey, B. M., & Snijder, B. (n.d.). Multiplexed high-throughput immune cell imaging reveals molecular health-associated phenotypes. *Science Advances*, *8*(44), eabn5631. https://doi.org/10.1126/sciadv.abn5631

Shan, L., Zhang, T., Fan, K., Cai, W., & Liu, H. (2021). Astrocyte-Neuron Signaling in Synaptogenesis. *Frontiers in Cell and Developmental Biology*, *9*. https://doi.org/10.3389/fcell.2021.680301

Sharlow, E. R., Llaneza, D. C., Grever, W. E., Mingledorff, G. A., Mendelson, A. J., Bloom, G. S., & Lazo, J. S. (2023). High content screening miniaturization and single cell imaging of mature human feeder layer-free iPSC-derived neurons. *SLAS Discovery: Advancing Life Sciences R & D*, *28*(6), 275–283. https://doi.org/10.1016/j.slasd.2022.10.002

Sharma, S. D., Reddy, B. K., Pal, R., Ritakari, T. E., Cooper, J. D., Selvaraj, B. T., Kind, P. C., Chandran, S., Wyllie, D. J. A., & Chattarji, S. (2023). Astrocytes mediate cell non-autonomous correction of aberrant firing in human FXS neurons. *Cell Reports*, *42*(4), 112344. https://doi.org/10.1016/j.celrep.2023.112344

Shea, Y.-F., Chu, L.-W., Chan, A. O.-K., Ha, J., Li, Y., & Song, Y.-Q. (2016). A systematic review of familial Alzheimer's disease: Differences in presentation of clinical features among three mutated genes and potential ethnic differences. *Journal of the Formosan Medical Association*, *115*(2), 67–75. https://doi.org/10.1016/j.jfma.2015.08.004

Shen, W., Tang, Y., Yang, J., Zhu, L., Zhou, W., Xiang, L., Zhu, F., Dong, J., Xie, Y., & Zeng, L.-H. (2023). *Astrocytes gate long-term potentiation in hippocampal interneurons*. https://doi.org/10.7554/eLife.89804.1

Shi, Y., Inoue, H., Wu, J. C., & Yamanaka, S. (2017). Induced pluripotent stem cell technology: A decade of progress. *Nature Reviews. Drug Discovery*, *16*(2), 115–130. https://doi.org/10.1038/nrd.2016.245

Shi, Y., Kirwan, P., & Livesey, F. J. (2012). Directed differentiation of human pluripotent stem cells to cerebral cortex neurons and neural networks. *Nature Protocols*, *7*(10), Article 10. https://doi.org/10.1038/nprot.2012.116

Shulman, M., Wu, S., Ziogas, N., et al. (2026). Exploratory analyses of clinical outcomes from the BIIB080 phase 1b study in mild Alzheimer ' s disease. Nature Aging, 6(2), 445 – 453. https://doi.org/10.1038/s43587-025-01031-9

Shvetcov, A., Johnson, E. C. B., Winchester, L. M., Walker, K. A., Wilkins, H. M., Thompson, T. G., Rothstein, J. D., Krish, V., Imam, F. B., Global Neurodegeneration Proteomics Consortium (GNPC), Burns, J. M., Swerdlow, R. H., Slawson, C., & Finney, C. A. (2025). APOE ε4 carriers share immune-related proteomic changes across neurodegenerative diseases. *Nature Medicine*, *31*(8), 2590–2601. https://doi.org/10.1038/s41591-025-03835-z

Sims JR, Zimmer JA, Evans CD, et al. (2023). Donanemab in early symptomatic Alzheimer disease: The TRAILBLAZER-ALZ 2 randomized clinical trial. JAMA, 330, 512 – 527. https://doi.org/10.1001/jama.2023.13239

Simonovitch, S., Schmukler, E., Masliah, E., Pinkas-Kramarski, R., & Michaelson, D. M. (2019). The Effects of APOE4 on Mitochondrial Dynamics and Proteins in vivo. *Journal of Alzheimer's Disease : JAD*, *70*(3), 861–875. https://doi.org/10.3233/JAD-190074

Sloan, S. A., Darmanis, S., Huber, N., Khan, T. A., Birey, F., Caneda, C., Reimer, R., Quake, S. R., Barres, B. A., & Paşca, S. P. (2017). Human Astrocyte Maturation Captured in 3D Cerebral Cortical Spheroids Derived from Pluripotent Stem Cells. *Neuron*, *95*(4), 779-790.e6. https://doi.org/10.1016/j.neuron.2017.07.035

Smit, T., Deshayes, N. A. C., Borchelt, D. R., Kamphuis, W., Middeldorp, J., & Hol, E. M. (2021). Reactive astrocytes as treatment targets in Alzheimer's disease—Systematic review of studies using the APPswePS1dE9 mouse model. *Glia*, *69*(8), 1852–1881. https://doi.org/10.1002/glia.23981

Smith, M. D., Chamling, X., Gill, A. J., Martinez, H., Li, W., Fitzgerald, K. C., Sotirchos, E. S., Moroziewicz, D., Bauer, L., Paull, D., Gharagozloo, M., Bhargava, P., Zack, D. J., Fossati, V., & Calabresi, P. A. (2022). Reactive Astrocytes Derived From Human Induced Pluripotent Stem Cells Suppress Oligodendrocyte Precursor Cell Differentiation. *Frontiers in Molecular Neuroscience*, *15*, 874299. https://doi.org/10.3389/fnmol.2022.874299

Smolič, T., Zorec, R., & Vardjan, N. (2022). Pathophysiology of Lipid Droplets in Neuroglia. *Antioxidants*,

*11*(1), 22. https://doi.org/10.3390/antiox11010022

Song, C., Wu, Y.-S., Yang, Z.-Y., Kalueff, A. V., Tsao, Y.-Y., Dong, Y., & Su, K.-P. (2019). Astrocyte-Conditioned Medium Protects Prefrontal Cortical Neurons from Glutamate-Induced Cell Death by Inhibiting TNF-α Expression. *Neuroimmunomodulation*, *26*(1), 33–42. https://doi.org/10.1159/000495211

Song, J.-J., Oh, S.-M., Kwon, O.-C., Wulansari, N., Lee, H.-S., Chang, M.-Y., Lee, E., Sun, W., Lee, S.-E., Chang, S., An, H., Lee, C. J., & Lee, S.-H. (n.d.). Cografting astrocytes improves cell therapeutic outcomes in a Parkinson's disease model. *The Journal of Clinical Investigation*, *128*(1), 463–482. https://doi.org/10.1172/JCI93924

Song, S., Miranda, C. J., Braun, L., Meyer, K., Frakes, A. E., Ferraiuolo, L., Likhite, S., Bevan, A. K., Foust, K. D., McConnell, M. J., Walker, C. M., & Kaspar, B. K. (2016). MHC class I protects motor neurons from astrocyte-induced toxicity in amyotrophic lateral sclerosis (ALS). *Nature Medicine*, *22*(4), 397–403. https://doi.org/10.1038/nm.4052

Sourial, M., & Doering, L. C. (2016). Astrocyte-Secreted Factors Selectively Alter Neural Stem and Progenitor Cell Proliferation in the Fragile X Mouse. *Frontiers in Cellular Neuroscience*, *10*, 126. https://doi.org/10.3389/fncel.2016.00126

Spira, M. E., & Hai, A. (2013). Multi-electrode array technologies for neuroscience and cardiology. *Nature Nanotechnology*, *8*(2), 83–94. https://doi.org/10.1038/nnano.2012.265

Stöberl, N., Maguire, E., Salis, E., Shaw, B., & Hall-Roberts, H. (2023). Human iPSC-derived glia models for the study of neuroinflammation. *Journal of Neuroinflammation*, *20*(1), 231. https://doi.org/10.1186/s12974-023-02919-2

Stogsdill, J. A., Ramirez, J., Liu, D., Kim, Y.-H., Baldwin, K. T., Enustun, E., Ejikeme, T., Ji, R.-R., & Eroglu, C. (2017). Astrocytic Neuroligins Control Astrocyte Morphogenesis and Synaptogenesis. *Nature*, *551*(7679), 192–197. https://doi.org/10.1038/nature24638

Storck, S. E., Meister, S., Nahrath, J., Meißner, J. N., Schubert, N., Di Spiezio, A., Baches, S., Vandenbroucke, R. E., Bouter, Y., Prikulis, I., Korth, C., Weggen, S., Heimann, A., Schwaninger, M., Bayer, T. A., & Pietrzik, C. U. (n.d.). Endothelial LRP1 transports amyloid-β1–42 across the blood-brain barrier. *The Journal of Clinical Investigation*, *126*(1), 123–136. https://doi.org/10.1172/JCI81108

Supakul, S., Murakami, R., Oyama, C., Shindo, T., Hatakeyama, Y., Itsuno, M., Bannai, H., Shibata, S., Maeda, S., & Okano, H. (2024). Mutual interaction of neurons and astrocytes derived from iPSCs with APP V717L mutation developed the astrocytic phenotypes of Alzheimer's disease. *Inflammation and Regeneration*, *44*, 8. https://doi.org/10.1186/s41232-023-00310-5

Tabuena, D. R., Jang, S.-S., Grone, B., Yip, O., Jones, E. A. A., Blumenfeld, J., Liang, Z., Koutsodendris, N., Rao, A., Ding, L., Zhang, A. R., Hao, Y., Xu, Q., Yoon, S. Y., Leon, S. D., Huang, Y., & Zilberter, M. (2024). *Neuronal APOE4-induced Early Hippocampal Network Hyperexcitability in Alzheimer's Disease*

*Pathogenesis* (p. 2023.08.28.555153). bioRxiv. https://doi.org/10.1101/2023.08.28.555153

Tai, L. M., Ghura, S., Koster, K. P., Liakaite, V., Maienschein-Cline, M., Kanabar, P., Collins, N., Ben-Aissa, M., Lei, A. Z., Bahroos, N., Green, S. J., Hendrickson, B., Van Eldik, L. J., & LaDu, M. J. (2015). APOE-modulated Aβ-induced neuroinflammation in Alzheimer's disease: Current landscape, novel data, and future perspective. *Journal of Neurochemistry*, *133*(4), 465–488. https://doi.org/10.1111/jnc.13072

Takahashi, K., Tanabe, K., Ohnuki, M., Narita, M., Ichisaka, T., Tomoda, K., & Yamanaka, S. (2007). Induction of pluripotent stem cells from adult human fibroblasts by defined factors. *Cell*, *131*(5), 861–872. https://doi.org/10.1016/j.cell.2007.11.019

Taubes, A., Nova, P., Zalocusky, K. A., Kosti, I., Bicak, M., Zilberter, M. Y., Hao, Y., Yoon, S. Y., Oskotsky, T., Pineda, S., Chen, B., Aery Jones, E. A., Choudhary, K., Grone, B., Balestra, M. E., Chaudhry, F., Paranjpe, I., De Freitas, J., Koutsodendris, N., … Huang, Y. (2021). Experimental and real-world evidence supporting the computational repurposing of bumetanide for APOE4-related Alzheimer's disease. *Nature Aging*, *1*(10), 932–947. https://doi.org/10.1038/s43587-021-00122-7

Taylor, A. M., Blurton-Jones, M., Rhee, S. W., Cribbs, D. H., Cotman, C. W., & Jeon, N. L. (2005). A microfluidic culture platform for CNS axonal injury, regeneration and transport. *Nature Methods*, *2*(8), 599–605. https://doi.org/10.1038/nmeth777

Tchieu, J., Calder, E. L., Guttikonda, S. R., Gutzwiller, E. M., Aromolaran, K. A., Steinbeck, J. A., Goldstein, P. A., & Studer, L. (2019). NFIA is a gliogenic switch enabling rapid derivation of functional human astrocytes from pluripotent stem cells. *Nature Biotechnology*, *37*(3), 267–275. https://doi.org/10.1038/s41587-019-0035-0

Tcw, J., Qian, L., Pipalia, N. H., Chao, M. J., Liang, S. A., Shi, Y., Jain, B. R., Bertelsen, S. E., Kapoor, M., Marcora, E., Sikora, E., Andrews, E. J., Martini, A. C., Karch, C. M., Head, E., Holtzman, D. M., Zhang, B., Wang, M., Maxfield, F. R., … Goate, A. M. (2022). Cholesterol and matrisome pathways dysregulated in astrocytes and microglia. *Cell*, *185*(13), 2213-2233.e25. https://doi.org/10.1016/j.cell.2022.05.017

Tegtmeyer, M., Liyanage, D., Han, Y., Hebert, K. B., Pei, R., Way, G. P., Ryder, P. V., Hawes, D., Tromans-Coia, C., Cimini, B. A., Carpenter, A. E., Singh, S., & Nehme, R. (2025). Combining phenomics with transcriptomics reveals cell-type-specific morphological and molecular signatures of the 22q11.2 deletion. *Nature Communications*, *16*(1), 6332. https://doi.org/10.1038/s41467-025-61547-x

Theendakara, V., Peters-Libeu, C. A., Bredesen, D. E., & Rao, R. V. (2018). Transcriptional Effects of ApoE4: Relevance to Alzheimer's Disease. *Molecular Neurobiology*, *55*(6), 5243–5254. https://doi.org/10.1007/s12035-017-0757-2

Tesi, N., van der Lee, S., Hulsman, M., van Schoor, N. M., Huisman, M., Pijnenburg, Y., van der Flier, W. M., Reinders, M., & Holstege, H. (2024). Cognitively healthy centenarians are genetically protected against Alzheimer ' s disease. Alzheimer ' s & Dementia, 20(6), 3864 – 3875.

https://doi.org/10.1002/alz.13810

Vadodaria, K. C., Mendes, A. P. D., Mei, A., Racha, V., Erikson, G., Shokhirev, M. N., Oefner, R., Heard, K. J., McCarthy, M. J., Eyler, L., Kelsoe, J. R., Santos, R., Marchetto, M. C., & Gage, F. H. (2021). Altered Neuronal Support and Inflammatory Response in Bipolar Disorder Patient-Derived Astrocytes. *Stem Cell Reports*, *16*(4), 825–835. https://doi.org/10.1016/j.stemcr.2021.02.004

van Dyck CH, Swanson CJ, Aisen P, et al. (2023). Lecanemab in early Alzheimer's disease. New England Journal of Medicine, 388, 9 – 21. https://doi.org/10.1056/NEJMoa2212948

Van Eldik, L. J., & Griffin, W. S. (1994). S100 beta expression in Alzheimer's disease: Relation to neuropathology in brain regions. *Biochimica Et Biophysica Acta*, *1223*(3), 398–403. https://doi.org/10.1016/0167-4889(94)90101-5

VanderWall, K. B., Vij, R., Ohlemacher, S. K., Sridhar, A., Fligor, C. M., Feder, E. M., Edler, M. C., Baucum, A. J., Cummins, T. R., & Meyer, J. S. (2019). Astrocytes Regulate the Development and Maturation of Retinal Ganglion Cells Derived from Human Pluripotent Stem Cells. *Stem Cell Reports*, *12*(2), 201–212. https://doi.org/10.1016/j.stemcr.2018.12.010

Visan, A. I., & Negut, I. (2024). Integrating Artificial Intelligence for Drug Discovery in the Context of Revolutionizing Drug Delivery. *Life*, *14*(2), Article 2. https://doi.org/10.3390/life14020233

Vitali, C., Wellington, C. L., & Calabresi, L. (2014). HDL and cholesterol handling in the brain. *Cardiovascular Research*, *103*(3), 405–413. https://doi.org/10.1093/cvr/cvu148

Vitek, M. P., Brown, C. M., & Colton, C. A. (2009). APOE genotype-specific differences in the innate immune response. *Neurobiology of Aging*, *30*(9), 1350–1360. https://doi.org/10.1016/j.neurobiolaging.2007.11.014

Volpato, V., & Webber, C. (2020). Addressing variability in iPSC-derived models of human disease: Guidelines to promote reproducibility. *Disease Models & Mechanisms*, *13*(1), dmm042317. https://doi.org/10.1242/dmm.042317

von Bartheld, C. S., Bahney, J., & Herculano-Houzel, S. (2016). The search for true numbers of neurons and glial cells in the human brain: A review of 150 years of cell counting. *Journal of Comparative Neurology*, *524*(18), 3865–3895. https://doi.org/10.1002/cne.24040

Wang, C., Najm, R., Xu, Q., Jeong, D., Walker, D., Balestra, M. E., Yoon, S. Y., Yuan, H., Li, G., Miller, Z. A., Miller, B. L., Malloy, M. J., & Huang, Y. (2018). Gain of toxic apolipoprotein E4 effects in human iPSC-derived neurons is ameliorated by a small-molecule structure corrector. *Nature Medicine*, *24*(5), 647–657. https://doi.org/10.1038/s41591-018-0004-z

Wang, C., Xiong, M., Gratuze, M., Bao, X., Shi, Y., Andhey, P. S., Manis, M., Schroeder, C., Yin, Z., Madore, C., Butovsky, O., Artyomov, M., Ulrich, J. D., & Holtzman, D. M. (2021). Selective removal of astrocytic APOE4 strongly protects against tau-mediated neurodegeneration and decreases synaptic

phagocytosis by microglia. *Neuron*, *109*(10), 1657-1674.e7. https://doi.org/10.1016/j.neuron.2021.03.024

Wang, D., Wang, P., Bian, X., Xu, S., Zhou, Q., Zhang, Y., Ding, M., Han, M., Huang, L., Bi, J., Jia, Y., & Xie, Z. (2020). Elevated plasma levels of exosomal BACE1-AS combined with the volume and thickness of the right entorhinal cortex may serve as a biomarker for the detection of Alzheimer's disease. *Molecular Medicine Reports*, *22*(1), 227–238. https://doi.org/10.3892/mmr.2020.11118

Watanabe, H., Murakami, R., Tsumagari, K., Morimoto, S., Hashimoto, T., Imaizumi, K., Sonn, I., Yamada, K., Saito, Y., Murayama, S., Iwatsubo, T., & Okano, H. (2023). Astrocytic APOE4 genotype-mediated negative impacts on synaptic architecture in human pluripotent stem cell model. *Stem Cell Reports*, *18*(9), 1854–1869. https://doi.org/10.1016/j.stemcr.2023.08.002

Way, G. P., Natoli, T., Adeboye, A., Litichevskiy, L., Yang, A., Lu, X., Caicedo, J. C., Cimini, B. A., Karhohs, K., Logan, D. J., Rohban, M. H., Kost-Alimova, M., Hartland, K., Bornholdt, M., Chandrasekaran, S. N., Haghighi, M., Weisbart, E., Singh, S., Subramanian, A., & Carpenter, A. E. (2022). Morphology and gene expression profiling provide complementary information for mapping cell state. *Cell Systems*, *13*(11), 911-923.e9. https://doi.org/10.1016/j.cels.2022.10.001

Weaver, D. F., Meek, A., Reed, M., & Barden, C. (2023). Alzheimer's Disease as an Autoimmune Disease. *Alzheimer's & Dementia*, *19*(S1), e065537. https://doi.org/10.1002/alz.065537

Welby, E., & Ebert, A. D. (2023). Diminished motor neuron activity driven by abnormal astrocytic EAAT1 glutamate transporter activity in spinal muscular atrophy is not fully restored after lentiviral SMN delivery. *Glia*, *71*(5), 1311–1332. https://doi.org/10.1002/glia.24340

Werneburg, S., Jung, J., Kunjamma, R. B., Ha, S.-K., Luciano, N. J., Willis, C. M., Gao, G., Biscola, N. P., Havton, L. A., Crocker, S. J., Popko, B., Reich, D. S., & Schafer, D. P. (2020). Targeted complement inhibition at synapses prevents microglial synaptic engulfment and synapse loss in demyelinating disease. *Immunity*, *52*(1), 167-182.e7. https://doi.org/10.1016/j.immuni.2019.12.004

Wiedenmann, B., & Franke, W. W. (1985). Identification and localization of synaptophysin, an integral membrane glycoprotein of Mr 38,000 characteristic of presynaptic vesicles. *Cell*, *41*(3), 1017–1028. https://doi.org/10.1016/S0092-8674(85)80082-9

Wilcock, D. M., & Colton, C. A. (2008). Anti-Aß immunotherapy in Alzheimer's disease; relevance of transgenic mouse studies to clinical trials. *Journal of Alzheimer's Disease : JAD*, *15*(4), 555–569. https://doi.org/10.3233/jad-2008-15404

Williams, T., Borchelt, D. R., & Chakrabarty, P. (2020). Therapeutic approaches targeting Apolipoprotein E function in Alzheimer's disease. *Molecular Neurodegeneration*, *15*, 8. https://doi.org/10.1186/s13024-020-0358-9

Windham, I. A., Powers, A. E., Ragusa, J. V., Wallace, E. D., Zanellati, M. C., Williams, V. H., Wagner, C. H., White, K. K., & Cohen, S. (2024). APOE traffics to astrocyte lipid droplets and modulates triglyceride

saturation and droplet size. *The Journal of Cell Biology*, *223*(4), e202305003. https://doi.org/10.1083/jcb.202305003

Wisniewski, T., & Drummond, E. (2020). APOE-amyloid interaction: Therapeutic targets. *Neurobiology of Disease*, *138*, 104784. https://doi.org/10.1016/j.nbd.2020.104784

Wu, M., Zhang, R., Fu, P., & Mei, Y. (2025). Disrupted astrocyte-neuron signaling reshapes brain activity in epilepsy and Alzheimer's disease. *Neuroscience*, *570*, 132–151. https://doi.org/10.1016/j.neuroscience.2025.02.029

Wuerch, E. C., & Yong, V. W. (2025). Cholesterol in the CNS: Functions, recycling and remyelination. *Journal of Neuroinflammation*, *22*(1), 180. https://doi.org/10.1186/s12974-025-03490-8

Xian, X., Pohlkamp, T., Durakoglugil, M. S., Wong, C. H., Beck, J. K., Lane-Donovan, C., Plattner, F., & Herz, J. (2018). Reversal of ApoE4-induced recycling block as a novel prevention approach for Alzheimer's disease. *eLife*, *7*, e40048. https://doi.org/10.7554/eLife.40048

Yamazaki, Y., Zhao, N., Caulfield, T. R., Liu, C.-C., & Bu, G. (2019). Apolipoprotein E and Alzheimer disease: Pathobiology and targeting strategies. *Nature Reviews Neurology*, *15*(9), 501–518. https://doi.org/10.1038/s41582-019-0228-7

Yang, Y., Ge, W., Chen, Y., Zhang, Z., Shen, W., Wu, C., Poo, M., & Duan, S. (2003). Contribution of astrocytes to hippocampal long-term potentiation through release of d-serine. *Proceedings of the National Academy of Sciences of the United States of America*, *100*(25), 15194–15199. https://doi.org/10.1073/pnas.2431073100

Yeh, F. L., Wang, Y., Tom, I., Gonzalez, L. C., & Sheng, M. (2016). TREM2 Binds to Apolipoproteins, Including APOE and CLU/APOJ, and Thereby Facilitates Uptake of Amyloid-Beta by Microglia. *Neuron*, *91*(2), 328–340. https://doi.org/10.1016/j.neuron.2016.06.015

Yi, C., Mei, X., Ezan, P., Mato, S., Matias, I., Giaume, C., & Koulakoff, A. (2016). Astroglial connexin43 contributes to neuronal suffering in a mouse model of Alzheimer's disease. Cell Death & Differentiation, 23(10), 1691–1701.

Ying, W. (2023). Phenomic Studies on Diseases: Potential and Challenges. *Phenomics*, *3*(3), 285–299. https://doi.org/10.1007/s43657-022-00089-4

You, Y., Lai, X., Pan, Y., Zheng, H., Vera, J., Liu, S., Deng, S., & Zhang, L. (2022). Artificial intelligence in cancer target identification and drug discovery. *Signal Transduction and Targeted Therapy*, *7*(1), 1–24. https://doi.org/10.1038/s41392-022-00994-0

Zannis, V. I., Su, S., & Fotakis, P. (2017). Role of apolipoproteins, ABCA1 and LCAT in the biogenesis of normal and aberrant high density lipoproteins. *Journal of Biomedical Research*, *31*(6), 471–485. https://doi.org/10.7555/JBR.31.20160082

Zhang, B., Gaiteri, C., Bodea, L.-G., Wang, Z., McElwee, J., Podtelezhnikov, A. A., Zhang, C., Xie, T., Tran, L., Dobrin, R., Fluder, E., Clurman, B., Melquist, S., Narayanan, M., Suver, C., Shah, H., Mahajan, M., Gillis, T., Mysore, J., … Emilsson, V. (2013). Integrated systems approach identifies genetic nodes and networks in late-onset Alzheimer's disease. *Cell*, *153*(3), 707–720. https://doi.org/10.1016/j.cell.2013.03.030

Zhang, J., Zhang, Y., Wang, J., Xia, Y., Zhang, J., & Chen, L. (2024). Recent advances in Alzheimer's disease: Mechanisms, clinical trials and new drug development strategies. *Signal Transduction and Targeted Therapy*, *9*(1), 1–35. https://doi.org/10.1038/s41392-024-01911-3

Zhao, J., Davis, M. D., Martens, Y. A., Shinohara, M., Graff-Radford, N. R., Younkin, S. G., Wszolek, Z. K., Kanekiyo, T., & Bu, G. (2017). APOE ε4/ε4 diminishes neurotrophic function of human iPSC-derived astrocytes. *Human Molecular Genetics*, *26*(14), 2690–2700. https://doi.org/10.1093/hmg/ddx155

Zhao, J., Ikezu, T. C., Lu, W., Macyczko, J. R., Li, Y., Lewis-Tuffin, L. J., Martens, Y. A., Ren, Y., Zhu, Y., Asmann, Y. W., Ertekin-Taner, N., Kanekiyo, T., & Bu, G. (2023). APOE deficiency impacts neural differentiation and cholesterol biosynthesis in human iPSC-derived cerebral organoids. *Stem Cell Research & Therapy*, *14*(1), 214. https://doi.org/10.1186/s13287-023-03444-y

Zhao, N., Attrebi, O. N., Ren, Y., Qiao, W., Sonustun, B., Martens, Y. A., Meneses, A. D., Li, F., Shue, F., Zheng, J., Van Ingelgom, A. J., Davis, M. D., Kurti, A., Knight, J. A., Linares, C., Chen, Y., Delenclos, M., Liu, C.-C., Fryer, J. D., … Bu, G. (2020). APOE4 exacerbates α-synuclein pathology and related toxicity independent of amyloid. *Science Translational Medicine*, *12*(529), eaay1809. https://doi.org/10.1126/scitranslmed.aay1809

Zhao, N., Liu, C.-C., Ingelgom, A. J. V., Martens, Y. A., Linares, C., Knight, J. A., Painter, M. M., Sullivan, P. M., & Bu, G. (2017). Apolipoprotein E4 Impairs Neuronal Insulin Signaling by Trapping Insulin Receptor in the Endosomes. *Neuron*, *96*(1), 115-129.e5. https://doi.org/10.1016/j.neuron.2017.09.003

Zhu, Z.-H., Yang, R., Fu, X., Wang, Y.-Q., & Wu, G.-C. (2006). Astrocyte-conditioned medium protecting hippocampal neurons in primary cultures against corticosterone-induced damages via PI3-K/Akt signal pathway. *Brain Research*, *1114*(1), 1–10. https://doi.org/10.1016/j.brainres.2006.07.070